INTERACTIVE BUCKLING IN THIN-WALLED I-SECTION STRUTS

A thesis submitted to Imperial College London for the degree of Doctor of Philosophy

by
Li Bai
MEng ACGI

Department of Civil and Environmental Engineering,
Imperial College of Science, Technology and Medicine
London SW7 2AZ, United Kingdom

May 2014

Declaration:

I confirm that this thesis is my own work and that any material from published or unpublished work from others is appropriately referenced.

Abstract

Compression members, made from slender metallic plate elements, are prone to a wide range of different elastic instability phenomena. A thin-walled I-section strut, made from a linear elastic material, can suffer from the nonlinear interaction between a global (Euler) buckling mode, and a local flange plate buckling mode. The interactive buckling behaviour is usually much more unstable than when the modes are triggered individually and hence significantly reduces the load-carrying capacity of real struts. The current work focuses on such a problem using an analytical approach, the methodology of which has been well established in previous works on sandwich struts and I-section beams.

An analytical model that describes the interactive buckling of a thin-walled I-section strut under pure compression based on variational principles is presented. Analytical formulations combining the Rayleigh–Ritz method and continuous displacement functions are presented to derive a series of systems that comprise differential and integral equilibrium equations for the structural component. Solving the systems of equations with numerical continuation reveals progressive cellular buckling (or *snaking*) arising from the nonlinear interaction between the weakly stable global buckling mode and the strongly stable local buckling mode. The resulting behaviour is highly unstable and when the model is extended to include geometric imperfections it compares excellently with some recently

published experiments.

Imperfection sensitivity studies reveal high sensitivity to both global and local imperfection types. The worst forms of local imperfection are identified in terms of the initial wavelength, amplitude and degree of localization. The effect of the varying rigidity of the joint of the section web and flanges is also studied and a rapid erosion of the cellular buckling response is revealed with increasing rigidity of the flange–web joint. A shell-based nonlinear finite element model is presented, primarily for validation purposes. The results from the analytical and finite element models show a good comparison, particularly for higher rigidities of the flange–web joint.

A parametric study is conducted for two limiting cases, where the flange–web joint is assumed to be fully pinned or fully rigid. For a chosen set of geometries, the most undesirable interactive region is identified for both global and local slendernesses, in terms of the strut length and the flange width respectively. Practical implications are discussed in terms of the idealized buckling design curve. An analytical framework for the structural analysis of the thin-walled I-section struts that exhibit the nonlinear interaction of a global and a local buckling mode, including cellular buckling, has therefore been established.

Acknowledgements

At this moment of time, I feel so grateful to many people who have helped me, in one way or another, in the past three and half years. Firstly, I would like to express my sincere gratitude to my PhD supervisor, Dr M. Ahmer Wadee, whom I first met in 2006 when I started my MEng degree at Imperial. Ahmer has always been able to provide the guidance and the encouragement that I needed throughout my entire research. This thesis will have never been realized without his dedication. As a researcher, Ahmer inspired me in so many ways and it has been a great pleasure to be able to learn from him. Secondly, I would like to thank the Civil and Environmental Engineering Department for providing everything necessary which made my postgraduate study at Imperial so enjoyable. I am indebted to many colleagues that I have worked with, especially Stylianos Yiatros, Maryam Farsi, Chi Hui and Elizabeth Liu who shared my problems and offered me so much help in the past three and a half years. I am also thankful to Professor Leroy Gardner who has always been very close to our research group; his advice was certainly inspiring.

I am deeply indebted to my lovely companion, Yishu Gao, who shared all kinds of emotions with me in the past two years. Without her love and support, it would have been much more stressful during difficult times. Finally, I would like to dedicate this thesis to my parents, Jianying Li and Liang Bai. I could not imagine how difficult it was for them to

let their only child study in a country that is six thousand miles from home. Nevertheless, they always encouraged me to reach a higher level of education and always supported me in every aspects. It was their great love and sacrifice that made the completion of this thesis possible. Therefore, I would like to express my deepest gratitude to my parents and hope they would feel proud when they read this thesis.

Contents

List of Figures

List of Tables

Nomenclature

Coordinates, Stress, Strains, Loads and Energy

x	Transverse direction along flange widths
y	Transverse direction along section depth
z	Longitudinal direction
σ_x, σ_y, σ_z	Direct stress in directions x, y, z respectively
ε_x, ε_y, ε_z	Direct strain in directions x, y, z respectively
τ_{xy}, τ_{xz}, τ_{yz}	Shear stress in planes xy, xz, yz respectively
γ_{xy}, γ_{xz}, γ_{yz}	Shear strain in planes xy, xz, yz respectively
σ_Y	Yield stress
χ	Bending curvature
V	Total potential energy
$\mathcal{L}$	Lagrangian
U_{bo}	Global bending energy
U_{bl}	Local bending energy
U_m	Membrane energy
U_d	Membrane energy from the contributions of direct strains
U_s	Membrane energy from the contribution of shear strains

U_{sp}	Energy stored in discrete springs
P	Applied axial load
P^C	Critical load
P_o^{C}	Global critical buckling load
σ_o^{C}	Global critical buckling stress
P_l^{C}	Local critical buckling load
σ_l^{C}	Local critical buckling stress
P_U	Ultimate load
P_E	Euler load
P^{M}	Maxwell load
p	Nondimensional normalized load
p_U	Normalized ultimate load
C	Critical bifurcation point
S	Secondary bifurcation point
$C1...C11$	Cell number
$\mathcal{E}$	Total end shortening

Section and material properties

L	Strut length
b	Total flange width
b_f	Flat width of the flange
h	Total cross-section depth
t	Flange thickness
t_w	Web thickness

A	Cross-section area
E	Young's modulus
ν	Poisson's ratio
I	Second moment of area of cross-section
r	Radius of gyration
D	Plate flexural rigidity
G	Shear modulus
c	Rotational stiffness of springs
λ_o, λ_l	Global and local slendernesses respectively
$\bar{\lambda}_o$, $\bar{\lambda}_l$	Normalized global and local slendernesses respectively

Displacement functions and generalized coordinates

$W(z)$	Lateral displacment (sway component)
$\theta(z)$	Rotation of the plane section (tilt component)
q_s	Amplitude of the sway component
q_s^{S}	q_s at secondary bifurcation point
q_t	Amplitude of the tilt component
Δ	Pure in-plane compressive strain
$w(x,z)$	Local out-of-plane displacement of the flange plates
w_{max}^{U}	Maximum $w(z)$ at ultimate load
$u(x,z)$	Local in-plane displacment of the flange plates
$w_1(x,z)$	$w(x,z)$ of the more compressive side of the flange plates
$u_1(x,z)$	$u(x,z)$ of the more compressive side of the flange plates
$w_2(x,z)$	$w(x,z)$ of the less compressive side of the flange plates

$u_2(x,z)$	$u(x,z)$ of the less compressive side of the flange plates
$f(x)$	Transverse component of $w(x,z)$
Λ	Wavelength of $w(z)$

Imperfections

χ_0	Initial curvature
W_0	Initial out-of-straightness of global mode
θ_0	Initial rotation of the plane-section
q_{s0}	Amplitude of W_0
q_{t0}	Amplitude of θ_0
w_0	Initial out-of-plane displacement of the flange plates
A_0	Amplitude of w_0
α	Degree of localization
$\beta\pi/L$	Wave number
$\mathcal{E}_0$	Initial total end shortening

Chapter 1

Introduction

Thin-walled structures generally refer to structural components which consist of one or more thin plates or shells connected together at one or more common edges. The definition of thin-walled is fairly vague; a general definition for thin-walled members would be such that the plate elements having a relatively large width to thickness ratio. Thin-walled structures, including various structural types such as plates, girders, beams, columns and shells, have a wide range of applications in many fields such as in the sporting and automotive industries, alongside the fields of aeronautical, mechanical and civil engineering. Structural components with thin-walled elements can be made of approximately isotropic materials such as steel and aluminium, or anisotropic and orthotropic materials such as laminated composites. For different applications, thin-walled elements can be relatively easily formed into open or closed, singly or doubly symmetric cross-sections, as shown in Figure 1.1 (van der Neut, 1969; Brockenbrough & Merritt, 1999). They provide good strength and stiffness with a relatively small amount of material. Designers have been taking the advantage of this weight efficiency in various applications where self-weight of the structure is a key design factor. The application of thin-walled structures continues

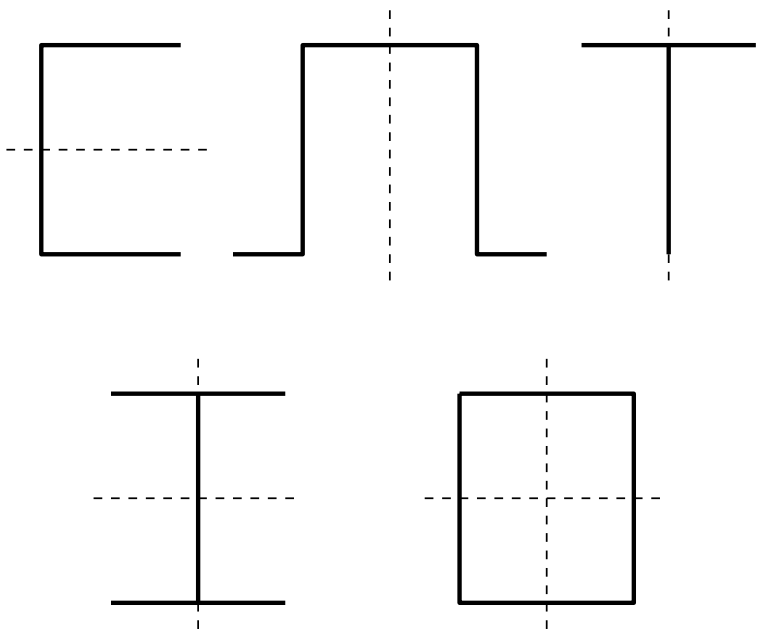

Figure 1.1: Different types of thin-walled structural cross-sections including a C-section, hat section, T-section, I-section and box section (from top left to bottom right). Dashed lines show the lines of reflective symmetry.

to grow in number as new and innovative designs are developed.

1.1 Applications

In aeronautical engineering applications, structural components with thin-walled elements are extensively used in aircraft, space vehicles and satellites. Stiffened panels, for example, are very commonly found in many iconic aircraft such as the Concorde supersonic airliner, Figure 1.2(a), the Boeing 747 family and most lately the commercial aircraft from Airbus, the double-decker $A380$, Figure 1.2(b). The locations that utilize thin-walled elements are almost everywhere including the wings, fuselage, tails, as well as interior components. Composite structures such as sandwich panels, made from two stiff metallic plates separated by a soft core material, are also widely used in aircraft construction. A major step

(a) Concorde supersonic airliner, photograph taken from Orlebar (2004).

(b) Airbus A380, photograph taken from Norris and Wagner (2005).

Figure 1.2: Iconic aircrafts made from structural components with thin-walled elements.

towards composite materials in commercial aeroplanes was perhaps the Boeing-NASA ACEE program in 1975. In 1984, five Boeing 737-200 airplanes, fitted with experimental composite horizontal stabilizers were placed into regular service. The graphite epoxy composite material, NARMCO T300-5208 (Tsai, 1979), replaced aluminium in a co-cured, stiffened-skin structural box arrangement with I-section stiffener panels. Since composite structures have a very high strength to weight ratio, they have been increasingly popular in aircraft construction over the recent decades. The recent Boeing 787 Dreamliner, for example, comprises approximately 50% composites, 20% aluminum and 15% titanium in terms of total weight (Wagner & Norris, 2009).

In civil engineering applications, thin-walled structures are commonly found in buildings, bridges, nuclear and defence structures, and offshore structures. Figure 1.3(a) shows a cold-formed steel thin-walled frame comprising lipped C-section columns. These are commonly found in residential and commercial buildings, temporary structures, roof trusses and warehouses. Stiffened plates are found in long span bridges, such as the famous Humber Bridge in the UK that had the longest span in the world of 1.41km when it was completed (Kawada, 2010). The lower face of the box-girder bridge deck is essentially made from steel plates with longitudinal T-section stiffeners welded to form the stiffened panel, as shown in Figure 1.3(b). Cold-formed, thin-walled, metallic elements are also

(a)

(b)

Figure 1.3: Thin-walled structures in civil engineering applications; (a) a typical thin-walled frame, available from `http://www.sem.cee.vt.edu/research/thin_walled_structures.html`, and (b) the Humber Bridge box-girder lower flange with stiffened plates.

commonly used as purlins, roof sheeting and wall cladding to minimize the self-weight of the integral structure without compromising on strength and stiffness. Other applications of thin-walled metallic structures include canopies, crane girders, storage tanks and racks as well as a variety of domestic appliances (Schafer, 2011).

1.2 Materials

Structural components with thin-walled elements are associated with a wide range of materials. Examples of these materials and their properties are listed in Table 1.1. Steel is perhaps the most commonly used material in civil engineering applications. Mild steel is usually produced at a relatively low cost while it provides material properties that are acceptable in many applications. Owing to its much higher corrosion resistance, stainless steel is sometimes used in highly vulnerable environments, such as in the chemical, wastewater and food processing industries. The production method is another key factor that affects the material properties of steel. The hot-rolling process is usually adopted for manufacturing relatively compact universal columns and beams, whereas the cold-forming

Material	ρ (kg/m^3)	E_x (kN/mm^2)	E_y (kN/mm^2)
Mild Steel	7800	206	206
Stainless Steel	7800	206	206
Aluminium Alloy	2700	73	73
Titanium	4500	108	108
GFRP	1800	39	8
CFRP	1600	180	10

Table 1.1: Mechanical properties of some materials commonly used in engineering applications. The quantity ρ is the material density; E_x and E_y are the Young's moduli in two orthogonal directions of the material.

process is usually adopted for manufacturing thin steel plates and sheeting. Compared to the hot-rolled sections, cold-formed steel (Tata Steel, 2011) generally has a higher yield stress and less ductility due to the work hardening effect during the cold rolling process, as shown by the stress–strain curves in Figure 1.4 (Den Hartog, 1961). As mentioned

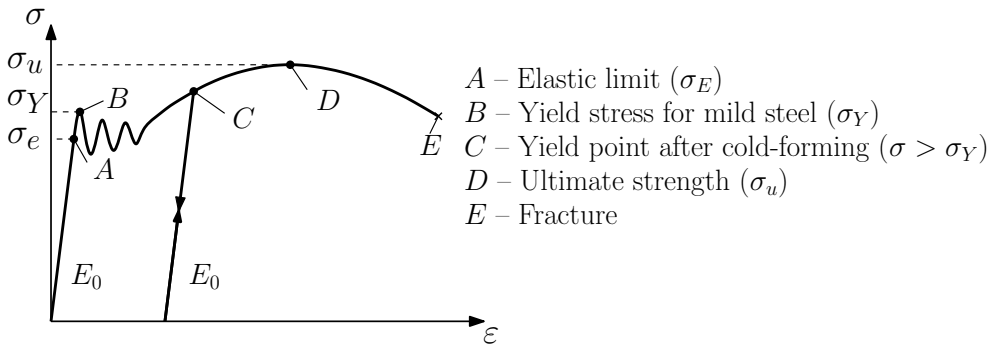

Figure 1.4: Stress–strain curve for mild steel including the effect of cold working.

above, aluminium alloys and titanium are also commonly found in aeronautical engineering applications. Carbon-fibre reinforced polymers (CFRP), glass-fibre reinforced polymers (GFRP) are typical materials used for thin face plates in sandwich structures.

1.3 Research objectives

Since thin-walled structures tend to be slender, they are vulnerable to buckling instabilities at the local as well as the global scales. The current research focuses on investigating the interactive buckling phenomenon of a global (flexural) and a local (plate) buckling mode in thin-walled I-section steel columns. It was found in the literature that such columns may exhibit an Euler buckling mode, where flexure about the column weak axis occurs, and a local buckling mode primarily within the flange plates. When the two buckling modes are triggered in combination, the resulting response is usually far more unstable than when they are triggered individually. This problem has been studied experimentally and numerically by Becque and Rasmussen (2009a; 2009b) recently. An example of the test specimen before and after the experiment is shown in Figure 1.5. The current research

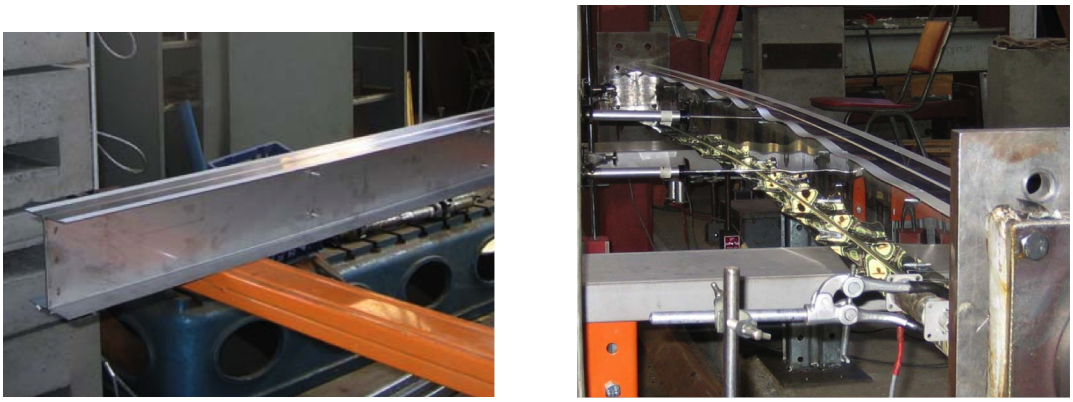

(a) (b)

Figure 1.5: Experiments by Becque and Rassmussen (2009a), showing interactive buckling phenomenon in thin-walled I-section columns made of stainless steel.

will study the same problem but from an analytical approach, for a strut made from an elastic, homogeneous and isotropic material. The primary objectives are given as follows:

- To investigate the potentially dangerous interaction between a global and a local

buckling mode in terms of the deformation and the nonlinear mechanical response.

- To investigate the effect of different types of imperfections in reducing the load-carrying capacity and to identify the most severe form of imperfections.
- To investigate the effect of varying the rigidity of the flange–web connection in terms of the deformation and the mechanical response.
- To investigate the buckling and the post-buckling behaviour of the strut with different global and local slenderness such that the most dangerous interactive zone, which can be designed for with caution, are identified in terms of the strut length and the flange widths.

1.4 Thesis outline

The present thesis contains seven chapters, a brief outline of those that follow is given below.

1.4.1 Literature review

Chapter 2 comprises a literature review, starting from the basic buckling theory to the more specific interactive buckling phenomenon in thin-walled structures. The chapter reviews different research works including those presenting relevant analytical, experimental and numerical developments. Also reviewed in some depth are the analytical works by Hunt and Wadee (1998) and Wadee and Gardner (2012), on sandwich struts and thin-walled I-section beams respectively. A similar methodology is used to develop the analytical models for the thin-walled I-section strut in the following chapters.

1.4.2 Cellular buckling thin-walled I-section struts

An analytical model is developed in Chapter 3 for the thin-walled I-section strut based on total potential energy principles. It is assumed that the web provides no more than a simple support to the flanges. A system of equilibrium and integral equations is derived from a variational formulation. The equations are first solved numerically for the perfect system using the software package AUTO (Doedel & Oldeman, 2009). The cases where either local buckling or global buckling is critical are considered in turn. For validation purposes, a global type of imperfection – an initial out-of-straightness is introduced to the perfect system, and the results are compared favourably against the experimental and numerical works by Becque and Rasmussen (2009a; 2009b).

1.4.3 Imperfection sensitivity studies

The analytical model in Chapter 3 is further developed to include a local imperfection – an initial out-of-plane deflection in the flange plates. Imperfection sensitivity studies are conducted for three cases in Chapter 4. The first case considers the global imperfection only, for the case where global buckling is critical. The second case considers local imperfections only, again for the case where global buckling is critical, and the third case considers both types of imperfections, for the case where local buckling is critical. The latter two cases also identify the worst form of local imperfection, in terms of the wavelength and the degree of localization of the initial out-of-plane flange deflection.

1.4.4 Rigidity of the flange–web connection and finite element modelling

As mentioned above, the analytical models in Chapter 3 and 4 are associated with an assumption such that the joint between the web and the flanges is pinned. Chapter 5 presents an extension to the earlier model by including a rotational spring at the flange–web joint, for the case where global buckling is critical. By varying the rotational stiffness parameter, investigations are conducted for a series of cases ranging from a pin joint to essentially a fully rigid joint between the web and the flanges. A finite element model is developed in the commercial software package Abaqus (Abaqus, 2011), the results from which are then compared against the analytical model with good results.

1.4.5 Parametric studies

Chapter 6 comprises a parametric study for the limiting cases where the web is assumed to provide a pinned or a fully rigid support to the flanges. The study focuses on changing the global and the local slendernesses by varying the strut length and the width of the flange plate respectively. The investigation highlights, within a particular parametric space, the interactive region. This is where the strut exhibits post-buckling equilibrium paths with distinctive characteristics, the features of which explicitly include localization and cellular buckling. This is in terms of the deformation and the sudden change from stability to instability, in terms of the nonlinear mechanical response. A deflection based criterion is used to define the interactive region and a methodology is developed such that designers may be able to evaluate the potential dangers of such instabilities in the elastic range.

1.4.6 Conclusions and Further work

Chapter 7 presents some general conclusions to the thesis. Some potential areas for further investigation are also highlighted.

Chapter 2

Literature review

2.1 Nonlinear buckling of compression members

It is well known that metallic structural components might fail in different ways. The failure mechanism of tension members is often governed by the material properties such as the yield stress. For compression members, however, the failure mechanism is normally associated with instability issues whereby members suffer from some kind of buckling phenomenon. Various buckling phenomena associated with different structural components have been studied by a vast number of researchers in the past decades. The history of buckling theory dates back to the middle part of the 18^{th} century, when Euler (1744) studied the buckling phenomenon of an incompressible, axially-loaded simply supported thin strut, or elastica, as shown in Figure 2.1(a). He described the mechanics of the strut using a mathematical technique that he had devised, known as 'the calculus of variations'; the governing differential equation for the strut for small deflections being expressed as:

$$EI\frac{\mathrm{d}^4 w}{\mathrm{d}x^4} + P\frac{\mathrm{d}^2 w}{\mathrm{d}x^2} = 0, \tag{2.1}$$

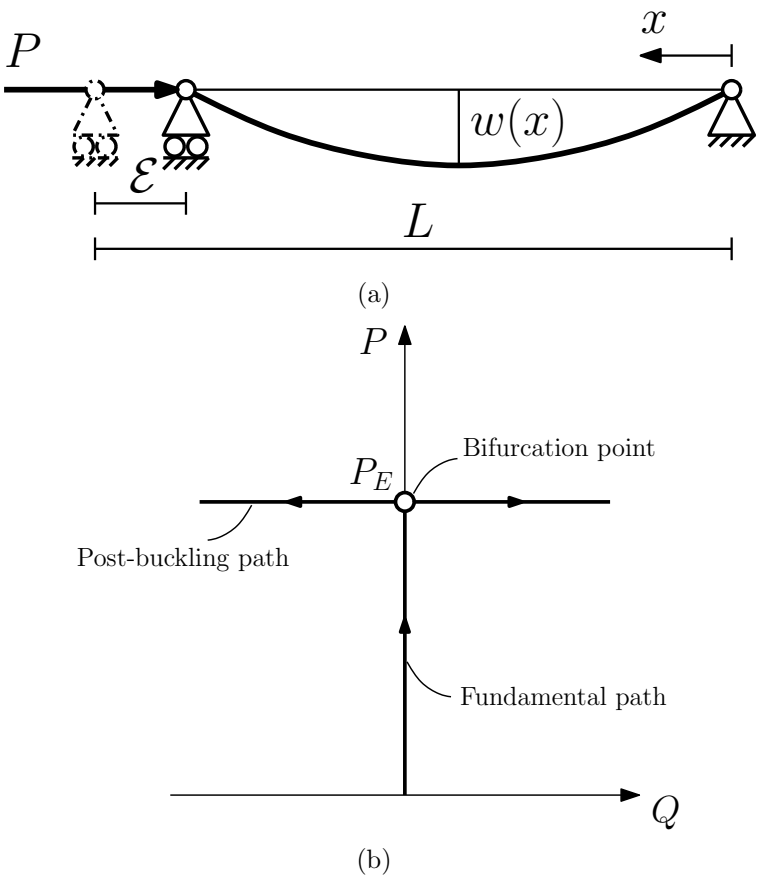

Figure 2.1: The Euler strut with (a) showing the loaded strut with flexural rigidity EI and deflection $w(x)$; (b) shows the load–deflection graph of P versus the modal amplitude Q. The post-buckling equilibrium path is shown as a flat line, which is a small-deflection approximation.

where EI is the strut flexural rigidity, a measure of its bending stiffness, P is the applied axial force and w is the lateral deflection. Note that E is the material Young's modulus and I is the strut cross-section second moment of area. For pin-ended conditions, this equation has a trivial solution $w = 0$, but non-trivial solutions exist for:

$$w_n(x) = Q \sin \frac{n\pi x}{L}, \quad P_n = \frac{n^2 \pi^2 EI}{L^2}, \tag{2.2}$$

where n is an integer and Q is the amplitude of the deflection. The lowest value of P_n is of course associated with $n = 1$ and it becomes the well-known *Euler load* (P_E), where:

$$P_E = \frac{\pi^2 EI}{L^2}. \tag{2.3}$$

The buckling of the strut is known as a *bifurcation* problem since $w = 0$ for the initial equilibrium but once the load reaches P_E, the solution $w = 0$ loses stability and the strut has equal probability of exhibiting positive or negative lateral displacement. This is shown by the load–deflection relationship sketch in Figure 2.1(b), which shows the relationship when small deflections are assumed.

Another classic buckling problem is that of a plate. An early piece of work on plate buckling is associated with St. Venant (1883), who derived the governing partial differential equation describing the buckling of an in-plane uniaxially loaded rectangular elastic plate:

$$\frac{\partial^4 w}{\partial x^4} + 2\frac{\partial^4 w}{\partial x^2 \partial y^2} + \frac{\partial^4 w}{\partial y^4} + \frac{\sigma t}{D}\frac{\partial^2 w}{\partial x^2} = 0, \tag{2.4}$$

as represented in Figure 2.2, where w is the out-of-plane deflection of the plate, σ is the applied stress in the longitudinal x-direction, t is the plate thickness and D is the plate flexural rigidity. Note that for the chosen example, all edges of the plate are assumed to be simply supported. The equation was solved by Bryan (1891) for simply supported

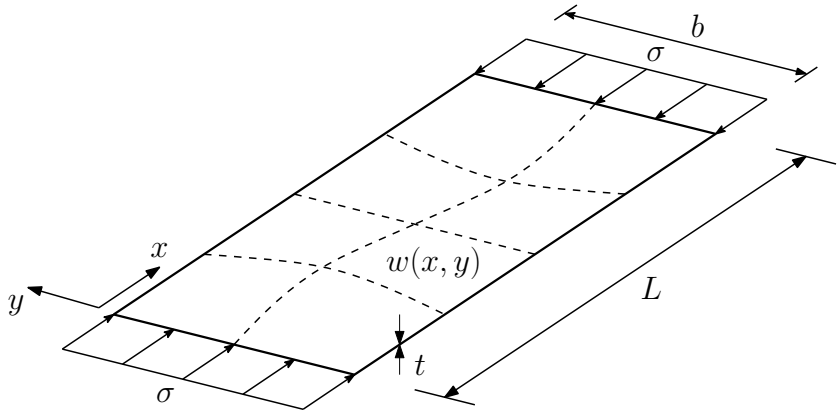

Figure 2.2: An example of elastic buckling in a simply supported plate with width b, length L and thickness t.

edges and later on by Timoshenko (1910) for other boundary conditions. Linear buckling analysis provides important information on critical loads and the buckling mode profile, not only for struts and columns, but also for other structural components such as plates

and shells (Timoshenko & Gere, 1961). However, it is well known now that plates exhibit a strongly stable post-buckling equilibrium path, implying that the structure is able to carry an increasing load as the deformation progresses. Moreover, shells can only carry a reduced load once buckling occurs (Thompson & Hunt, 1973; Wadee, 2007). It is therefore important to study the post-buckling behaviour of structures in order to investigate the true load-carrying capacity and to design safe and economical structures.

It is for the analysis of post-buckling behaviour for which geometric nonlinearities must be accounted. Euler's work on the elastica, for example, investigated in fact both the pre-buckling and the nonlinear post-buckling behaviour of the particular problem. It was not until the middle of the 20^{th} century that Koiter (1945) provided a general approach to conduct nonlinear post-buckling analysis on a wide range of structural components including struts, plates and cylindrical shells. The governing differential equations of equilibrium were derived from minimizing a continuous nonlinear potential energy functional V that is formulated over a domain S:

$$V = \int_S \mathcal{L}\,\mathrm{d}S, \tag{2.5}$$

where $\mathcal{L}$ is similar to the Lagrangian function from dynamical systems theory (Fox, 1987). For equilibrium, the total potential energy V must be stationary and so the first variation of the total potential energy δV must be zero. Solving the equilibrium equations, it was found that struts and plated structures normally exhibit a stable post-buckling response whereas cylindrical shells exhibit an unstable post-buckling response, as sketched in the load–deflection graphs in Figure 2.3. It is clear that systems exhibiting an unstable post-buckling response are highly sensitive to initial imperfections, indicating a significant reduction in the load-carrying capacity of real structures when compared against the theoretically perfect ones. It is therefore potentially dangerous or wasteful to ignore nonlinear effects in the design of real structures.

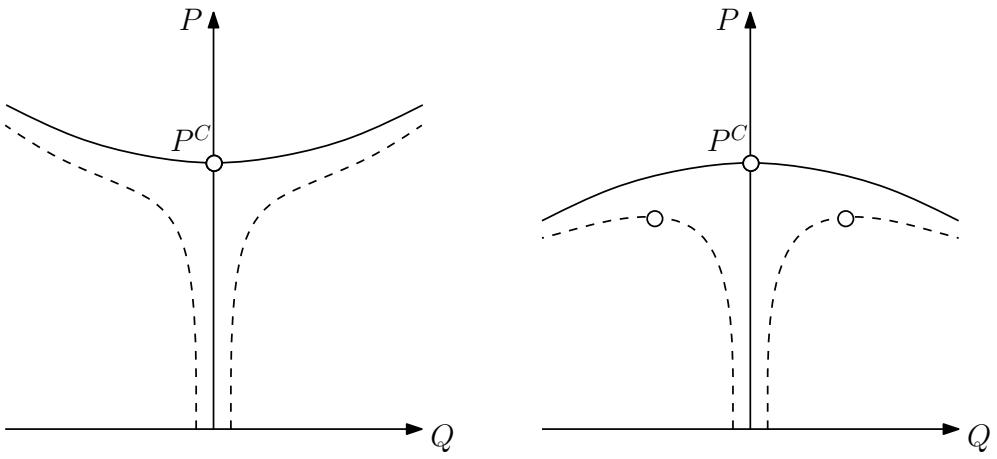

(a) Stable–symmetric (supercritical) bifurcation

(b) Unstable–symmetric (subcritical) bifurcation

Figure 2.3: Stable and unstable post-buckling characteristics. Graphs show the applied load P versus the modal amplitude Q; solid and dashed lines represent the perfect and imperfect cases respectively.

Koiter's pioneering work was progressed by Thompson and Hunt (1973) by applying the total potential energy principles to a discretized system, leading to the development of a systematic perturbation method of post-buckling analysis, which was also found in parallel works by Sewell (1965; 1970). In that formulation, the total potential energy V was expressed in terms of a system of discrete coordinates or modal amplitudes, Q_i:

$$V = V(Q_1, Q_2, .., Q_i, .., Q_n). \tag{2.6}$$

For any static system to be in an equilibrium state, the following condition must be satisfied:

$$V_i = \frac{\partial V}{\partial Q_i} = 0, \tag{2.7}$$

which can be proved by Newton's laws of motion. To examine the stability of any equilibrium state, the second derivatives of V with respect to the generalized coordinates must be considered:

$$V_{ij} = \frac{\partial^2 V}{\partial Q_i \partial Q_j}. \tag{2.8}$$

For the equilibrium state to be stable, the matrix of $\mathbf{V}_{ij}$ must be positive-definite. Singularity in the matrix of $\mathbf{V}_{ij}$ indicates that the equilibrium state is critical; hence quadratic

terms in V give information on critical loads but higher order terms are necessary for post-buckling analysis (Thompson & Hunt, 1973). Fundamental to the perturbation method of post-buckling analysis are two axioms that respectively relate V to equilibrium and stability:

- **Axiom 1** *A stationary value of the total potential energy with respect to the generalized coordinates is necessary and sufficient for the equilibrium of the system.*
- **Axiom 2** *A complete relative minimum of the total potential energy with respect to the generalized coordinates is necessary and sufficient for the stability of an equilibrium state.*

Note that the axioms apply to elastic systems under conservative static loading.

In addition to geometric nonlinearities, the buckling of compression members with nonlinear material properties has also been the subject of research in the past decades. Perhaps the first practical insight into the inelastic buckling of columns was provided by Shanley (1947), where the conventional approach of the usage of the reduced-modulus, E_r, in determining the critical load, which was regarded as the ultimate column strength within the plastic range of the material constitutive relationship, was first questioned. The reduced modulus E_r was greater than E_t, but less than E, where E_t is the tangent modulus, *i.e.* the instantaneous slope of the stress–strain curve in the nonlinear plastic range. Shanley stated that it is impossible for the column to remain straight until the applied axial compression reaches $P_r = \pi^2 E_r I/L^2$, because if this were true the whole cross-section of the column would have a stiffness proportional to E_t. The buckling load would hence be governed by $P_t = \pi^2 E_t I/L^2$ which is lower than P_r. The fact that the column starts to deflect at P_t would violate the initial assumption of column being straight until P_r.

Instead, the column would begin to deflect at P_t. Shanley also stated that strain reversal must occur at P_t on the less compressed side of the member when the column starts to bend. This means that some compression would be released on the convex side where strain hardening would take place. During unloading, the corresponding stiffness would become the original Young's modulus as for the elastic range, as shown in Figure 2.4(a). This increase in stiffness is responsible for a higher load carrying capacity. The above

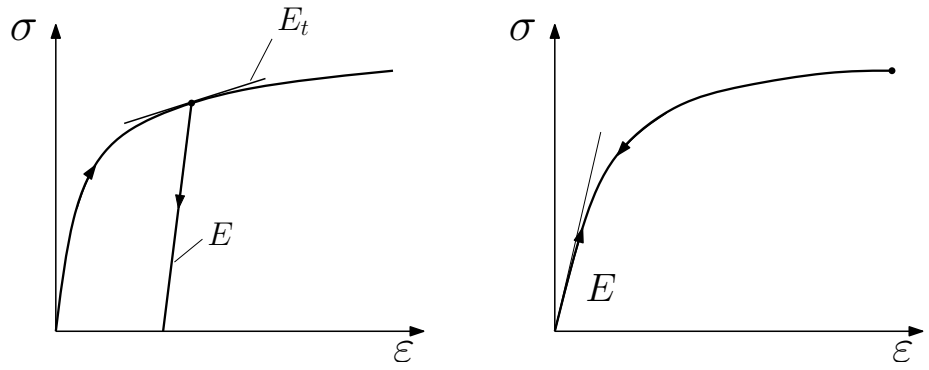

Figure 2.4: Strain reversal in (a) inelastic and (b) nonlinear elastic systems, where E_t is the tangent modulus.

statements were demonstrated by studying a simplified model which consisted of a two-legged hinged column in which the hinge consisted of a unit 'cell' formed from two axial elements. On the other hand, if only the elastic buckling of the column was considered, the release of the compressive stress in the convex side after buckling would follow the initial stress–strain curve in reverse until the compressive strain becomes tensile as shown in Figure 2.4(b).

2.2 Interactive buckling phenomena

It is commonly found in practice that structural components may exhibit more than one buckling mode during the loading history. Although the behaviour of the individual

buckling modes might be well understood, when these buckling modes are triggered in combination, the behaviour of the system is normally much more complex than when they are triggered individually (Budiansky, 1976). A major step towards a general theory for nonlinear coupled instability problems is associated with Supple (1967). The work focused on elastic systems with two-degrees-of freedom that exhibited symmetric bifurcations; equilibrium equations were derived for uncoupled and coupled modes based on total potential energy principles. The total potential energy V was a function of the load p and the deflection u_i, thus:

$$V = V(u_i, p), \tag{2.9}$$

where $i = 1, 2$. A perturbation scheme allowed the development of the equilibrium equations for the doubly symmetric system, in a truncated form of a power series:

$$\begin{aligned} V_{11}u_1 + \frac{1}{3!}(V_{1111}u_1^3 + 3V_{1122}u_1u_2^2) + \delta p V'_{11}u_1 = 0, \\ V_{22}u_2 + \frac{1}{3!}(V_{2222}u_2^3 + 3V_{1122}u_1^2u_2) + \delta p V'_{22}u_2 = 0, \end{aligned} \tag{2.10}$$

where a subscript i on V denotes partial differentiation with respect to the corresponding generalized coordinate u_i; a prime on V denotes partial differentiation with respect to p and δp is the incremental change in p from a known state p_0. For uncoupled modes ($u_1 = 0$ or $u_2 = 0$), evaluating Equation (2.10) at the corresponding critical loads leads to $V_{11}^{\mathrm{C}} = 0$ and $-(V_{22}/V'_{22})|^{\mathrm{C}} = \Delta p$, where Δp is the difference between the critical loads of the two modes ($i = 1, 2$). Equation (2.10) thus simplifies to:

$$\begin{aligned} \delta p &= -\frac{1}{3}\frac{V_{1111}}{V'_{11}}u_1^2, \\ \delta p &= \Delta p - \frac{1}{3}\frac{V_{2222}}{V'_{22}}u_2^2. \end{aligned} \tag{2.11}$$

It was found that the system would exhibit a stable or unstable symmetric bifurcation when $V_{iiii} > 0$ and $V_{iiii} < 0$ respectively. For coupled modes, a relationship between u_1 and u_2 was obtained on eliminating δp from Equation (2.10), thus:

$$Xu_1^2 + Yu_2^2 = -6V'_{11}V'_{22}\Delta p, \tag{2.12}$$

where X and Y are the coefficients given by the following expressions:

$$\begin{aligned} X &= V'_{22}V_{1111} - 3V'_{11}V_{1122}, \\ Y &= 3V'_{22}V_{1122} - V'_{11}V_{2222}. \end{aligned} \tag{2.13}$$

It was found that the behaviour of the coupled modes are predominantly controlled by the coefficients X and Y, where each can be positive or negative. Supple summarized the solutions for various conditions of X, Y and Δp. In general, for $\Delta p \neq 0$, there are two types of solutions, represented by an ellipse and a hyperbola in the u_1u_2 plane, shown in Figure 2.5. The post-buckling stability for different conditions of X, Y and Δp was

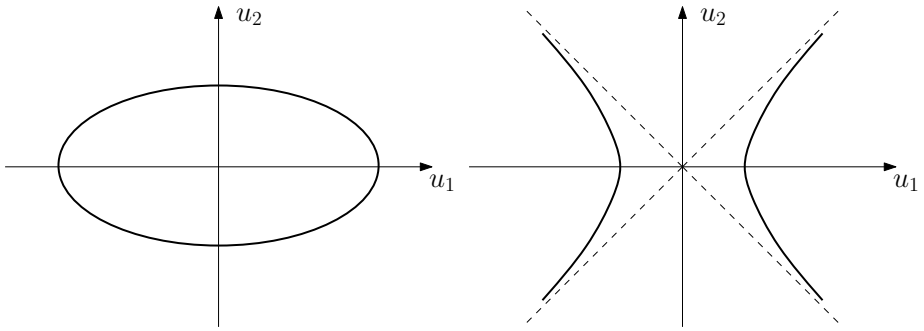

(a) Elliptic (b) Hyperbolic

Figure 2.5: Major forms of coupled solutions relating generalized coordinates in the post-buckling range.

summarized into four theorems. The work highlighted an important feature such that the post-buckling behaviour from the coupled instabilities can be unstable, even if individual modes exhibit a stable symmetric bifurcation. Parallel work was conducted by Chilver (1967) with the focus being on both symmetric and asymmetric systems; the work also applied the general theory to a structural model comprising three rigid links hinged at the joints and restrained at their mid-span by elastic translational springs. This phenomenon is also known as *interactive* buckling where one degree of freedom destabilizes the structure in another.

Various types of structural components that exhibit interactive buckling have been stud-

ied analytically (Lundquist & Stowell, 1942a; Lundquist & Stowell, 1942b; van der Neut, 1969; van der Neut, 1973; Koiter & Pignataro, 1976; Møllmann & Goltermann, 1989; Goltermann & Møllmann, 1989; Hunt & Wadee, 1998; Wadee & Gardner, 2012), whereas a large number of numerical studies such as the implementation of the finite element and finite strip methods (Rajasekaran & Murray, 1973; Johnson & Will, 1974; Plank & Wittrick, 1974) have also been carried out in the past decades. Experimental studies (Cherry, 1960; Menken *et al.*, 1997; Becque & Rasmussen, 2009a) have also found the highly unstable nature of the mode interaction in various examples. An illustrative example is the reticulated column (Thompson & Hunt, 1973), also known as a built-up or compound column, where small elements are assembled together to form a large compression member, as shown in Figure 2.6. It is clear that in addition to the global buckling mode, in

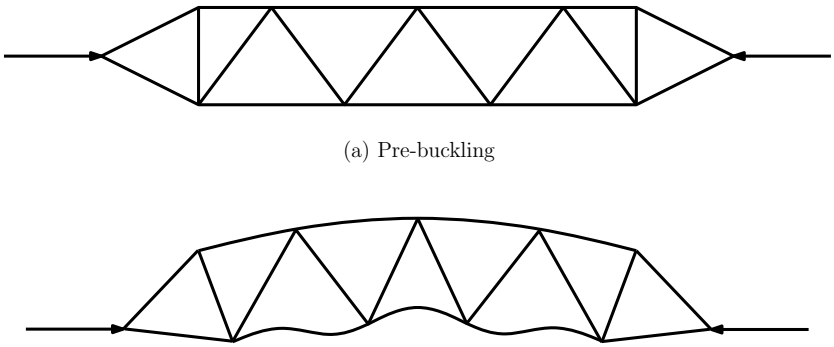

(a) Pre-buckling

(b) Interactive post-buckling

Figure 2.6: Reticulated or compound column; (a) initial configuration and (b) possible interactive buckling mode combining global and local modes.

this specific case the Euler buckling mode, individual elements may also buckle locally in the more compressive side of the globally bent structure. The resulting behaviour can be undesirably unstable.

Cylindrical shells (Hutchinson & Koiter, 1970; Hunt *et al.*, 1986; Shen & Chen, 1991) may also exhibit the nonlinear interaction between different buckling modes, leading to the classic diamond buckling mode pattern (Hunt & Lucena Neto, 1991; Lord *et al.*, 1997;

Hunt *et al.*, 2003), as sketched in Figure 2.7(a). Despite the fact that cylindrical shells are

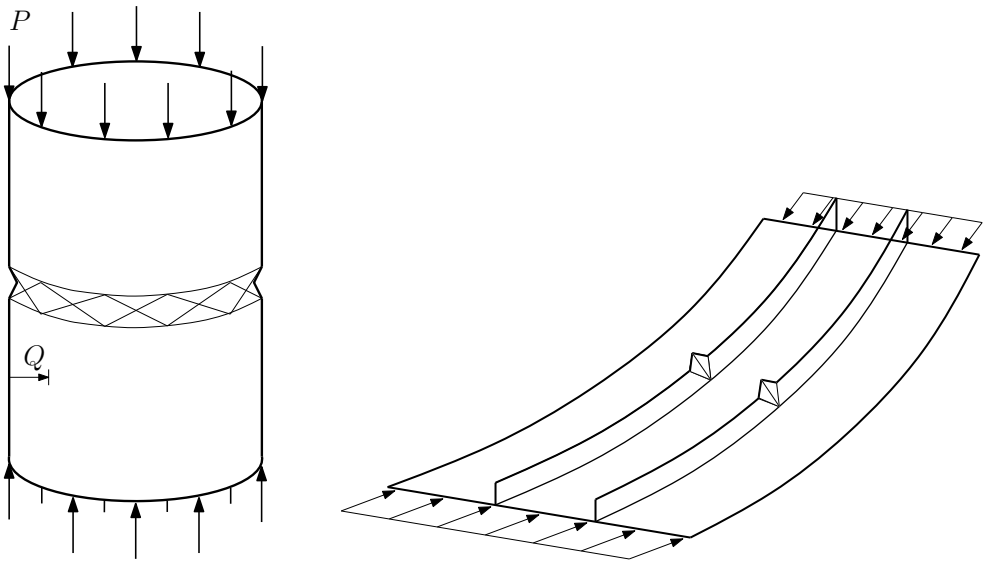

(a) Cylindrical shell (b) Stiffened plate

Figure 2.7: Examples of structural components exhibiting interactive buckling.

normally regarded as the most efficient structural component to carry axial compression, the post-buckling behaviour is highly unstable due to the nonlinear interaction of the buckling modes.

Plated structures are also susceptible to interactive buckling, such as stiffened plates (Murray, 1973; Koiter & Pignataro, 1976; Wadee & Farsi, 2014), Figure 2.7(b), I-section columns and beams (Hancock, 1981; Menken *et al.*, 1991; Wadee & Gardner, 2012) and sandwich panels (Allen, 1969; Hunt *et al.*, 1988; Hunt & Wadee, 1998; Wadee *et al.*, 2010); such components are widely used in bridge and aircraft construction where mass is a critical design variable. Although individual plates exhibit stable post-buckling behaviour, the nonlinear interaction with the global mode often leads to a reduction in the post-buckling stiffness. Structural components exhibiting nonlinear mode interaction, leading to an unstable post-buckling response can also be highly imperfection sensitive (Wadee, 2000; Saito & Wadee, 2009). Designers must therefore exercise great caution in predicting

the true load-carrying capacity for the aforementioned structural types.

2.2.1 Analytical studies

Perhaps the most classic piece of work on the interactive buckling of columns is associated with van der Neut (1969). He studied the interaction of local and global (Euler) buckling of an idealized thin-walled compression member, which comprised two load carrying flanges with width b, thickness h and length L, and a web with depth $2c$ that was laterally rigid and had no longitudinal stiffness, as shown in Figure 2.8. A perfect column, a column with an initial local deformation in the flanges and a column with an initial out-of-straightness were investigated, by first considering the stiffness reduction factor η. This quantity was expressed as:

$$\eta = \frac{\mathrm{d}P/P_l}{\mathrm{d}\varepsilon/\varepsilon_l}, \tag{2.14}$$

where P and ε were the applied compressive force and the direct strain within the flanges respectively and P_l and ε_l were the local critical buckling load and the direct strain at this load state within the flat flanges. The quantity η indicated the reduction of the flexural stiffness after the flanges had buckled locally. For the perfect column, the ratio of the slope of the P–ε relationship after local buckling almost remains at a constant value of 0.4083 (Hemp, 1945), indicating that the stiffness dropped by approximately 60% due to the flange plate buckling. By fixing the flange width b and thickness h, the investigation examined the impact of the column length L on the critical buckling mode and the stability of the corresponding critical state. The findings are summarized in Table 2.1. The results in Table 2.1 are also illustrated by the classic curves shown in Figure 2.8. Note that K is the applied compression on the entire strut (as distinct from P) with K_E and K_l being the Euler load and the local buckling critical load respectively. It should be noted that L_0 corresponds to the point where the Euler load is reduced by a factor given by the

Category	Column Length	Critical mode	Post-buckling characteristics
1	$L \geqslant L_1$	Euler buckling	Neutral (approx)
2	$L \leqslant L_2$	Local buckling	Neutral (approx)
3	$L_2 \leqslant L \leqslant L_0$	Local buckling	Stable
4	$L_0 \leqslant L \leqslant L_1$	Local buckling	Unstable

Table 2.1: Critical buckling modes and post-buckling characteristics for the column length constraints in categories 1–4, Length $L = L_1$ is the case where the local buckling load and Euler buckling load are equal; $L_2 = \eta^{1/2} L_1$; $L_0 = (2\eta/1+\eta)^{1/2} L_1$.

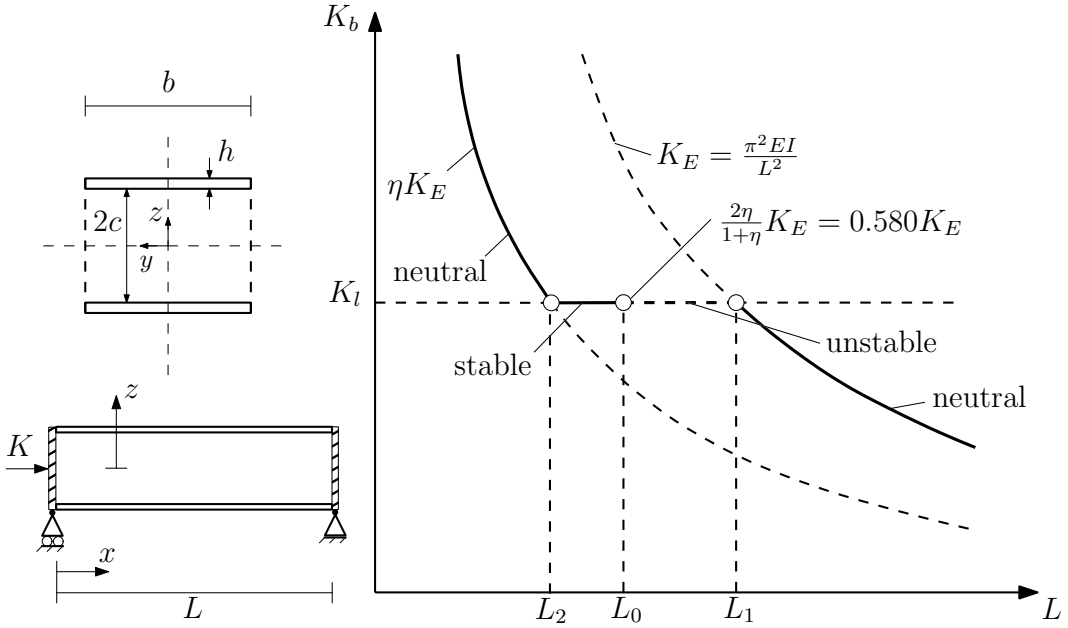

(a)

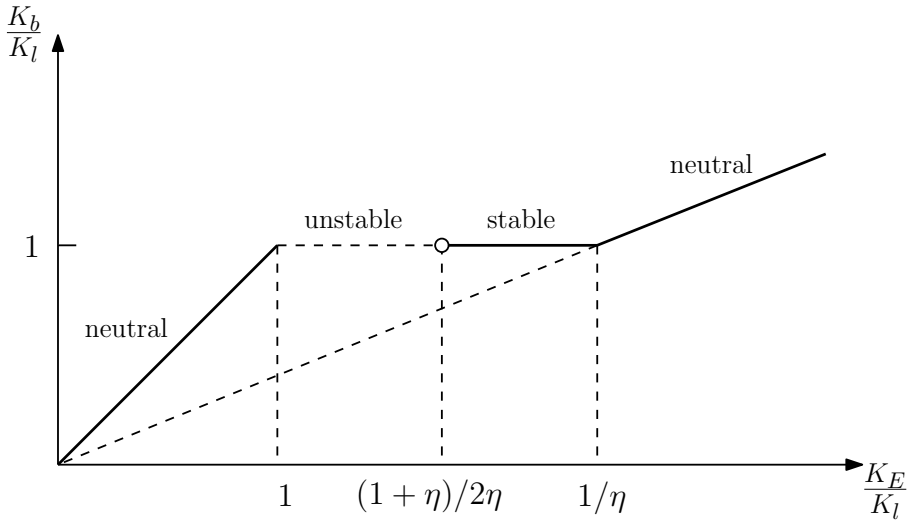

(b)

Figure 2.8: The van der Neut strut and curves.

Engesser 'double-modulus' formula:

$$R_d = \frac{2\eta_o\eta_u}{\eta_o + \eta_u}, \tag{2.15}$$

where η_o and η_u are the stiffness reduction factors within the compression and tension flanges respectively. As Euler buckling takes place, more compression would be accumulated in one flange causing further local buckling, whereas the other flange would be subjected to unloading causing it to return to the unbuckled state. In this situation, $\eta_o = 1$ and $\eta_u = 0.4083$, and the reduction factor R_d, for this case, would therefore be 0.580.

An initial local imperfection was then introduced to the flanges; the expression being given by:

$$z = \alpha h \cos\left(\frac{\pi y}{b}\right) \sin\left(\frac{\pi x}{L}\right), \tag{2.16}$$

where α is the imperfection size parameter with x and y being the longitudinal and transverse coordinates, as shown in Figure 2.8(a). In contrast with the perfect case, where the stiffness remains constant until local buckling occurs, the stiffness would begin to drop as the load is applied. The stiffness reduction factor η is therefore a function of P and ε as well as the imperfection parameter α. It was found that the buckling loads for different imperfection amplitudes deviate the most from the perfect case in the vicinity of $P_E/P_l = 1$, where P_E is the Euler load. This was defined as the imperfection sensitive zone, which corresponds to the columns with length $L_0 < L < L_1$ in the perfect case, where the equilibrium state at the critical buckling load is highly unstable.

The study continued to investigate the post-buckling behaviour. A direct equilibrium approach was utilized, which involved bending theory expressions. The bending moment M was given by:

$$M = (P_o - P_u)\, c = -KW, \tag{2.17}$$

where W was the lateral deflection, P_o and P_u were the forces within top and bottom flanges respectively. The curvature κ, to leading order, was given by:

$$\kappa = \frac{\mathrm{d}^2 W}{\mathrm{d}x^2} = \frac{\varepsilon_o - \varepsilon_u}{2c}. \tag{2.18}$$

Since the equilibrium state was investigated in the neighbourhood of the buckling load, P was expanded about the strain at buckling, ε_b as a Taylor series in ε. As stated above, the first derivative of P with respect to ε is given by the stiffness reduction factor, η which was then expanded about the buckling state. The applied load K was expressed as $K_b + k$, where K_b is the buckling load and k is a small perturbation in the vicinity of K_b. Since all these terms were expressed about a known state, a differential equation was formulated for the lateral deflection W as follows:

$$(\eta_b + \theta_b)\, EI \frac{\mathrm{d}^2 W}{\mathrm{d}x^2} + (K_b + k)\, W = 0, \tag{2.19}$$

where

$$\theta_b = \eta_b' \frac{k}{K_l} + \frac{1}{2}\eta_b'' \left(\frac{K_b}{K_l}\right)^2 \frac{W^2}{c^2} - \frac{1}{3}\left(\eta^2\eta'' + \eta\eta'^2\right)_b \frac{c^2}{\varepsilon_l^2} \left(\frac{\mathrm{d}^2 W}{\mathrm{d}x^2}\right)^2, \tag{2.20}$$

and the subscript b indicates the state of buckling. As θ_b approaches zero, the differential equation tends to that for the Euler strut, which has a known solution $W_0 \sin(\pi x/L)$. Van der Neut introduced an additional function w, which was linearly superimposed on this. The differential equation was rearranged and solved for w. The stability of the post-buckling path was then studied by inspecting the first derivative of the load K with respect to both the lateral deflection and the end shortening. It was found that the slope of the equilibrium path of K with respect to W was positive when $\eta'' < 2\eta'^2/\eta$. It was concluded that for the equilibrium at K_b to be stable, both $\mathrm{d}K/\mathrm{d}W$ and $\mathrm{d}K/\mathrm{d}\Delta$ have to be positive, where Δ represents the end-shortening. Columns with an initial out-of-straightness were then investigated by following the same approach as for the local imperfection case. It was concluded that the global imperfection has a minor effect in

reducing the load carrying capacity in comparison with the local imperfection, which in turn has a relatively strong effect.

Based on the van der Neut model, Thompson and Lewis (1972) developed an optimization scheme for both perfect and imperfect columns. To optimize the load-carrying capacity of the column, the weight and thus the cross-sectional area of the column was kept constant. The only independent variable was therefore taken as the flange width b. The optimization scheme first denotes K_E/K_l and K_b/K_l from Figure 2.8(b) as x and y. Since K_E and K_l are both dependent on b, which can be expressed in terms of x, substituting for b in the K_b expressions led to the following relationship:

$$P(x) \equiv K_b/R = y(x)x^{-2/3}, \tag{2.21}$$

where $P(x)$ is a nondimensional parameter representing the buckling load K_b and R is a constant comprising the Young's modulus E and Poisson's ratio ν. Figure 2.8 was then transformed to Figure 2.9(a). Conventionally, the optimum design takes $x = 1$, where

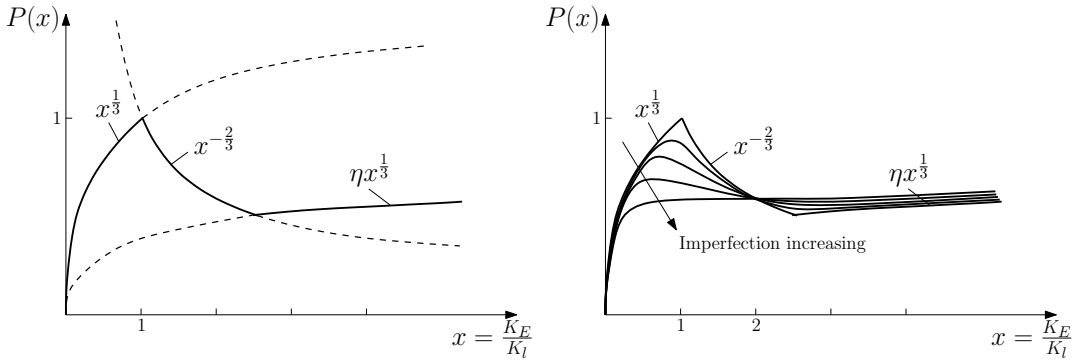

Figure 2.9: The optimum design curve for perfect and imperfect column.

the load-carrying capacity reaches a local maximum; however this region was referred to by van der Neut as the 'imperfection sensitive' region, and the optimum was therefore eroded by initial imperfections as shown in Figure 2.9(b). Another distinctive feature shown in Figure 2.9(b) was that the local maximum initially shifts to the left indicating

that $K_E < K_l$. Later, Thompson and Supple (1973) developed an optimization scheme for structural systems with coupled instabilities that exhibit an unstable bifurcation. The two-degree-of-freedom Augusti model (1964), shown in Figure 2.10, was selected

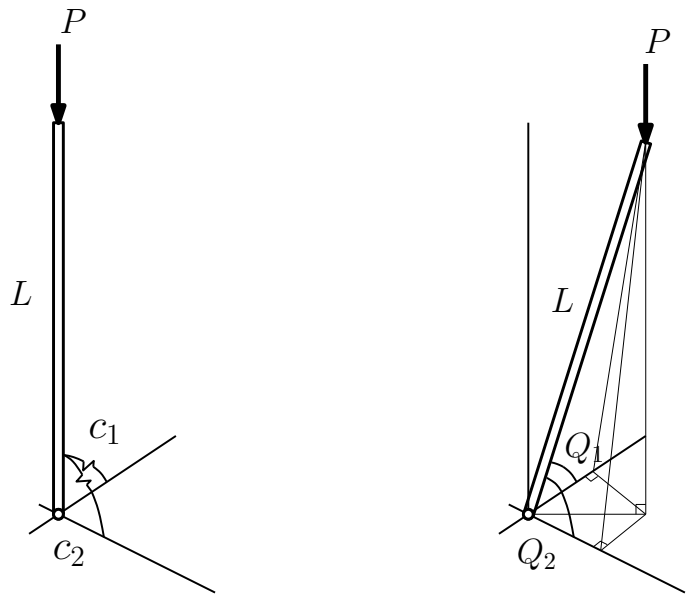

Figure 2.10: The Augusti model – a two-degree-of-freedom structural model.

for a specific example. The conventional optimum design would be such that the two rotational springs have equal stiffness. However, erosion of the optimum was revealed for the imperfect system until the local optimum was no longer that case where the springs have equal stiffness.

Very similar behaviour, as found in the van der Neut model, was captured by Koiter and Pignataro (1976) from a more realistic model of a stiffened plate. In contrast with the direct force balance approach utilized by van der Neut (1969), a total potential energy approach was adopted. The investigation first reviewed the post-buckling behaviour of flat plates under longitudinal compression. The buckling mode was described by the lateral

and longitudinal displacement fields:

$$\begin{aligned} w(x,y) &= fg(y)\sin\left(\frac{\pi x}{a}\right), \\ u(x,y) &= -\Delta x - \frac{\pi}{8a}f^2 g^2(y)\sin\left(\frac{\pi x}{a}\right), \end{aligned} \tag{2.22}$$

where x and y were the longitudinal and transverse Cartesian coordinates respectively, a was the half-wave length of the buckled mode shape in the longitudinal direction, $g(y)$ modelled the transverse wave profile of the buckled mode shape, f was the amplitude factor and Δ was the unit overall shortening in the buckled mode shape. The membrane energy, U_s stored in the system was given by:

$$U_s = \frac{1}{2}E\int \varepsilon_x^2 \mathrm{d}S, \tag{2.23}$$

where ε_x was the longitudinal direct strain component given by the standard von Kármán strain expression (Timoshenko & Woinowsky-Krieger, 1959):

$$\varepsilon_x = \frac{\partial u}{\partial x} + \frac{1}{2}\left(\frac{\partial w}{\partial x}\right)^2, \tag{2.24}$$

and the expression for U_s represented a volume integral. It should be emphasized that the transverse and shear stress components σ_y and τ_{xy} were ignored. This assumption was then shown to provide a lower bound approximation of the stiffness reduction factor η. In contrast with earlier work by Koiter (1943), where the transverse and shear stress components were included in the energy formulation, this assumption provided a less accurate but safe solution, hence applicable for many practical purposes. The bending energy formulation also followed a simpler approach, where the bending energy is equivalent to the release of the membrane energy when the plate buckles at the critical stress. The total potential energy was formed by summing the membrane energy, the bending energy and the work done by load, which was then minimized with respect to both the lateral deflection amplitude, f and the end shortening Δ. The stiffness reduction factor η was evaluated thus:

$$\eta = \frac{E*}{E} = 1 - \frac{\left[\frac{1}{b}\int_{-b/2}^{b/2} g^2(y)\,\mathrm{d}y\right]^2}{\left[\frac{1}{b}\int_{-b/2}^{b/2} g^4(y)\,\mathrm{d}y\right]}. \tag{2.25}$$

For simply supported edges, η was found to be 1/3 which is approximately 20% lower than the well-known exact value of 0.408. For clamped edges, η was found to be 0.449 which is 9% lower than the exact value of 0.497. For one simply-supported edge without in-plane edge tractions and one free edge, η was found to be the same as the exact value, indicating that the assumption of neglecting transverse and shear component was perfectly acceptable for that specific case.

The interactive buckling behaviour of stiffened panels was then studied by first investigating a locally buckled stiffener. A local coordinate s was used for the transverse direction of the local plate. The direct strain component ε_x only varied slightly due to the inclusion of an additional term, χ_{zx} in the longitudinal displacement field $u\,(x, s)$, where χ was the curvature about the x-axis and z was the lateral coordinate. This arose from the assumption of zero lateral deflection and rigid connections at the intersections of the plates. The transverse and shear stress components were neglected and the stiffness reduction factor found was again a lower bound solution. The global mode followed the same as for an Euler strut:

$$\begin{aligned} W(x) &= F \sin\left(\frac{\pi x}{L}\right), \\ \sigma_E &= \frac{\pi^2 E r^2}{L^2}, \end{aligned} \tag{2.26}$$

where r was the radius of gyration of the cross-section of the panel and L was the panel length. This was then combined with the local modes described in the previous paragraph to give the direct strain component ε_x necessary for the membrane energy formulation. It should be stressed that the amplitude factor f in the local mode was no longer a constant, but a function of x, highlighting the nonlinear feature of the interaction and the potential for non-periodic or localized solutions to the governing equations.

The stability of the critical state was found to be very similar in essence to the results of van der Neut (1969). For $\lambda_E > (1 - B^2)$, where λ_E was the ratio between the Euler stress

and the critical stress for plate buckling and B was defined as a representative factor of η, the panel was found to be governed by local buckling of the plate. For longer panels with $\lambda = \lambda_E < 1$, the panel was found to be governed by global buckling. The post-buckling behaviour was studied for $1 < \lambda_E < (1 - B^2)$; it was presented as a series of plotted curves of the load parameter $\lambda = \sigma/\sigma^{\mathrm{C}}$ against a representative function of the end shortening Δ for different values of λ_E. It was found that the post-buckling equilibrium was always stable when $\lambda_E > (1 - B^2/2)^2$, and was always unstable when $\lambda_E < (1 - B^2/2)^2$. The work went on to study the effect of local and global imperfections. The findings once again strongly agreed with van der Neut's model, showing high imperfection sensitivity at $\lambda_E = 1$.

Svensson and Croll (1975) also reviewed van der Neut's model. They followed the same force balance approach with the governing equation being solved by a combination of a perturbation and a Newton–Raphson method. The results showed once again the imperfection sensitivity when global buckling and local buckling were triggered simultaneously. Their discussion went on to take into account material yielding, in order to develop design criteria. A non-dimensional quantity H, referred to as the 'slenderness index' was defined as:

$$H = \frac{\sigma_Y}{\sqrt{\sigma_l^{\mathrm{C}} \sigma_E}}, \tag{2.27}$$

where σ_Y was the yield stress, σ_l^{C} was the local buckling critical stress and σ_E was the critical stress of Euler buckling. The merit of this quantity was such that it could be kept constant when the local slenderness b/h, and therefore the $\sigma_E/\sigma_l^{\mathrm{C}}$ ratio is varied, while the total weight could also be kept constant by fixing the beam length L with the cross-sectional area A. This was referred to as the 'simultaneous mode design criterion', where the column load carrying capacity is optimized against both local and global buckling, as well as yielding. Results were presented as a series of plots of $\bar{\sigma}/\sigma_Y$ against $\sigma_E/\sigma_l^{\mathrm{C}}$, for

different values of H as well as for different amplitudes of local and global imperfections; $\bar{\sigma}$ is the column strength and was determined by the well-known Perry–Robertson formula:

$$(\bar{\sigma} - \sigma_E)(\bar{\sigma} - \sigma_Y) = a_E \bar{\sigma} \sigma_E, \tag{2.28}$$

where a_E is the global imperfection amplitude. They stressed the fact that the Perry–Robertson formula should be modified as the ultimate average stress within buckled flanges must be smaller than the yield stress for elastic buckling to take place within the flanges. Therefore, the σ_Y term in the Perry–Robertson formula should be replaced by $c\sigma_Y$, where $c \leqslant 1$.

The nonlinear interaction of local and global buckling is also found commonly in sandwich structures (Hunt *et al.*, 1988; Hunt & Wadee, 1998; Wadee *et al.*, 2010; Yiatros & Wadee, 2011). These usually consist of two stiff face plates separated by a relatively soft core. Hunt and his co-workers (Hunt *et al.*, 1988; Hunt & da Silva, 1990) studied the sandwich panel based on a Rayleigh–Ritz approach. The investigation considered two modal contributions named 'snake' and 'hourglass', as shown in Figure 2.11, which seem to originate from Goodier (1946). The 'snake' shape essentially reflects the global mode with an arbitrary number of half waves i. Timoshenko beam theory (Reissner, 1945; Wang, 1997) was considered, where shear strain becomes important, leading to two generalized coordinates q_s and q_t, known as 'sway' and 'tilt'; the lateral displacement W and the rotation of the plane section θ thus became:

$$W = q_s \frac{L}{i} \sin \frac{i\pi x}{L}, \quad \theta = q_t \pi \cos \frac{i\pi x}{L}, \tag{2.29}$$

where L is the panel length, and x is the longitudinal Cartesian coordinate. It should be noted that, under standard Euler–Bernoulli bending theory, where shear strains are neglected, q_s and q_t would be equivalent. It can be seen that for $i = 1$, the buckling mode shape is simply a half sine wave, which is the lowest mode of an Euler strut.

Snake:

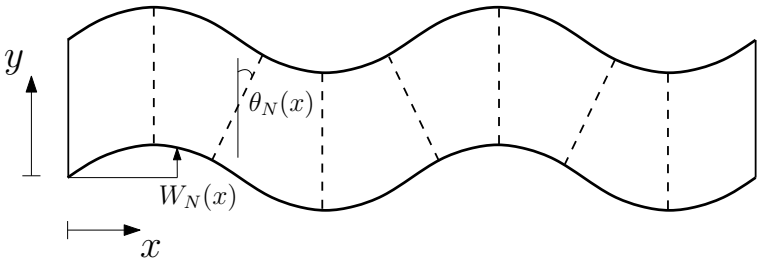

(a) Snake component

Hourglass:

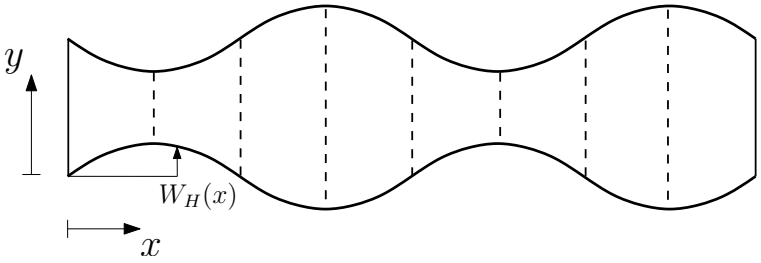

(b) Hourglass component

Figure 2.11: Decomposed modes for critical buckling of a sandwich panel.

The 'hourglass' mode, on the other hand, treats the two face plates as two back-to-back struts on elastic foundations (Allen, 1969) and two generalized coordinates q_h and q_l were introduced that were analogous to 'sway' and 'tilt' for the hourglass mode, accounting for the out-of-plane deflection w and the in-plane displacement u

$$\begin{aligned} w &= q_h \frac{2y}{b} \frac{L}{i} \sin \frac{i\pi x}{L}, \\ u &= -\frac{2}{b} q_l \pi \cos \frac{i\pi x}{L}, \end{aligned} \tag{2.30}$$

where b is the core thickness and y is the transverse Cartesian coordinate. Two further generalized coordinates A_5 and A_6 were also introduced, accounting for the total end shortening and total transverse shortening. The system was hence associated with six generalized coordinates in total. The total potential energy comprised the bending energy, the membrane energy, the core energy and the work done by the load. In Hunt and da Silva (1990), the formulation contained the work done term in a general form, capable of dealing with different loading conditions. Three examples were presented for uniform

moment, mid-span concentrated load, and a uniformly distributed load. It was found that all equilibrium paths exhibit an initial linear stage corresponding to the global buckling and a nonlinear stage where local modes begin to interact. All solutions represented upper bounds in terms of the load-carrying capacities reflecting the generic properties of the Rayleigh–Ritz method.

Hunt and Wadee (1998) studied the interactive buckling behaviour in an axially loaded sandwich panel using a variational formulation. The approach also followed Timoshenko beam theory since shear strain was found to be essential for the nonlinear interaction between the global and the local buckling modes. The global mode used the snake mode for $i = 1$ as in Hunt and da Silva (1988; 1990). The local mode was described by a set of continuous displacement functions w and u, representing the out-of-plane and the longitudinal in-plane displacements of the face plates, respectively. The face plates were assumed to take all the direct stress, whereas the core would take all shear and transverse strain components. The total potential energy functional V was formulated by summing the bending energy, the membrane energy, the core energy and the work done by the loads. The calculus of variations was used to derive a coupled system of nonlinear ordinary differential equations comprising a fourth order equation in terms of the out-of-plane local buckling displacement w and a second order equation in terms of the in-plane-displacement u. These governing equations were also subjected to three integral conditions, which were obtained by minimizing V with respect to three generalized coordinates q_s, q_t and the end shortening Δ. The equations were then solved using the numerical continuation package AUTO (Doedel & Oldeman, 2009). The results showed that the sandwich panel indeed exhibits a global buckling mode at a critical load determined from a linear eigenvalue analysis, after which the system was found to be weakly stable until a secondary bifurcation point was encountered on the equilibrium path, which causes a further instability.

The interactive mode that was triggered was found to be highly localized at mid-span and depending on core nonlinearities, the localization persisted or the buckling mode evolved to a periodic mode (Hunt *et al.*, 2000), as discussed below.

More recently, Wadee and Gardner (2012) have studied the interaction of flange local buckling and lateral torsional buckling in a thin-walled I-beam subjected to a uniform moment. The model introduced two additional degrees of freedom q_τ and q_ϕ to account for the global mode of lateral torsional buckling. The approach was adapted from the sandwich problem (Hunt & Wadee, 1998). The equilibrium paths after the secondary bifurcation point exhibited a behaviour known as 'cellular buckling' (Hunt *et al.*, 2000) or 'snaking' (Burke & Knobloch, 2007). This is the phenomenon where the equilibrium path after the secondary bifurcation exhibits a sequence of destabilizing and restabilizing processes, which is represented by a sequence of snap-backs on the equilibrium paths, as shown in Figure 2.12. Referring to the buckling modes, this phenomenon tracks the

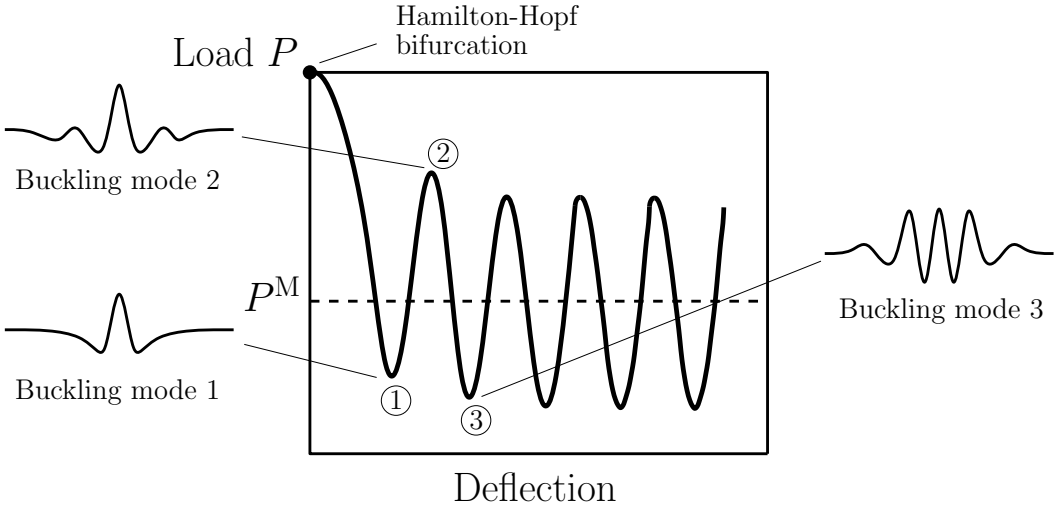

Figure 2.12: An example of cellular buckling or snaking in the equilibrium path of a structural system; P^{M} is the Maxwell load.

progressively spreading waves in the flanges, which was initially localized at mid-span. Cellular buckling is also observed in systems such as cylindrical shells and compressed

confined layers (Hunt *et al.*, 2000; Wadee & Edmunds, 2005). These systems are associated with the Maxwell load P^{M}, where the load oscillates about a fixed load P^{M} as the deflection progresses, as shown in Figure 2.12, and is associated with the eventual periodic profile of the post-buckling mode (Budd *et al.*, 2001).

Structural systems exhibiting cellular buckling or snaking were conventionally treated as dynamical systems involving periodic, homoclinic and heteroclinic orbits of various kinds in the phase space (Woods & Champneys, 1999; van der Heijden *et al.*, 2002; Chapman & Kozyreff, 2009; Taylor & Dawes, 2010), as sketched in Figure 2.13. Consider a two degree-

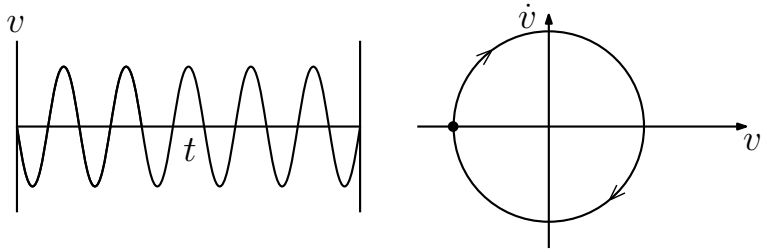

(a) Periodic orbit

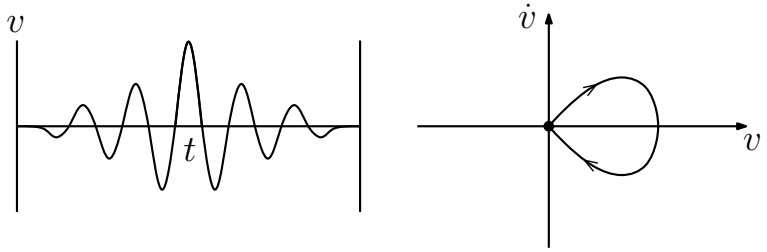

(b) Homoclinic orbit

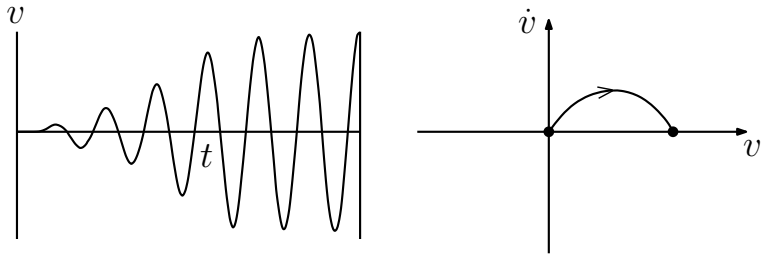

(c) Heteroclinic orbit

Figure 2.13: Examples of different kinds of orbits in nonlinear dynamical systems, where v and t represent displacement and time respectively. Dots represent the derivative of v with respect to t. Such solutions can also appear in nonlinear static systems.

of-freedom Hamiltonian (energy conserving) system $\mathcal{H}$; localized solutions exist in the form of a pair of reversible homoclinic orbits (Figure 2.13(b)) which bifurcate into the region of a saddle-focus equilibrium O. Suppose that the homoclinic orbits 'collide' with a finite-amplitude periodic orbit L at some specific values of the system parameters; the unstable manifold of the saddle-focus equilibrium, $W^u(O)$ then contains a heteroclinic connection with L. Under parameter perturbations, $W^u(O)$ and the stable manifold of the periodic orbit $W^s(O)$ pass through each other, forming a pair of successive heteroclinic tangencies between $W^u(O)$ and $W^s(L)$; the unfolding of the successive heteroclinic tangencies leads to an infinite number of symmetric homoclinic solutions at the intersection of $W^u(O)$ and a symmetric section $\mathcal{S}$. It was found that these solutions lie on a single curve, snaking back and forth in the bifurcation diagram. The simplest localized (single hump) symmetric homoclinic solution, emanating from a Hamiltonian–Hopf bifurcation, develops towards a periodic solution by gaining an extra peak or trough each time at the limit point is encountered on the equilibrium path, as shown in the sketch in Figure 2.12 for a structural system. Recall Figure 1.4, the fluctuations observed on the stress-strain curve between point B and C were conventionally considered as one of the characteristics of the loading rig. However, it was found that this is actually caused by snaking where Lüders bands are formed progressively from the loading edges to the mid-span of the tensile test coupon, as shown in Figure 2.14 (Den Hartog, 1961). Such a phenomenon was found in physical models of a strut on an elastic foundation (Woods & Champneys, 1999), in the twisting of an elastic rod (van der Heijden *et al.*, 2002), cylindrical shell buckling (Hunt *et al.*, 1999; Hunt *et al.*, 2003), in thin-walled I-section beams under pure bending (Wadee & Gardner, 2012) and sandwich panels for certain core material nonlinearities as mentioned previously.

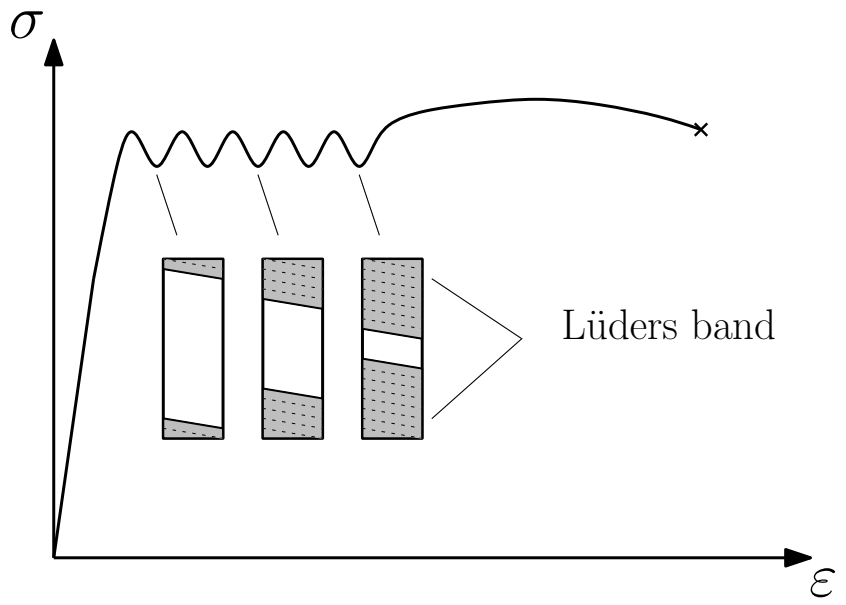

Figure 2.14: An example of Lüders band (Meier, 2009) on a tensile test coupon exhibiting snaking.

2.2.2 Numerical studies

Alongside the analytical work already highlighted, a large number of numerical studies have also been conducted to investigate the interactive buckling behaviour in various types of structural components. Two most commonly adopted approaches are the finite element method (Rajasekaran & Murray, 1973; Johnson & Will, 1974; Becque & Rasmussen, 2009b) and the finite strip method (Plank & Wittrick, 1974; Hancock, 1978; Ádány & Schafer, 2006). One-dimensional finite element models were used in 1960s and 1970s principally for predicting global buckling (Clark & Hill, 1960; Powell & Klingner, 1970), since they could not easily capture the local plate buckling behaviour.

Rajasekaran and Murray (1973) used one-dimensional thin-walled beam elements in their study of the wide flange beam-column problem. In addition, assumed plate flexural displacements were superimposed to the global displacements of the beam element. These

local modes were regarded as 'coupled local buckling'. Some important assumptions were also made in their model such as the omission of shear strain, fixity at plate intersection points, as well as the mentioned superposition of the local and global displacements. For local flange buckling, the predicted buckling loads have shown strong agreement with some theoretical values obtained in the literature. However for local web buckling, the model failed to produce accurate results because the assumed local displacements at the web could not represent the fundamental mode accurately.

In contrast to the one-dimensional finite element models, Akay and his co-workers (1977) used two-dimensional plane stress elements for the web and one-dimensional elements for the flanges, which were believed to produce more accurate results with relatively high computational efficiency. This method was initially used in a beam analysis, then extended to a gable frame and a deep bridge girder analysis.

Hancock (1978) investigated the buckling modes of an I-beam using the finite strip method. The finite strip method differs from the finite element method in such a way that the flange of an I-beam, for instance, is divided into a number of longitudinal strips (Graves Smith & Sridharan, 1978). The behaviour of each strip is then determined using energy concepts; hence this method is often termed as 'semi-analytical'. Hancock's model has yielded good results in predicting the critical mode of the I-beam with different beam lengths and cross-sectional dimensions, as well as with lateral and torsional restraints. Hancock (1981) also studied a thin-walled I-section column exhibiting local and weak-axis Euler buckling. The work provided a first insight into the implementation of the finite strip method in studying the nonlinear interactive behaviour of the global and the local modes. Davids and Hancock (1986) obtained good comparisons between the finite strip method and the experimental results on thin-walled I-section columns. Later on

in the 1980s, Hancock and his co-workers successfully developed and implemented the so-called 'spline finite strip method' to cope with non-simply-supported columns, as well as the inelastic buckling behaviour within such elements (Lau & Hancock, 1986; Lau & Hancock, 1989).

Schafer (2002) focused on the distortional buckling behaviour in lipped thin-walled sections and highlighted the lack of attention to such buckling modes in current design methods. The linear distortional buckling response of a thin-walled I-section column was approached analytically, as an extension of earlier work by Schafer and Peköz (1999), where the distortional buckling behaviour of beams was studied. The post-buckling behaviour was then studied using the finite element method facilitated by the software package ABAQUS (2011). It had shown that the distortional buckling mode had a lower post-buckling stiffness than local buckling.

Another well-known method of analysis for coupled instability problems is so-called 'generalized beam theory' (GBT), which was originally developed by Schardt (1994). The early applications of GBT was for the elastic critical buckling behaviour of open cross-sections (Leach & Davies, 1996); Silvestre and Camotim (2003) developed nonlinear GBT formulations for closed cross-sections while Goncalves and Camotim (2004; 2007) extended the application of GBT to account for plasticity. An extensive set of investigations using GBT have been carried out for the interactions between local, global and distortional buckling modes for various types of cross-sections (Dinis *et al.*, 2010; Basaglia *et al.*, 2013).

2.2.3 Experimental studies

Since the 1960s, a large number of experimental investigations have also been conducted for cold-formed thin-walled steel columns with various types of cross-sections such as hat sections, channel sections, I-sections and box sections (Cherry, 1960; Johnson & Winter, 1966; Rasmussen & Hancock, 1993; Gardner & Nethercot, 2004a; Becque & Rasmussen, 2009a). Although the majority of the test data are associated with pure global buckling, some results highlighted the importance of the interaction between global and local buckling modes. In particular, Becque and Rasmussen (2009a; 2009b) approached an I-section column problem both experimentally and numerically for stainless steel specimens. These investigations have captured some important features of the nonlinear interactive behaviour in thin-walled I-section columns.

In the experiments, I-section columns were effectively made from two channels connected back to back. The depth, width and thickness of the channel were fixed. Tests were carried out for columns with different lengths ranging from 500 mm to 3000 mm. Two specimens with the same properties were tested for comparison, which were referred to as 'twin tests'. A simple calculation of the Euler load and the critical stress for plate buckling showed that, in all the test specimens, local buckling was the critical mode. This has been shown by the experiments where all columns exhibit local buckling first. As the load was increased, the specimen also started to bend about its minor axis and then the local and global modes started to interact. It was found that the amplitude of the local mode on the concave side increased most rapidly near the mid-span of the column, whereas the convex side of the flange tended to be straightened out. The buckling pattern then tended to localize at mid-span. The test results have shown that the ultimate column strengths, determined from the twin tests, show a close match for columns with lengths ranging

from 500 mm up to 2500 mm. Columns with lengths ranging from 2500 mm to 3000 mm exhibited a much larger difference in the ultimate load P_U between the twin tests. This was the range of the previously mentioned 'imperfection sensitive zone' defined by van der Neut (1969).

The numerical validation of this test result was attempted using finite element analysis facilitated by the software package ABAQUS (2011). The I-section column was again formed by joining back-to-back channels with analytically rigid end plates that distributed the axial force onto the cross-section uniformly. A shell element with four nodes and reduced integration, S4R, was used in the analysis. A linear eigenvalue analysis was first conducted to obtain both the lowest global and local modes. The eigenvectors with appropriate amplitudes were introduced to the system as imperfections. A nonlinear arclength method known as the Riks method (Riks, 1972) was then run to trace the equilibrium path within the post-buckling range. The results from this model have shown reasonably good agreement with the test results, with slightly larger discrepancies being found for the columns with lengths ranging from 2500 mm to 3000 mm which corresponded to the aforementioned 'imperfection sensitive zone'. It should be stressed that the numerical predictions were at least always on the safe side.

2.2.4 Concluding remarks

The present chapter has reviewed some of the most important works that are relevant to the current research, from the middle of the 18^{th} century to the state of the art. The general nonlinear buckling theory was first discussed. Some classic works, on the nonlinear interaction of different buckling modes, were then reviewed. The review then focused specifically on the interactive buckling behaviour in structural components with thin-

walled metallic elements. Some analytical works, including the classic van der Neut (1969) model and the more recent work by Hunt and Wadee (1998), which provides a general methodology for the current research, were highlighted. Some numerical studies on the current subject were highlighted, including the finite element and the finite strip method alongside generalized beam theory. Finally, some experimental studies were highlighted, in particular the fairly recent works by Becque and Rasmussen (2009a; 2009b), the results from which will be compared against in the following chapter.

Chapter 3

Variational modelling of I-section strut

In the current chapter, the classic problem of a strut under axial compression made from a linear elastic material with an open and doubly-symmetric cross section – an 'I-section' (van der Neut, 1969; Hancock, 1981) – is studied in detail using an analytical approach. Under this type of loading, long members are primarily susceptible to a global (or overall) mode of instability namely Euler buckling, where flexure about the weak axis occurs once the theoretical Euler buckling load is reached. However, when the individual plate elements of the strut cross-section, namely the flanges and the web, are relatively thin or slender, elastic local buckling of these may also occur; if this happens in combination with the global instability, then the resulting behaviour is usually far more unstable than when the modes are triggered individually. Recent work on the interactive buckling of struts include experimental and finite element studies (Becque & Rasmussen, 2009a; Becque & Rasmussen, 2009b), where the focus was on the behaviour of struts made from stainless steel. Apart from these works where some numerical modelling was presented (Becque & Rasmussen, 2009b), the formulation of a mathematical model accounting for the nonlinear

interactive buckling behaviour has not been forthcoming.

Presently, a variational model that accounts for the mode interaction between global Euler buckling and local buckling of a flange is developed, such that the perfect elastic post-buckling response of the strut can be evaluated. A system of nonlinear ordinary differential equations subject to integral constraints is derived and is solved using the numerical continuation package AUTO (Doedel & Oldeman, 2009). Such a procedure has been well established in previous works (Wadee & Gardner, 2012; Hunt *et al.*, 2000; Hunt & Wadee, 1998). It needs to be emphasized that in the current chapter, the web is assumed to provide a simple support to both top and bottom flanges, in which case the flanges and the web are considered as five individual plate members. Although representing a limiting case when the web does not buckle, it is indeed found that the system is highly unstable when interactive buckling is triggered; snap-backs in the response, showing sequential destabilization and restabilization and a progressive spreading of the initial localized buckling mode, are also revealed. This latter type of response has become known in the literature as *cellular buckling* (Hunt *et al.*, 2000) or *snaking* (Burke & Knobloch, 2007) and it is shown to appear naturally in the numerical results of the current model. Similar behaviour has been discovered in various other mechanical systems such as in the post-buckling of cylindrical shells (Hunt *et al.*, 2003), the sequential folding of geological layers (Wadee & Edmunds, 2005) and most recently in the lateral buckling of thin-walled beams under pure bending (Wadee & Gardner, 2012). Models representing more rigid, and hence more practically realistic flange–web connections will be developed in the later chapters.

3.1 Analytical model

3.1.1 Problem definition

Consider a thin-walled I-section strut of length L made from a linear elastic, homogeneous and isotropic material with Young's modulus E and Poisson's ratio ν. It is loaded by an axial force P that is applied at the centroid of the cross-section, as shown in Figure 3.1(a) and (b) respectively, with rigid end plates that transfer the force uniformly to the entire

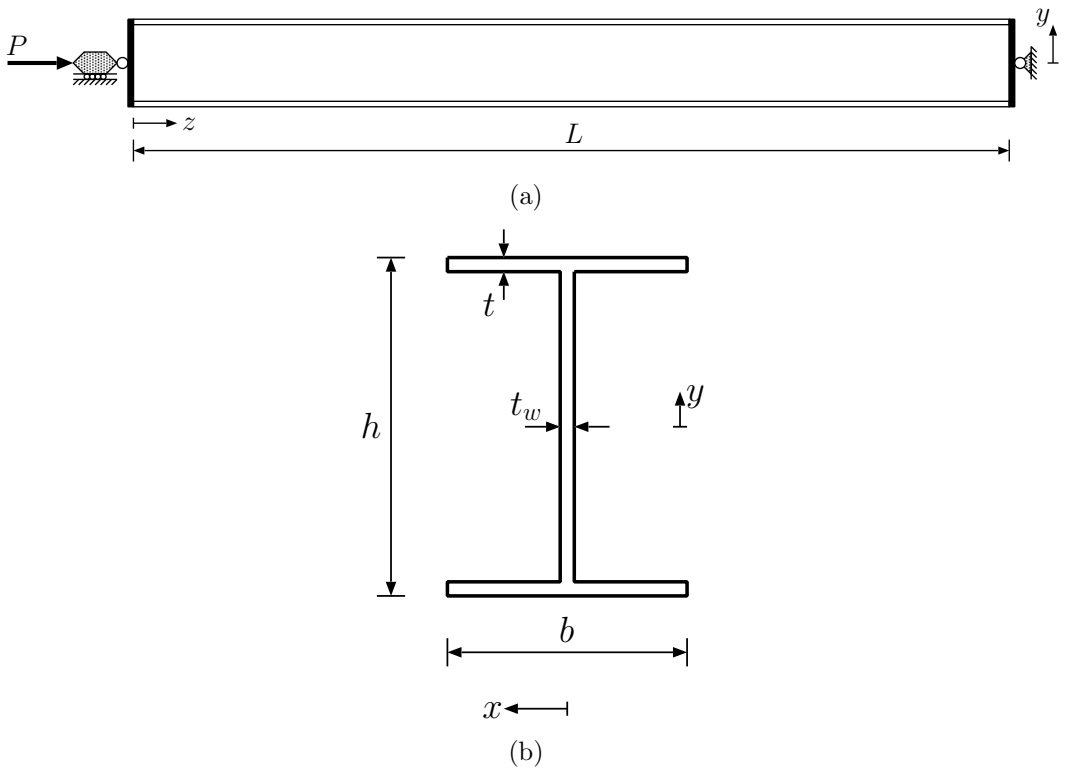

Figure 3.1: (a) Elevation of an I-section strut of length L that is compressed axially by a force P. The lateral and longitudinal coordinates are y and z respectively. (b) Cross-section geometry of strut – the transverse coordinate being x.

cross-section. The web is assumed to provide a simple support to both flanges and not to buckle locally under the axial compression, an assumption that is justified later. The total cross-section depth is h with each flange having width b and thickness t. It is also assumed

currently that the I-section is effectively made up from two channel members connected back-to-back; hence, the web thickness $t_w = 2t$, a type of arrangement that has been successfully used in recent experimental studies (Becque & Rasmussen, 2009a; Wadee & Gardner, 2012; Becque, 2008), provided that there is sufficient number of closely spaced connectors so that the webs from each channel section behave as an integral member. The strut length L is varied such that in one case, which is presented later, Euler buckling about the weaker y-axis occurs before any flange buckles locally whereas in the other case the reverse is true – flange local buckling is critical.

3.1.2 Modal description

The formulation begins with the definitions for both the global and the local modal displacements. Timoshenko beam theory is assumed, meaning that although plane sections remain plane, the effect of shear is not neglected, as it is in standard Euler–Bernoulli beam theory. A diagrammatic explanation of the basic assumptions in the two bending theories is shown in Figure 3.2. Although it turns out that the amount of shear strain is

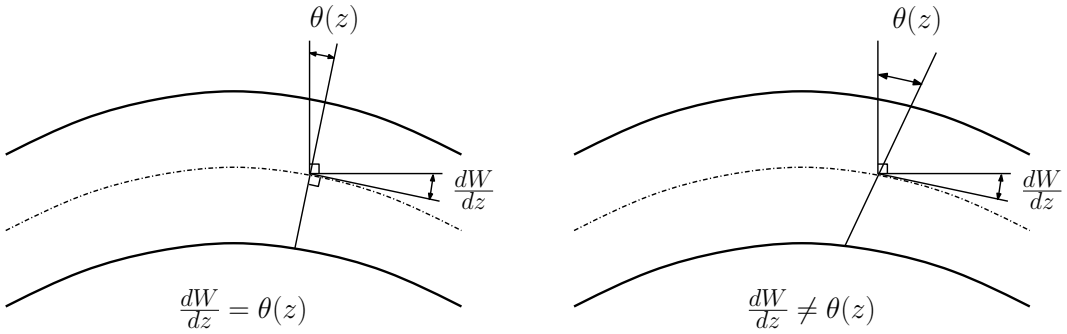

(a) Euler–Bernoulli beam theory (b) Timoshenko beam theory

Figure 3.2: Outline of the beam theories, the dotted line represents the neutral axis of bending.

small, it is necessary for it to be accounted since it provides the key terms within the total

potential energy that allow buckling mode interaction to be modelled (Hunt & Wadee, 1998; Wadee & Gardner, 2012). As mentioned in Chapter 2, to account for shear, two generalized coordinates q_s and q_t, defined as the amplitudes of the degrees of freedom known as 'sway' and 'tilt' (Hunt & Wadee, 1998) are introduced to model the global mode, as shown in Figure 3.3(a), where the lateral displacement W and the rotation θ

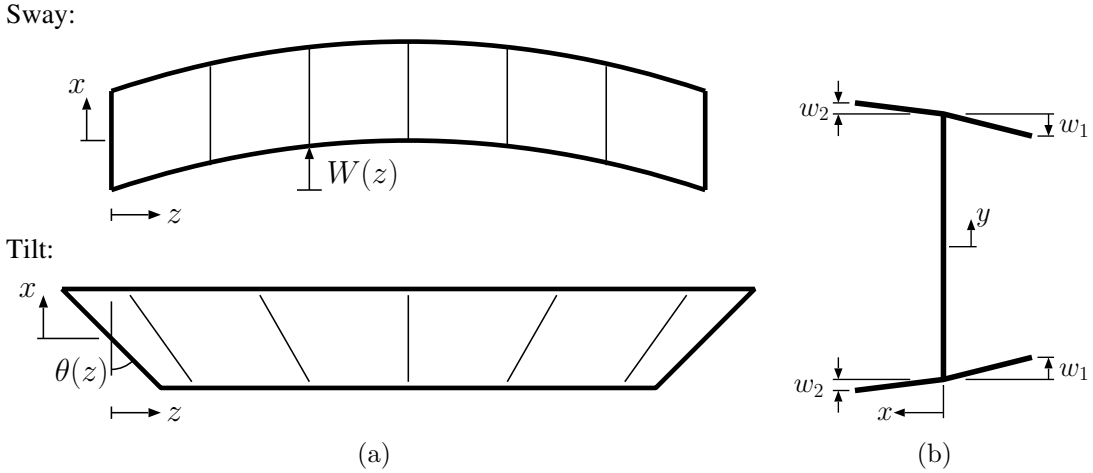

Figure 3.3: (a) Sway and tilt components of the minor axis global buckling mode. (b) Local buckling mode: out-of-plane flange displacement functions $w_i(x, z)$; note the linear distribution in the x direction.

are given by the following expressions:

$$\begin{aligned} W(z) &= q_s L \sin \frac{\pi z}{L}, \\ \theta(z) &= q_t \pi \cos \frac{\pi z}{L}. \end{aligned} \tag{3.1}$$

For the present case, the shear strain in the xz plane, γ_{xz}, is included and is given by the following expression:

$$\gamma_{xz} = \frac{\mathrm{d}W}{\mathrm{d}z} - \theta = (q_s - q_t)\, \pi \cos \frac{\pi z}{L}. \tag{3.2}$$

Of course, if Euler–Bernoulli beam theory were being used it would imply that since $\gamma_{xz} = 0$, then $q_s = q_t$.

The local mode is modelled with appropriate boundary conditions. Moreover, the possibility of a distinct local buckling mode occurring before global buckling implies that the

entire flange may deflect. However, if the interaction between local and global modes occurs then the symmetry of the local buckling mode would be broken and the flanges would not buckle with the same displacement. Hence, two separate lateral displacement functions w_1 and w_2 need to be defined, as shown in Figure 3.3(b), to allow for the break in symmetry. Since the outstands of the flanges have free edges, whereas the web is assumed to provide no more than a simple support to the flanges, a linear distribution is assumed in the x direction; Bulson (1970) showed this distribution is correct for the local buckling eigenmode for that type of rectangular plate. For the local mode, in-plane displacements u_i, the distributions are also assumed to be linear in x, as shown in Figure 3.4. This is

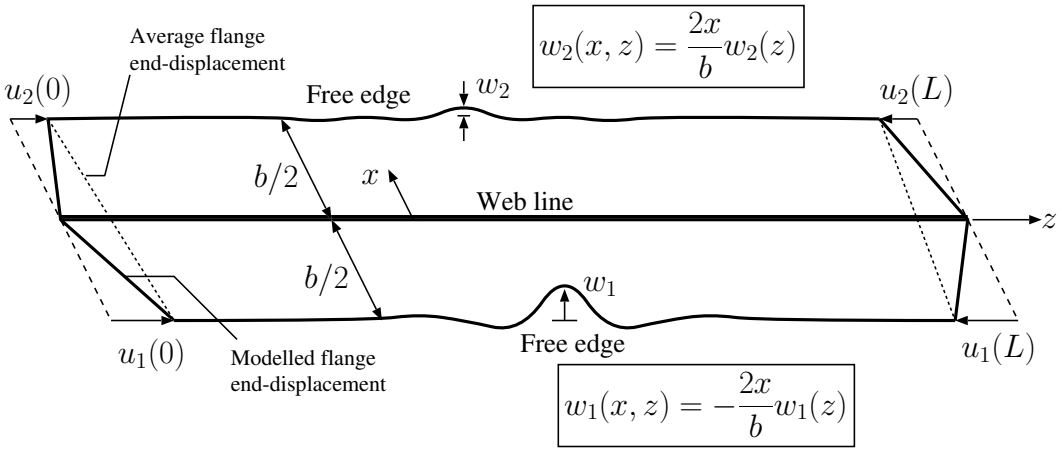

Figure 3.4: Displacement functions of the local buckling mode in the flanges. Longitudinal and lateral flange displacements $u_i(x,z)$ and $w_i(x,z)$ respectively. Note the linear distributions in the x direction and the average end-displacement, as opposed to the modelled flange end-displacement, which is used to calculate the local contribution to the work done.

in fact another consequence of the Timoshenko beam theory assumption where plane sections are assumed to remain plane. These assumptions lead to the following expressions for the local out-of-plane displacements w_i with the in-plane displacements u_i:

$$\begin{aligned} w_i(x,z) &= (-1)^i \left(\frac{2x}{b}\right) w_i(z), \\ u_i(x,z) &= (-1)^i \left(\frac{2x}{b}\right) u_i(z), \end{aligned} \tag{3.3}$$

where $i = \{1, 2\}$ throughout the current chapter. The transverse in-plane displacement $v(z, x)$ is assumed to be small and is hence neglected for the current case; this reflects the findings from Koiter and Pignataro (1976) for rectangular plates with three pinned edges and one free edge.

Since, in practice, perfect geometries do not exist, an initial out-of-straightness in the x-direction, W_0, is introduced as a global imperfection to the web and flanges in the current model. An initial rotation of the plane section θ_0 is also introduced to simulate the out-of-straightness in the flanges. The expressions for W_0 and θ_0 are given by:

$$\begin{aligned} W_0 &= q_{s0} L \sin \frac{\pi z}{L}, \\ \theta_0 &= q_{t0} \pi \cos \frac{\pi z}{L}, \end{aligned} \tag{3.4}$$

and are analogous to Equation (3.1). Local imperfections are considered in Chapter 4.

3.1.3 Total Potential Energy

Having defined both the global and the local modal displacements, the total potential energy, V, of the strut was determined with the main contributions being the global and the local bending energy U_{bo} and U_{bl} respectively, the membrane energy U_m, and the work done $P\mathcal{E}$. Note that the global bending energy U_{bo} only comprises the bending energy stored in the web, since the membrane energy stored in the flanges accounts for the effect of bending in the flanges through the tilt mode. The initial out-of-straightness $W_0(z)$ is stress-relieved (Thompson & Hunt, 1984; Wadee, 2000), implying that the elemental moment M drops to zero as illustrated in Figure 3.5(a). The global bending energy involves the second derivative of W is hence given by:

$$U_{bo} = \frac{1}{2} EI_w \int_0^L \left(\ddot{W} - \ddot{W}_0 \right)^2 \mathrm{d}z = \frac{1}{2} EI_w \int_0^L \left(q_s - q_{s0} \right)^2 \frac{\pi^4}{L^2} \sin^2 \frac{\pi z}{L} \mathrm{d}z, \tag{3.5}$$

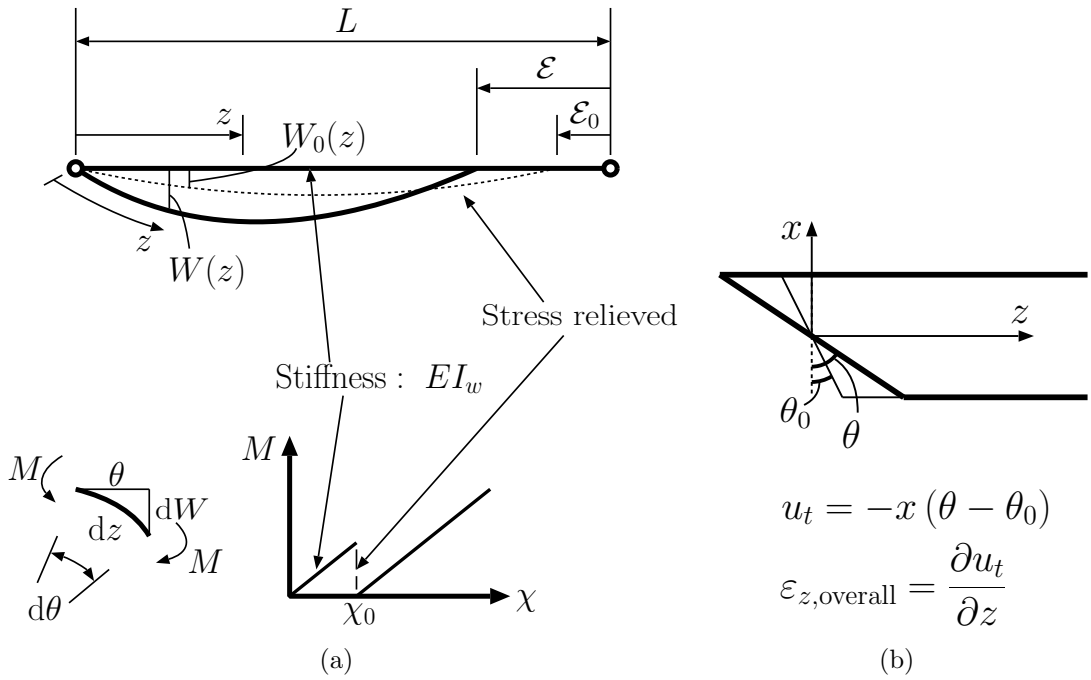

Figure 3.5: Introduction of geometric imperfections W_0 and θ_0 in (a) the web and (b) the flanges. The quantity χ represents the bending curvature of the member.

where dots represent differentiation with respect to z and $I_w = t_w^3(h-2t)/12$ is the second moment of area of the web about the global weak axis. Obviously, for the case where $t_w = 2t$, the expression becomes $I_w = 2t^3(h-2t)/3$. The local bending energy, accounting for both flanges, is determined as:

$$\begin{aligned} U_{bl} &= D\int_0^L \left[\int_{-b/2}^0 B_1 \mathrm{d}x + \int_0^{b/2} B_2 \mathrm{d}x\right] \mathrm{d}z \\ &= D\int_0^L \left[\frac{b}{6}\left(\ddot{w}_1^2 + \ddot{w}_2^2\right) + \frac{4\left(1-\nu\right)}{b}\left(\dot{w}_1^2 + \dot{w}_2^2\right)\right] \mathrm{d}z, \end{aligned} \tag{3.6}$$

where B_i, the contribution from w_i to the standard expression for the incremental strain energy from bending a plate (Timoshenko & Gere, 1961), is given by:

$$B_i = \left(\frac{\partial^2 w_i}{\partial z^2} + \frac{\partial^2 w_i}{\partial x^2}\right)^2 - 2\left(1-\nu\right)\left[\frac{\partial^2 w_i}{\partial z^2}\frac{\partial^2 w_i}{\partial x^2} - \left(\frac{\partial^2 w_i}{\partial z \partial x}\right)^2\right], \tag{3.7}$$

with $D = Et^3/[12(1-\nu^2)]$ being the plate flexural rigidity. The buckled configuration of the flange plate involves double curvature in the x and z directions, indicating the non-developable nature of plate deformation. The so-called membrane strain energy (U_m)

is derived from considering the direct strains (ε) and the shear strains (γ) in the flanges thus:

$$U_m = U_d + U_s = \int_0^L \left[\int_{-h/2}^{-h/2+t} F \mathrm{d}y + \int_{h/2-t}^{h/2} F \mathrm{d}y \right] \mathrm{d}z, \tag{3.8}$$

where:

$$\begin{aligned} F = \frac{1}{2} \Bigg\{ & \int_{-b/2}^{0} \left[E \left(\varepsilon_{z1}^2 + \varepsilon_{x1}^2 + 2\nu \varepsilon_{z1} \varepsilon_{x1} \right) + G \gamma_{xz1}^2 \right] \mathrm{d}x \\ & + \int_0^{b/2} \left[E \left(\varepsilon_{z2}^2 + \varepsilon_{x2}^2 + 2\nu \varepsilon_{z2} \varepsilon_{x2} \right) + G \gamma_{xz2}^2 \right] \mathrm{d}x \Bigg\}. \end{aligned} \tag{3.9}$$

The transverse component of strain ε_{xi} is neglected since it has been shown that it has no effect on the post-buckling behaviour of a long plate with three simply-supported edges and one free edge (Koiter & Pignataro, 1976). The longitudinal strain ε_z has to be modelled separately for different outstand flanges. Recall that the tilt component of the in-plane displacement from the global mode, is given by $u_t = -\theta x$, hence:

$$\varepsilon_{z,\mathrm{global}} = \frac{\partial u_t}{\partial z} = x \left(q_t - q_{t0} \right) \frac{\pi^2}{L} \sin \frac{\pi z}{L}. \tag{3.10}$$

The local mode contribution is based on von Kármán plate theory. A pure in-plane compressive strain Δ is also included. The direct strains in the compression and tension side of the flanges, denoted as ε_{z1} and ε_{z2} respectively, are given by the general expression:

$$\begin{aligned} \varepsilon_{zi} &= \varepsilon_{z,\mathrm{global}} - \Delta + \frac{\partial u_i}{\partial z} + \frac{1}{2} \left(\frac{\partial w_i}{\partial z} \right)^2 \\ &= x \left(q_t - q_{t0} \right) \frac{\pi^2}{L} \sin \frac{\pi z}{L} - \Delta + (-1)^i \left(\frac{2x}{b} \right) u_i + \frac{2x^2}{b^2} \dot{w}_i^2. \end{aligned} \tag{3.11}$$

The strain energy from direct strains (U_d) is thus, assuming that $h \gg t$:

$$\begin{aligned} U_d = Etb \int_0^L \Bigg\{ & \frac{b^2}{12} \left(q_t - q_{t0} \right)^2 \frac{\pi^4}{L^2} \sin^2 \frac{\pi z}{L} + \Delta^2 + \frac{1}{6} \left(\dot{u}_1^2 + \dot{u}_2^2 \right) + \frac{1}{40} \left(\dot{w}_1^4 + \dot{w}_2^4 \right) \\ & - \left(q_t - q_{t0} \right) \frac{b\pi^2}{2L} \sin \frac{\pi z}{L} \left[\frac{1}{3} \left(\dot{u}_1 - \dot{u}_2 \right) + \frac{1}{8} \left(\dot{w}_1^2 - \dot{w}_2^2 \right) \right] - \frac{1}{2} \Delta \left(\dot{u}_1 + \dot{u}_2 \right) \\ & - \frac{1}{6} \Delta \left(\dot{w}_1^2 + \dot{w}_2^2 \right) + \frac{1}{8} \left(\dot{u}_1 \dot{w}_1^2 + \dot{u}_2 \dot{w}_2^2 \right) + \frac{h}{b} \Delta^2 \Bigg\} \mathrm{d}z, \end{aligned} \tag{3.12}$$

where, apart from the final term which represents the energy stored in the web, the contributions are from the direct strains in both flanges. The shear strain energy U_s contains the shear modulus G, which is given by $E/[2(1+\nu)]$ for a homogeneous and isotropic material. The shear strain γ_{xz} contributions are also modelled separately for the compression and the tension side of the flanges. The expression for each outstand is given by the general expression:

$$\begin{aligned}\gamma_{xzi} &= \frac{\partial}{\partial z}\left(W - W_0\right) - \left(\theta - \theta_0\right) + \frac{\partial u_i}{\partial x} + \frac{\partial w_i}{\partial z}\frac{\partial w_i}{\partial x} \\ &= \left(q_s - q_t - q_{s0} + q_{t0}\right)\pi\cos\frac{\pi z}{L} + (-1)^i\left(\frac{2}{b}\right)u_i + \frac{4x}{b^2}w_i\dot{w}_i.\end{aligned} \tag{3.13}$$

The expression for the strain energy from shear is thus:

$$\begin{aligned}U_s = Gtb\int_0^L\Bigg[&\left(q_s - q_t - q_{s0} + q_{t0}\right)^2\pi^2\cos^2\frac{\pi z}{L} \\ &- \left(q_s - q_t - q_{s0} + q_{t0}\right)\frac{\pi}{b}\cos\frac{\pi z}{L}\left(2u_1 - 2u_2 + w_1\dot{w}_1 - w_2\dot{w}_2\right) \\ &+ \frac{2}{b^2}\left({u_1}^2 + {u_2}^2 + \frac{1}{3}{w_1}^2\dot{w}_1^2 + \frac{1}{3}{w_2}^2\dot{w}_2^2 + u_1w_1\dot{w}_1 + u_2w_2\dot{w}_2\right)\Bigg]\mathrm{d}z.\end{aligned} \tag{3.14}$$

Finally, the work done by the axial load P is given by:

$$P\mathcal{E} = P\int_0^L\left[q_s^2\frac{\pi^2}{2}\cos^2\frac{\pi z}{L} - \frac{1}{2}\left(\dot{u}_1 + \dot{u}_2\right) + \Delta\right]\mathrm{d}z, \tag{3.15}$$

where $\mathcal{E}$ comprises the longitudinal displacement due to global buckling, the in-plane displacement due to local buckling and the initial end-shortening. Note that the displacement due to local buckling is taken as the average value between the maximum in-plane displacement in the more compressed outstand u_1 and the maximum in-plane displacement in the less compressed outstand u_2, which is illustrated in Figure 3.4. Moreover, the possible term in q_{s0} has been neglected since it would vanish on differentiation for

equilibrium anyway. The total potential energy V is therefore assembled thus:

$$\begin{aligned}
V =& U_{bo} + U_{bl} + U_m - P\mathcal{E} \\
=& \int_0^L \Bigg\{ \frac{1}{2} EI_w (q_s - q_{s0})^2 \frac{\pi^4}{L^2} \sin^2 \frac{\pi z}{L} + D \left[\frac{b}{6} \left(\ddot{w}_1^2 + \ddot{w}_2^2 \right) + \frac{4\left(1-\nu\right)}{b} \left(\dot{w}_1^2 + \dot{w}_2^2 \right) \right] \\
&+ Etb \Bigg\{ \frac{b^2}{12} (q_t - q_{t0})^2 \frac{\pi^4}{L^2} \sin^2 \frac{\pi z}{L} + \Delta^2 + \frac{1}{6} \left(\dot{u}_1^2 + \dot{u}_2^2 \right) + \frac{1}{40} \left(\dot{w}_1^4 + \dot{w}_2^4 \right) \\
&- (q_t - q_{t0}) \frac{b\pi^2}{2L} \sin \frac{\pi z}{L} \left[\frac{1}{3} \left(\dot{u}_1 - \dot{u}_2 \right) + \frac{1}{8} \left(\dot{w}_1^2 - \dot{w}_2^2 \right) \right] - \frac{1}{2} \Delta \left(\dot{u}_1 + \dot{u}_2 \right) \\
&- \frac{1}{6} \Delta \left(\dot{w}_1^2 + \dot{w}_2^2 \right) + \frac{1}{8} \left(\dot{u}_1 \dot{w}_1^2 + \dot{u}_2 \dot{w}_2^2 \right) + \frac{h}{b} \Delta^2 \Bigg\} \\
&+ Gtb \Bigg[\left(q_s - q_t - q_{s0} + q_{t0} \right)^2 \pi^2 \cos^2 \frac{\pi z}{L} - \left(q_s - q_t - q_{s0} + q_{t0} \right) \frac{\pi}{b} \cos \frac{\pi z}{L} \Bigg(2u_1 \\
&- 2u_2 + w_1 \dot{w}_1 - w_2 \dot{w}_2 \Bigg) + \frac{2}{b^2} \Bigg({u_1}^2 + {u_2}^2 + \frac{1}{3} {w_1}^2 \dot{w}_1^2 + \frac{1}{3} {w_2}^2 \dot{w}_2^2 \\
&+ u_1 w_1 \dot{w}_1 + u_2 w_2 \dot{w}_2 \Bigg) \Bigg] - P \left[q_s^2 \frac{\pi^2}{2} \cos^2 \frac{\pi z}{L} - \frac{1}{2} \left(\dot{u}_1 + \dot{u}_2 \right) + \Delta \right] \Bigg\} \mathrm{d}z.
\end{aligned} \tag{3.16}$$

3.1.4 Variational Formulation

The governing differential equations are obtained by performing the calculus of variations on the total potential energy V following a well established procedure that has been detailed in Hunt and Wadee (1998). The integrand of the total potential energy V can be expressed as the Lagrangian ($\mathcal{L}$) of the form:

$$V = \int_0^L \mathcal{L} \left(\ddot{w}_i, \dot{w}_i, w_i, \dot{u}_i, u_i, z \right) \mathrm{d}z. \tag{3.17}$$

The first variation of V, which is denoted as δV, is given by the general expression:

$$\delta V = \int_0^L \left[\frac{\partial \mathcal{L}}{\partial \ddot{w}_i} \delta \ddot{w}_i + \frac{\partial \mathcal{L}}{\partial \dot{w}_i} \delta \dot{w}_i + \frac{\partial \mathcal{L}}{\partial w_i} \delta w_i + \frac{\partial \mathcal{L}}{\partial \dot{u}_i} \delta \dot{u}_i + \frac{\partial \mathcal{L}}{\partial u_i} \delta u_i \right] \mathrm{d}z. \tag{3.18}$$

By differentiating partially with respect to the corresponding parameters, δV is determined, thus:

$$\begin{aligned}
\delta V = \int_0^L \Bigg[& \left(\frac{1}{3}Db\ddot{w}_1\right)\delta\ddot{w}_1 + \left(\frac{1}{3}Db\ddot{w}_2\right)\delta\ddot{w}_2 \\
& + \Bigg\{\frac{8D(1-\nu)}{b}\dot{w}_1 + Etb\left[\frac{1}{10}\dot{w}_1^3 - \frac{b}{8}(q_t - q_{t0})\frac{\pi^2}{L}\sin\left(\frac{\pi}{L}z\right)\dot{w}_1 - \frac{1}{3}\dot{w}_1\Delta + \frac{1}{4}\dot{u}_1\dot{w}_1\right] \\
& \quad + Gtb\left[\frac{2}{b^2}\left(\frac{2}{3}{w_1}^2\dot{w}_1 + u_1 w_1\right) - \frac{1}{b}\left(q_s - q_t - q_{s0} + q_{t0}\right)\pi\cos\left(\frac{\pi}{L}z\right)w_1\right]\Bigg\}\delta\dot{w}_1 \\
& + \Bigg\{\frac{8D(1-\nu)}{b}\dot{w}_2 + Etb\left[\frac{1}{10}\dot{w}_2^3 + \frac{b}{8}(q_t - q_{t0})\frac{\pi^2}{L}\sin\left(\frac{\pi}{L}z\right)\dot{w}_2 - \frac{1}{3}\dot{w}_2\Delta + \frac{1}{4}\dot{u}_2\dot{w}_2\right] \\
& \quad + Gtb\left[\frac{2}{b^2}\left(\frac{2}{3}{w_2}^2\dot{w}_2 + u_2 w_2\right) + \frac{1}{b}\left(q_s - q_t - q_{s0} + q_{t0}\right)\pi\cos\left(\frac{\pi}{L}z\right)w_2\right]\Bigg\}\delta\dot{w}_2 \\
& + \left\{Gtb\left[\frac{2}{b^2}\left(\frac{2}{3}w_1\dot{w}_1^2 + u_1\dot{w}_1\right) - \frac{1}{b}\left(q_s - q_t - q_{s0} + q_{t0}\right)\pi\cos\left(\frac{\pi}{L}z\right)\dot{w}_1\right]\right\}\delta w_1 \\
& + \left\{Gtb\left[\frac{2}{b^2}\left(\frac{2}{3}w_2\dot{w}_2^2 + u_2\dot{w}_2\right) + \frac{1}{b}\left(q_s - q_t - q_{s0} + q_{t0}\right)\pi\cos\left(\frac{\pi}{L}z\right)\dot{w}_2\right]\right\}\delta w_2 \\
& + \left\{Etb\left[\frac{1}{3}\dot{u}_1 - \frac{b}{6}(q_t - q_{t0})\frac{\pi^2}{L}\sin\left(\frac{\pi}{L}z\right) - \frac{1}{2}\Delta + \frac{1}{8}\dot{w}_1^2\right] + \frac{1}{2}P\right\}\delta\dot{u}_1 \\
& + \left\{Etb\left[\frac{1}{3}\dot{u}_2 + \frac{b}{6}(q_t - q_{t0})\frac{\pi^2}{L}\sin\left(\frac{\pi}{L}z\right) - \frac{1}{2}\Delta + \frac{1}{8}\dot{w}_2^2\right] + \frac{1}{2}P\right\}\delta\dot{u}_2 \\
& + \left\{Gtb\left[\frac{2}{b^2}\left(2u_1 + \dot{w}_1 w_1\right) - \frac{2}{b}\left(q_s - q_t - q_{s0} + q_{t0}\right)\pi\cos\left(\frac{\pi}{L}z\right)\right]\right\}\delta u_1 \\
& + \left\{Gtb\left[\frac{2}{b^2}\left(2u_2 + \dot{w}_2 w_2\right) + \frac{2}{b}\left(q_s - q_t - q_{s0} + q_{t0}\right)\pi\cos\left(\frac{\pi}{L}z\right)\right]\right\}\delta u_2\Bigg]\mathrm{d}z.
\end{aligned} \tag{3.19}$$

To find the equilibrium states, V must be stationary, which requires δV to vanish for any small change in w_i and u_i. Since the following relations are true:

$$\delta\ddot{w}_i = \frac{\mathrm{d}(\delta\dot{w}_i)}{\mathrm{d}z}, \quad \delta\dot{w}_i = \frac{\mathrm{d}(\delta w_i)}{\mathrm{d}z}, \quad \delta\dot{u}_i = \frac{\mathrm{d}(\delta u_i)}{\mathrm{d}z}, \tag{3.20}$$

integration by parts allows the development of the Euler–Lagrange equations for w_i and u_i; these comprise fourth order ordinary differential equations (ODEs) for w_i and second order ODEs for u_i. For the equations to be solved by the continuation package AUTO, the system variables need to be rescaled with respect to the non-dimensional spatial coordinate $\tilde{z} = 2z/L$. Non-dimensional out-of-plane displacements $\tilde{w}_i$ and in-plane displacements $\tilde{u}_i$

are also introduced as $2w_i/L$ and $2u_i/L$ respectively. The non-dimensional scalings for higher order derivatives with respect to w_i and u_i are determined by the chain rule of differentiation and summarized in Table 3.1. Note that these scalings assume symmetry

First order derivatives	$\tilde{\dot{w}}_i = \tilde{w}_i$, $\tilde{\dot{u}}_i = \tilde{u}_i$
Second order derivatives	$\tilde{\ddot{w}}_i = L\tilde{w}_i/2$, $\tilde{\ddot{u}}_i = L\tilde{u}_i/2$
Fourth order derivatives	$\tilde{\dddot{w}}_i = L^3\tilde{w}_i/8$

Table 3.1: Non-dimensional scalings for higher order derivatives with respect to w_i and u_i.

about the midspan and the differential equations are solved for half the length of the strut; this assumption has been shown to be perfectly acceptable for cases where global buckling is critical (Wadee, 2000). For cases where local buckling is critical, this condition is also acceptable so long as the length of the strut L is much larger than the flange outstand width $b/2$ (Wadee & Yiatros, 2011); hence the critical loads for symmetric and antisymmetric modes are sufficiently close for the buckling plate. The non-dimensional differential equations for w_i and u_i are thus:

$$\begin{aligned}
&\tilde{\dddot{w}}_1 - 6\phi^2(1-\nu)\,\tilde{\ddot{w}}_1 + \left(\frac{3\tilde{D}}{8}\right)\left\{(q_t - q_{t0})\frac{\pi^2}{4\phi}\left(\sin\frac{\pi\tilde{z}}{2}\tilde{\ddot{w}}_1 + \frac{\pi}{2}\cos\frac{\pi\tilde{z}}{2}\tilde{\dot{w}}_1\right)\right.\\
&\quad\left. + \tilde{\ddot{w}}_1\left(\frac{2}{3}\Delta - \frac{3}{5}\tilde{w}_1^2\right) - \frac{1}{2}\left(\tilde{\ddot{u}}_1\tilde{w}_1 + \tilde{\dot{u}}_1\tilde{\dot{w}}_1\right)\right\}\\
&\quad - \frac{3\tilde{G}}{8}\phi^2\tilde{w}_1\left[\frac{2}{3}\tilde{\dot{w}}_1^2 + \frac{2}{3}\tilde{w}_1\tilde{\ddot{w}}_1 + \tilde{\dot{u}}_1 + (q_s - q_t - q_{s0} + q_{t0})\frac{\pi^2}{2\phi}\sin\frac{\pi\tilde{z}}{2}\right] = 0,
\end{aligned} \tag{3.21}$$

$$\begin{aligned}
&\tilde{\ddot{u}}_1 + \frac{3}{4}\tilde{\dot{w}}_1\tilde{\ddot{w}}_1 - \left\{(q_t - q_{t0})\frac{\pi^3}{4\phi}\cos\frac{\pi\tilde{z}}{2} - \left(\frac{3\tilde{G}\phi^2}{\tilde{D}}\right)\left[(q_s - q_t - q_{s0} + q_{t0})\frac{\pi}{\phi}\cos\frac{\pi\tilde{z}}{2}\right.\right.\\
&\quad\left.\left. - \frac{1}{2}\tilde{w}_1\tilde{\dot{w}}_1 - \tilde{u}_1\right]\right\} = 0,
\end{aligned} \tag{3.22}$$

$$\begin{aligned}
&\tilde{\dddot{w}}_2 - 6\phi^2(1-\nu)\,\tilde{\ddot{w}}_2 - \left(\frac{3\tilde{D}}{8}\right)\left\{(q_t - q_{t0})\frac{\pi^2}{4\phi}\left(\sin\frac{\pi\tilde{z}}{2}\tilde{\ddot{w}}_2 + \frac{\pi}{2}\cos\frac{\pi\tilde{z}}{2}\tilde{\dot{w}}_2\right)\right.\\
&\quad\left. - \tilde{\ddot{w}}_2\left(\frac{2}{3}\Delta - \frac{3}{5}\tilde{w}_2^2\right) + \frac{1}{2}\left(\tilde{\ddot{u}}_2\tilde{w}_2 + \tilde{\dot{u}}_2\tilde{\dot{w}}_i\right)\right\}\\
&\quad - \frac{3\tilde{G}}{8}\phi^2\tilde{w}_2\left[\frac{2}{3}\tilde{\dot{w}}_2^2 + \frac{2}{3}\tilde{w}_2\tilde{\ddot{w}}_2 + \tilde{\dot{u}}_2 - (q_s - q_t - q_{s0} + q_{t0})\frac{\pi^2}{2\phi}\sin\frac{\pi\tilde{z}}{2}\right] = 0,
\end{aligned} \tag{3.23}$$

$$\tilde{\ddot{u}}_2 + \frac{3}{4}\tilde{\dot{w}}_2\tilde{\ddot{w}}_2 + \left\{(q_t - q_{t0})\frac{\pi^3}{4\phi}\cos\frac{\pi\tilde{z}}{2} - \left(\frac{3\tilde{G}\phi^2}{\tilde{D}}\right)\left[(q_s - q_t - q_{s0} + q_{t0})\,\frac{\pi}{\phi}\cos\frac{\pi\tilde{z}}{2} + \frac{1}{2}\tilde{w}_2\tilde{\dot{w}}_2 + \tilde{u}_2\right]\right\} = 0, \tag{3.24}$$

where $\tilde{D} = EtL^2/D$, $\tilde{G} = GtL^2/D$ and $\phi = L/b$. Note that there is no interaction between the terms with $i = 1$ and the terms with $i = 2$; each set of local displacement functions interacts with the global coordinates q_s and q_t, indicated by the cross terms which carry opposite signs for $i = 1$ and $i = 2$.

Equilibrium also requires the minimization of the total potential energy with respect to the generalized coordinates q_s, q_t and Δ. This provides three integral equations, which in non-dimensional form are:

$$\begin{aligned}
\frac{\partial V}{\partial q_s} &= \pi^2(q_s - q_{s0}) + \tilde{s}\,(q_s - q_t - q_{s0} + q_{t0}) - \frac{PL^2}{EI_w}q_s \\
&\quad - \frac{\tilde{s}\phi}{\pi}\int_0^1 \cos\frac{\pi\tilde{z}}{2}\left[\frac{1}{2}\left(\tilde{w}_1\tilde{\dot{w}}_1 - \tilde{w}_2\tilde{\dot{w}}_2\right) + (\tilde{u}_1 - \tilde{u}_2)\right]\mathrm{d}\tilde{z} = 0, \\
\frac{\partial V}{\partial q_t} &= \pi^2(q_t - q_{t0}) - \tilde{t}\,(q_s - q_t - q_{s0} + q_{t0}) + \phi\int_0^1 \left\{\frac{\tilde{t}}{\pi}\cos\frac{\pi\tilde{z}}{2}\left[\frac{1}{2}\left(\tilde{w}_1\tilde{\dot{w}}_1 - \tilde{w}_2\tilde{\dot{w}}_2\right)\right.\right. \\
&\quad \left.\left. + (\tilde{u}_1 - \tilde{u}_2)\right] - \sin\frac{\pi\tilde{z}}{2}\left[2\left(\tilde{\dot{u}}_1 - \tilde{\dot{u}}_2\right) + \frac{3}{4}\left(\tilde{\dot{w}}_1^2 - \tilde{\dot{w}}_2^2\right)\right]\right\}\mathrm{d}\tilde{z} = 0, \\
\frac{\partial V}{\partial \Delta} &= \int_0^1 \left[2\left(1 + \frac{h}{b}\right)\Delta - \frac{1}{2}\left(\tilde{\dot{u}}_1 + \tilde{\dot{u}}_2\right) - \frac{1}{6}\left(\tilde{\ddot{w}}_1^2 + \tilde{\ddot{w}}_2^2\right) - \frac{P}{Etb}\right]\mathrm{d}\tilde{z} = 0,
\end{aligned} \tag{3.25}$$

where $\tilde{s} = 2GtbL^2/(EI_w)$ and $\tilde{t} = 12G\phi^2/E$. Since the strut is an integral member the expressions in Equation (3.25) provide a relationship linking q_s and q_t before any interactive buckling occurs, *i.e.* when $w_i = u_i = 0$. This relationship is assumed to hold also between q_{s0} and q_{t0}, which has the beneficial effect of reducing the number of imperfection amplitude parameters to one.

The boundary conditions for $\tilde{w}_i$ and $\tilde{u}_i$ and their derivatives are for pin ended conditions for $\tilde{z} = 0$ and for symmetry at $\tilde{z} = 1$:

$$\tilde{w}_i(0) = \tilde{\ddot{w}}_i(0) = \tilde{\dot{w}}_i(1) = \tilde{\dddot{w}}_i(1) = \tilde{u}_i(1) = 0, \tag{3.26}$$

with further conditions from matching the in-plane strain:

$$\frac{1}{3}\tilde{u}_i(0) + \frac{1}{8}\tilde{w}_i^2(0) - \frac{1}{2}\Delta + \frac{P}{2Etb} = 0. \tag{3.27}$$

This final expression is derived from minimizing the terms $\delta\dot{u}_i$ in Equation (3.19). For both cases, the imposed symmetry reduces computational effort considerably.

3.1.5 Linear eigenvalue analysis

Before solving the differential equations, linear eigenvalue analysis for the perfect strut is conducted to determine the critical load for global buckling P_o^{C}. This is achieved by considering that the Hessian matrix $\mathbf{V}_{\mathrm{st}}$ at the critical load is singular. Hence:

$$\det\left(\mathbf{V}_{\mathrm{st}}\right) = \begin{vmatrix} \frac{\partial^2 V}{\partial q_s^2} & \frac{\partial^2 V}{\partial q_s \partial q_t} \\ \frac{\partial^2 V}{\partial q_t \partial q_s} & \frac{\partial^2 V}{\partial q_t^2}. \end{vmatrix} = 0. \tag{3.28}$$

Recalling of course that in fundamental equilibrium for this case, $q_s = q_t = w_i = u_i = 0$. Hence, the critical load for global buckling is:

$$P_o^{\mathrm{C}} = \frac{\pi^2 E I_w}{L^2} + \frac{2Gtb}{1 + \tilde{t}/\pi^2}. \tag{3.29}$$

If the limit $G \to \infty$ is taken, which represents a principal assumption in Euler–Bernoulli bending theory, the critical load expression converges to the Euler buckling load for an I-section strut buckling about the weak axis.

3.2 Numerical examples of perfect behaviour

Two numerical examples, representing the perfect behaviour of the strut, are presented in this section for the cases where local buckling and global buckling are critical in turn.

Obviously, the critical buckling mode is controlled by the section properties and member length. In the current chapter, a fixed set of cross-section and material properties are chosen and shown in Table 3.2, whereas the strut length, L, is varied such that the

Flange width b	96 mm
Flange thickness t	1.2 mm
Cross-section depth h	120 mm
Cross-section area A	513 mm^2
Young's modulus E	210 kN/mm^2
Poisson's ratio ν	0.3

Table 3.2: Cross-section and material properties of an example strut. Recall that the thickness of the web $t_w = 2t$. The geometric properties are similar to those tested in Becque and Rasmussen (2009a).

cases where local buckling or global buckling are critical can be presented. The global critical load P_o^{C} can be calculated using Equation (3.29), whereas an estimate for the local buckling critical stress σ_l^{C} can be evaluated using the well-known plate buckling formula:

$$\sigma_l^{\mathrm{C}} = \frac{kD\pi^2}{b^2 t}, \tag{3.30}$$

where the coefficient k depends on the boundary conditions; values of $k = 0.426$ and $k = 4$ are chosen for the rectangular plates representing the flange outstands (three edges pinned and one edge free) and the web (all four edges pinned) respectively, assuming that the plates are relatively long (Bulson, 1970). Table 3.3 summarizes the critical stresses

L (m)	σ_o^{C} (N/mm^2)	$\sigma_{l,\mathrm{flange}}^{\mathrm{C}}$ (N/mm^2)	$\sigma_{l,\mathrm{web}}^{\mathrm{C}}$ (N/mm^2)	Critical mode
3.5	58.3	51.1	2731	Local (flange)
4.0	44.7	51.1	2731	Global

Table 3.3: Theoretical values of the global and local critical buckling stresses for two separate lengths. The expression for $\sigma_o^{\mathrm{C}} = P_o^{\mathrm{C}}/A$ and the web is obviously not vulnerable to local buckling.

and shows that the assigned cross-section dimensions satisfy the assumptions that the local mode is critical for one of the lengths and the global mode is critical for the other. Moreover, the critical stress of the web is two orders of magnitude higher than that of the

flange, which justifies the assumption stated earlier that the web would not be susceptible to local buckling. It should be noted that $t_w = 2t$ has been taken to evaluate $\sigma^{\mathrm{C}}_{l,\mathrm{web}}$ and this assumes that there are a sufficient number of closely spaced connectors to make the two web plates act as one. However, since $\sigma^{\mathrm{C}}_{l,\mathrm{web}} \gg \sigma^{\mathrm{C}}_{l,\mathrm{flange}}$ the assumption that the web does not buckle before the flange still holds even if $t_w = t$.

3.2.1 AUTO-07P

The full nonlinear differential equations are obviously too complicated to be solved analytically. The continuation and bifurcation software AUTO-07P (Doedel & Oldeman, 2009) has been shown in the literature (Hunt & Wadee, 1998; Wadee & Hunt, 1998; Wadee, 2000; Wadee & Blackmore, 2001; Wadee *et al.*, 2010) to be an ideal tool to solve the equations numerically. For this type of mechanical problem, one of its major attributes is that it has the capability to show the evolution of the solutions to the equations with parametric changes. The solver is very powerful in locating bifurcation points and tracing branching paths as model parameters are varied.

The current study comprises nonlinear non-autonomous ordinary differential equations subject to boundary and integral conditions, which are solved by numerical techniques including the modified Newton–Raphson method and the pseudo-arclength continuation method. AUTO initially discretizes the problem by the method of orthogonal collocation (de Boor & Swartz, 1973). The mesh size can be manually controlled before each numerical run to achieve convergence. The mesh is automatically adapted during the run to distribute the local discretization error evenly (Russell & Christiansen, 1978). The solver starts at an initial point in the solution space and estimates a solution that is then iteratively corrected using the modified Newton–Raphson method, until the solution is

within the specified error tolerance. Beyond folds and limit points, the pseudo-arclength continuation method is utilized in conjunction with Newton's method (Riks, 1972). This is important in the current investigation since the expected cellular behaviour comprises a sequence of limit points in the post-buckling range. Furthermore, the solver is powerful in locating bifurcation points by recognizing that the rank of the Jacobian matrix of the system reduces by at least one at the location of a bifurcation point (Doedel & Oldeman, 2009). Upon the evaluation of the derivative of the Jacobian, the different post-bifurcation paths can be traced by finding the solution of the roots of the resulting algebraic bifurcation equation. The solver allows branch switching after the detection of the bifurcation points, which will be shown to be very powerful in the numerical examples presented later. The software package can also identify other critical points such as folds, Hopf bifurcations, and period doubling bifurcations, which shows its wide applicability in solving nonlinear problems, although most of these features are beyond the scope of the current problem.

3.2.2 Local buckling critical

In this section, the strut with properties given in Table 3.2 with length L being 3.5 m is analysed, where the flange plates buckle locally first. In this case, both sets of the local displacement functions are solved. In general, the current case where local buckling is critical requires a finer mesh and therefore more computational effort.

Solution strategy

Numerical continuations were performed in AUTO. The governing differential equations were first transformed into a system of first order differential equations. The principal parameters used in the continuation process were interchangeable, but generally q_s was varied for computing the equilibrium paths for the distinct buckling modes and P was varied for evaluating the interactive buckling paths. For the case of local buckling being critical, the continuation process initiated from zero load with the local buckling critical load P_l^{C} being obtained numerically. The post-buckling path was then computed by using the branch switching facility within the software and the distinct local buckling equilibrium path was computed until a secondary bifurcation point S was found. It was from this point that the interactive buckling path was found, again through the use of branch switching. Figure 3.6(a) shows the procedure diagrammatically.

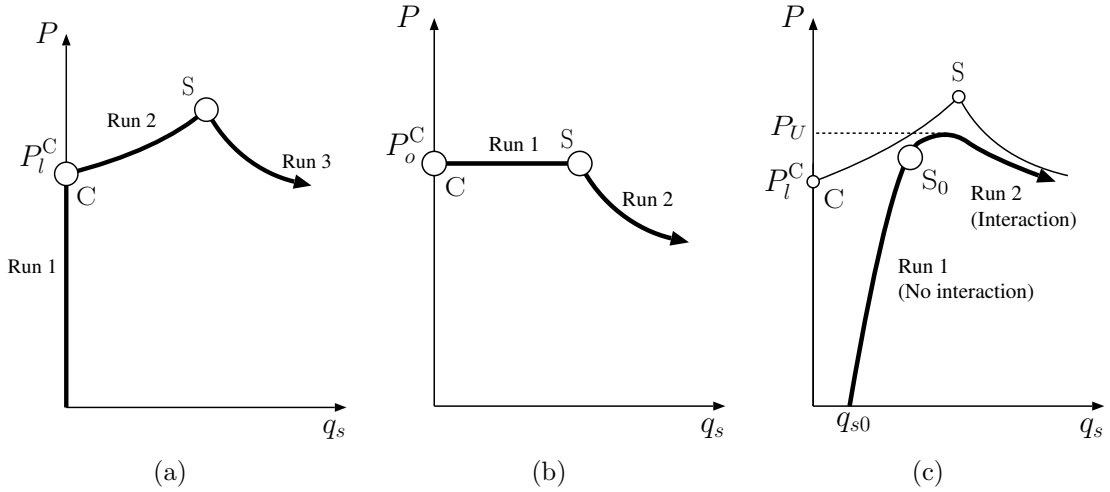

Figure 3.6: Numerical continuation procedures. (a) Local buckling being critical. (b) Global buckling being critical. (c) Imperfect case – example of local buckling being critical shown. The thicker line shows the actual solution path in each of the examples shown. Points C and S represent the critical and secondary bifurcations respectively, whereas the point S_0 represents the bifurcation leading to interactive buckling in the imperfect case with the load P_U being the ultimate load for the imperfect case.

Results and discussion

Figure 3.7 shows a plot of the normalized axial load $p = P/P_o^{\mathrm{C}}$ versus (a) the local mode and (b) the global mode amplitudes. Figure 3.8(a) shows the local and global mode relative magnitudes during post-buckling and (b) shows that there is a small but importantly, non-zero shear strain during global buckling. The local critical buckling load is calculated at $p = 0.905$, whereas according to Table 3.3, this value should be 0.877, which represents a small error of 3%, particularly since it is well known that the theoretical expression for the critical buckling stress for an infinitely long plate is a lower bound value for the relevant boundary condition and current plate geometry.

One of the most distinctive features of the equilibrium paths, as shown in Figure 3.7(a)–(b) and Figure 3.8(a), is the sequence of snap-backs that effectively divides the equilibrium path into 10 individual parts (or *cells*) in total. The fourth, seventh and the tenth paths are labelled as $C4$, $C7$ and $C10$ respectively. Each path or cell corresponds to the formation of a new local buckling displacement peak or trough. Figure 3.9 illustrates the corresponding progression of the numerical solutions for the local buckling functions w_1 and u_1 from cell $C1$ to $C10$, where $C1$ represents the initial post-buckling equilibrium path generated from the critical bifurcation point C. Once a secondary bifurcation is triggered at S, it is observed that the local buckling mode is contaminated by the global mode and interactive buckling ensues with the buckling deformation spreading towards the supports as new peaks and troughs are formed. Figure 3.10 shows a selection of 3-dimensional representations of the deflected strut that comprise the components of global buckling (W and θ) and local buckling (w_i and u_i) at a specific state on paths $C1$, $C4$, $C7$ and $C10$. As the equilibrium path develops to $C10$, the maximum out-of-plane displacement $w_{\max}$ approaches a value of 2.5 mm which is approximately twice

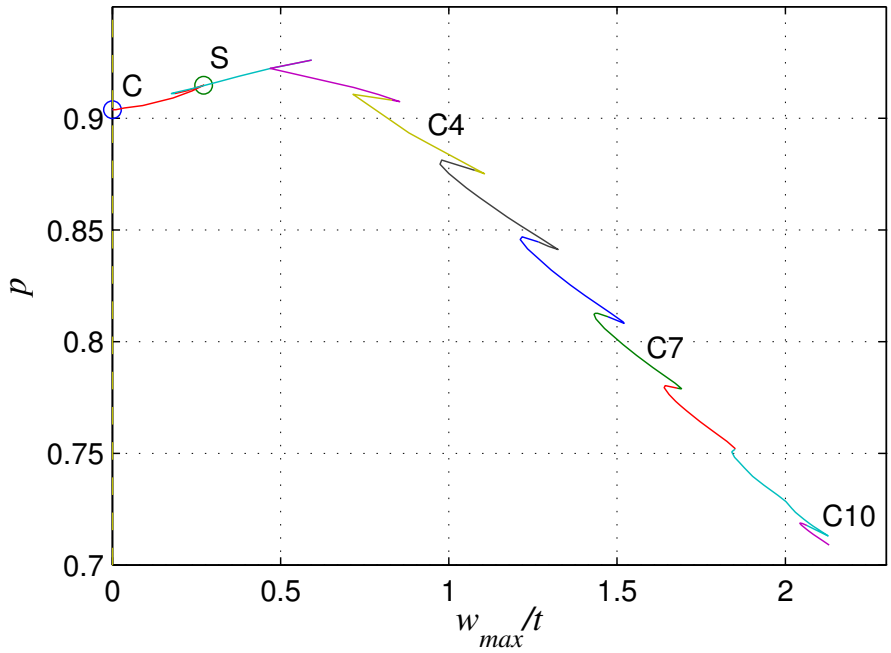

(a)

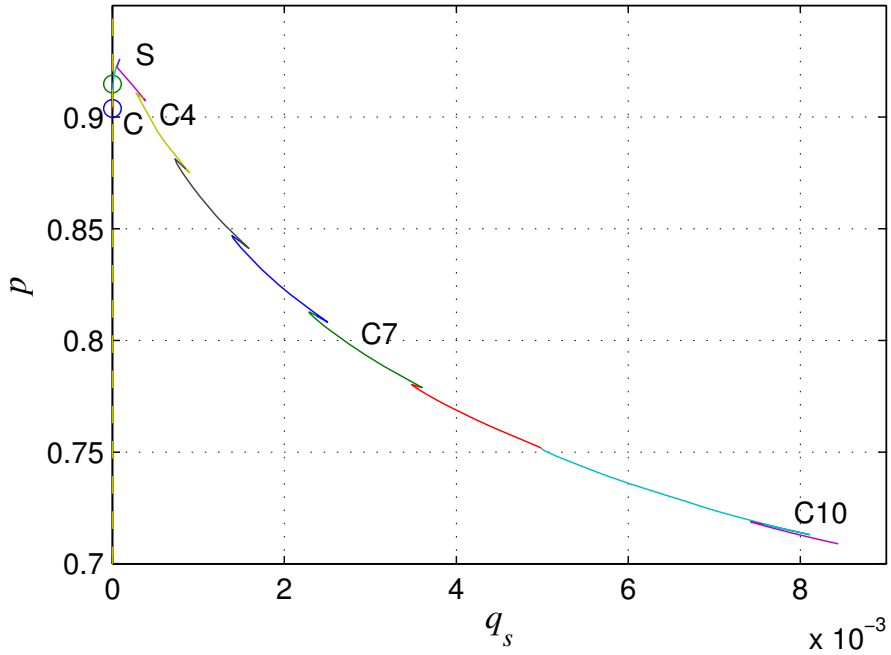

(b)

Figure 3.7: Numerical equilibrium paths for $L = 3.5$ m where local buckling is critical. Graphs of the normalized force ratio p versus (a) the maximum out-of-plane displacement of the buckled flange plate, in non-dimensional form, $w_{\max}/t$ and (b) the generalized coordinate q_s are shown.

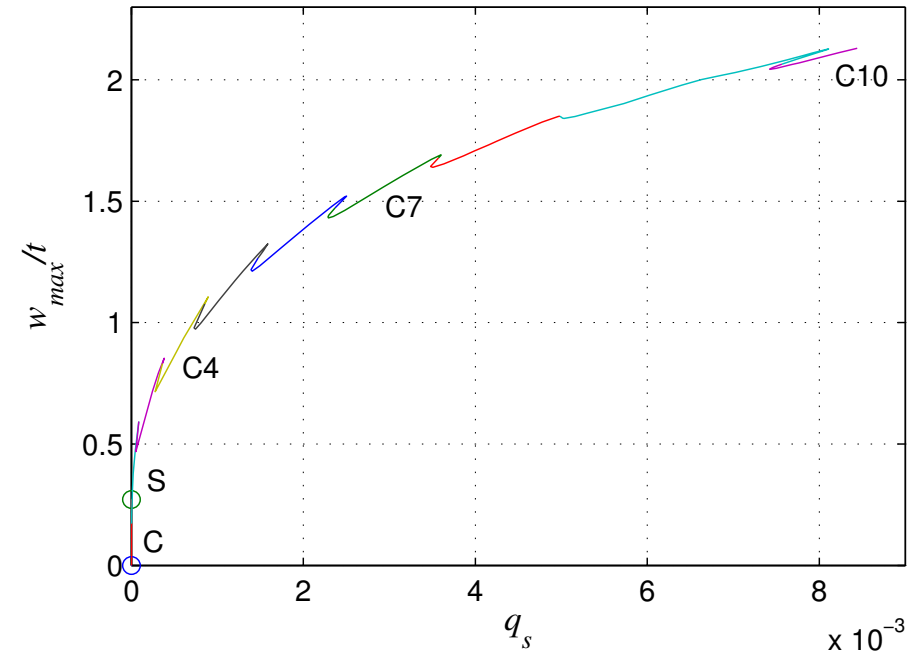

(a)

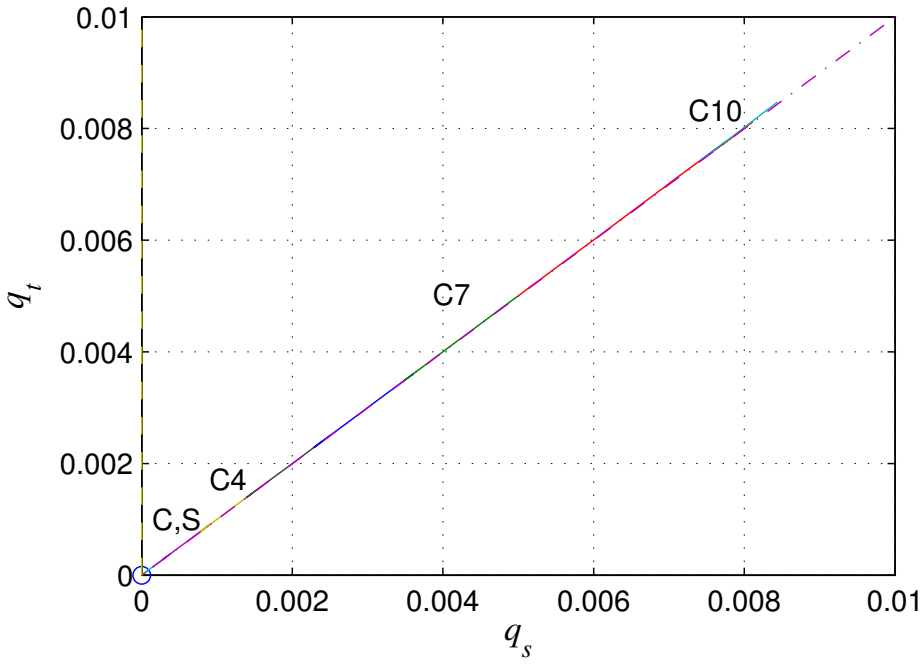

(b)

Figure 3.8: Numerical equilibrium paths for $L = 3.5$ m where local buckling is critical. Graph (a) shows $w_{\max}/t$ versus q_s and (b) shows the relationship between the generalized coordinates q_s and q_t (average percentage difference $\approx 0.11\%$) defining the global buckling mode during interactive buckling, with the dot-dashed line showing the Euler–Bernoulli bending condition $q_s = q_t$.

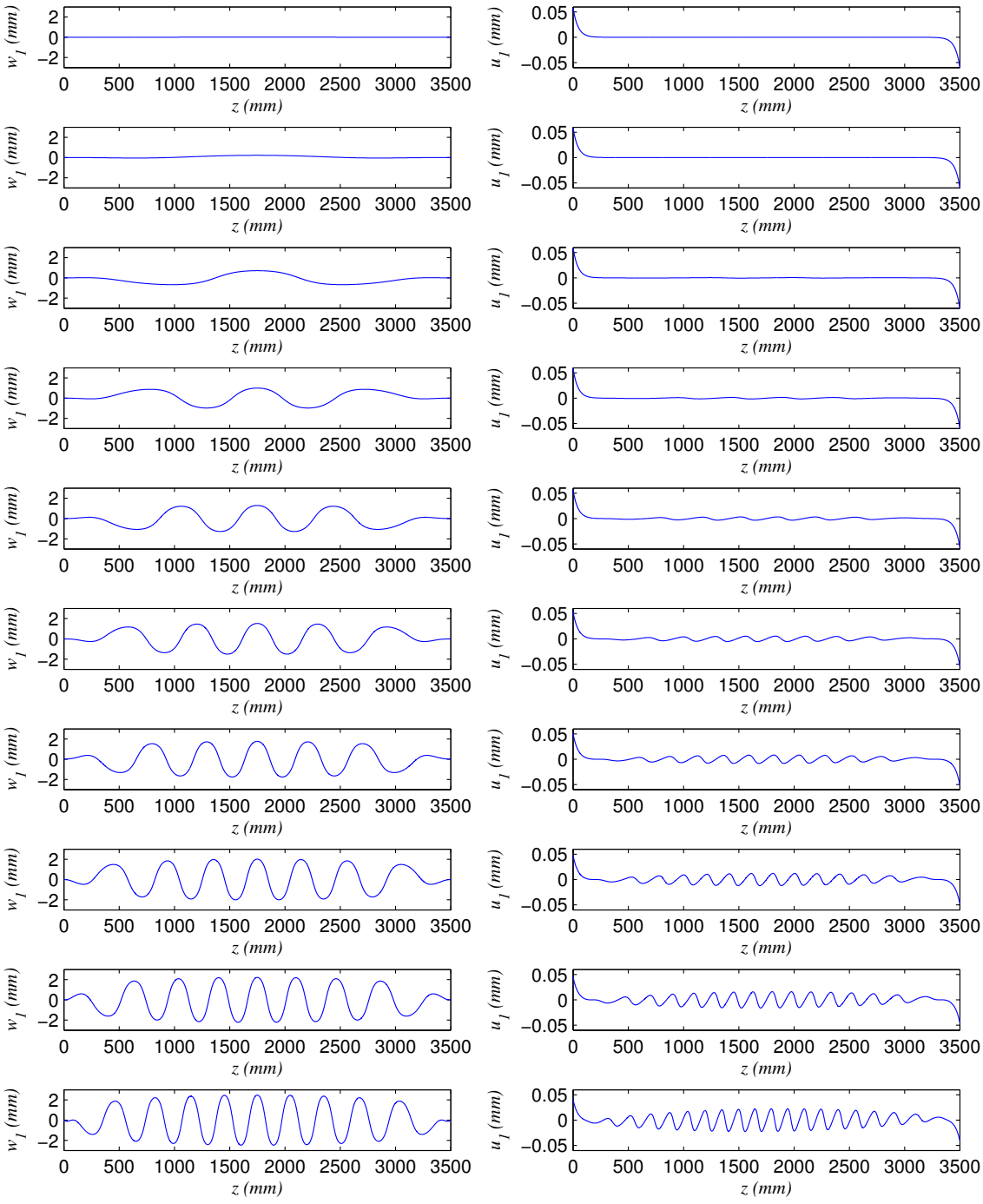

Figure 3.9: Numerical solutions for the local out-of-plane displacement w_1 (left) and local in-plane displacement u_1 (right) for the tip ($x = -b/2$) of the vulnerable flange. Individual solutions on equilibrium paths $C1$ to $C10$ are shown in sequence from top to bottom respectively.

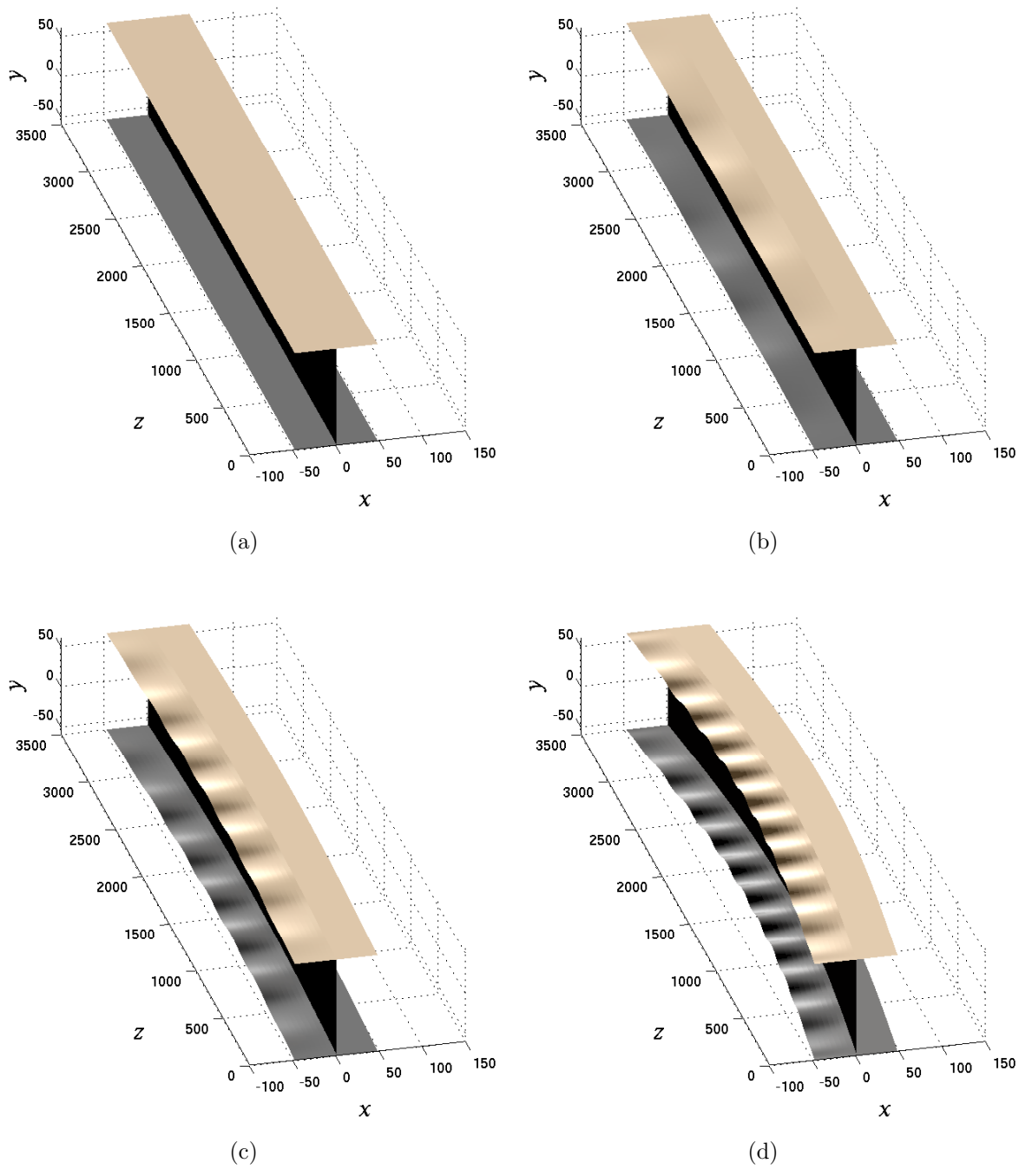

(a) (b)

(c) (d)

Figure 3.10: Numerical solutions of the system of equilibrium equations visualized on 3-dimensional representations of the strut. The results are shown for individual points on paths (a) $C1$ ($p = 0.9039$), (b) $C4$ ($p = 0.9081$), (c) $C7$ ($p = 0.8111$) and (d) $C10$ ($p = 0.7177$). All dimensions are in millimetres.

the flange thickness and can be regarded as large in terms of geometric assumptions. The interactive buckling pattern becomes effectively periodic on path $C10$. Any further deformation along the equilibrium path would be expected to cause restabilization to the system since the boundaries would begin to confine the spread of the buckling deformation. It should be stressed of course that any plastic deformation during the loading stage would destabilize the system significantly. Figure 3.11 shows the comparison between the lateral

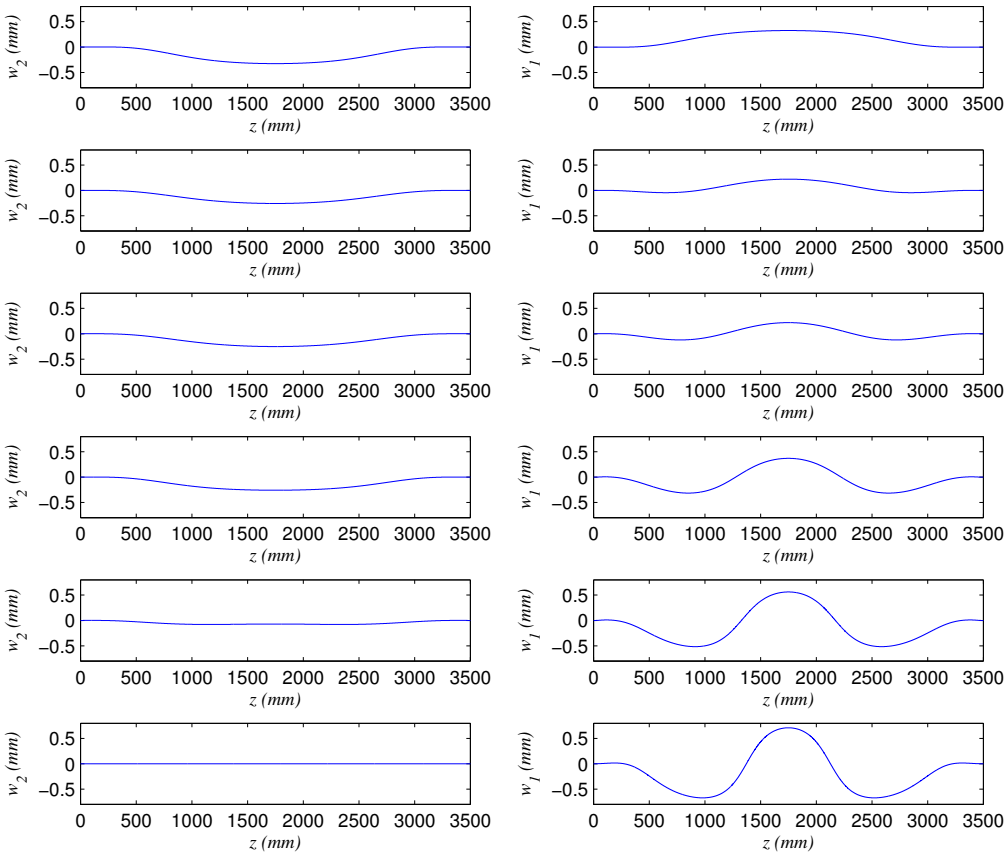

Figure 3.11: Numerical solutions for the local out-of-plane displacement w_2 (left) for the tip of the non-vulnerable flange ($x = b/2$) and w_1 (right) for the tip of the vulnerable flange ($x = -b/2$) for cells 1–3. Note the rapid decay of w_2 reflecting the reducing compression in that outstand once global buckling is triggered.

displacement of the two flange outstands. The local buckling displacement in the non-vulnerable outstand w_2 decays to zero rapidly as the global mode amplitude increases during interactive buckling; by the third cell, w_2 has vanished implying that if global

buckling occurs first, both w_2 and u_2 would be negligible.

The magnitude of direct and shear strains may be calculated once the governing differential equations are solved. Figure 3.12(a) shows the direct strains, ε_{z1} and ε_{z2} in the extreme fibre of the flange outstands, at the equilibrium states specified in Figure 3.10, whereas the corresponding shear strains are shown in Figure 3.12(b). The direct strain in the non-vulnerable part of the flange becomes tensile at $C10$ due to bending, whereas the maximum direct strain in the vulnerable part of the flange is approximately $1.3 \times 10^{-3} (= 0.13\%)$. This level of strain is confined to the ends of the strut and is also well below the yield strain of most structural steels; moreover for the stainless steels given in the works by Becque and Rasmussen (Becque & Rasmussen, 2009a; Becque, 2008), significant reduction in stiffness only begins from approximately 0.15% strain and so quantitative comparisons can be made later for the post-buckling response for the majority of the cells.

As mentioned earlier, systems that exhibit the phenomenon described above are termed in the literature to show 'cellular buckling' (Hunt *et al.*, 2000) or 'snaking' (Burke & Knobloch, 2007). In such systems, progressive destabilization and restabilization is exhibited; currently, the destabilization is caused primarily by the interaction of the global and local instabilities, whereas the restabilization is caused by the stretching of the buckled plates when they bend into double curvature. As the amplitude of the global buckling mode q_s increases, the compressive bending stress in the flange outstands increases also, which implies that progressively longer parts of the flange are susceptible to local buckling. Since local buckling is inherently stable, the drop in the load from the unstable mode interaction is limited due to the stretching of the plate when it buckles into progressively smaller wavelengths. Therefore, the cellular buckling occurs due to the complementary

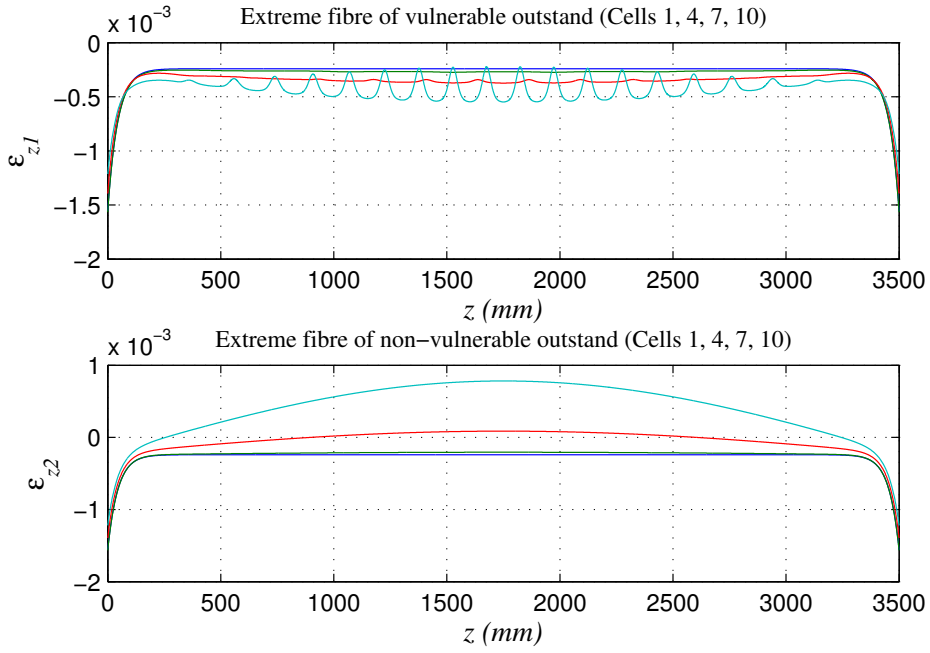

(a)

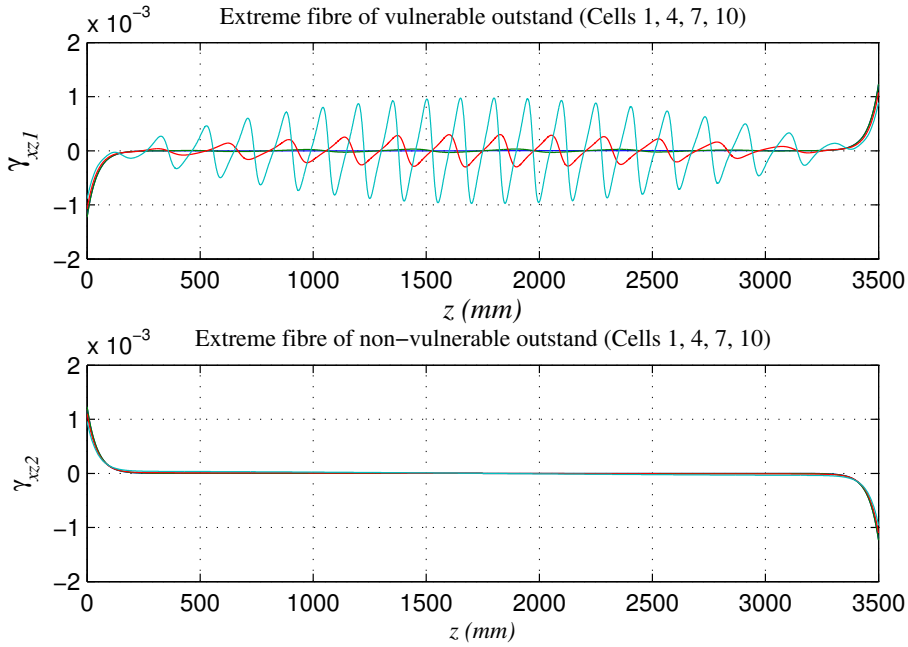

(b)

Figure 3.12: Graphs (a) and (b) show direct and shear strains respectively, in the extreme fibre of the vulnerable and non-vulnerable flange outstands, at the equilibrium states specified in Figure 3.10. The more oscillatory solutions are for those with higher cell numbers.

effects of the unstable mode interaction and the stable local buckling.

Cellular buckling is also strongly associated with the Maxwell load P^{M} (Hunt *et al.*, 2000; Wadee & Edmunds, 2005), where the load oscillates about a fixed load P^{M}. The Maxwell load is associated with a purely periodic solution of the governing equations to which the localized solutions evolve for large values of the deformation (Hunt *et al.*, 2000). However, in the systems such as the cylinder or in compressed confined layers, there is only one loading source (the axial load). In the current case, the global mode provides an effective additional loading source through the coordinate q_t, and hence the total load on the flange continues to increase while equilibrium demands that the external load continues to decrease. Hence a fixed Maxwell load is not seen. The detailed considerations of the level of the load P when the local buckling mode becomes periodic is much more complex and is left for the future. However, it is noted that the total loading, identified as the 'body force' in Hunt and Wadee (1998) could be used to begin this analysis, since it has been shown in Wadee (1998) to give a reasonably good approximation of the total load in a local element such as the flange.

3.2.3 Global buckling critical

In this section, the strut with length L being 4 m is analysed. After global buckling is triggered, one half of the flange is subject to more compression whereas the other half is subject to less compression, due to the bending of the strut about the weak axis. As a consequence, only a half of the flange is vulnerable to local buckling; the functions w_2 and u_2 can therefore be neglected due to the evidence shown in Figure 3.11. This simplifies the formulation considerably and the number of the governing differential equations reduces from four to two.

Solution Strategy

Since the critical load was determined analytically in Equation (3.29), the initial post-buckling path was computed first from P_o^{C} and many bifurcation points were detected on the weakly stable post-buckling path; the focus being on the one with the lowest value of q_s, the secondary bifurcation point S. A subsequent run was then necessary starting from S using the branch switching function, after which the equilibrium path again exhibits the interaction between the global and the local modes; Figure 3.6(b) shows the procedure diagrammatically.

Results and discussion

Figures 3.13 and 3.14 show plots of the equilibrium diagrams that correspond directly to Figures 3.7 and 3.8 respectively. This time, cellular buckling is triggered when the pure global mode is contaminated by the local mode. Since the global mode is only weakly stable, no significant post-buckling stiffness is exhibited initially. Figure 3.15 shows the progression of the numerical solutions for the local buckling functions w_1 and u_1 from cell $C1$ to $C10$. The emergence of the buckling cells in sequence is very similar to that shown for the case where local buckling is critical. However, a more localized local buckling pattern is observed for the early cells. A selection of 3-dimensional representations of the deflected strut is shown in Figure 3.16. Figure 3.17 shows the direct and shear strains, corresponding directly to Figure 3.12, for the equilibrium states specified in Figure 3.16. The direct strain in the non-vulnerable part of the flange again becomes tensile at $C11$, whereas the maximum direct strain in the vulnerable part of the flange is approximately $1.3 \times 10^{-3} (= 0.13\%)$.

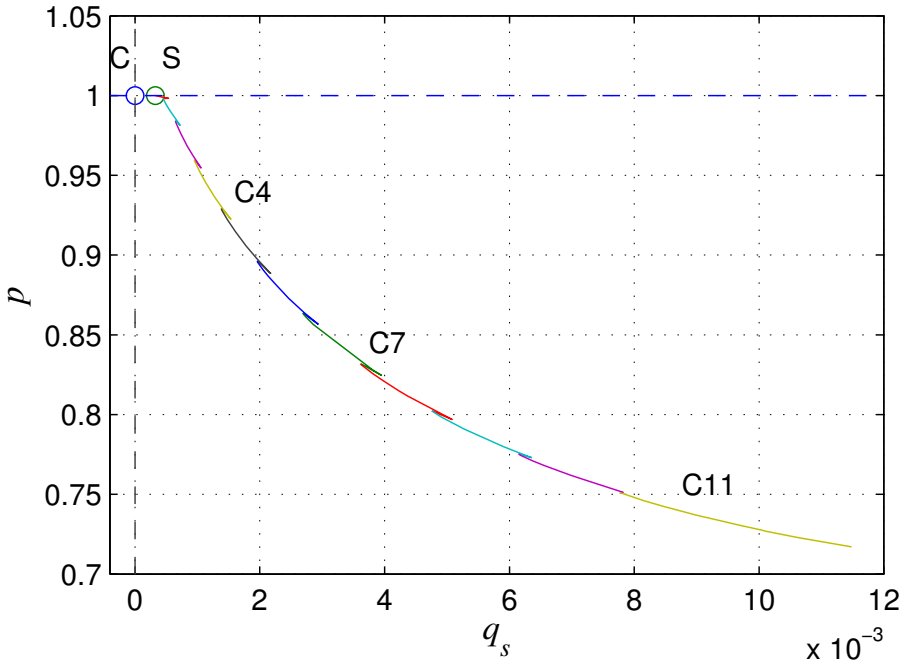

(a)

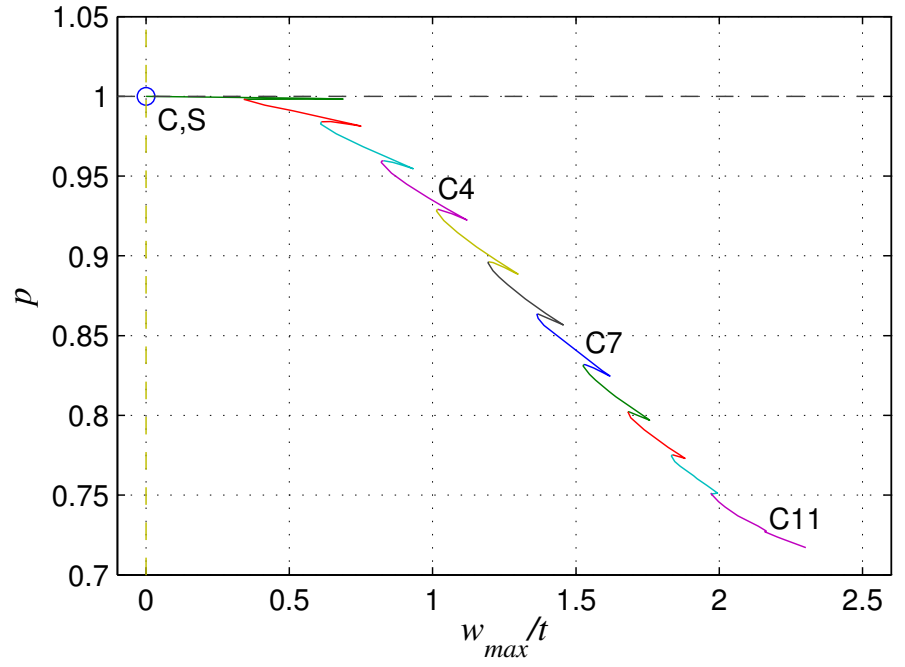

(b)

Figure 3.13: Numerical equilibrium paths for $L = 4.0$ m where global buckling is critical. Graphs of the normalized force ratio p versus (a) the generalized coordinate q_s and (b) the maximum out-of-plane displacement of the buckled flange plate, in non-dimensional form $w_{\max}/t$, are shown.

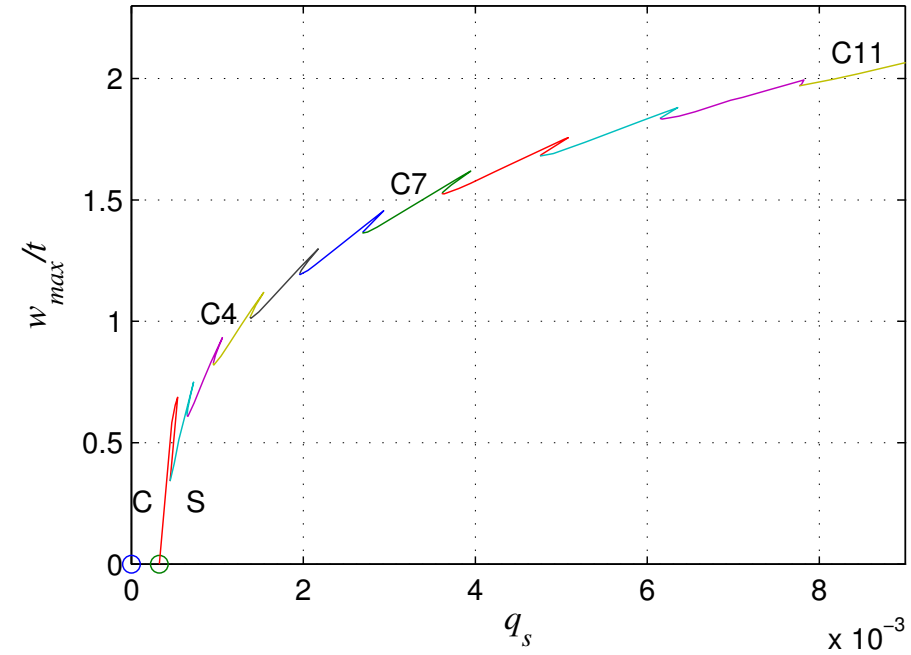

(a)

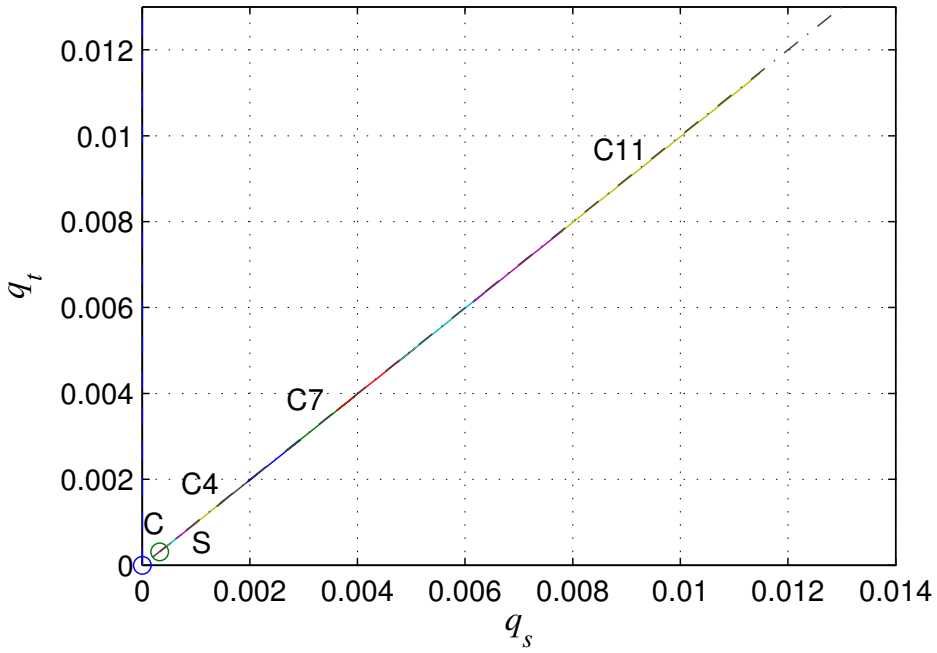

(b)

Figure 3.14: Graph (a) shows $w_{\max}/t$ versus q_s and (b) shows the relationship between the generalized coordinates q_s and q_t (average percentage difference $\approx 0.49\%$) defining the global buckling mode during interactive buckling, with the dot-dashed line showing the Euler–Bernoulli bending condition $q_s = q_t$.

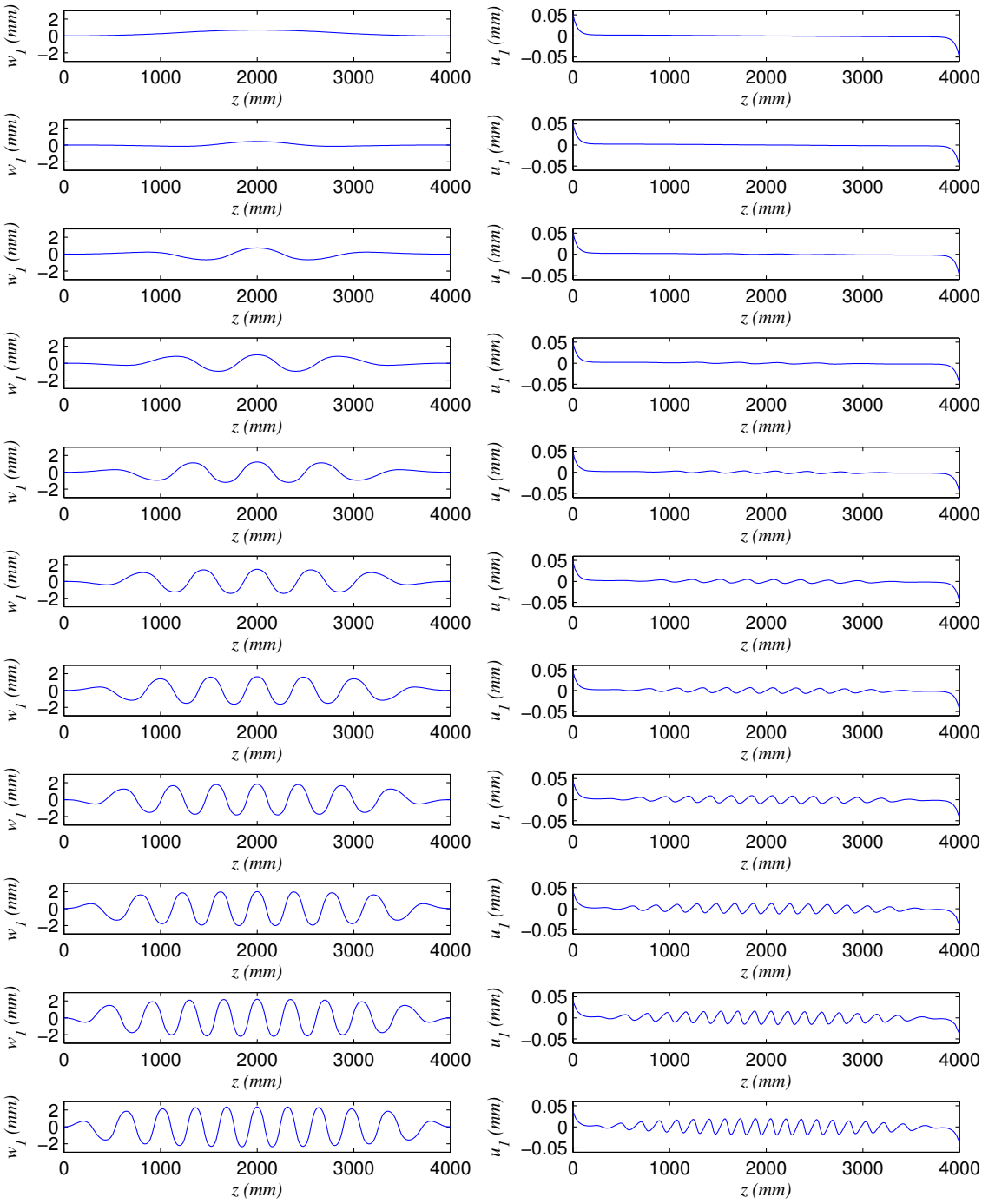

Figure 3.15: Numerical solutions for the local out-of-plane displacement w_1 (left) and local in-plane displacement u_1 (right) for the tip ($x = -b/2$) of the vulnerable flange. Individual solutions on equilibrium paths $C1$ to $C11$ are shown in sequence from top to bottom respectively.

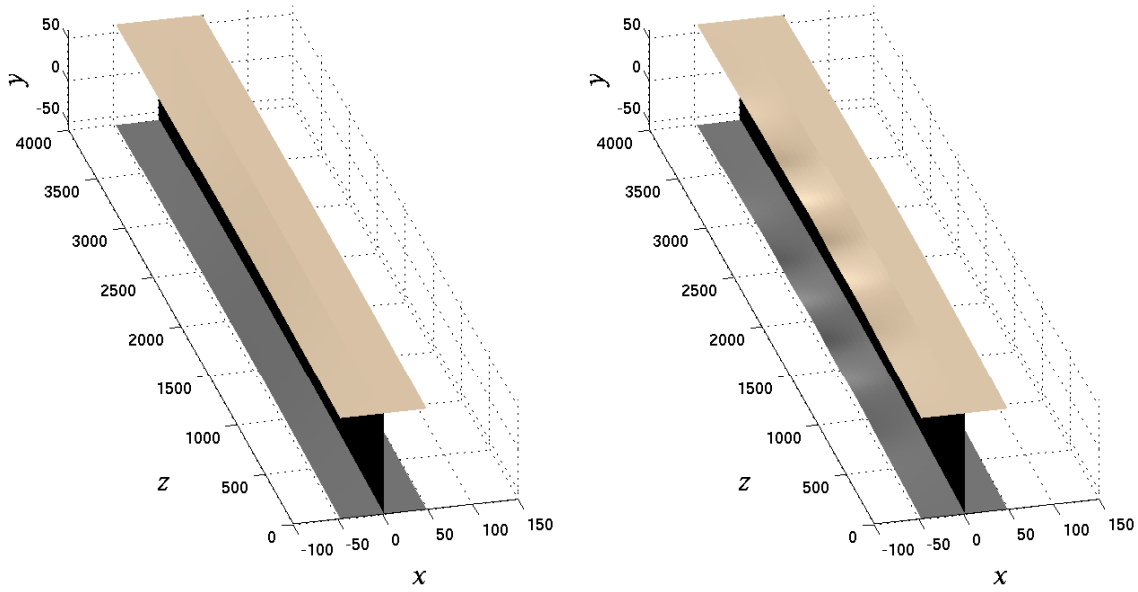

(a)

(b)

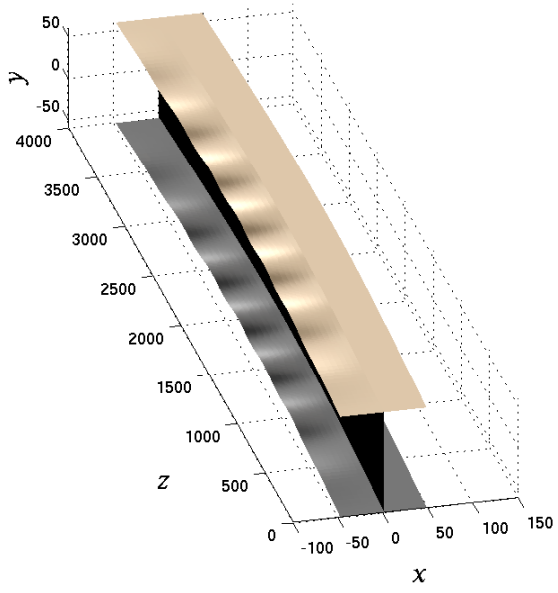

(c)

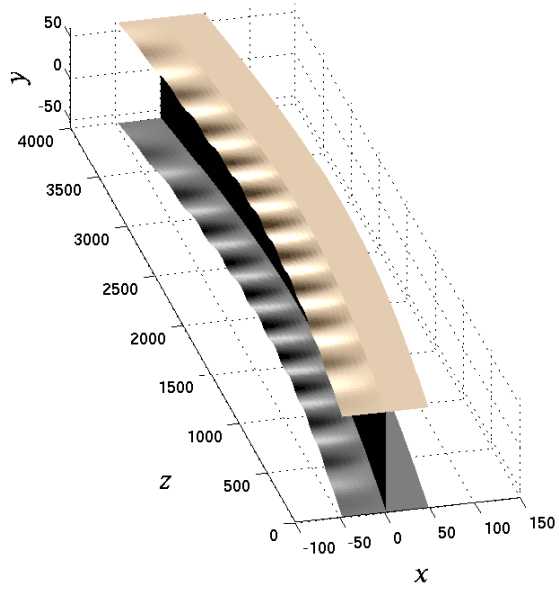

(d)

Figure 3.16: Numerical solutions of the system of equilibrium equations visualized on 3-dimensional representations of the strut. The results are shown for individual points on paths (a) $C1$ ($p = 0.9988$), (b) $C4$ ($p = 0.9597$), (c) $C7$ ($p = 0.8635$) and (d) $C10$ ($p = 0.7753$). All dimensions are in millimetres.

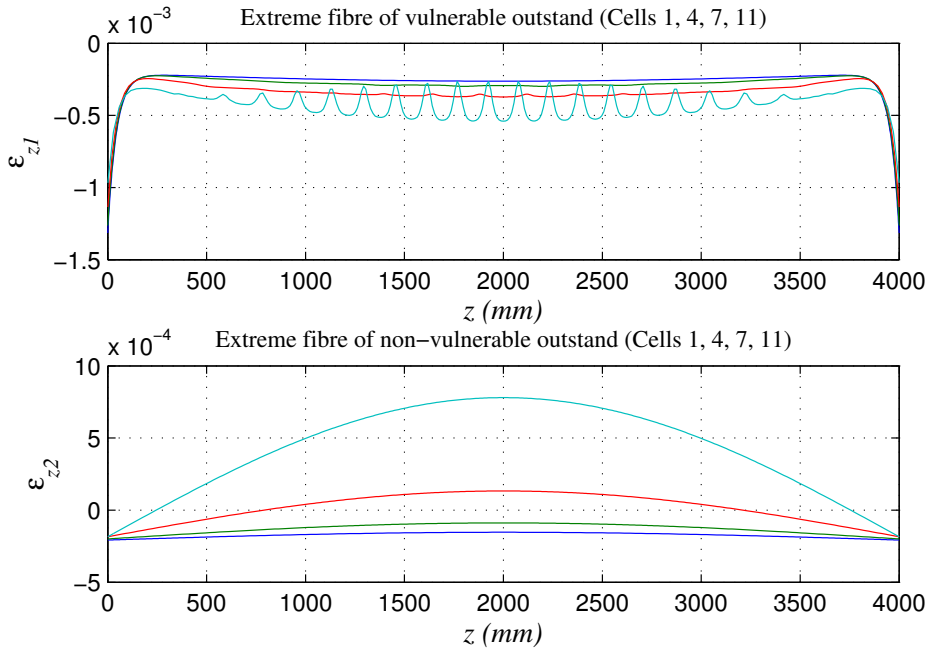

(a)

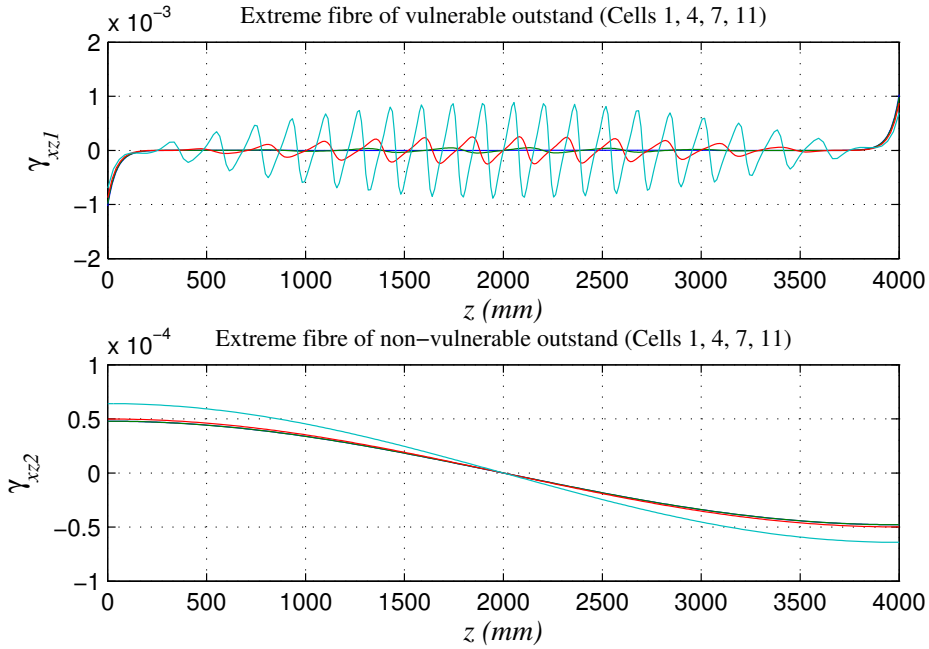

(b)

Figure 3.17: Graphs (a) and (b) show direct and shear strains respectively, in the extreme fibre of the vulnerable and non-vulnerable flange outstands, at the equilibrium states specified in Figure 3.16. The more oscillatory solutions are for those with higher cell numbers.

3.3 Validation and discussion

3.3.1 Comparison with experiments of Becque and Rasmussen

A fairly recent experimental study of thin-walled I-section struts by Becque and Rasmussen (Becque & Rasmussen, 2009a; Becque, 2008) focused on the case where local buckling is critical. Although the struts were made from a stainless steel alloy (ferritic AISI404), the compressive stress–strain curve showed that the material remained linearly elastic when the axial strain was below approximately 0.15%. Two specific tests were conducted on struts with material and geometric properties as given in Table 3.4. The

Strut length L	3.0 m	2.5 m
Flange width b	96.64 mm	96.80 mm
Corner Radius r	3.06 mm	3.02 mm
Flange thickness t	1.21 mm	1.21 mm
Section depth h	125.12 mm	125.24 mm

Table 3.4: Geometric properties for the strut tests taken directly from (Becque & Rasmussen, 2009a; Becque, 2008). Recall that the thickness of the web $t_w = 2t$. For both struts the initial Young's modulus $E = 195$ kN/mm^2 and Poisson's ratio $\nu = 0.3$.

initial out-of-straightness mid-length lateral deflections of the specimens of length L, being 3 m and 2.5 m, were measured to be $L/3352$ and $L/16234$ respectively (Becque, 2008). In order to make direct comparisons, numerical runs were conducted in AUTO with the initial global buckling mode imperfection amplitude ratio q_{s0} being equal to 3×10^{-4} and 6×10^{-5} respectively. The solution strategy for the imperfect system is illustrated diagrammatically in Figure 3.6(c). The cross-section properties given in Table 3.4 were adapted slightly to consider the flat width of the flange, $b_f = b - 2r$; the flat width was used in the numerics for the analytical model, the results for which follow.

The numerical continuation process was initiated from zero load. The value of q_s was

increased up to a bifurcation point, shown as S_0 in Figure 3.6(c), beyond which interactive buckling was introduced. The equilibrium path then progressed to a limit point at which P can be defined as the ultimate load P_U. Then destabilization and the cellular buckling behaviour was observed as described in the previous section. Figures 3.18, 3.19, 3.20 and 3.21 show comparisons between the current analytical model, the experimental results and the previous numerical models. The comparisons show strong agreement between the analytical model and the results from the physical experiments, the correlation being clearly superior to the previous numerical results. However, as deformation progresses beyond the cross marks in Figure 3.18 to Figure 3.21, a larger difference in the slope of the post-buckling paths between the analytical model and the experiments is observed, with the analytical model showing a slightly stiffer response. This is perhaps caused by the material nonlinearities in the physical experiments where significant reduction in the material strength takes place after the strain reaches 0.15%, whereas in the analytical model, a linear elastic material is assumed.

For the 3 m length strut, the ultimate load was found to be 25.2 kN from the experiment, which is approximately 3% higher than the numerical value from the analytical model where $P_U = 24.4$ kN. It is also observed in Figure 3.19(b) that the theoretical local out-of-plane displacement w_1, at a location that was remote from the strut midspan ($z = 400$ mm), changes from positive to negative and *vice versa* several times. This is evidence of the cellular behaviour, indicating the progressive change in wavelength of the local buckling mode pattern. The actual experimental response, on the other hand, did not in fact pick up the cellular buckling response with progressive snap-backs; the reason for this is perhaps two-fold:

1. The relative fixity between the web and the flanges makes the experiment differ

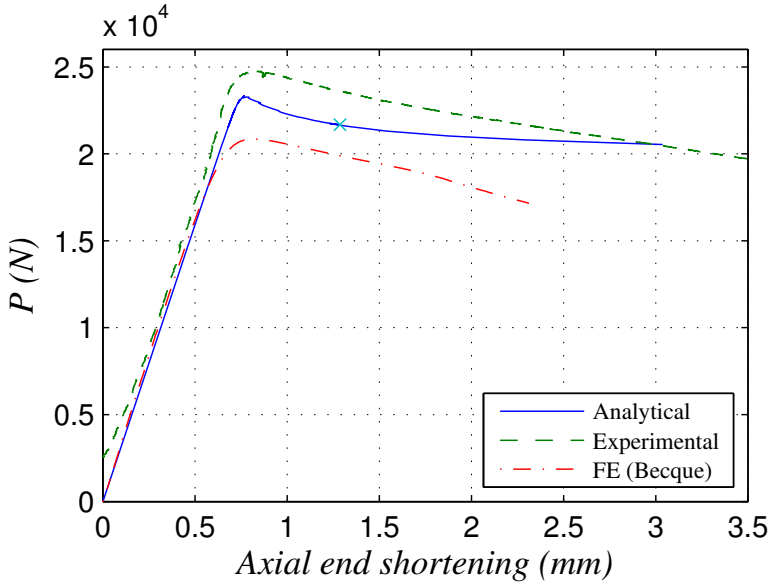

(a)

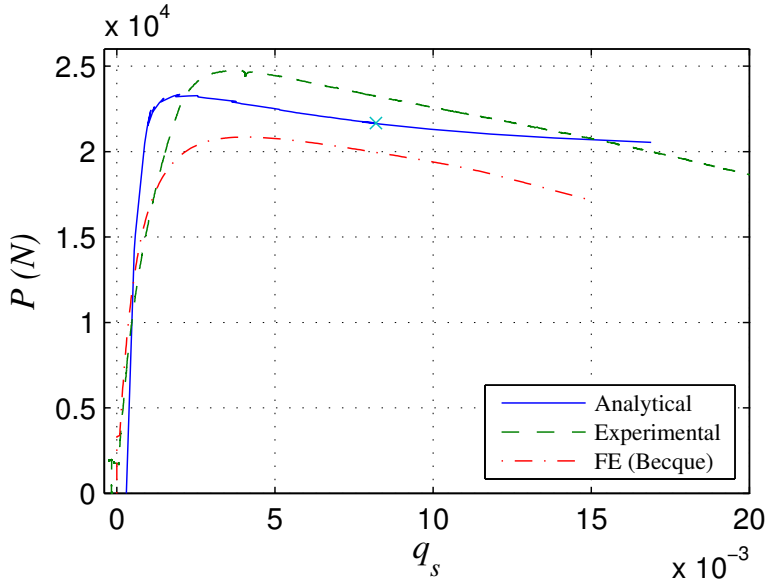

(b)

Figure 3.18: Numerical equilibrium paths comparing with Becque's experiment with a strut of length 3 m. Graphs of the applied axial load P versus (a) the total end-shortening and (b) the generalized coordinate q_s. Solid lines show the current analytical model, whereas the dashed and dot-dashed lines respectively show the experimental and finite element results from Becque (2008). The crosses represent the equilibrium state where $\varepsilon_z > 0.15\%$ in the analytical model.

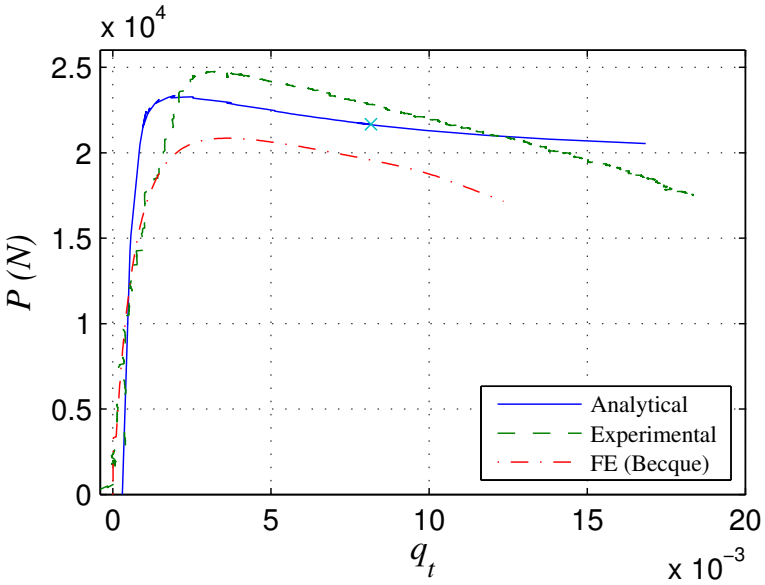

(a)

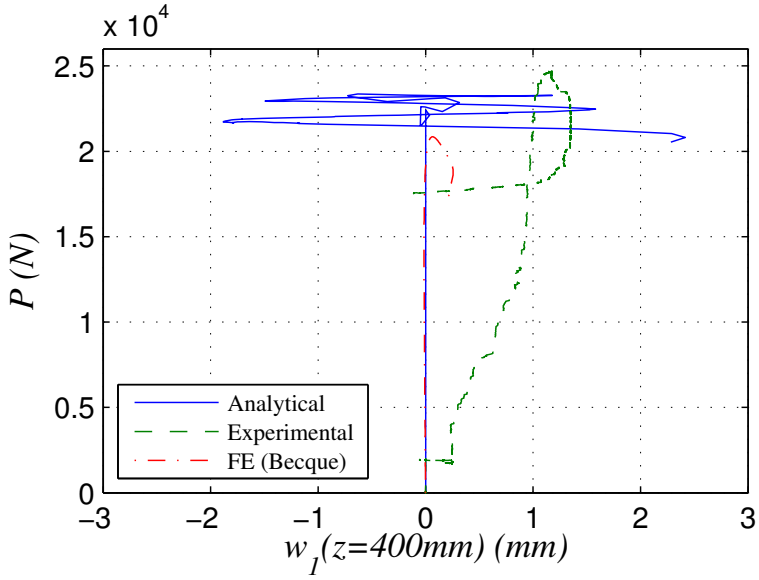

(b)

Figure 3.19: Numerical equilibrium paths comparing with Becque's experiment with a strut of length 3 m. Graphs of the applied axial load P versus (a) the generalized coordinate q_t and (b) the out-of-plane displacement of the buckled flange plate w_1 measured at $z = 400$ mm are shown. Solid lines show the current analytical model, whereas the dashed and dot-dashed lines respectively show the experimental and finite element results from Becque (2008). The cross represents the equilibrium state where $\varepsilon_z > 0.15\%$ in the analytical model.

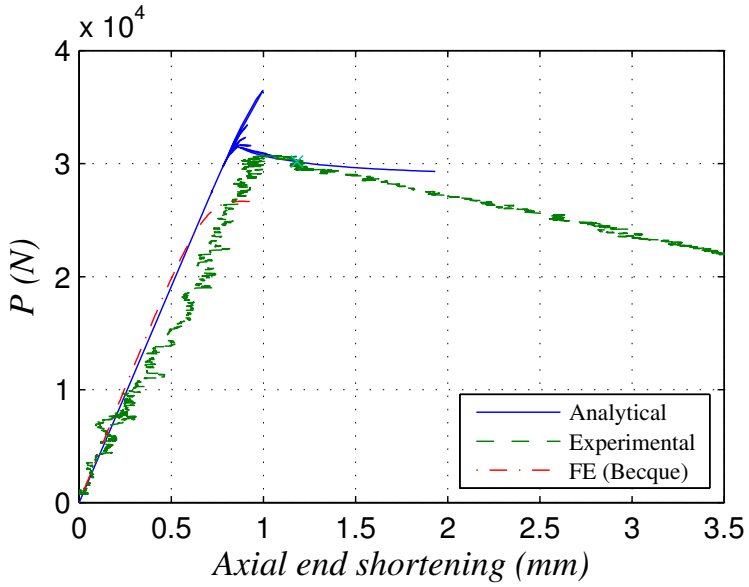

(a)

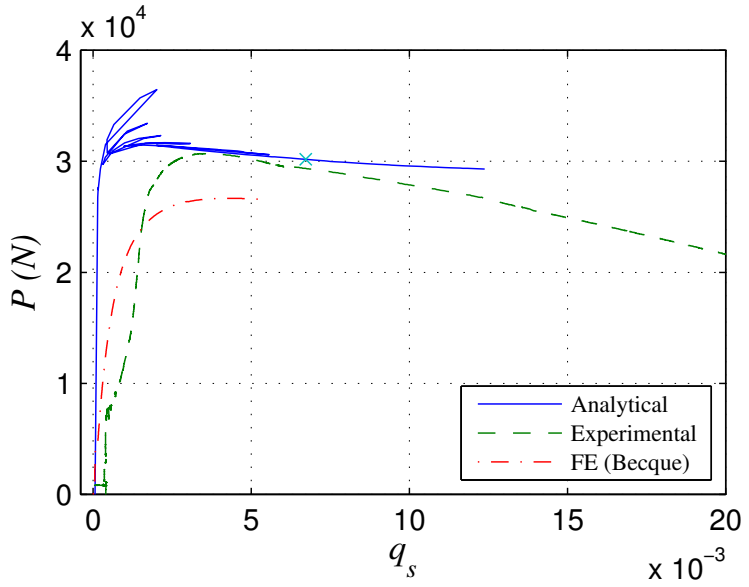

(b)

Figure 3.20: Numerical equilibrium paths comparing with Becque's experiment with a strut of length 2.5 m. Graphs of the applied axial load P versus (a) the total end shortening and (b) the generalized coordinate q_s. Solid lines show the current analytical model, whereas the dashed and dot-dashed lines respectively show the experimental and finite element results from Becque (2008). The crosses represent the equilibrium state where $\varepsilon_z > 0.15\%$ in the analytical model.

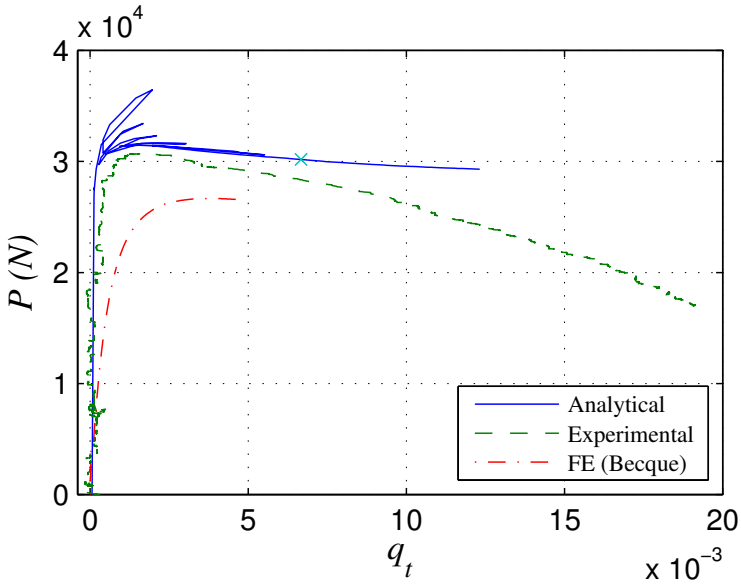

(a)

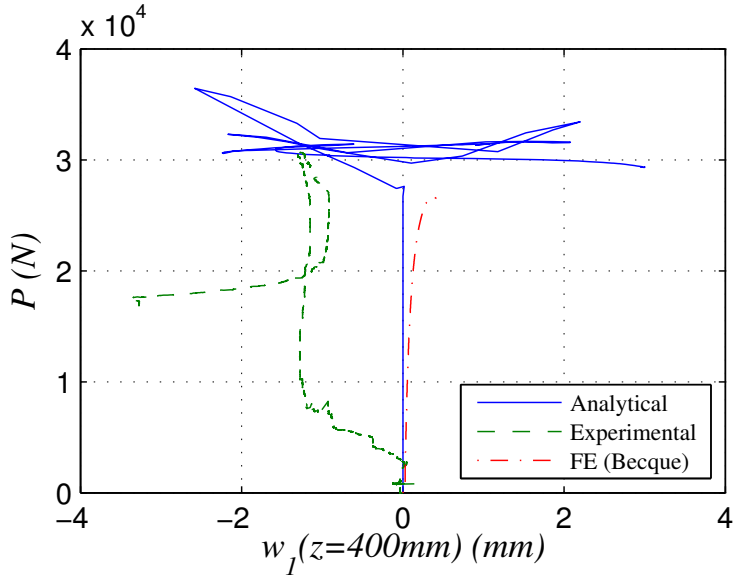

(b)

Figure 3.21: Numerical equilibrium paths comparing with Becque's experiment with a strut of length 2.5 m. Graphs of the applied axial load P versus (a) the generalized coordinate q_t and (b) the out-of-plane displacement of the buckled flange plate w_1 measured at $z = 400$ mm are shown. Solid lines show the current analytical model, whereas the dashed and dot-dashed lines respectively show the experimental and finite element results from Becque (2008). The cross represents the equilibrium state where $\varepsilon_z > 0.15\%$ in the analytical model.

from the pinned assumption presented in the model. This would also mean that the local buckling pattern is more modulated rather than localized once the instability is triggered.

2. In a physical experiment, even with displacement control, the mechanical response in a region with snap-backs in the perfect behaviour exhibits dynamic, rather than static, behaviour, which smoothes the load versus deflection path.

Even though in the current case the experiment did not pick up the full cellular response, it did show the change from positive to negative for w_1, which is a clear indication of the changing wavelength in the local buckling mode pattern. The interactive buckling wavelength Λ can also be compared, which is defined in Figure 3.22. The local buckling

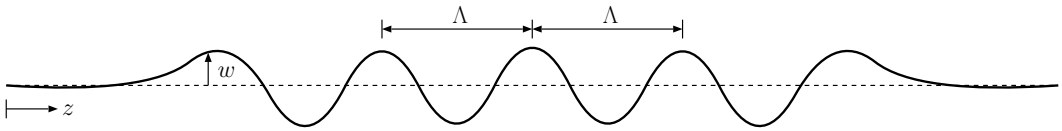

Figure 3.22: Definition of local buckling wavelength Λ from results for $w(\equiv w_1)$ from the variational model.

mode had a plate buckling wavelength that was measured to be 275 mm with a modulated amplitude for this specific test (Becque & Rasmussen, 2009a). The numerical results in the current work show that the value of Λ is 280 mm for the interactive buckling wavelength at the end of the equilibrium paths from the analytical model shown in Figure 3.18 and Figure 3.19. The close comparison (less than 2% difference) offers further grounds for encouragement for developing of the current model further.

For the 2.5 m length strut, the features are similar; the ultimate load P_U is 16% higher than the maximum load shown in the experiment. However, this is only a very small part of the global picture. The graphs in Figure 3.20(a), (b) and Figure 3.21(a) show

sequential snap-backs in the theoretical response almost immediately in the post-buckling range that reduce the true load-carrying capacity to levels which practically coincide with the experimental result, demonstrating an excellent overall comparison. In Figure 3.21(b), a similar response is observed to Figure 3.19(b). Unfortunately, a numerical measurement of the plate buckling wavelength was not reported for this particular experiment.

Finally, it can be seen that the results from the analytical model and the experiments begin to diverge after a certain level of displacement. This is postulated to be as a result of onset and spread of plasticity due to the use of stainless steel in the experiments, whereas linear elasticity is assumed throughout the analytical model. However, the opinion of the author is that for the most part the close comparisons between the analytical model and the experimental results, validate the current modelling approach both qualitatively and quantitatively.

3.4 Concluding remarks

A nonlinear analytical model based on variational principles has been presented for a perfect axially-loaded thin-walled I-section strut buckling about the weak axis of bending. Two numerical examples, representing the cases where global buckling and local buckling are critical, were examined in turn. The model identifies an important and potentially dangerous interaction between global and local modes of instability, which in a limiting case leads to highly unstable cellular buckling through a series of snap-back instabilities that change the local buckling profile from localized to distributed. These instabilities result from the increasing contributions of buckling mode amplitudes forcing the flanges in more compression to buckle progressively. This process had also been observed in recent

experimental work, apart from the snap-back instabilities (although the changing local buckling wavelength is indeed observed), which is superior to previous nonlinear finite element analyses. Comparisons with published experiments are excellent and validate the model. The following chapters build on the findings of this preliminary study and extend them to analyse more practical cases with initial local imperfections and cases where the flange and web have a finite rotational stiffness.

Chapter 4

Imperfection sensitivity

In the previous chapter, an axially loaded thin-walled I-section strut (van der Neut, 1969; Hancock, 1981), made from a linear elastic material with an open and doubly-symmetric cross-section, was studied using an analytical approach. The nonlinear mode interaction between global Euler buckling and local buckling of the flange plates was fully described by the analytical model, which was validated against recent experimental and numerical works (Becque & Rasmussen, 2009a; Becque & Rasmussen, 2009b). The primary focus was on the perfect elastic post-buckling response; and the highly unstable cellular buckling behaviour was highlighted. Such systems have been shown in the literature to be highly imperfection sensitive when the global critical load and the local critical load are sufficiently close (van der Neut, 1969; Becque & Rasmussen, 2009a). In the current chapter, the previous analytical model is extended to study the behaviour of imperfect systems. The two most common types of imperfection, an initial out-of-straightness of the strut and an initial local out-of-plane displacement of the flange plates (van der Neut, 1969; van der Neut, 1973), are introduced and investigated individually and in combination.

4.1 Development of the analytical model

The analytical model that governs the perfect system and the imperfect system with an initial out-of-straightness has been fully developed in Chapter 3. In this chapter, the previous model is extended to include an initial out-of-plane deflection in the flange plates as a type of local imperfection. Recalling the analytical model in Chapter 3, the same definitions for the section properties are used and shown in Figure 3.1(a) and (b). Figure 3.3(a) shows the description of the global buckling mode, where the lateral displacement W and the rotation of the plane section θ are given by Equation (3.1). Figure 3.3(b) shows the description of the local buckling mode, where the out-of-plane displacement function, w_i and the in-plane displacement function, u_i are given by Equation (3.3). Recall also that $i = \{1, 2\}$ representing the more and the less compressive sides of the flanges respectively. The initial out-of-straightness W_0, and the initial rotation of the plane section θ_0 are given by Equation (3.4). Note that all assumptions made in Chapter 3 also hold in the current chapter.

The extension of the previous analytical model begins with introducing the local imperfection by defining an initial out-of-plane deflection, $w_{0i}(x, z)$, which has the form:

$$w_{0i}(x,z) = (-1)^i \left(\frac{2x}{b}\right) A_0 \operatorname{sech}\left[\alpha\left(\frac{z}{L} - \frac{1}{2}\right)\right] \cos\left[\beta\pi\left(\frac{z}{L} - \frac{1}{2}\right)\right], \tag{4.1}$$

where $z \in [0, L]$, A_0 is the amplitude of the imperfection and β is the parameter that controls the number of waves along the length in the imperfection. The parameter α controls the degree of localization of the imperfection; it is periodic when $\alpha = 0$, and modulated when $\alpha > 0$. This expression for w_{0i} is derived from a first-order approximation from a multiple scale perturbation analysis of a strut on a nonlinear softening foundation, which closely matches the least stable localized buckling mode shape (Wadee *et al.*, 1997). This form of imperfection, illustrated in Figure 4.1 has been shown to be fully applicable

to struts on a softening quadratic foundation and sandwich struts that undergo global and local buckling mode interaction (Wadee, 2000). The current work applies a similar approach. Note that the imperfection is always assumed to be symmetric about the mid-

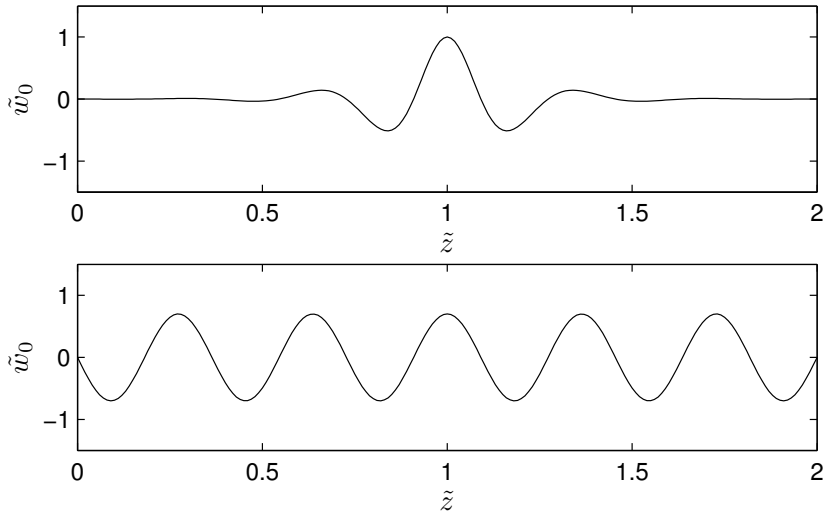

Figure 4.1: Examples of modulated and periodic imperfections; nondimensional initial deflection $\tilde{w}_0$ are plotted versus the nondimensional longitudinal coordinate $\tilde{z}$. Note the symmetry at $\tilde{z} = 1$.

span of the strut. The distribution in the transverse direction x is assumed to be linear, which is consistent with the definition of the local out-of-plane displacement $w_i(x, z)$.

4.1.1 Total potential energy

The full formulation of the total potential energy, V, of the perfect strut and the strut with an initial out-of-straightness W_0 was fully established in the previous chapter. Similar to the global imperfection, the local imperfection is introduced by assuming that the initial out-of-plane deflection w_0 is stress-relieved (Thompson & Hunt, 1984; Wadee, 2000), implying that the elemental moment M and thus the local bending energy drops to zero, as illustrated in Figure 4.2(a). The local imperfections are introduced to the more compressed flange with $i = 1$ and the less compressed flange with $i = 2$, respectively. Note

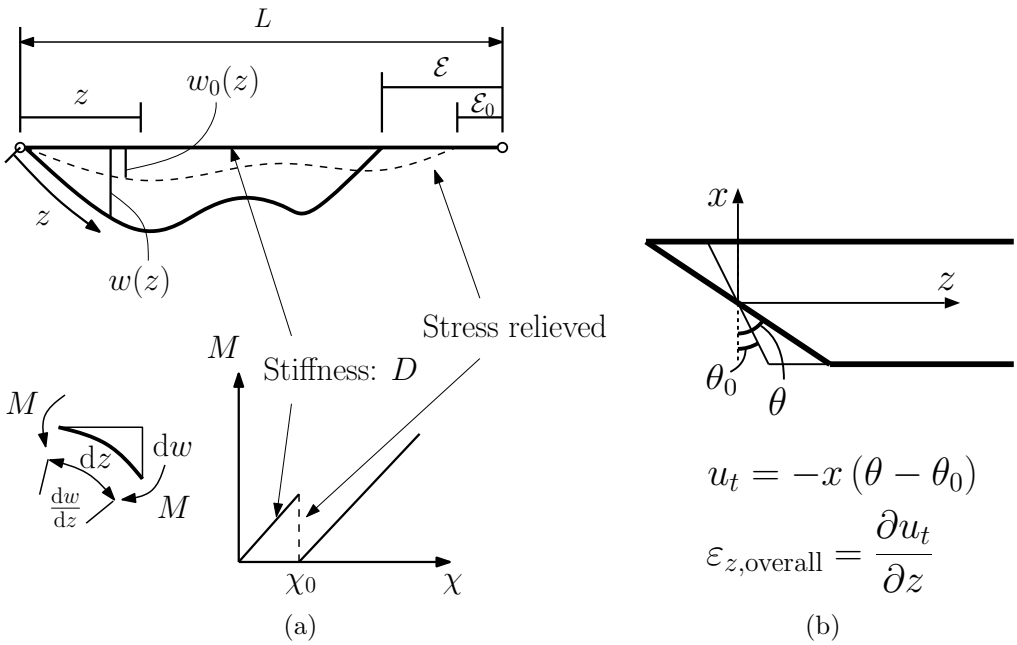

Figure 4.2: Introduction of (a) local geometric imperfections w_0 and (b) the global geometric imperfection θ_0 in the flange plates. The quantity χ represents the bending curvature of the member.

that although $w_{01}(z)$ and $w_{02}(z)$ are identical after integration over the flange width, the notation cannot be used interchangeably. This is because in the case of global buckling being critical, the local buckling deformation in the less compressed half of the flange ($i = 2$) can be neglected; the local imperfection is also assumed to exist only in the vulnerable half of the flange ($i = 1$). The introduction of the local imperfection provides additional expressions to the local bending, membrane and shear strain energy functions. However, the global bending energy U_{bo} and the work done $P\mathcal{E}$ remain the same as in the system with the global imperfection only, and given in Equations (3.5) and (3.15) respectively. The local bending energy, U_{bl} accounting for both top and bottom flanges is

determined as:

$$\begin{aligned} U_{bl} &= D\int_0^L \left[\int_{-b/2}^0 B_{01}\mathrm{d}x + \int_0^{b/2} B_{02}\mathrm{d}x\right]\mathrm{d}z \\ &= D\int_0^L \left\{\frac{b}{6}\left[(\ddot{w}_1-\ddot{w}_{01})^2+(\ddot{w}_2-\ddot{w}_{02})^2\right]\right. \\ &\qquad \left. +\frac{4\,(1-\nu)}{b}\left[(\dot{w}_1-\dot{w}_{01})^2+(\dot{w}_2-\dot{w}_{02})^2\right]\right\}\mathrm{d}z, \end{aligned} \tag{4.2}$$

where B_{0i}, the contribution from w_i to the standard expression for the incremental strain energy from plate bending (Timoshenko & Gere, 1961), including the contribution from the initial out-of-plane displacement w_{0i}, is given by:

$$\begin{aligned} B_{0i} &= \left[\left(\frac{\partial^2 w_i}{\partial z^2}-\frac{\partial^2 w_{0i}}{\partial z^2}\right)+\left(\frac{\partial^2 w_i}{\partial x^2}-\frac{\partial^2 w_{0i}}{\partial x^2}\right)\right]^2 \\ &\quad -2\,(1-\nu)\left[\left(\frac{\partial^2 w_i}{\partial z^2}\frac{\partial^2 w_i}{\partial x^2}-\frac{\partial^2 w_{0i}}{\partial z^2}\frac{\partial^2 w_{0i}}{\partial x^2}\right)-\left(\frac{\partial^2 w_i}{\partial z\partial x}-\frac{\partial^2 w_{0i}}{\partial z\partial x}\right)^2\right], \end{aligned} \tag{4.3}$$

with $D = Et^3/[12(1-\nu^2)]$ being the plate flexural rigidity. The direct strains ε_{z1} and ε_{z2}, including the contribution from w_{0i}, are given by the following expression:

$$\begin{aligned} \varepsilon_{zi} &= \frac{\partial u_t}{\partial z}-\Delta+\frac{\partial u_i}{\partial z}+\frac{1}{2}\left[\left(\frac{\partial w_i}{\partial z}\right)^2-\left(\frac{\partial w_{0i}}{\partial z}\right)^2\right] \\ &= x\,(q_t-q_{t0})\,\frac{\pi^2}{L}\sin\frac{\pi z}{L}-\Delta+(-1)^i\left(\frac{2x}{b}\right)\dot{u}_i+\frac{2x^2}{b^2}\left(\dot{w}_i^2-\dot{w}_{0i}^2\right), \end{aligned} \tag{4.4}$$

where $u_t = -(\theta-\theta_0)x$, which is essentially the in-plane displacement from the tilt component of the global buckling mode, as shown in Figure 4.2(b). The membrane energy from the direct strains (U_d), assuming that $h \gg t$, is given thus:

$$\begin{aligned} U_d &= Et\int_0^L\left[\int_{-b/2}^0 \varepsilon_{z1}^2\mathrm{d}x+\int_0^{b/2}\varepsilon_{z2}^2\mathrm{d}x\right]\mathrm{d}z \\ &= Etb\int_0^L\left\{\frac{b^2}{12}(q_t-q_{t0})^2\frac{\pi^4}{L^2}\sin^2\frac{\pi z}{L}-(q_t-q_{t0})\frac{b\pi^2}{2L}\sin\frac{\pi z}{L}\left[\frac{1}{3}(\dot{u}_1-\dot{u}_2)\right.\right. \\ &\qquad \left.+\frac{1}{8}\left(\dot{w}_1^2-\dot{w}_{01}^2\right)-\frac{1}{8}\left(\dot{w}_2^2-\dot{w}_{02}^2\right)\right]+\left(1+\frac{h}{b}\right)\Delta^2+\frac{1}{6}\left(\dot{u}_1^2+\dot{u}_2^2\right) \\ &\qquad +\frac{1}{40}\left[\left(\dot{w}_1^2-\dot{w}_{01}^2\right)^2+\left(\dot{w}_2^2-\dot{w}_{02}^2\right)^2\right]-\frac{1}{2}\Delta\left(\dot{u}_1+\dot{u}_2\right)-\frac{1}{6}\Delta\left(\dot{w}_1^2-\dot{w}_{01}^2\right) \\ &\qquad \left.-\frac{1}{6}\Delta\left(\dot{w}_2^2-\dot{w}_{02}^2\right)+\frac{1}{8}\dot{u}_1\left(\dot{w}_1^2-\dot{w}_{01}^2\right)+\frac{1}{8}\dot{u}_2\left(\dot{w}_2^2-\dot{w}_{02}^2\right)\right\}\mathrm{d}z, \end{aligned} \tag{4.5}$$

The shear strains γ_{xz1} and γ_{xz2}, including the contribution from w_{0i} are given by the following expression:

$$\begin{aligned}\gamma_{xzi} &= \frac{\partial}{\partial z}\left(W - W_0\right) - \left(\theta - \theta_0\right) + \frac{\partial u_i}{\partial x} + \frac{\partial w_i}{\partial z}\frac{\partial w_i}{\partial x} - \frac{\partial w_{0i}}{\partial z}\frac{\partial w_{0i}}{\partial x} \\ &= \left(q_s - q_t - q_{s0} + q_{t0}\right)\pi\cos\frac{\pi z}{L} + (-1)^i\left(\frac{2}{b}\right)u_i + \frac{4x}{b^2}\left(w_i\dot{w}_i - w_{0i}\dot{w}_{0i}\right).\end{aligned} \tag{4.6}$$

The membrane energy from the shear strain component is thus:

$$\begin{aligned}U_s &= Gt\int_0^L\left[\int_{-b/2}^0\gamma_{xz1}^2\mathrm{d}x + \int_0^{b/2}\gamma_{xz2}^2\mathrm{d}x\right]\mathrm{d}z \\ &= Gtb\int_0^L\Bigg\{\left(q_s - q_t - q_{s0} + q_{t0}\right)^2\pi^2\cos^2\frac{\pi z}{L} + \frac{2}{b^2}\Bigg[{u_1}^2 + {u_2}^2 + \frac{1}{3}\left(w_1\dot{w}_1 - w_{01}\dot{w}_{01}\right)^2 \\ &\qquad + \frac{1}{3}\left(w_2\dot{w}_2 - w_{02}\dot{w}_{02}\right)^2 + u_1\left(w_1\dot{w}_1 - w_{01}\dot{w}_{01}\right) + u_2\left(w_2\dot{w}_2 - w_{02}\dot{w}_{02}\right)\Bigg] \\ &\qquad - \left(q_s - q_t - q_{s0} + q_{t0}\right)\frac{\pi}{b}\cos\frac{\pi z}{L}\Bigg[2u_1 - 2u_2 + \left(w_1\dot{w}_1 - w_{01}\dot{w}_{01}\right) \\ &\qquad - \left(w_2\dot{w}_2 - w_{02}\dot{w}_{02}\right)\Bigg]\Bigg\}\mathrm{d}z.\end{aligned} \tag{4.7}$$

The final expression of the total potential energy, V is assembled thus:

$$V = U_{bo} + U_{bl} + U_d + U_s - P\mathcal{E}. \tag{4.8}$$

4.1.2 Governing equations

The governing equilibrium equations are obtained by performing the calculus of variations on the total potential energy V following the procedure detailed in Chapter 3. The system is again nondimensionalized with respect to the non-dimensional spatial coordinate $\tilde{z}$, which is defined as $\tilde{z} = 2z/L$. The non-dimensional expressions for the out-of-plane displacement $\tilde{w}_i$, the in-plane displacement $\tilde{u}_i$ and their derivatives are summarized in Table 3.1. Moreover, the non-dimensional initial out-of-plane displacement, $\tilde{w}_{0i}$ is given

by the following expression:

$$\tilde{w}_{0i} = \frac{2A_0}{L}\,\mathrm{sech}\left[\frac{1}{2}\alpha\left(\tilde{z}-1\right)\right]\cos\left[\frac{1}{2}\beta\pi\left(\tilde{z}-1\right)\right]. \tag{4.9}$$

The differential equations for the rescaled variables $\tilde{w}_i$ and $\tilde{u}_i$ are thus:

$$\begin{aligned}
&\dddot{\tilde{w}}_i - 6\phi^2\left(1-\nu\right)\ddot{\tilde{w}}_i - (-1)^i\left(\frac{3\tilde{D}}{8}\right)\left\{\left(q_t-q_{t0}\right)\frac{\pi^2}{4\phi}\left(\sin\frac{\pi\tilde{z}}{2}\ddot{\tilde{w}}_i + \frac{\pi}{2}\cos\frac{\pi\tilde{z}}{2}\dot{\tilde{w}}_i\right)\right.\\
&\quad\left. - (-1)^i\left[\ddot{\tilde{w}}_i\left(\frac{2}{3}\Delta - \frac{3}{5}\tilde{w}_i^2\right) - \frac{1}{2}\left(\ddot{\tilde{u}}_i\tilde{w}_i + \dot{\tilde{u}}_i\dot{\tilde{w}}_i\right)\right]\right\}\\
&\quad - \frac{3\tilde{G}}{8}\phi^2\tilde{w}_i\left[\frac{2}{3}\dot{\tilde{w}}_i^2 + \frac{2}{3}\tilde{w}_i\ddot{\tilde{w}}_i + \dot{\tilde{u}}_i - (-1)^i\left(q_s-q_t-q_{s0}+q_{t0}\right)\frac{\pi^2}{2\phi}\sin\frac{\pi\tilde{z}}{2}\right]\\
&\quad = \dddot{\tilde{w}}_{0i} - 6\phi^2\left(1-\nu\right)\ddot{\tilde{w}}_{0i} - \frac{3}{40}\tilde{D}\tilde{w}_{0i}\left(\ddot{\tilde{w}}_i\tilde{w}_{0i} + 2\dot{\tilde{w}}_i\dot{\tilde{w}}_{0i}\right) - \frac{1}{4}\tilde{G}\phi^2\tilde{w}_i\left(\ddot{\tilde{w}}_{0i}\tilde{w}_{0i} + \dot{\tilde{w}}_{0i}{}^2\right),
\end{aligned} \tag{4.10}$$

$$\begin{aligned}
&\ddot{\tilde{u}}_i + \frac{3}{4}\dot{\tilde{w}}_i\ddot{\tilde{w}}_i + (-1)^i\left\{\left(q_t-q_{t0}\right)\frac{\pi^3}{4\phi}\cos\frac{\pi\tilde{z}}{2} - \left(\frac{3\tilde{G}\phi^2}{\tilde{D}}\right)\left[\left(q_s-q_t-q_{s0}+q_{t0}\right)\frac{\pi}{\phi}\cos\frac{\pi\tilde{z}}{2}\right.\right.\\
&\quad\left.\left. + (-1)^i\left(\frac{1}{2}\tilde{w}_i\dot{\tilde{w}}_i + \tilde{u}_i\right)\right]\right\} = \frac{3}{4}\dot{\tilde{w}}_{0i}\ddot{\tilde{w}}_{0i} - \frac{3\phi^2\tilde{G}}{2\tilde{D}}\dot{\tilde{w}}_{0i}\tilde{w}_{0i},
\end{aligned} \tag{4.11}$$

where $\tilde{D} = EtL^2/D$, $\tilde{G} = GtL^2/D$, $\phi = L/b$ as in Chapter 3 and dots now represent derivatives with respect to $\tilde{z}$. The integral conditions, including the local imperfection becomes:

$$\begin{aligned}
\frac{\partial V}{\partial q_s} &= \pi^2\left(q_s-q_{s0}\right) + \tilde{s}\left(q_s-q_t-q_{s0}+q_{t0}\right) - \frac{PL^2}{EI_w}q_s - \frac{\tilde{s}\phi}{\pi}\int_0^1\cos\frac{\pi\tilde{z}}{2}\left[\left(\tilde{u}_1-\tilde{u}_2\right)\right.\\
&\qquad\left. + \frac{1}{2}\left(\tilde{w}_1\dot{\tilde{w}}_1 - \tilde{w}_{01}\dot{\tilde{w}}_{01}\right) - \frac{1}{2}\left(\tilde{w}_2\dot{\tilde{w}}_2 - \tilde{w}_{02}\dot{\tilde{w}}_{02}\right)\right]\mathrm{d}\tilde{z} = 0,\\
\frac{\partial V}{\partial q_t} &= \pi^2\left(q_t-q_{t0}\right) - \tilde{t}\left(q_s-q_t-q_{s0}+q_{t0}\right)\\
&\qquad + \phi\int_0^1\left\{\frac{\tilde{t}}{\pi}\cos\frac{\pi\tilde{z}}{2}\left[\frac{1}{2}\left(\tilde{w}_1\dot{\tilde{w}}_1 - \tilde{w}_{01}\dot{\tilde{w}}_{01}\right) - \frac{1}{2}\left(\tilde{w}_2\dot{\tilde{w}}_2 - \tilde{w}_{02}\dot{\tilde{w}}_{02}\right) + \left(\tilde{u}_1-\tilde{u}_2\right)\right]\right.\\
&\qquad\left. - \sin\frac{\pi\tilde{z}}{2}\left[2\left(\dot{\tilde{u}}_1-\dot{\tilde{u}}_2\right) + \frac{3}{4}\left(\dot{\tilde{w}}_1^2 - \dot{\tilde{w}}_{01}^2\right) - \frac{3}{4}\left(\dot{\tilde{w}}_2^2 - \dot{\tilde{w}}_{02}^2\right)\right]\right\}\mathrm{d}\tilde{z} = 0,\\
\frac{\partial V}{\partial \Delta} &= \int_0^1\left[2\left(1+\frac{h}{b}\right)\Delta - \frac{1}{2}\left(\dot{\tilde{u}}_1+\dot{\tilde{u}}_2\right)\right.\\
&\qquad\left. - \frac{1}{6}\left(\ddot{\tilde{w}}_1^2 - \ddot{\tilde{w}}_{01}^2\right) - \frac{1}{6}\left(\ddot{\tilde{w}}_2^2 - \ddot{\tilde{w}}_{02}^2\right) - \frac{P}{Etb}\right]\mathrm{d}\tilde{z} = 0,
\end{aligned} \tag{4.12}$$

where $\tilde{s} = 2GtbL^2/(EI_w)$ and $\tilde{t} = 12G\phi^2/E$ as before. The boundary conditions for $\tilde{w}_i$ and $\tilde{u}_i$ and their derivatives are for pinned end conditions at $\tilde{z} = 0$ and for symmetry at $\tilde{z} = 1$, and given by Equation (3.26). The boundary condition from matching the in-plane strains becomes:

$$\frac{1}{3}\tilde{\dot{u}}_i(0) + \frac{1}{8}\left[\tilde{\dot{w}}_i^2(0) - \tilde{\dot{w}}_{0i}^2(0)\right] - \frac{1}{2}\Delta + \frac{P}{2Etb} = 0. \tag{4.13}$$

The global critical load, P_o^{C}, determined by the linear eigenvalue analysis of the perfect system, remains the same and is given by Equation (3.29).

4.2 Numerical examples

In this section, three representative numerical examples are presented. The material and section properties that were used for the perfect system are given in Table 3.2. The same material and section properties are used throughout the current chapter. The strut length L is chosen to be 3.5 m and 4 m for cases where local buckling and global buckling are critical respectively. The first numerical example considers the case where global buckling is critical ($L = 4$ m), where initially the local imperfection amplitude A_0 is set to zero so that only the global imperfection exists. The generalized initial out-of-straightness coordinate, q_{s0}, is varied for the imperfection sensitivity study. The second and third numerical example focus on the local imperfections. The second numerical example considers the case where global buckling is critical, but only an initial local out-of-plane displacement w_0 is considered ($q_{s0} = 0$). The third numerical example considers the case where local buckling is critical ($L = 3.5$ m), with both q_{s0} and w_0 present in the model. The initial out-of-straightness, q_{s0} is kept constant at a very small value. For the latter two cases, the local imperfection amplitude A_0, the periodicity parameter β and the localization parameter α are varied to determine the worst case combination which

gives the lowest peak load. A measure for the relative size of the imperfection is taken from earlier work (Wadee, 2000).

Numerical continuation is performed in AUTO-07P. The solution strategies for the aforementioned cases are demonstrated diagrammatically in Figure 4.3. Note that it is only the

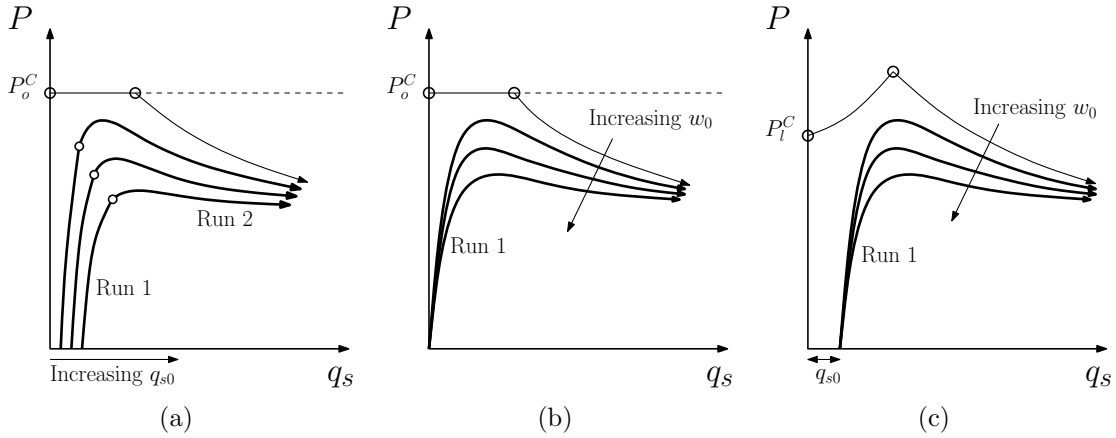

Figure 4.3: Numerical continuation procedures. (a) Global buckling being critical with initial out-of straightness q_{s0} only. (b) Global buckling being critical with initial local out-of-plane displacement w_0 only. (c) Local buckling being critical with both q_{s0} and w_0. The thicker line shows the actual solution path in each of the examples shown. The thinner solid line shows the equilibrium path of the perfect system and circles represent bifurcation points.

latter two cases that require a single run without any branch switching. This is because in the second case, Figure 4.3(b), where global buckling is critical, the local imperfection is introduced only to the vulnerable half of the flange ($i = 1$). This imposes the break in symmetry as soon as the numerical run begins and therefore q_s and q_t are introduced without the need of branch switching. In the third case, Figure 4.3(c), although the local imperfections are introduced to both the vulnerable and the non-vulnerable flanges, the initial out-of-straightness allows the strut to bend as soon as the load is applied. These procedures reduce the computational effort as well as avoiding the possibilities of non-convergence.

4.2.1 Global buckling critical ($q_{s0} \neq 0$, $w_0 = 0$)

In this section, the strut with properties given in Table 3.2 with length L being 4 m is analysed. Only an initial out-of-straightness, W_0 is introduced at this stage. A set of values of the normalized initial out-of-straightness amplitude q_{s0} ranging from 1/10000 to 1/1000 are selected for analysis. Table 4.1 summarizes the values of q_{s0} and the corresponding peak loads. Figure 4.4 shows a family of plots of the normalized axial load p versus (a) the global mode and (b) the local mode amplitudes. Figure 4.5(a) shows the local and global mode relative magnitudes during post-buckling. Each curve within the family corresponds to one particular imperfection size, as specified in Table 4.1. Figure

$q_{s0}(\times 10^{-4})$	0	1	2	3	4	5	10
p_U	1	0.8949	0.8419	0.8055	0.7788	0.7562	0.6864

Table 4.1: The values of the initial out-of-straightness coordinate, q_{s0} in the numerical continuation and the corresponding normalized peak loads, $p_U = P_U/P_o^{\mathrm{C}}$.

4.5(b) shows a scatter plot of the peak load, P_U, against the global imperfection amplitudes. It is clearly observed that the peak load P_U decreases as the size of the imperfection increases. A further inspection of the imperfection sensitivity plot in Figure 4.5(b) shows that the peak load takes a significant drop as soon as a small imperfection is applied. For $q_{s0} = 1/1000$, the peak load drops approximately 30% as compared with the global critical load, P_o^{C}, of the perfect system, which shows that the strut is highly sensitive to global imperfections. Examining the post-buckling paths, where interactive buckling takes place, it can be observed that the system converges asymptotically to the same equilibrium state for all sizes of imperfection. As a result, struts with large global imperfections are expected to be approximately neutrally stable in the post-buckling range. It is worth noting that cellular buckling behaviour is captured for all sizes of imperfection. The final buckling mode shape of the imperfect system is very similar to that of the perfect system in terms of both amplitude and wavelength.

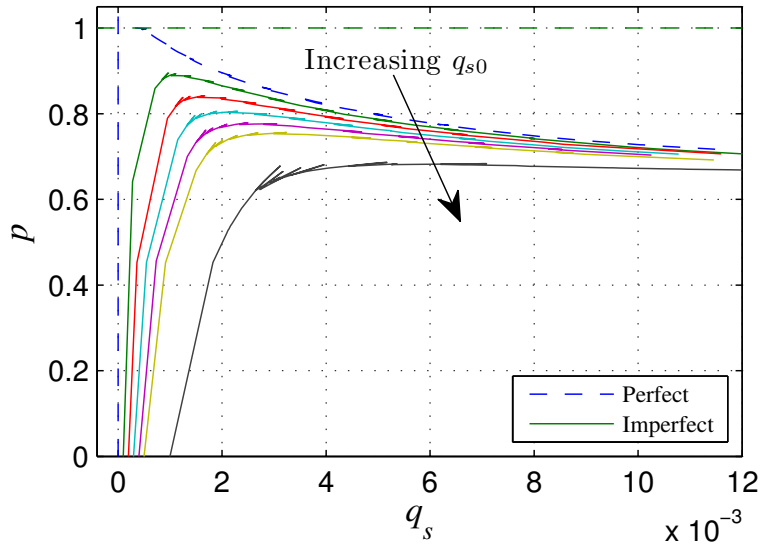

(a)

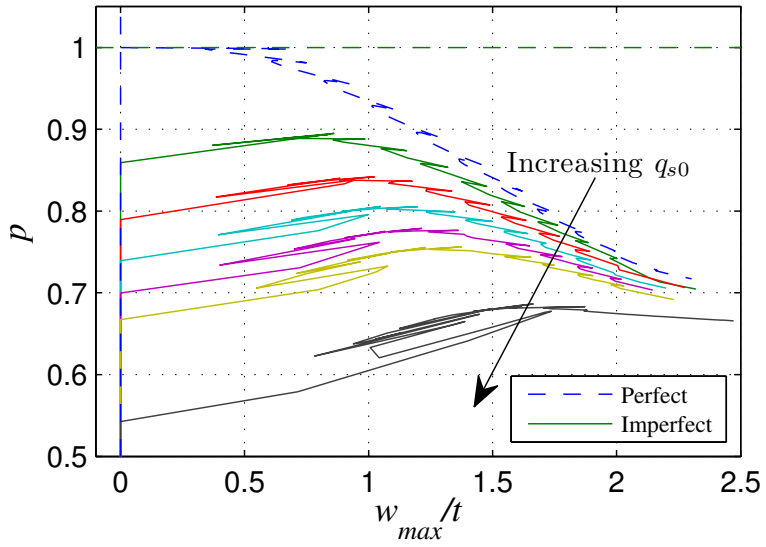

(b)

Figure 4.4: Numerical equilibrium paths for $L = 4$ m. The graphs show a family of curves of the normalized force ratio $p = P/P_o^{\mathrm{C}}$ versus (a) the global mode amplitude q_s and (b) the normalized local mode amplitude, $w_{\max}/t$.

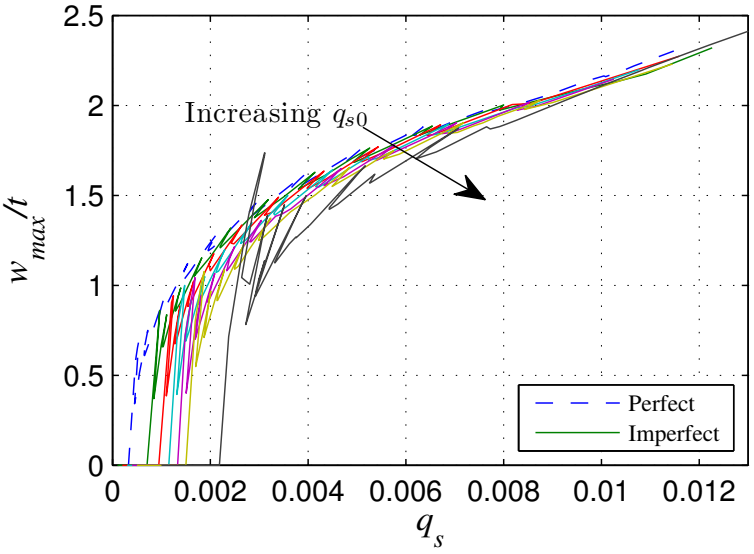

(a)

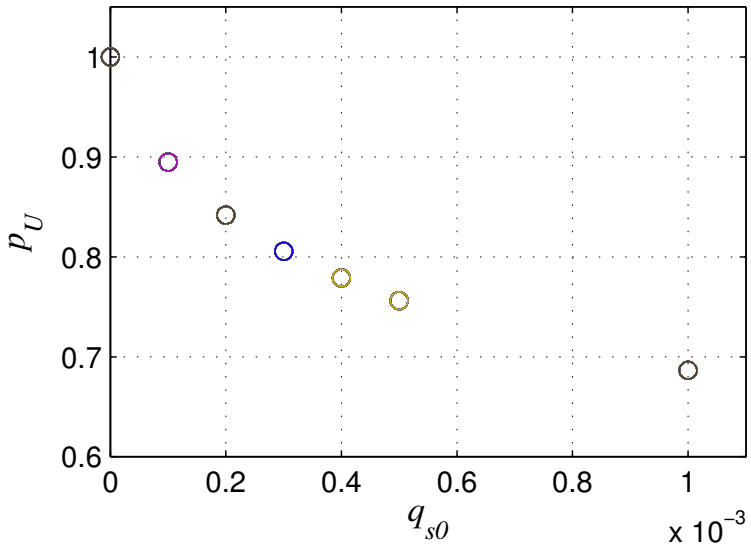

(b)

Figure 4.5: Graph (a) shows the numerical equilibrium path of the local versus the global mode amplitude; (b) shows the imperfection sensitivity diagram of the normalized peak load $p_U = P_U/P_o^{\mathrm{C}}$ versus the initial out-of-straightness coordinate q_{s0}.

4.2.2 Global buckling critical ($q_{s0} = 0$, $w_0 \neq 0$)

In this section, the 4 m strut with a local imperfection only is analysed. The reduced set of equilibrium equations is solved and therefore the initial out-of-plane displacement, w_0 is only present in the vulnerable half of the flange. The initial end shortening of the flange plate, $\mathcal{E}_0$, due to the local imperfection, is defined as:

$$\mathcal{E}_0 = \frac{1}{2}\int_0^L \dot{w}_0^2 \mathrm{d}z, \tag{4.14}$$

which can also be treated as a kind of mean square measure of the initial imperfection (Wadee, 2000). Since A_0, α and β are parameters that can have different combinations, this term provides a direct interpretation of the size of the local imperfection, which is particularly useful to facilitate meaningful comparisons between different imperfection types. Three types of local imperfections are studied in separate stages. During the first stage, α and β are kept at constant values of 0 and 1 respectively. This form of imperfection is essentially the linear eigenvalue solution for the axially loaded plate with three edges simply supported and one edge free (Bulson, 1970). The amplitude A_0 and therefore $\mathcal{E}_0$ are varied. The peak loads are recorded for each value of $\mathcal{E}_0$. During the second stage, the imperfections are periodic where $\mathcal{E}_0$ is kept constant with $\alpha = 0$ and β is the principal parameter. The amplitude, A_0, is varied accordingly to keep $\mathcal{E}_0$ constant, with an increase in β resulting in a decrease in A_0. Note that only odd integer values are taken for β takes to satisfy the boundary and symmetry conditions. The combination of β and A_0 that gives the lowest peak load is determined for particular values of $\mathcal{E}_0$. In the third stage, the modulated local imperfection is investigated by varying α, while $\mathcal{E}_0$ is again kept constant for each case. The amplitude, A_0 is varied accordingly whereas β is kept at the value that is determined in the second stage. As would be expected, increasing α results in a higher value of A_0. The combination of α and A_0 that gives the lowest peak load is also determined.

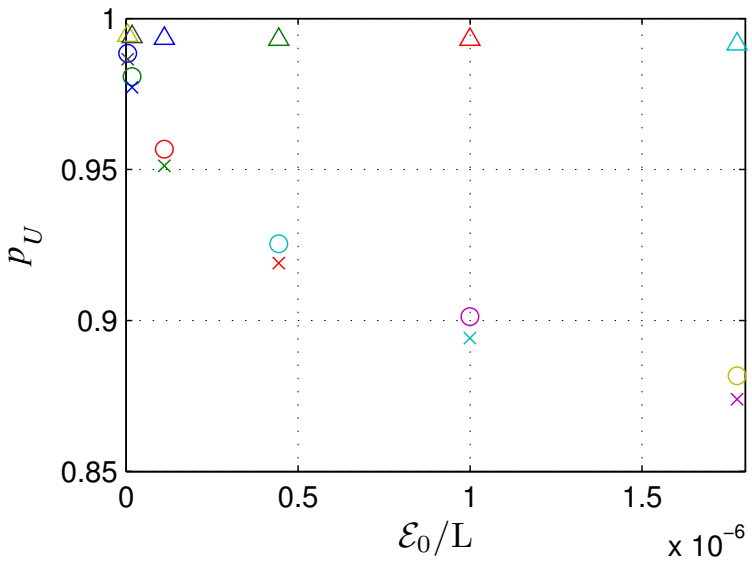

(a)

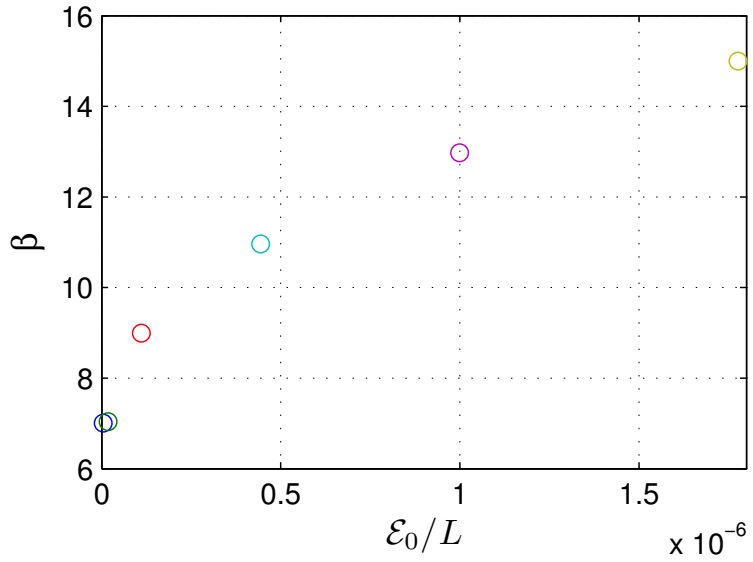

(b)

Figure 4.6: Imperfection sensitivity diagram with the abscissa in each case being the normalized imperfection size $\mathcal{E}_0/L$ plotted against: (a) the normalized peak load, p_U and (b) the periodicity parameter β which gives the lowest peak loads. In (a) the triangular symbols correspond to the imperfection with the form of the plate linear eigenvalue solution; the circular symbols correspond to the periodic imperfection, whereas the crosses correspond to the modulated imperfection. In (b) the crosses and the triangular symbols are not relevant.

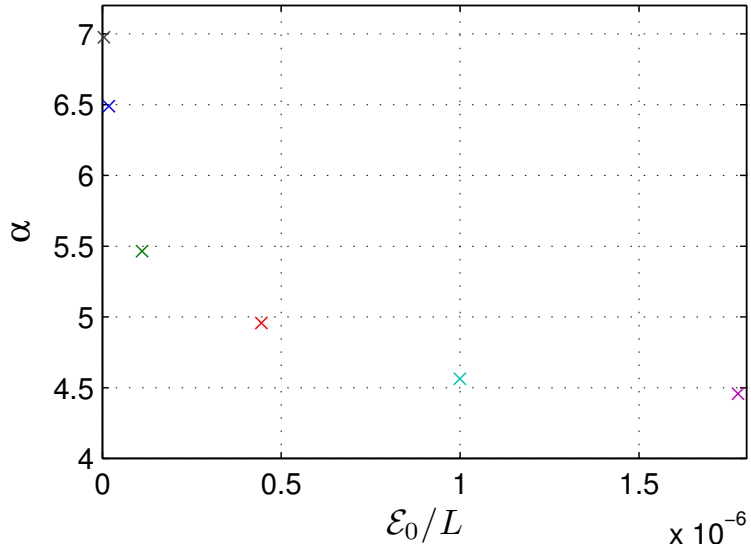

(a)

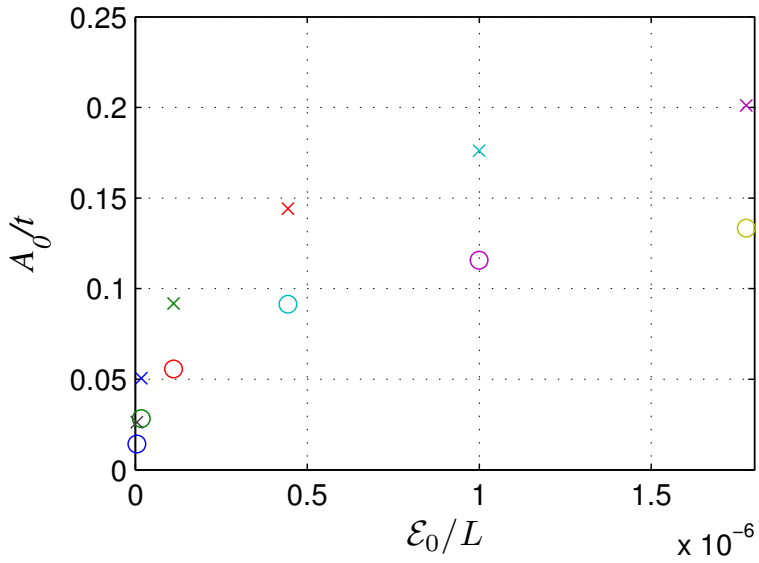

(b)

Figure 4.7: Imperfection sensitivity diagram with the abscissa in each case being the normalized imperfection size $\mathcal{E}_0/L$ plotted against: (a) the localization parameter α which gives the lowest peak loads and (b) the normalized imperfection amplitude A_0/t. The circular symbols correspond to the periodic imperfection, whereas the crosses correspond to the modulated imperfection.

Figures 4.6 and 4.7 show a series of imperfection sensitivity diagrams. It is observed in Figure 4.6(a) that for $\beta = 1$ and $\alpha = 0$, there is very little reduction in the peak load as $\mathcal{E}_0$ increases, indicating that the strut is fundamentally insensitive to this type of imperfection. However, for the periodic imperfections with β varied, the peak loads are reduced significantly as $\mathcal{E}_0$ increases. The periodicity parameter β that gives the lowest peak load is different for each value of $\mathcal{E}_0$, which is observed in Figure 4.6(b). It is found that for larger $\mathcal{E}_0$ values, periodic imperfections with larger wave numbers become critical. A further reduction in the peak loads is observed when the imperfection is modulated, for all values of $\mathcal{E}_0$. The variation in the localization parameter α shows that larger imperfections require less localization to give the worst combination of A_0, α and β. It is observed in Figure 4.7(b) that for the largest value of $\mathcal{E}_0$ in the graph, the amplitude A_0 for the worst periodic imperfection is more than $t/10$ whereas for the worst modulated imperfection, A_0 is slightly more than $t/5$. The reduction in the peak loads for the periodic and modulated imperfections for the largest $\mathcal{E}_0$ is approximately 11.8% and 12.6% respectively, indicating the strut is sensitive to both types of imperfection. Table 4.2 summarizes the values of

$\mathcal{E}_0(\times 10^{-9})$	0	4.441	17.77	111.0	444.1	999.3	1777
p_U $(\beta = 1)$	1	0.9943	0.9940	0.9934	0.9931	0.9931	0.9915
p_U (periodic)	1	0.9885	0.9808	0.9567	0.9254	0.9013	0.8817
p_U (modulated)	1	0.9865	0.9772	0.9513	0.9190	0.8941	0.8739

Table 4.2: The values of the initial local end shortening $\mathcal{E}_0$; and the corresponding normalized peak loads p_U for imperfections with $\beta = 1$, periodic and modulated imperfections.

the initial end shortening $\mathcal{E}_0$ presented in the imperfection sensitivity diagrams and the corresponding values of the normalized peak loads for all three types of imperfections considered. Figure 4.8 shows the shape of both periodic and modulated imperfections with the worst combination of A_0, β and α, for each $\mathcal{E}_0$ value in the imperfection sensitivity diagrams.

Figure 4.9 shows a family of equilibrium paths for the worst case modulated imperfections

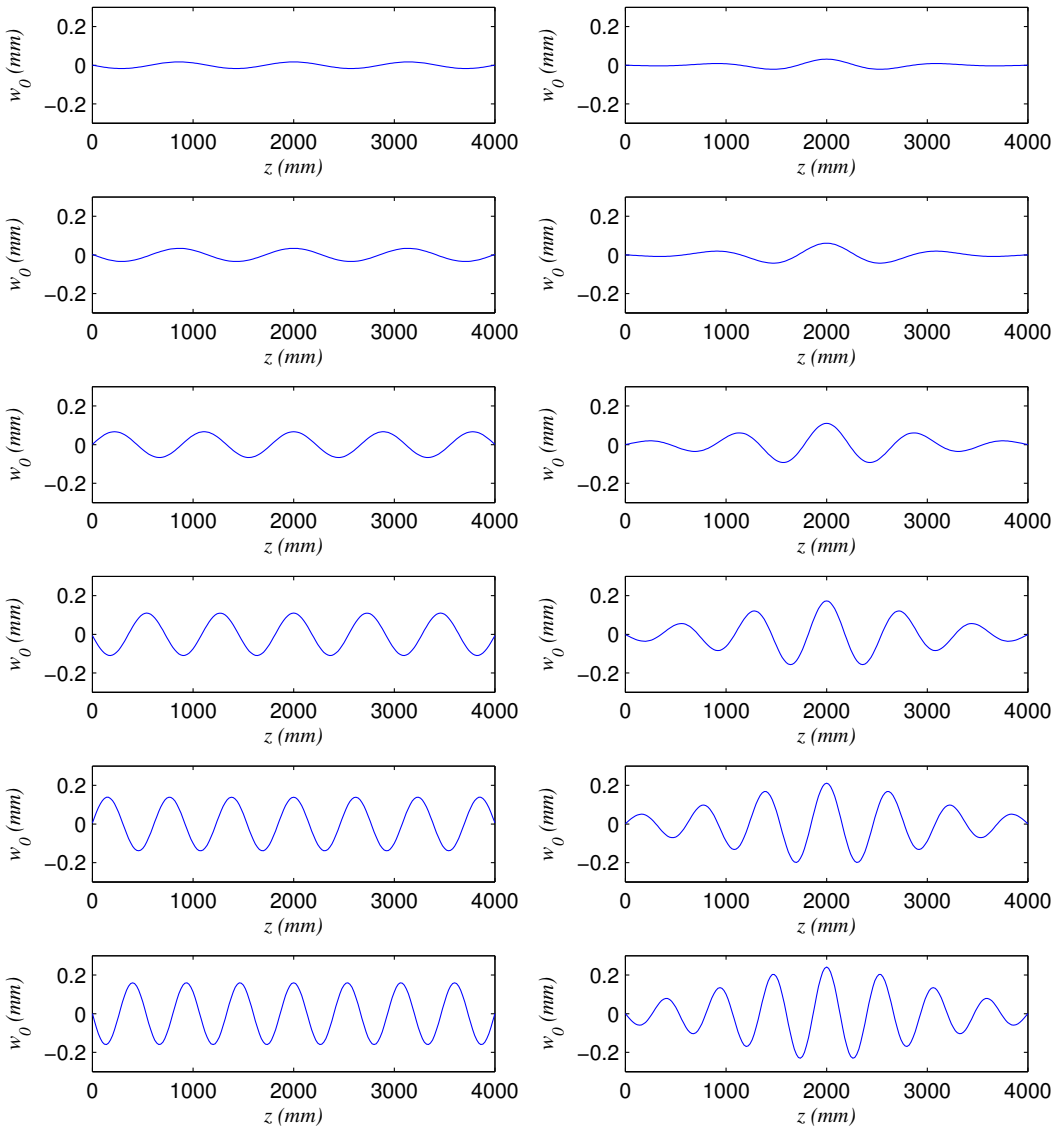

Figure 4.8: Mode shapes of the initial out-of-plane displacement, w_0 showing the worst combination of A_0, β and α for increasing $\mathcal{E}_0$ values from top to bottom. The left column shows the worst case periodic imperfection ($\alpha = 0$, $\beta > 0$), whereas the right column shows the worst case modulated imperfection ($\alpha, \beta > 0$). All dimensions are in millimetres.

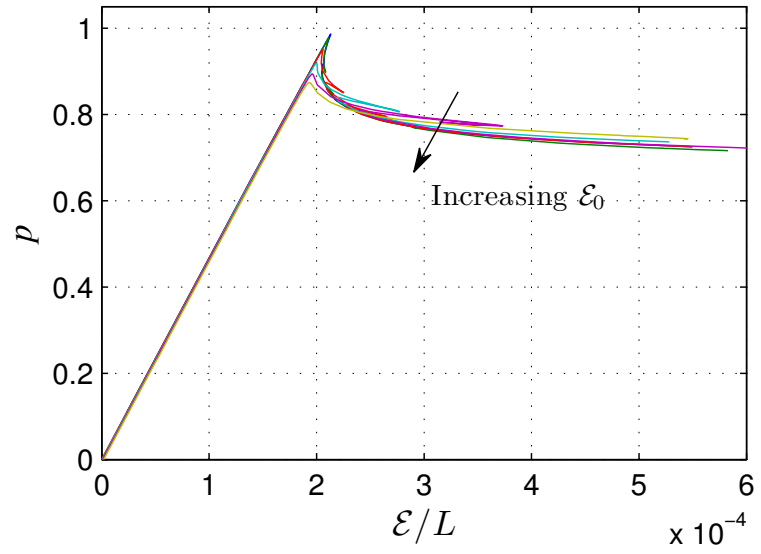

(a)

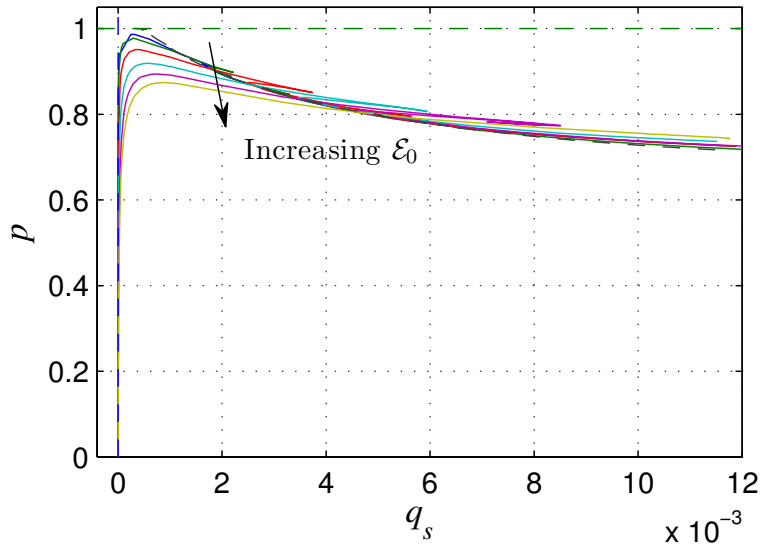

(b)

Figure 4.9: Numerical equilibrium paths for the worst case modulated imperfections for the 4 m strut. Graphs show a family of curves of the normalized force ratio p versus (a) the normalized total end shortening $\mathcal{E}/L$ and (b) the global mode amplitude q_s.

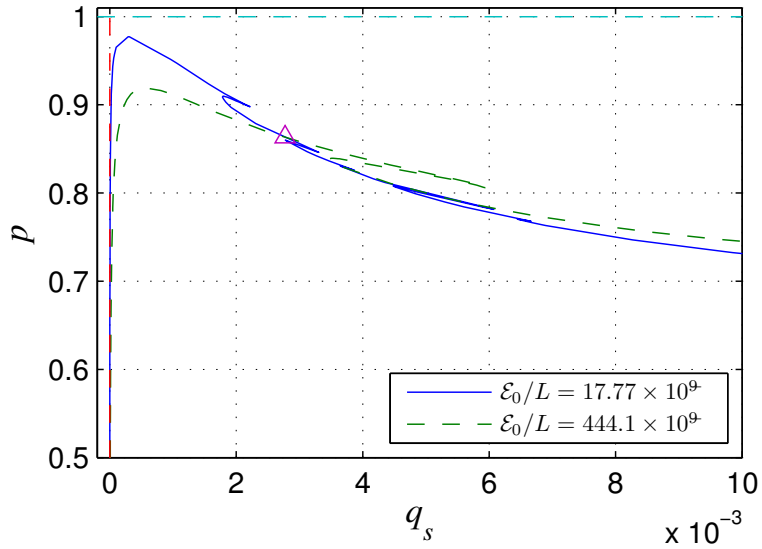

(a)

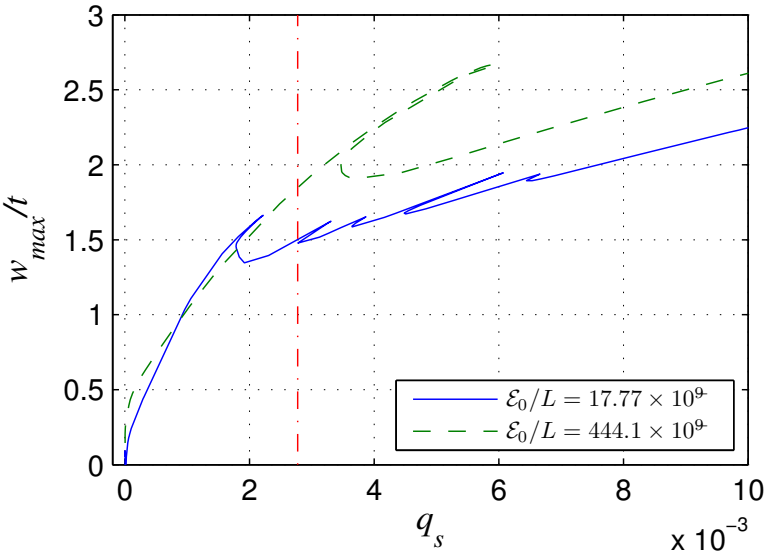

(b)

Figure 4.10: Numerical equilibrium paths for the worst case modulated imperfections for the 4 m strut: (a) shows a pair of equilibrium paths of p versus q_s, selected from Figure 4.9(b) for $\mathcal{E}_0/L = 17.77 \times 10^{-9}$ and $\mathcal{E}_0/L = 441.1 \times 10^{-9}$ and (b) shows the normalized maximum local mode amplitude $w_{\max}/t$ versus q_s for the two cases in (a). The triangle in (a) marks the point where the equilibrium paths cross, the corresponding q_s and $w_{\max}/t$ values are marked with the vertical dot-dashed line in (b).

for all $\mathcal{E}_0$ values stated in Table 4.2. Note that the normalized total end shortening $\mathcal{E}/L$ is determined by:

$$\mathcal{E}/L = \frac{1}{4}q_s^2\pi^2 + \frac{u_1(0) + u_2(0)}{L} + \Delta. \tag{4.15}$$

Note that since the symmetry is imposed, the in-plane displacement $u_1(L)$ and $u_2(L)$ are identical to $u_1(0)$ and $u_2(0)$ respectively. A slightly different response is observed in contrast to the system with a global imperfection only. The number of snap-backs in the equilibrium paths reduces as $\mathcal{E}_0$ increases. This is because the buckling mode shape starts to develop from a certain number of waves that is defined by the initial imperfection. As a result, the formation of the first new peak or trough (snap-back) takes place further down the post-buckling path for larger initial imperfections. It is also observed that the formation of the new peak or trough undergoes a longer restabilization path, and therefore a larger snap-back, meaning that more membrane stretching is required for the formation of the new peak or trough. It is also clear in Figure 4.10(a) that there is a cross-over between the equilibrium paths. This is a result of the different local buckling modes in those two particular cases. It is clear in Figure 4.10(b) that the maximum local out-of-plane deflections are different at the specific equilibrium state where the two curves in (a) cross.

4.2.3 Local buckling critical ($q_{s0} \neq 0$, $w_0 \neq 0$)

In this section, a 3.5 m strut with both global and local imperfections is analysed. The global imperfection coordinate q_{s0} is kept at a constant value of $L/10000$, whereas the local imperfections are introduced to the entire flange; and therefore the full set of the equilibrium equations are solved with w_1, w_2, u_1 and u_2 all included. Figures 4.11 and 4.12 show the imperfection sensitivity diagrams that correspond directly to Figures 4.6 and 4.7. Note that since the strut has been shown to be insensitive to the imperfection

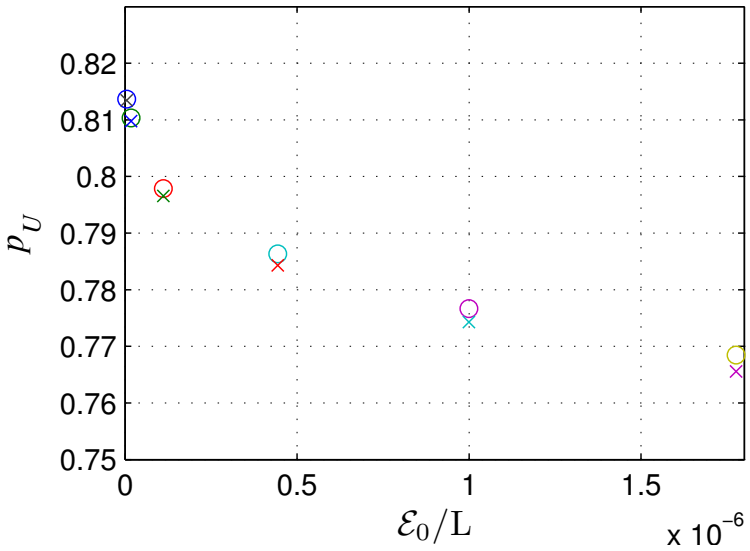

(a)

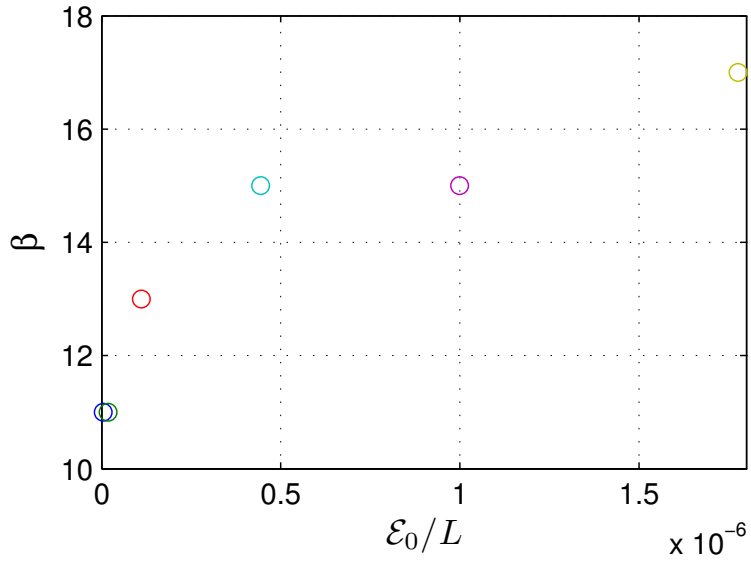

(b)

Figure 4.11: Imperfection sensitivity diagram with the abscissa in each case being the normalized imperfection size $\mathcal{E}_0/L$ plotted against: (a) the normalized peak load p_U, (b) the periodicity parameter β that gives the lowest peak loads. The circular symbols in (a) correspond to the periodic imperfection, whereas the crosses correspond to the modulated imperfection in both graphs.

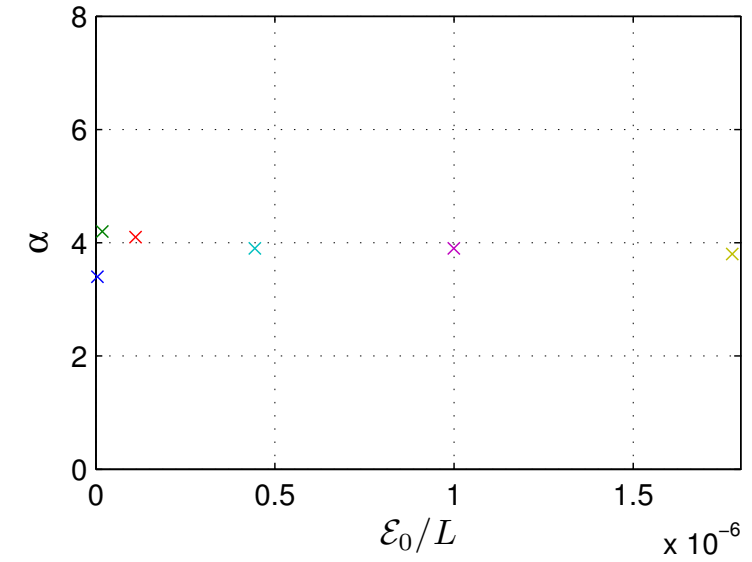

(a)

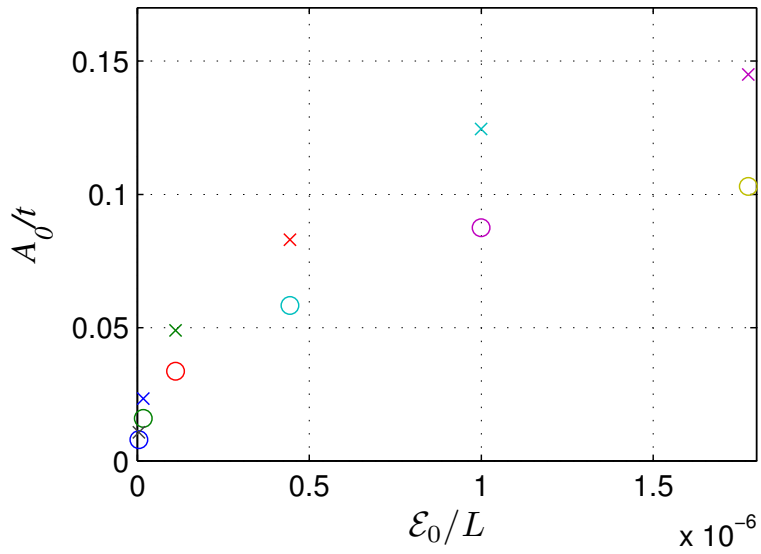

(b)

Figure 4.12: Imperfection sensitivity diagram with the abscissa in each case being the normalized imperfection size $\mathcal{E}_0/L$ plotted against: (a) the localization parameter α which gives the lowest peak loads and (b) the normalized imperfection amplitude A_0/t. The circular symbols in (a) correspond to the periodic imperfection, whereas the crosses correspond to the modulated imperfection in both graphs.

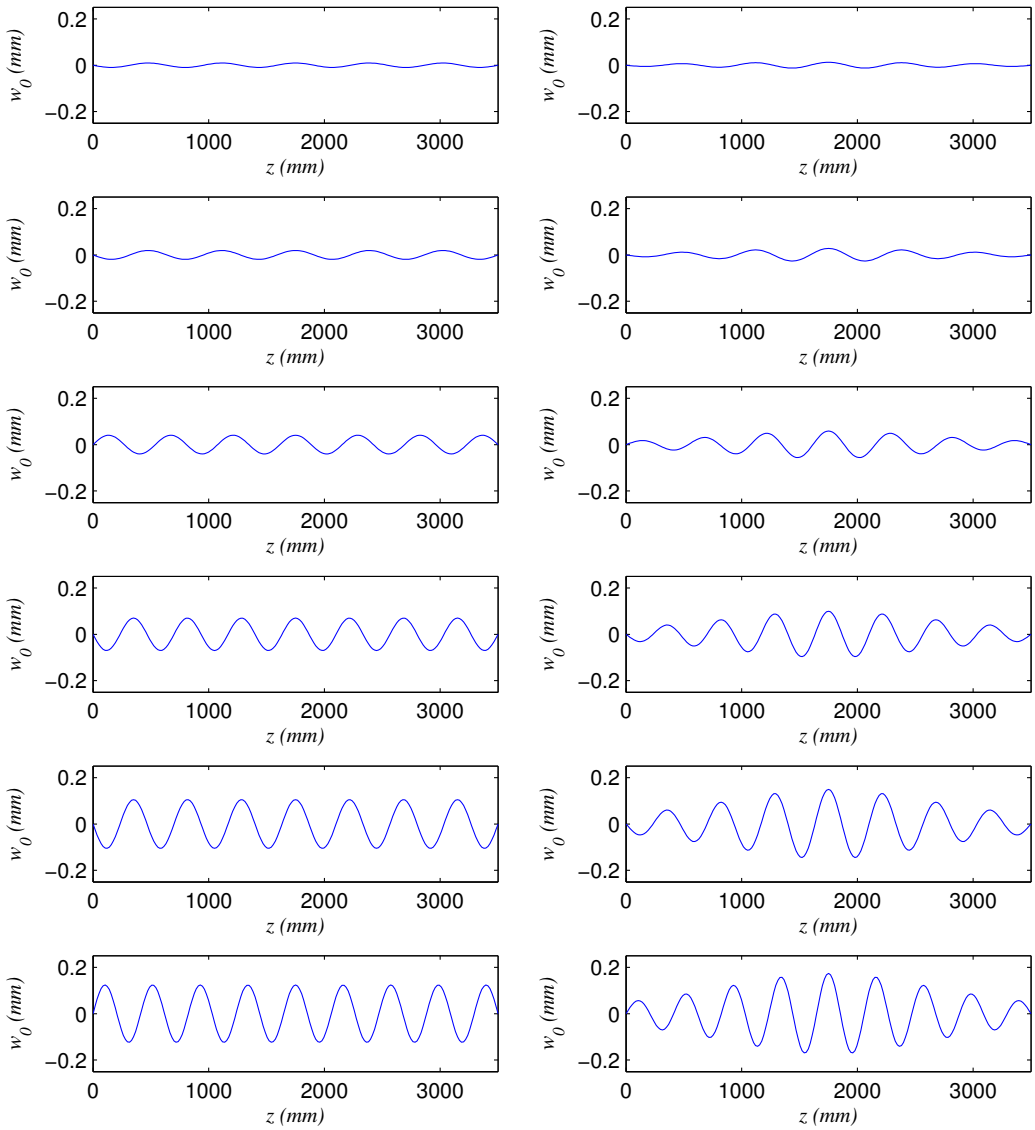

Figure 4.13: Mode shapes of the initial out-of-plane displacement, w_0 showing the worst combination of A_0, β and α for increasing $\mathcal{E}_0$ values from top to bottom. The left column shows the worst case periodic imperfection ($\alpha = 0, \beta > 0$), whereas the right column shows the worst case modulated imperfection ($\alpha, \beta > 0$). All dimensions are in millimetres.

with $\beta = 1$, the focus is on the cases of periodic imperfections with higher values of β and modulated imperfections. The same $\mathcal{E}_0$ values are used as in Table 4.2; and the corresponding peak loads are summarized in Table 4.3, for both periodic and modulated

$\mathcal{E}_0(\times 10^{-9})$	0	4.441	17.77	111.0	444.1	999.3	1777
p_U (periodic)	0.8215	0.8137	0.8103	0.7978	0.7863	0.7766	0.7685
p_U (modulated)	0.8215	0.8134	0.8098	0.7966	0.7843	0.7743	0.7655

Table 4.3: The values of the normalized peak loads, p_U for both periodic and modulated imperfections, which correspond to the $\mathcal{E}_0$ values in Table 4.2.

imperfections. It is observed that the strut is sensitive to both types of imperfections. However, although the modulated imperfections always give lower peak loads than the periodic imperfections, the reduction is much less severe as compared with the $L = 4$ m case. For the largest $\mathcal{E}_0$, the reduction in the peak loads are 6.5% and 6.8% for the periodic and modulated imperfections respectively. The graph in Figure 4.11(b) shows a similar trend as in Figure 4.6(b); however for the same $\mathcal{E}_0$, the profiles of w_{0i} for the $L = 3.5$ m model are generally associated with more waves. In the case of modulated imperfections, the degree of localization, which gives the worst combination, is roughly constant at $\alpha \approx 4$, as shown in Figure 4.12(a). The worst case mode shapes of the initial imperfections are shown in Figure 4.13.

Figures 4.14 and 4.15 show plots of equilibrium paths for the worst case modulated imperfections, which correspond directly to Figures 4.9 and 4.10. Similarly, for larger imperfections, the cellular behaviour is contaminated by the initial mode shape of the imperfection. Figure 4.16 shows a selection of 3-dimensional representations of the deflected strut that comprise all the components of global buckling (W and θ) and local buckling (w_i and u_i). The value of $\mathcal{E}_0$ increases from top to bottom; the left column corresponds to the equilibrium state at the peak load whereas the right column corresponds to the equilibrium state at a significantly larger magnitude of the global mode, where $q_s = 7 \times 10^{-3}$, for

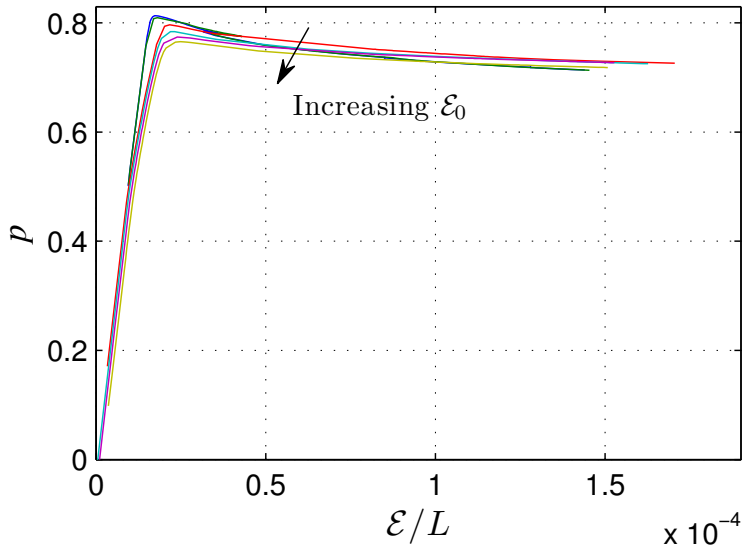

(a)

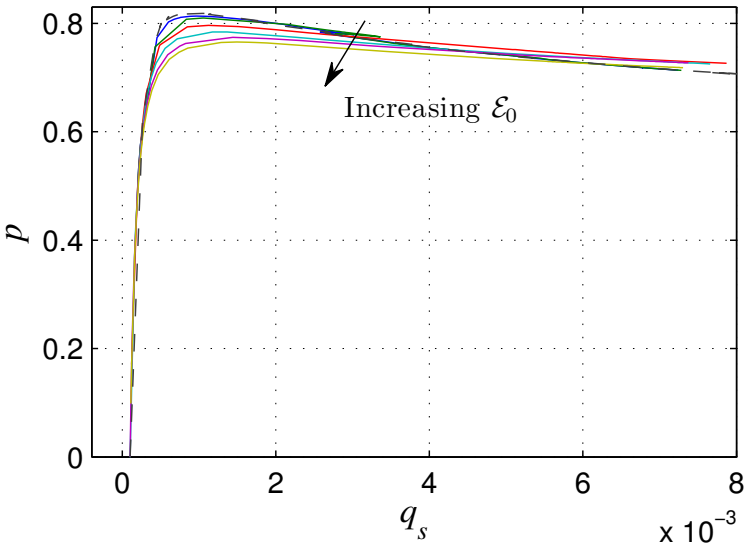

(b)

Figure 4.14: Numerical equilibrium paths for the worst case modulated imperfections for the 3.5 m strut. Graphs show a family of curves of the normalized force ratio p versus (a) the normalized total end shortening $\mathcal{E}/L$ and (b) the global mode amplitude q_s.

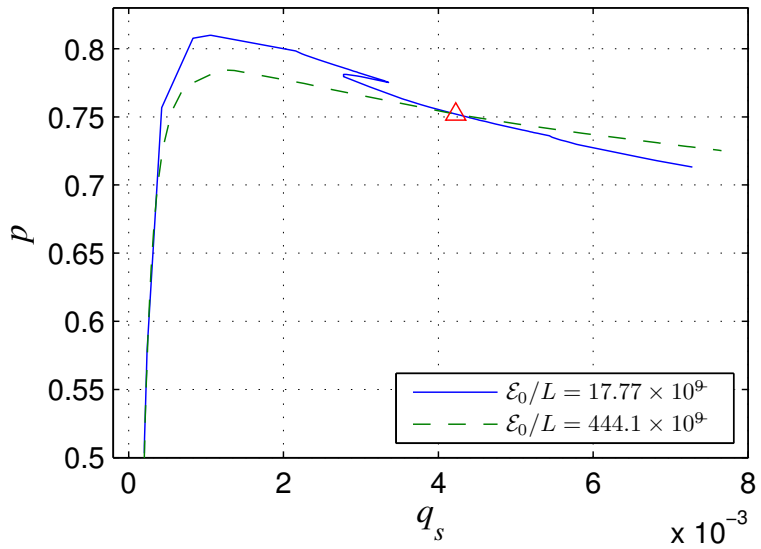

(a)

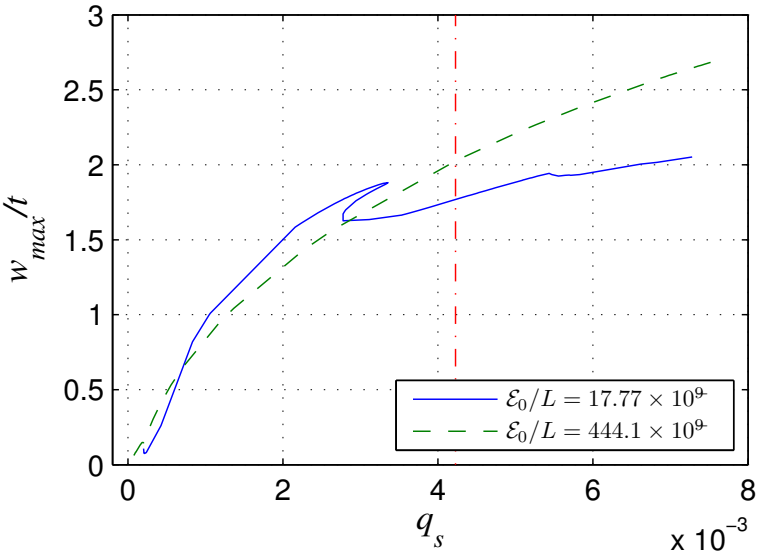

(b)

Figure 4.15: Numerical equilibrium paths for the worst case modulated imperfections for the 3.5 m strut: (a) shows a pair of equilibrium paths of p versus q_s, selected from Figure 4.14(b) for $\mathcal{E}_0/L = 17.77 \times 10^{-9}$ and $\mathcal{E}_0/L = 441.1 \times 10^{-9}$ and (b) shows the normalized maximum local mode amplitude $w_{\max}/t$ versus q_s for the two cases in (a). The triangle in (a) marks the point where the equilibrium paths cross, the corresponding q_s and $w_{\max}/t$ values are marked with the vertical dot-dashed line in (b).

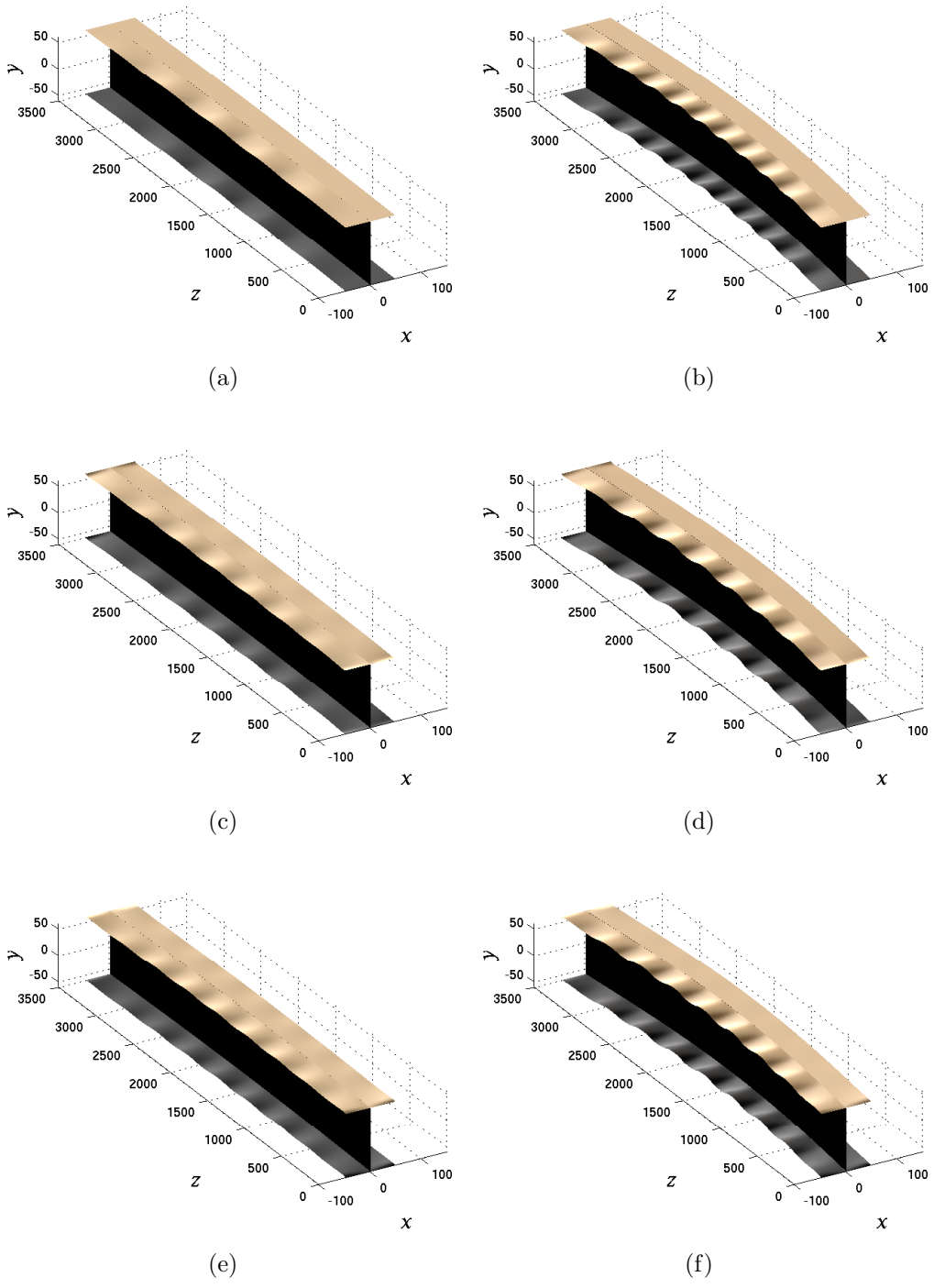

Figure 4.16: Numerical solutions of the system of equilibrium equations visualized on 3-dimensional representations of the strut. The results are shown for $\mathcal{E}_0/L = 17.77 \times 10^{-9}$, $\mathcal{E}_0/L = 444.1 \times 10^{-9}$ and $\mathcal{E}_0/L = 1777 \times 10^{-9}$ from top to bottom; (a), (c) and (e) correspond to the equilibrium states at the peak loads whereas (b), (d) and (f) correspond to the equilibrium states at approximately $q_s = 7{\times}10^{-3}$. All dimensions are in millimetres.

each case of $\mathcal{E}_0$. It is clear that at peak loads, struts with larger imperfections have more waves. Comparing the pair of struts with the smallest and the largest initial imperfection at $q_s = 7 \times 10^{-3}$, it is observed that the strut with smaller $\mathcal{E}_0$ has developed approximately ten sinusoidal peaks in total along the length whereas the strut with larger $\mathcal{E}_0$ has a total number of eight sinusoidal peaks, which is the essentially same mode shape as the initial imperfection. No snap-back is observed on the equilibrium path in the latter case, implying there is no formation of a new peak or trough. However, as the buckling progresses, a snap-back would be expected at a larger q_s value, followed by a longer restabilization path until a total number of 10 sinusoidal waves are fully formed. The corresponding equilibrium paths would then be expected to converge asymptotically.

4.3 Concluding remarks

The nonlinear analytical model for the axially-loaded thin-walled I-section strut in Chapter 3 has been developed to include an initial local out-of-plane displacement imperfection. Imperfection sensitivity studies have been conducted for the cases in the presence of global imperfections only, local imperfections only, and both imperfections types in combination. The highly imperfection sensitive nature of the struts that are susceptible to cellular buckling is highlighted. A significant reduction in the load-carrying capacity is observed for the struts with a small initial global deflection, local deflection and both in combination. The study also highlights the importance of the initial wavelength in the local imperfection, as well as the degree of localization. In contrast to the earlier work on the sandwich panel by Wadee (2000), the current study shows that the wavelength of the initial local deflection affects the load-carrying capacity more significantly than the degree of localization. However, the modulated local imperfection always seems to be the worst

case in terms of the load-carrying capacity, even though it is only by a narrow margin. Nevertheless, the study on different forms of global and local imperfections indicates the need of caution in design considerations, for actual thin-walled I-section columns that undergo cellular buckling behaviour.

Chapter 5

Analytical model enhancements and finite element validation

In the previous chapters, an open and doubly-symmetric thin-walled I-section strut under axial compression made from a linear elastic material was studied in detail using an analytical approach. One of the major assumptions was that the web provided a simple support to the flanges. So-called cellular buckling (Hunt *et al.*, 2000) or snaking (Burke & Knobloch, 2007) was captured, where snap-backs in the response, showing sequential destabilization and restabilization and a progressive spreading of the initial localized buckling mode were revealed. The results showed good comparisons with recent experimental and finite element studies (Becque & Rasmussen, 2009a; Becque & Rasmussen, 2009b). However, the full cellular buckling response with associated snap-backs was not picked up by the experiment and it has been postulated that one of the reasons is perhaps associated with the relative fixity between the web and the flanges, which makes the experiment differ from the fully pinned assumption. The current chapter presents an extension of the analytical model presented in the earlier chapters such that the relative fixity between the flange and the web can be varied parametrically. Note that the current work focuses

on the perfect system where global buckling is critical. A variational model accounting for the nonlinear mode interaction between global Euler buckling and local buckling is developed following the well established procedure in the previous chapters. The system of nonlinear ordinary differential equations subject to integral constraints is solved again using the numerical continuation package AUTO (Doedel & Oldeman, 2009). Erosion of the cellular buckling phenomenon is observed with increasing fixity between the web and the flanges. However, the changing wavelengths in the local buckling mode profile is revealed to persist for all cases from the pinned connection to the fully rigid connection between the web and the flanges – a phenomenon that was captured by experiments on I-section struts (Becque & Rasmussen, 2009a) and I-section beams under uniform bending (Wadee & Gardner, 2012).

A finite element model is also developed using the commercial code ABAQUS (2011) for validation purposes. The two models show good comparisons in terms of the mechanical destablilization and the nature of the post-buckling deformation. A brief discussion on the future enhancement of the current models is presented before final conclusions are drawn.

5.1 Development of the analytical model

5.1.1 Modal description

The analytical model of the perfect system for the case where the web is assumed to provide a simple support to the flanges has been fully developed in Chapter 3. In the current chapter, the model is extended by introducing a rotational spring of stiffness c to

the supporting edge of the flanges that are vulnerable to local plate buckling, as shown in Figure 5.1(a). Since the web is twice as thick as the flanges, it can be demonstrated

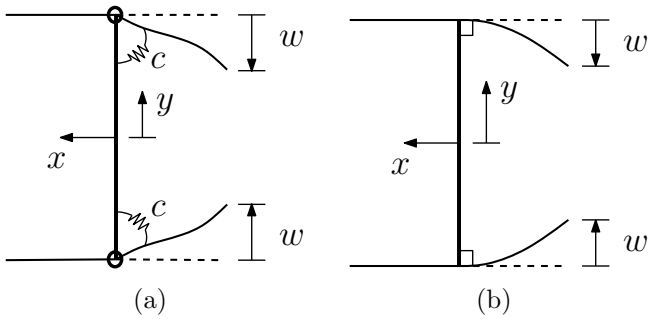

Figure 5.1: (a) and (b) show the out-of-plane flange displacement functions $w(x, z)$ of the local buckling, when $c \ll \infty$ and $c \to \infty$ respectively. Note that the web is assumed to be fully rigid.

that the local buckling in the web cannot occur before any local buckling in the flanges. The rotational stiffness c constrains the rotation of the supporting edge of the flange plate about the z-axis, whereas the other edge remains free. As a result, the local buckling mode shape of the flange plate in the transverse direction x differs from the pinned case; hence, the local buckling displacement functions therefore need to be refined. The local out-of-plane displacement $w(x, z)$ is expressed as $w(x, z) = f(x)w(z)$, where $f(x)$ represents the deflected shape in the transverse direction x (see Fig 5.2). It is assumed that $f(x)$ has a general form that is derived from the limiting conditions of a beam and a cantilever strut such that the cases for fully pinned or fully fixed conditions may be modelled, thus:

$$f\left(x\right) = A_0 + A_1\left(\frac{2x}{b}\right) + A_2\left(\frac{2x}{b}\right)^2 + A_3\left(\frac{2x}{b}\right)^3 + A_4 \sin\frac{\pi x}{b}, \tag{5.1}$$

where A_0, A_1, A_2, A_3 and A_4 are the coefficients that are determined by the boundary conditions:

$$\begin{array}{llllllll} (i) & f\left(0\right) & = & 0, & (ii) & Df''\left(0\right) & = & -cf'\left(0\right), \\ (iii) & f''\left(-b/2\right) & = & 0, & (iv) & f'''\left(-b/2\right) & = & 0, \end{array} \tag{5.2}$$

with $D = Et^3/[12(1-\nu^2)]$ being the plate flexural rigidity, and primes refer to the derivatives with respect to the transverse coordinate x. Substituting the corresponding

expressions into the boundary conditions, A_0 and A_3 are found to be zero, A_2 and A_4 can be expressed in terms of A_1 as $s_2 A_1$ and $s_4 A_1$ respectively, where s_2 and s_4 are determined as:

$$\begin{aligned} s_2 &= -\frac{\tilde{c}\pi}{4\left(\pi - \tilde{c}\right)}, \\ s_4 &= \frac{2\tilde{c}}{\pi\left(\pi - \tilde{c}\right)}, \end{aligned} \tag{5.3}$$

and $\tilde{c} = cb/D$. The expression for A_1 is determined by a fifth boundary condition that fixes the amplitude to unity, $f(-b/2) = 1$. The full expression of the out-of-plane deflection

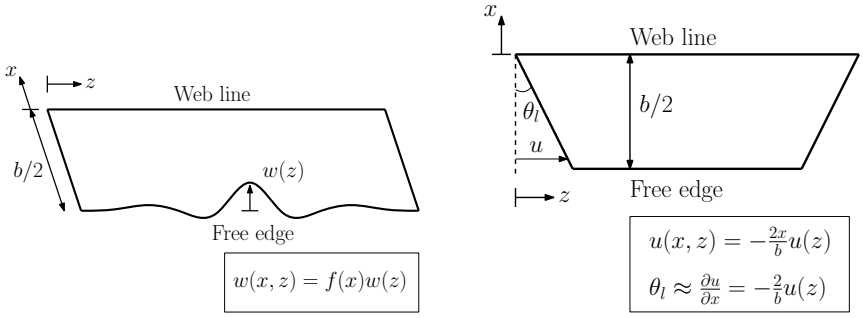

Figure 5.2: (a) Definition of the local out-of-plane displacement, $w(x, z)$, where $f(x)$ varies with increasing rotational stiffness c. (b) Definition of the local in-plane displacement $u(x, z)$, where a linear distribution is assumed across the width of the flange due to the assumption of Timoshenko beam bending of the flange in the xz plane.

$w(x, z)$ thus becomes:

$$w(x,z) = -\frac{w(z)}{(1 - s_2 + s_4)}\left[\frac{2x}{b} + s_2\left(\frac{2x}{b}\right)^2 + s_4 \sin\frac{\pi x}{b}\right]. \tag{5.4}$$

Note that if the rotational stiffness of the spring c tends to zero, s_2 and s_4 also tend to zero, implying that $f(x)$ becomes a linear function as in the case of the pinned flange–web connection as presented in Chapter 3. On the other hand, when c tends to infinity, $f(x)$ becomes:

$$f(x) = -\left[\frac{4\pi}{4\pi - \pi^2 - 8}\right]\left[\frac{2x}{b} + \frac{\pi}{4}\left(\frac{2x}{b}\right)^2 - \frac{2}{\pi}\sin\frac{\pi x}{b}\right], \tag{5.5}$$

which is essentially the model for the rigid connection between the flange and the web, shown in Figure 5.1(b).

The local in-plane displacement function, $u(x, z)$ has a linear distribution across the flange width due to the assumption of Timoshenko bending, which is the same as the case of the pinned flange–web connection, as shown in Figure 5.2(b). The global buckling mode has been fully described for the pinned flange–web connection in Chapter 3. The lateral displacement W and the rotation of the plane section θ were shown in Figure 3.3(a) and given by Equation (3.1).

5.1.2 Total potential energy

A procedure for deriving the total potential energy V for the pinned flange–web connection, was presented in Chapter 3; the current formulation follows the same approach with the focus being on the case where global buckling is critical. The derivation of the strain energy components and the work done by the axial load is outlined in this section. The global bending energy U_{bo} and the work done $P\mathcal{E}$ are the same as in Chapter 3 and given by Equations (3.5) and (3.15) respectively. The local bending energy, U_{bl} accounting for both top and bottom flanges is determined by the general expression:

$$U_{bl} = D \int_{-b/2}^{0} \int_{0}^{L} \left(\frac{\partial^2 w}{\partial z^2} + \frac{\partial^2 w}{\partial x^2} \right)^2 - 2\,(1-\nu) \left[\frac{\partial^2 w}{\partial z^2} \frac{\partial^2 w}{\partial x^2} - \left(\frac{\partial^2 w}{\partial z \partial x} \right)^2 \right] \mathrm{d}z\mathrm{d}x. \tag{5.6}$$

Once the partial derivatives of $w(x, z)$ are substituted into Equation (5.6), integration with respect to x leads to:

$$U_{bl} = D \int_{0}^{L} \left[\{f^2\}_x \ddot{w}^2 + \{f''^2\}_x w^2 - 2\nu \{f f''\}_x \ddot{w} w + 2\,(1-\nu)\,\{f'^2\}_x \dot{w}^2 \right] \mathrm{d}z, \tag{5.7}$$

where dots once again represent derivatives with respect to z; the braces with subscript x denote that a definite integration has been performed with respect to x for the range from $-b/2$ to 0, for example,

$$\{F\}_x \equiv \int_{-b/2}^{0} F(x)\mathrm{d}x, \tag{5.8}$$

where F is an example function. The integration is performed in the commercial computer algebra software MAPLE (Monagan *et al.*, 2005); the full integrated expressions are very long and are therefore presented in Appendix A.

The membrane strain energy (U_m) is derived by considering the longitudinal component of the direct strains (ε_z) and the shear strains (γ_{xz}) in the flanges. The general expressions of the direct strains, ε_{zt} and ε_{zc} in the non-vulnerable and vulnerable parts of the flange respectively are:

$$\begin{aligned} \varepsilon_{zt} &= \frac{\partial u_t}{\partial z} - \Delta, \\ \varepsilon_{zc} &= \frac{\partial u_t}{\partial z} - \Delta + \frac{\partial u}{\partial z} + \frac{1}{2}\left(\frac{\partial w}{\partial z}\right)^2, \end{aligned} \tag{5.9}$$

where $u_t = -\theta x$, which is the in-plane displacement from the tilt component of the global buckling mode. A pure in-plane compressive strain Δ is again included. The membrane energy from the direct strain U_d accounting for both top and bottom flanges, is thus:

$$\begin{aligned} U_d &= Et\int_0^L\int_0^{b/2}\varepsilon_{zt}^2 \mathrm{d}x\mathrm{d}z + Et\int_0^L\int_{-b/2}^0\varepsilon_{zc}^2\mathrm{d}x\mathrm{d}z + Eth\int_0^L\Delta^2\mathrm{d}z \\ &= Etb\int_0^L\left\{\frac{b^2}{12}q_t^2\frac{\pi^4}{L^2}\sin^2\frac{\pi z}{L} + \frac{1}{6}\dot{u}^2 + \frac{\{f^4\}_x}{4b}\dot{w}^4 - q_t\frac{b\pi^2}{6L}\sin\frac{\pi z}{L}\left[\dot{u} - \frac{6\{xf^2\}_x}{b^2}\dot{w}^2\right]\right. \\ &\qquad \left. - \frac{1}{2}\Delta\dot{u} - \frac{\{f^2\}_x}{b}\Delta\dot{w}^2 - \frac{2\{xf^2\}_x}{b^2}\dot{u}\dot{w}^2 + \left(1+\frac{h}{b}\right)\Delta^2\right\}\mathrm{d}z. \end{aligned} \tag{5.10}$$

The presence of shear strain, the contributions of which are γ_{xzc} and γ_{xzt}, also adds to the membrane energy, the general expressions being:

$$\begin{aligned} \gamma_{xzt} &= \frac{\partial W}{\partial z} - \theta, \\ \gamma_{xzc} &= \frac{\partial W}{\partial z} - \theta + \frac{\partial u}{\partial x} + \frac{\partial w}{\partial z}\frac{\partial w}{\partial x}. \end{aligned} \tag{5.11}$$

The membrane energy from the shear strain, U_s accounting for both top and bottom

flanges, is thus:

$$\begin{aligned} U_s &= Gt\int_0^L\int_0^{b/2}\gamma_{xzt}^2\mathrm{d}x\mathrm{d}z + Gt\int_0^L\int_{-b/2}^0\gamma_{xzc}^2\mathrm{d}x\mathrm{d}z \\ &= Gtb\int_0^L\Bigg\{\left(q_s-q_t\right)^2\pi^2\cos^2\frac{\pi z}{L} + \frac{2}{b^2}\left(u^2 + \frac{b}{2}\{f'^2f^2\}_x\dot{w}^2w^2 - 2\{f'f\}_x u\dot{w}w\right) \\ &\qquad - \frac{2}{b}\left(q_s-q_t\right)\pi\cos\frac{\pi z}{L}\left(u - \{f'f\}_x\dot{w}w\right)\Bigg\}\mathrm{d}z. \end{aligned} \tag{5.12}$$

The strain energy stored in the rotational spring, U_{sp}, accounting for the top and bottom flanges, is given by the following expression:

$$U_{sp} = \int_0^L c\left[\frac{\partial w(0,z)}{\partial x}\right]^2\mathrm{d}z \;\; = \frac{c}{b^2}\int_0^L\left(\frac{2+s_4\pi}{1-s_2+s_4}\right)^2 w^2\mathrm{d}z. \tag{5.13}$$

Finally, the total potential energy V is given by the following expression:

$$V = U_{bo} + U_{bl} + U_d + U_s + U_{sp} - P\mathcal{E}. \tag{5.14}$$

5.1.3 Variational formulation

The governing differential equations are obtained by performing the calculus of variations on the total potential energy V following the procedure presented in the previous chapters. The non-dimensional differential equations for $\tilde{w}$ and $\tilde{u}$ are thus:

$$\begin{aligned} &\ddot{\tilde{w}} - \frac{b^2\phi^2}{2\{f^2\}_x}\left[\nu\left(\{ff''\}_x - \{f'^2\}_x\right) + \{f'^2\}_x\right]\tilde{w} + \frac{b^4\phi^4}{16\{f^2\}_x}\left[\{f''^2\}_x + \frac{60\tilde{c}}{b}f'^2\right]\tilde{w} \\ &\quad - \frac{\tilde{G}\phi^2\tilde{w}}{16\{f^2\}_x}\left[b^2\{f'^2f^2\}_x\left(\tilde{\dot{w}}^2 + \tilde{w}\tilde{\ddot{w}}\right) - 2b\{f'f\}_x\tilde{\dot{u}} + \frac{b\pi^2\{f'f\}_x}{\phi}\left(q_s-q_t\right)\sin\frac{\pi\tilde{z}}{2}\right] \\ &\quad - \frac{\tilde{D}}{8\{f^2\}_x}\Bigg[3\{f^4\}_x\tilde{\dot{w}}^2\tilde{\ddot{w}} - \frac{4\{xf^2\}_x}{b}\left(\tilde{\ddot{u}}\tilde{\dot{w}} + \tilde{\dot{u}}\tilde{\ddot{w}}\right) - 2\{f^2\}_x\tilde{\ddot{w}}\Delta \\ &\quad + \frac{2\pi^2\{xf^2\}_x}{b\phi}q_t\left(\sin\frac{\pi\tilde{z}}{2}\tilde{\ddot{w}} + \frac{\pi}{2}\cos\frac{\pi\tilde{z}}{2}\tilde{\dot{w}}\right)\Bigg] = 0, \end{aligned} \tag{5.15}$$

$$\tilde{\ddot{u}} - \frac{12\{xf^2\}_x}{b^2}\tilde{\dot{w}}\tilde{\ddot{w}} - q_t\frac{\pi^3}{4\phi}\cos\frac{\pi\tilde{z}}{2} - \frac{3\tilde{G}\phi^2}{\tilde{D}}\left[\tilde{u} - \{f'f\}_x\tilde{w}\tilde{\dot{w}} - \left(q_s-q_t\right)\frac{\pi}{\phi}\cos\frac{\pi\tilde{z}}{2}\right] = 0, \tag{5.16}$$

where $\tilde{w}$, $\tilde{u}$, $\tilde{D}$, $\tilde{G}$ and ϕ were defined in Chapter 3. It is worth noting that the braces represent integration with respect to the originally defined variable x and limits. The minimization of V with respect to the generalized coordinates q_s, q_t and Δ lead to the integral conditions in non-dimensional form:

$$\begin{aligned}
\frac{\partial V}{\partial q_s} &= \pi^2 q_s + \tilde{s}\,(q_s - q_t) - \frac{PL^2}{EI_w} q_s - \frac{\tilde{s}\phi}{\pi} \int_0^1 \cos\frac{\pi\tilde{z}}{2} \left(\{f'f\}_x \tilde{w}\tilde{\dot{w}} + \tilde{u} \right) \mathrm{d}\tilde{z} = 0, \\
\frac{\partial V}{\partial q_t} &= \pi^2 q_t - \tilde{t}\,(q_s - q_t) \\
&\quad + \phi \int_0^1 \left[\frac{\tilde{t}}{\pi} \cos\frac{\pi\tilde{z}}{2} \left(\{f'f\}_x \tilde{w}\tilde{\dot{w}} + \tilde{u} \right) - \sin\frac{\pi\tilde{z}}{2} \left(2\tilde{\dot{u}} - \frac{12\{xf^2\}_x}{b^2} \tilde{\dot{w}}^2 \right) \right] \mathrm{d}\tilde{z} = 0, \\
\frac{\partial V}{\partial \Delta} &= \int_0^1 \left[2\left(1 + \frac{h}{b}\right)\Delta - \frac{1}{2}\tilde{\dot{u}} - \frac{\{f^2\}_x}{b} \tilde{\dot{w}}^2 - \frac{P}{Etb} \right] \mathrm{d}\tilde{z} = 0,
\end{aligned} \tag{5.17}$$

where $\tilde{s}$ and $\tilde{t}$ were defined in Chapter 3. The boundary conditions for $\tilde{w}$ and $\tilde{u}$ and their derivatives are for pinned end conditions for $\tilde{z} = 0$ and for symmetry at $\tilde{z} = 1$:

$$\tilde{w}(0) = \tilde{\ddot{w}}(0) = \tilde{\dot{w}}(1) = \dddot{\tilde{w}}(1) = \tilde{u}(1) = 0, \tag{5.18}$$

with further conditions from matching the in-plane strain:

$$\frac{1}{3}\tilde{\dot{u}}(0) + \frac{2\{xf^2\}_x}{b^2} \tilde{\dot{w}}^2(0) - \frac{1}{2}\Delta + \frac{P}{2Etb} = 0. \tag{5.19}$$

Linear eigenvalue analysis is conducted to determine the critical load for global buckling, P_o^{C} which is of course the same as for the pinned flange–web connection (Wadee & Bai, 2014), since the rotational spring stores no energy in the fundamental state and during global buckling; the expression is thus given by Equation (3.29).

5.2 Numerical examples

In this section, numerical examples with varying rotational stiffness c are presented for the perfect system. The current examples use the same material and section properties

that were used in the case of the pinned flange–web connection, given in Table 3.2. The strut length L is chosen to be 4 m. It has been shown in Chapter 3 that for this specific configuration, global buckling is critical where the web provides a simple support to the flanges ($c = 0$). Obviously increasing the rotational stiffness c increases the local critical buckling load of the flange plate, P_l^{C} whereas the value of the global critical load, P_o^{C} is unchanged. Therefore with $L = 4$ m, global buckling is always critical for any positive value of c.

Numerical continuation is performed in AUTO. A similar solution strategy, as for the pinned flange–web connection, is illustrated diagrammatically in Figure 5.3. The initial

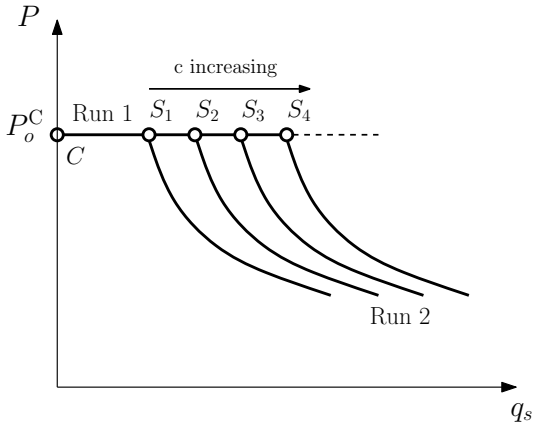

Figure 5.3: Numerical continuation procedure with varying rotational stiffness c. The thicker lines show the actual solution paths for different values of c. Points C and S_i are the critical and secondary bifurcation points respectively.

post-buckling path was computed first from P_o^{C} with q_s being varied. Many bifurcation points are detected on the weakly stable post-buckling path; the focus being on the one with the lowest value of q_s, the secondary bifurcation point S. Presently, a series of c values, listed in Table 5.1, with its nondimensional counterpart $\tilde{c}$, are substituted in turn. Note that the flange is connected to the web at $x = 0$, whereas the free edge of the flange is at $x = -48$ mm. As c is increased, the value of q_s at the secondary bifurcation is expected to increase due to the higher local buckling critical stress. After branch switching, the

c (Nm/m)	0	1	5	10	50	100	500	1000
$\tilde{c}$ ($\times 10^{-3}$)	0	2.9	14.4	29	144	289	1444	2888

Table 5.1: Rotational stiffnesses c and corresponding values of the non-dimensional scaling $\tilde{c} = cb/D$. These values are used in the numerical results presented in the current chapter.

subsequent equilibrium path exhibits a nonlinear interaction between the global and the local buckling modes. Figure 5.4(a) shows the plots of the transverse component of the out-of-plane displacement $f(x)$, for the vulnerable half of the flange according to each value of $\tilde{c}$ stated in Table 5.1. Figure 5.4(b) shows $f(x)$ versus x when $c \to \infty$; the dashed line shows the approximate solution from Bulson (1970) for an axially loaded rectangular plate with one edge fully fixed and the other edge free. Figures 5.5 and 5.6

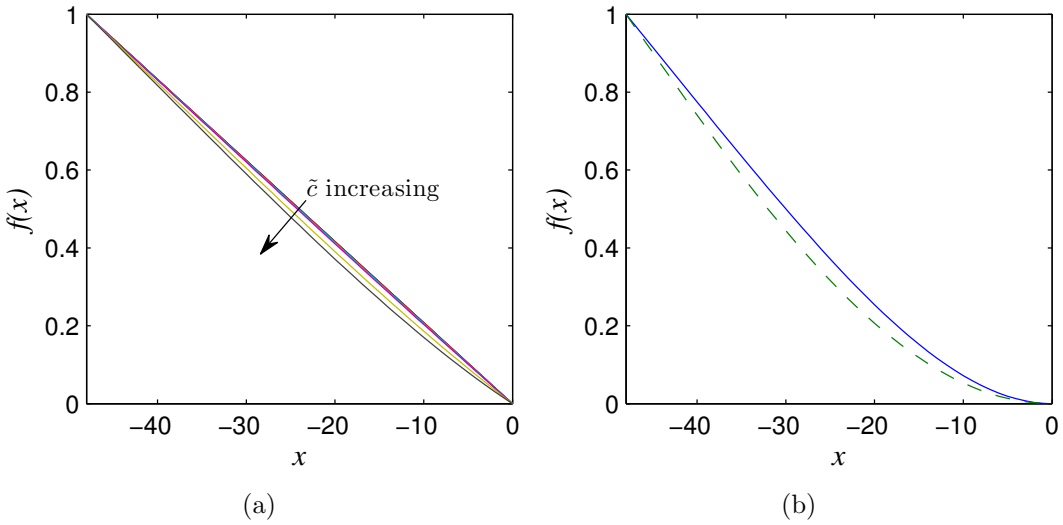

Figure 5.4: Transverse profiles of the out-of-plane displacement $f(x)$ for (a) the range of values of $\tilde{c}$ summarized in Table 5.1, and (b) an extremely large value of $\tilde{c}$ where the dashed line represents the approximate solution from Bulson (1970), with $f(x) = 1 - \cos(\pi x/b)$.

show the numerical equilibrium paths for each $\tilde{c}$ values listed in Table 5.1. Examining the post-buckling paths, it is observed that the cellular buckling behaviour found for the pinned case ($\tilde{c} = 0$), is rapidly eroded by increasing the rotational stiffness. Comparing the remaining equilibrium paths against the equilibrium paths for $\tilde{c} = 0$, it is observed that as $\tilde{c}$ increases, the snap-backs begin to vanish from the first cell to the last, and

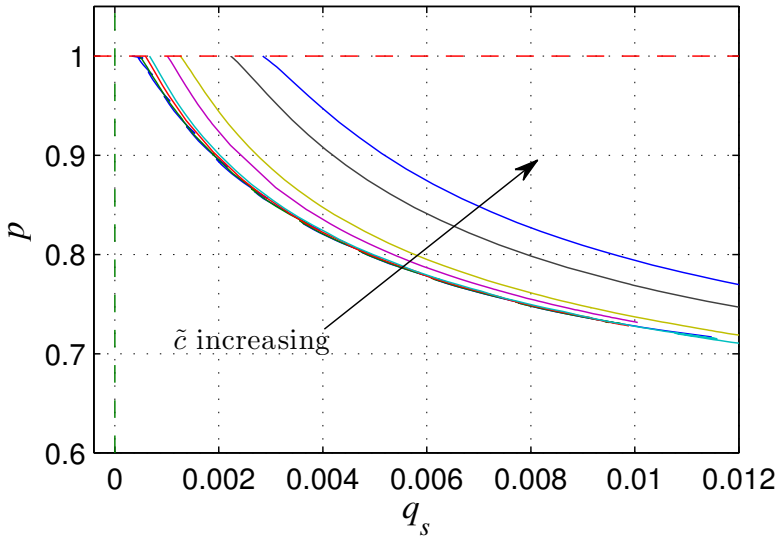

(a)

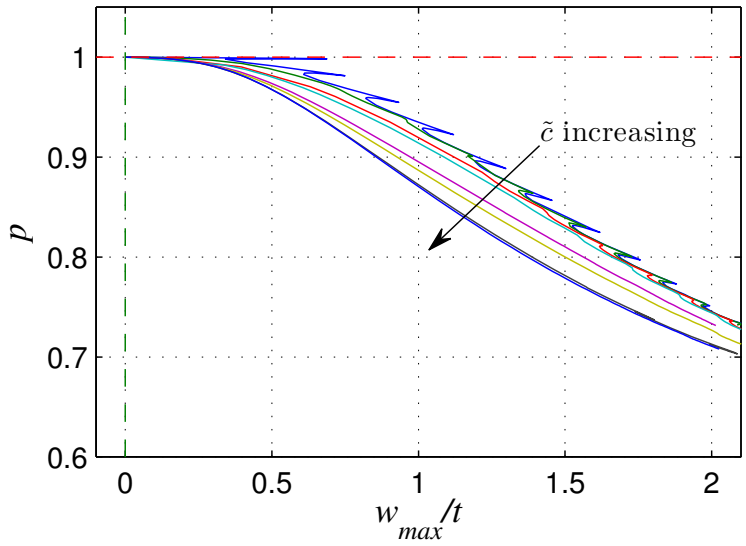

(b)

Figure 5.5: Numerical equilibrium paths. The graphs show a family of curves of the normalized force ratio $p = P/P_o^{\mathrm{C}}$ versus normalized modal amplitudes: (a) the global mode q_s and (b) the local mode $w_{\max}/t$.

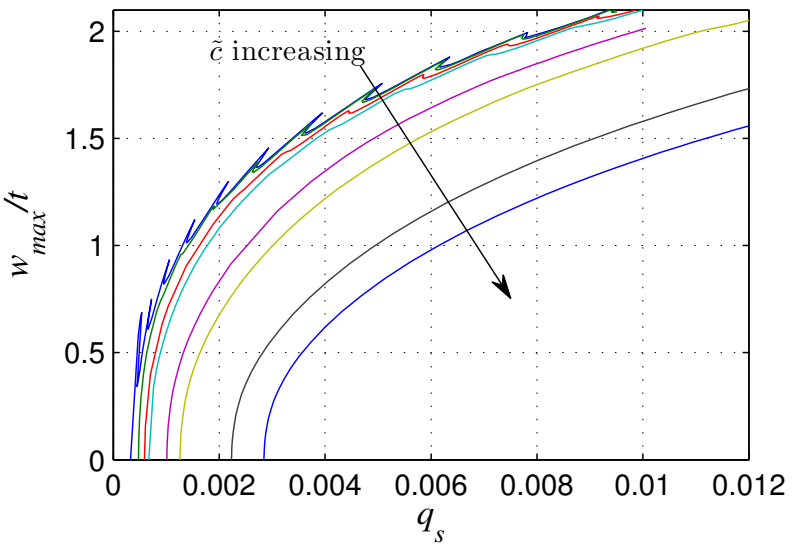

(a)

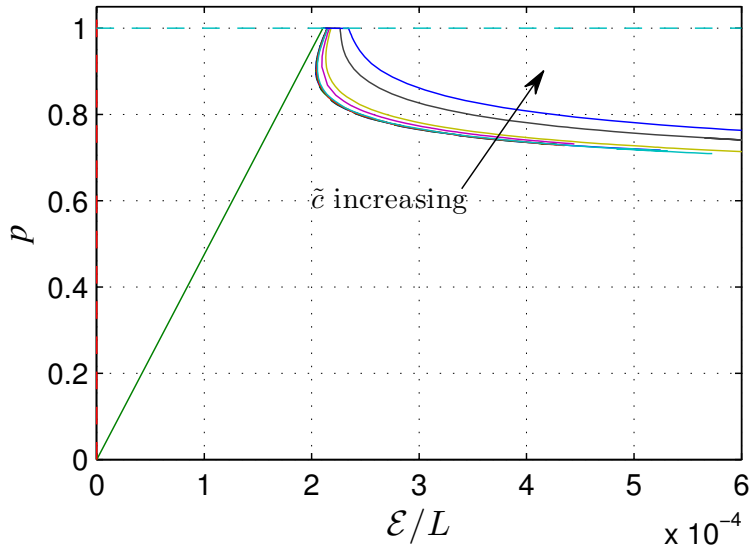

(b)

Figure 5.6: Normalized equilibrium paths: (a) local versus global modal amplitudes and (b) load p versus the total end-shortening $\mathcal{E}/L$.

the restabilization path of the snap-backs becomes shorter as $\tilde{c}$ increases. The cellular buckling behaviour vanishes almost completely when $\tilde{c} = 0.029$. For larger values of $\tilde{c}$ (from 0.14 to 2.9), no cellular behaviour is observed in the post-buckling paths. Another feature in Figure 5.5(a) is that, although with a larger $\tilde{c}$ value the local buckling mode is triggered at a larger magnitude of q_s, the post-buckling paths of p versus q_s seem to converge somewhat as the deformation progresses. Moreover, for the local out-of-plane displacement w, the post-buckling paths show a significantly stiffer response for higher values of $\tilde{c}$. At $p = 0.74$, the maximum local out-of-plane displacement w for $\tilde{c} = 0$ reaches a value of approximately $2.0t$, whereas for $\tilde{c} = 2.9$, it is approximately $1.6t$. Figure 5.6(b) shows the normalized axial load p versus the normalized total end shortening, $\mathcal{E}/L$, which is given by the following expression:

$$\frac{\mathcal{E}}{L} = \frac{1}{4}{q_s}^2\pi^2 + \frac{1}{2}\frac{u(0)}{L} + \Delta. \tag{5.20}$$

It is observed that just after the secondary instability is triggered, the total end shortening reduces with decreasing load for small values of $\tilde{c}$. This is a result of the local buckling of the flange plate releasing some proportion of the direct strain from the global mode and the pure in-plane compressive strain, Δ. The proportion of this release reduces as the rotational stiffness $\tilde{c}$ increases.

It was found in Chapter 3 that a snap-back signified the formation of a new local displacement peak or trough; the local buckling mode shifting from a localized to a periodic pattern and the wavelength reducing as a result. Since the snap-backs vanish for large $\tilde{c}$, it would be expected that, in contrast to the case where $\tilde{c} = 0$, the local buckling mode shape of the out-of-plane displacement, w would appear to be more periodic as soon as interactive buckling is triggered. Moreover, there would be less reduction in the wavelengths as the buckling progresses. Figure 5.7 illustrates the numerical solutions for the local out-of-plane displacement function w with the $\tilde{c}$ values stated in Table 5.1. The

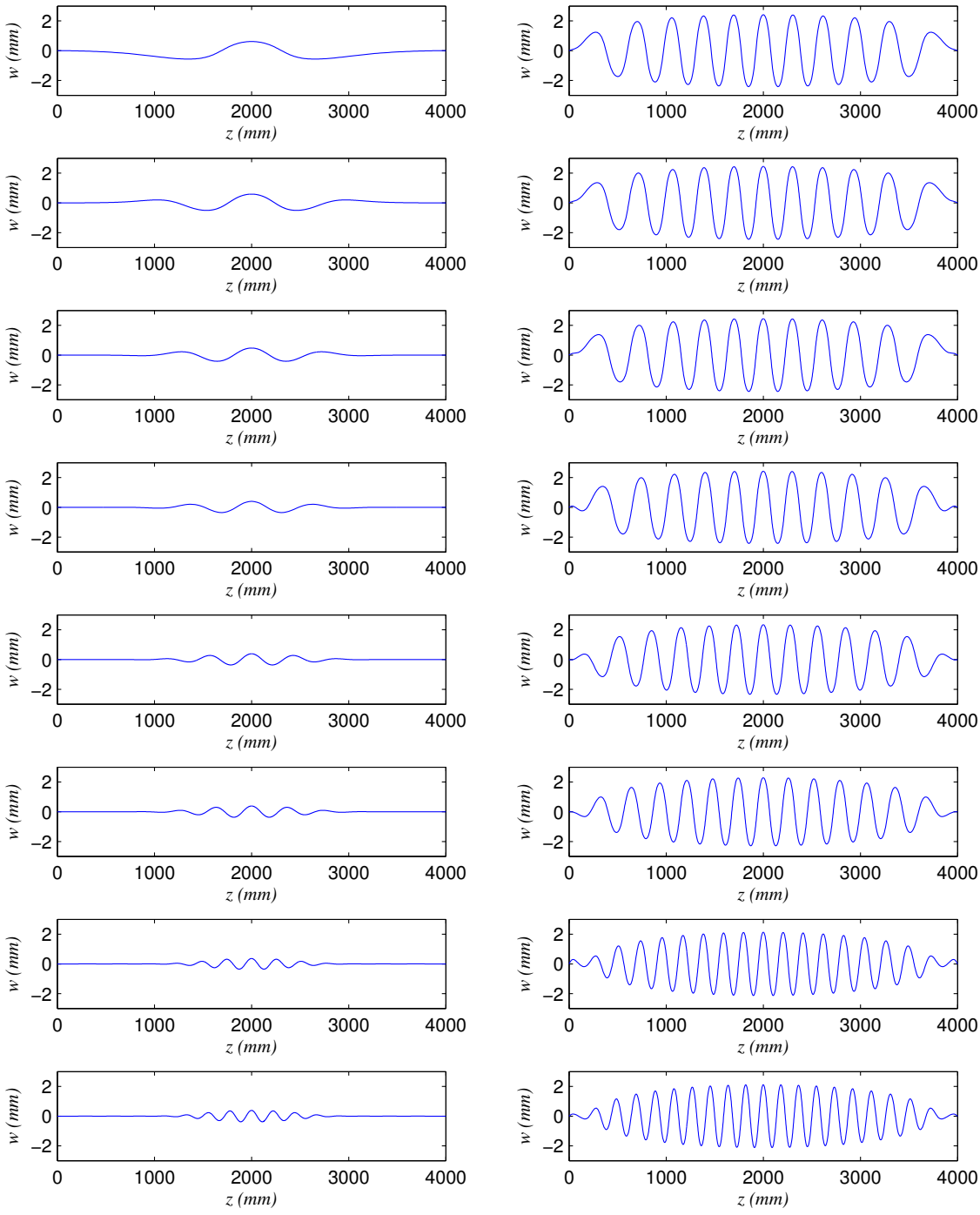

Figure 5.7: Numerical solutions for the local buckling displacement w. Each row corresponds to the $\tilde{c}$ values as given in Table 5.1 increasing downwards, whereas each column corresponds to the same normalized p, where $p = 0.99$ (left), $p = 0.74$ (right).

wavelengths of the buckling mode shapes are very similar at the same load in the top three rows of the graph in Figure 5.7, which correspond to the cases where cellular buckling is observed. As $\tilde{c}$ increases, a significant reduction in both the amplitude and the wavelengths is observed at the same load level. Recall the local buckling wavelength, Λ defined in Figure 3.22. It is found that Λ is measured to be 280 mm and 206 mm at $p = 0.74$ for $\tilde{c} = 0$ and $\tilde{c} = 2.9$ respectively, showing a significant reduction (approximately 26%) for the case with higher rotational stiffness at the joint. Figure 5.8 shows a selection of 3-dimensional representations of the deflected strut that include the components of global buckling (q_s and q_t) and local buckling (w and u) for $\tilde{c} = 0.014$, 0.29 and 2.9 from the top to the bottom row respectively. Figures from the left to the right columns correspond to the equilibrium states at $p = 0.99$, 0.85 and 0.74 respectively.

5.3 Finite element model

The commercial finite element (FE) code ABAQUS has been shown in the past to be capable of predicting the buckling modes and more importantly investigating the nonlinear interactive post-buckling behaviour of various types of thin-walled structures. Examples include sandwich struts with different core bending models (Wadee *et al.*, 2010), stainless steel square and rectangular hollow section columns (Gardner & Nethercot, 2004b) and stainless steel I-section columns formed by channel sections bolted back to back (Becque & Rasmussen, 2009b). It is therefore used in the current work to develop the FE model of the axially compressed I-section strut with the same section and material properties as for the analytical model, as shown in Table 3.2. Similar to the analytical model, the focus is on the cases where the flange–web connection with varying rigidity is modelled by introducing rotational springs to the edge of the flange that connects to the web.

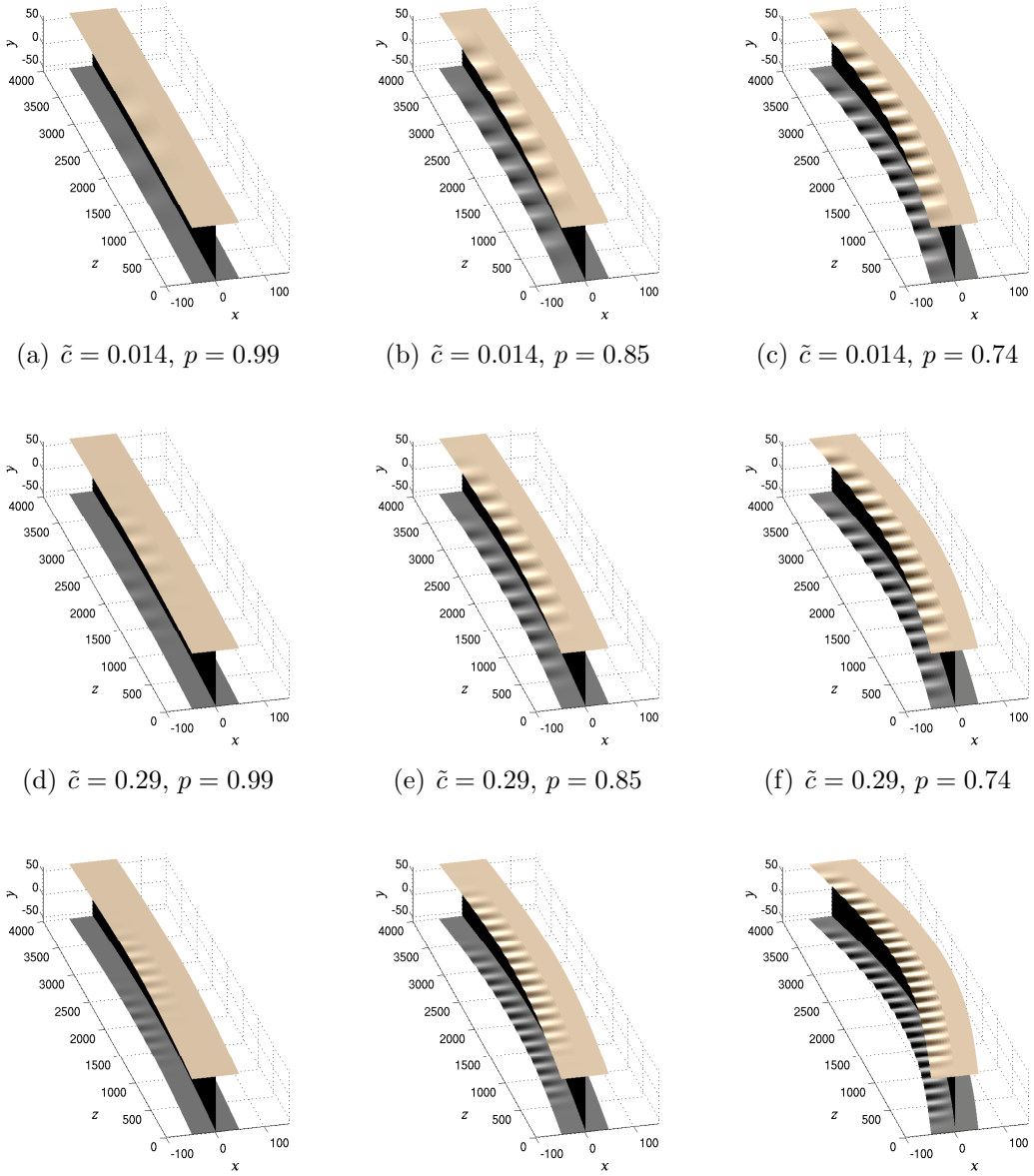

(a) $\tilde{c} = 0.014$, $p = 0.99$ (b) $\tilde{c} = 0.014$, $p = 0.85$ (c) $\tilde{c} = 0.014$, $p = 0.74$

(d) $\tilde{c} = 0.29$, $p = 0.99$ (e) $\tilde{c} = 0.29$, $p = 0.85$ (f) $\tilde{c} = 0.29$, $p = 0.74$

(g) $\tilde{c} = 2.9$, $p = 0.99$ (h) $\tilde{c} = 2.9$, $p = 0.85$ (i) $\tilde{c} = 2.9$, $p = 0.74$

Figure 5.8: Numerical solutions of the system of equilibrium equations visualized on a three dimensional representation of the strut. All dimensions are in millimetres.

5.3.1 Element type

A quadrilateral four-noded linear shell element (S4R) is chosen from the ABAQUS element library. Each node has three translational and three rotational degrees of freedom that allow the element to bend in double curvature. It has been shown to be applicable to the problems with geometrical nonlinearities since it accounts for finite membrane strains (Becque & Rasmussen, 2009b). The element uses reduced integration points and therefore hourglass control is applied to avoid unphysical solutions with excessive flexibility. It has been shown that the reduced integration significantly reduces the computational costs without compromising the accuracy, compared with full integration (Becque & Rasmussen, 2009b). Since no particular geometrical complexity exists in the current model, uniform rectangular elements were applied to the entire strut. A mesh sensitivity study was carried out for both linear eigenvalue and post-buckling analysis. It was found that a mesh size where the length of each element was approximately 10 mm provided a sufficiently high degree of accuracy versus computational costs. The total number of nodes in each flange and the web were 2406 and 5213 respectively for a strut length of 4 m.

5.3.2 Strut modelling

The individual parts of the strut, *i.e.* the flanges and the web were created. The nodes in the longitudinal edges of the flanges and the web were then tied with the rotational degrees of freedom released. A linear rotational spring element 'SPRINGA', which restrains the rotation about the longitudinal axis, was applied to each node in the longitudinal edge of the flange that joins the web, except the nodes at the ends of the strut. Axial compression was applied at both ends of the strut, where roller supports were introduced

as boundary conditions. An additional boundary condition '*ZSYMM' was applied at the midspan implying that the displacements of nodes were symmetric about the midspan – an assumption that was also made in the analytical model.

5.3.3 Method of analysis

Linear eigenvalue analysis was first conducted to investigate the critical buckling loads and modes. The first respective global buckling and local buckling modes were then introduced as imperfections in the nonlinear Riks analysis (Riks, 1972), using the command '*STATIC, RIKS', to investigate the post-buckling behaviour. The Newton–Raphson method was used internally to track the equilibrium paths and the increment size was limited to avoid the possibilities of non-convergence. The command '*STEP, NLGEOM' was active to account for geometric nonlinearities.

5.4 Validation

The models with small values of $\tilde{c}$ that exhibit cellular buckling were shown to be very similar to the case where a pinned connection is assumed between the web and the flanges. This was validated in Chapter 3 primarily by comparing against physical experiments. In the current chapter, the focus is on intermediate and large values of the rotational stiffness. Note that c is a rotational stiffness per unit length and it is assumed to be uniform along the length of the strut. Hence, the total rotational stiffness c_{total}, accounting for both top and bottom flanges, is $2cL$. In the FE model, since the rotational spring is applied at individual nodes and the same spring element is assumed along the length of the strut, the stiffness of the spring element, c_a is therefore c_{total}/N_{sp}, where N_{sp} is the total number

of springs which, in the current case, was 400 springs per joint for a 4 m long strut. Three FE models with the rotational stiffnesses being $c_a = 1000$ Nmm, $c_a = 10000$ Nmm and $c_a = 1 \times 10^{13}$ Nmm are studied and compared against the analytical model with $\tilde{c} = 0.29$, $\tilde{c} = 2.9$ and $\tilde{c} = 2.9 \times 10^{14}$ respectively, where c_a is the rotational stiffness of the spring element in the FE model. Note that the third case basically models a fully rigid connection between the flange and the web, as shown in Figure 5.1(b).

A linear eigenvalue analysis was initially conducted in ABAQUS, the global buckling critical mode being shown in Figure 5.9(a), whereas the local buckling critical modes for $c_a = 1000$ Nmm, $c_a = 10000$ Nmm and $c_a = 1 \times 10^{14}$ Nmm are shown in Figure 5.9(b), (c) and (d) respectively. The global critical load was found to be 22.72 kN, approximately 0.9%

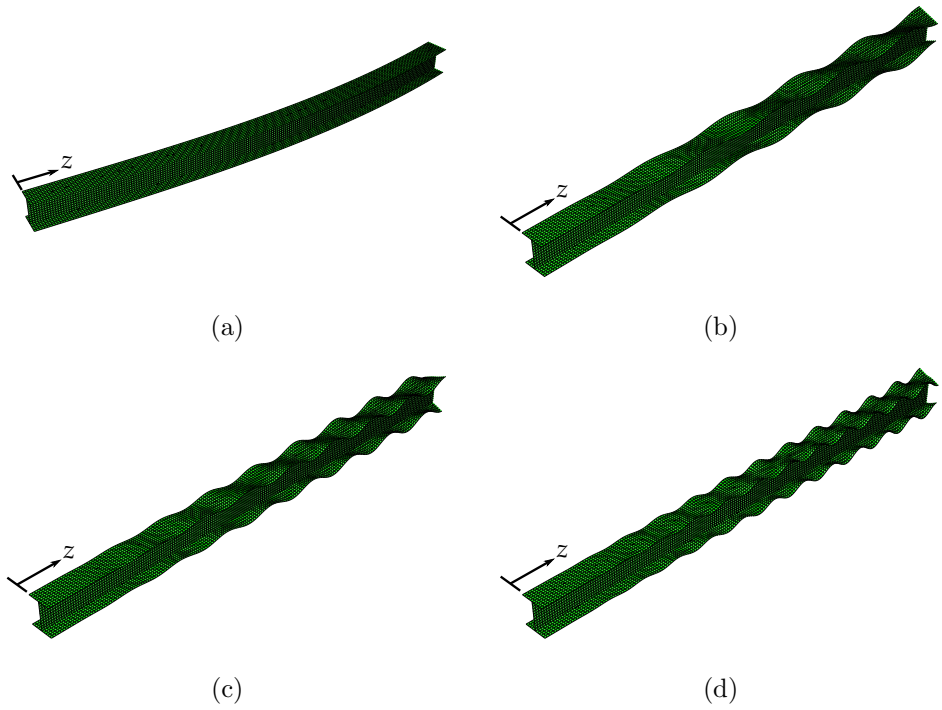

Figure 5.9: The critical eigenmodes from the linear eigenvalue analysis in ABAQUS, for (a) global buckling, (b) local buckling with $c_a = 1000$ Nmm, (c) local buckling with $c_a = 10000$ Nmm and (d) local buckling with $c_a \to +\infty$. The eigenmodes are shown for half of the strut length from $z = 0$ to $z = 2$ m.

lower than P_o^{C} from the analytical model. Shorter wavelengths were observed in the local

critical modes as c_a was increased, which agrees with the trend found in the analytical model qualitatively. The local critical modes in combination with the global critical mode were introduced as imperfections in the Riks analysis. The amplitudes of the global and local imperfections were set to $10^{-6}L$ and $10^{-3}t$ respectively, the values being sufficiently small such that the almost perfect response was studied and compared against the perfect system of the analytical model.

Figures 5.10, 5.11 and 5.12 show a series of equilibrium paths for $\tilde{c} = 0.29$, $\tilde{c} = 2.9$ and $\tilde{c} \rightarrow$

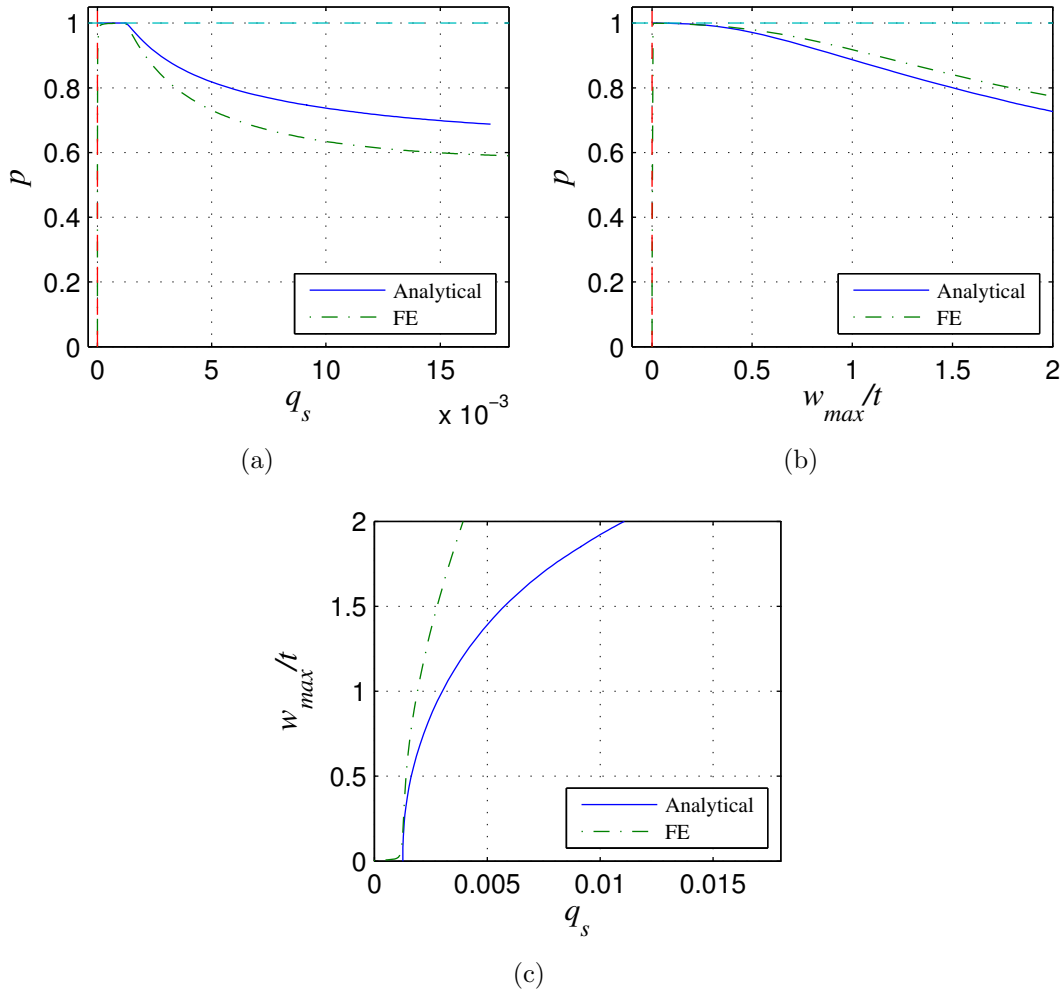

Figure 5.10: Comparisons of the equilibrium paths for $\tilde{c} = 0.29$; (a) shows the normalized force ratio p versus the global mode amplitude q_s; (b) shows p versus the normalized local mode amplitude $w_{\max}/t$ and (c) shows local versus global mode amplitudes.

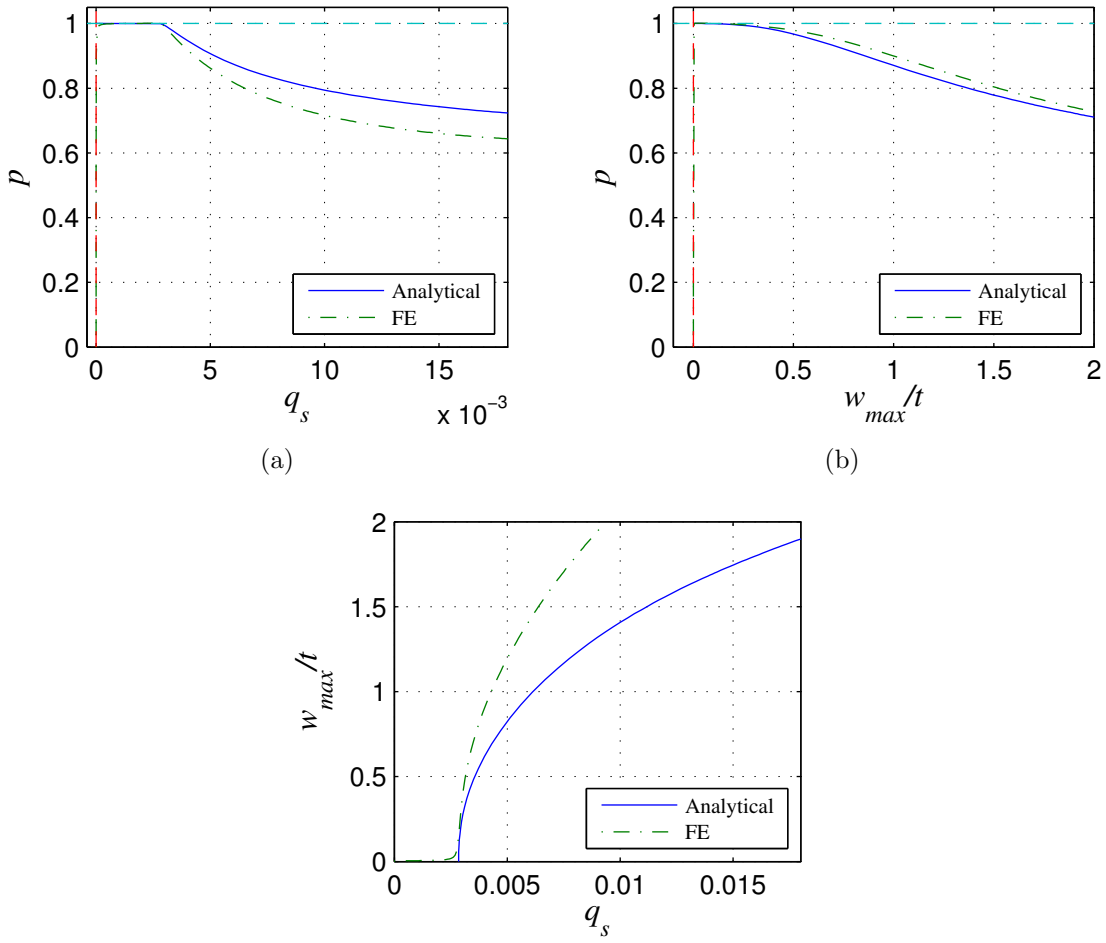

Figure 5.11: Comparisons of the equilibrium paths for $\tilde{c} = 2.9$; (a) shows the normalized force ratio p versus the global mode amplitude q_s; (b) shows p versus the normalized local mode amplitude $w_{\max}/t$ and (c) shows local versus global mode amplitudes.

$+\infty$ respectively. The equilibrium paths of the load versus the local deflection diagram show good comparisons between the analytical and FE models, with the analytical model showing a slightly stiffer response for all three cases of $\tilde{c}$. It is observed in all three cases of $\tilde{c}$ that the values of q_s at the secondary bifurcation points are extremely close between the two models, with errors that are negligible. It is also observed that the comparison improves as $\tilde{c}$ increases.

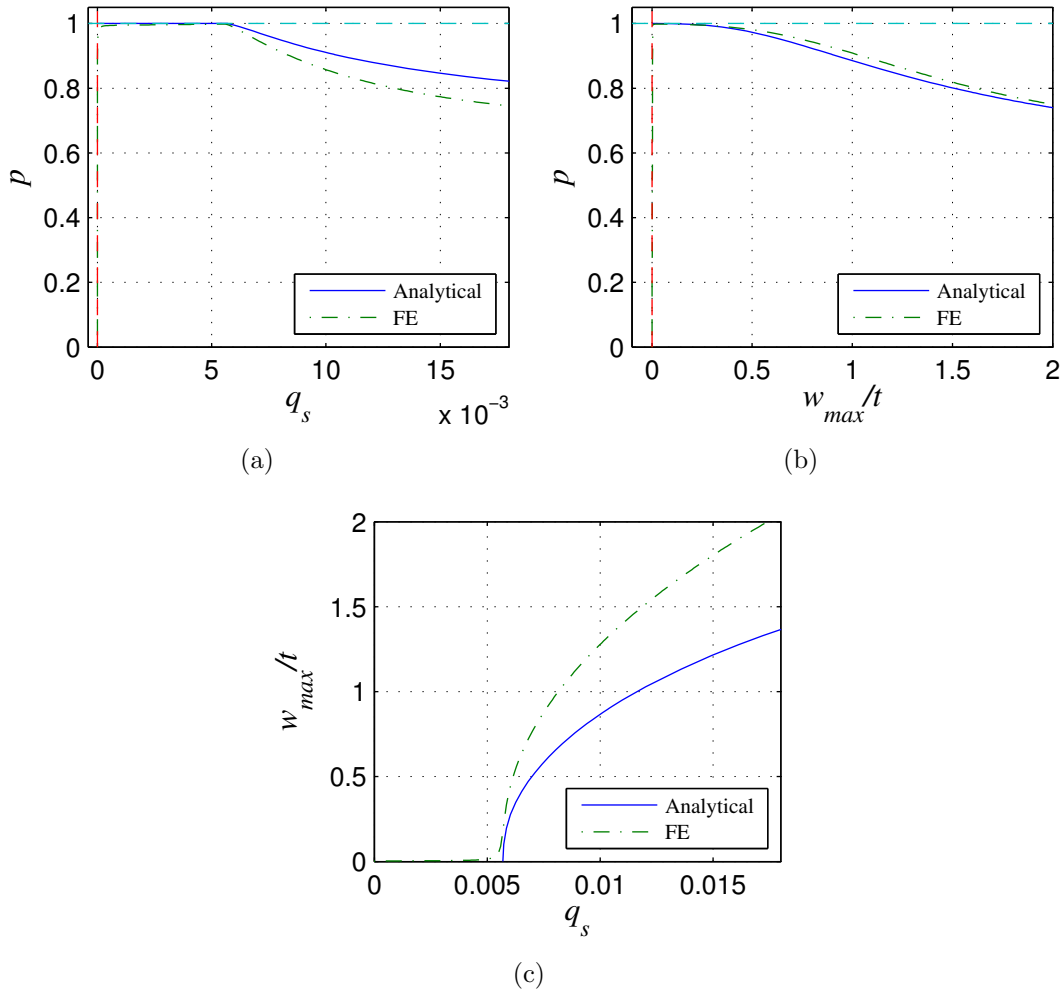

Figure 5.12: Comparisons of the equilibrium paths for $\tilde{c} \to \infty$; (a) shows the normalized force ratio p versus the global mode amplitude q_s; (b) shows p versus the normalized local mode amplitude $w_{\max}/t$ and (c) shows local versus global mode amplitudes.

For $w_{\max}/t \approx 2$, the errors in the normalized load p are approximately 6.2%, 2.3% and 1.9% for $\tilde{c} = 0.29$, $\tilde{c} = 2.9$ and $\tilde{c} \to +\infty$ respectively. The equilibrium paths of the load versus the global mode amplitude q_s show a slightly larger error. Similar to the equilibrium paths of the load versus the local deflection, the comparison of the load versus the global deflection improves as $\tilde{c}$ increases. At $q_s = 0.015$, the errors in p are approximately 14.3%, 11.1% and 8.3% for $\tilde{c} = 0.29$, $\tilde{c} = 2.9$ and $\tilde{c} \to +\infty$ respectively. For the same degree of q_s, the FE model generally shows a larger maximum local out-of-plane displacement

compared against the analytical model, with the percentage error reducing as $\tilde{c}$ increases, as shown in Figures 5.10(c), 5.11(c) and 5.12(c).

Figure 5.13 shows the solutions of the out-of-plane displacement $w(z)$ for $\tilde{c} = 0.29$ and

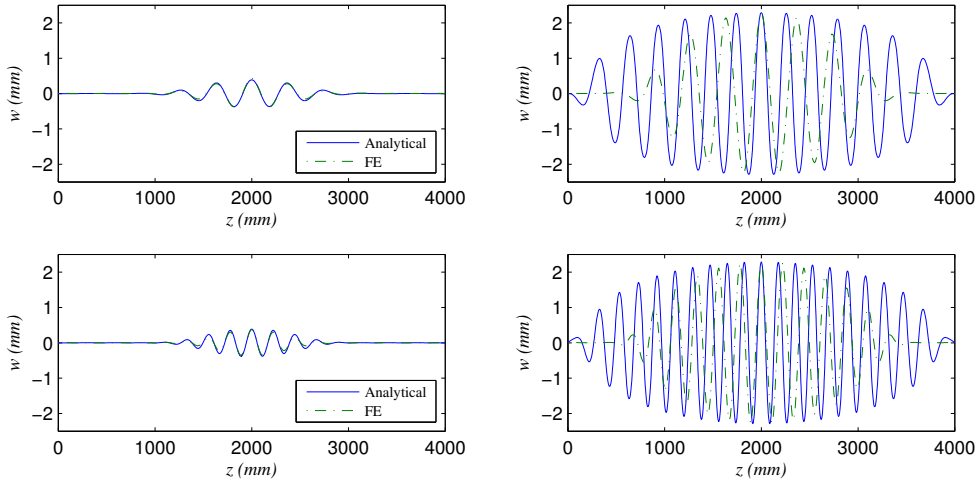

Figure 5.13: Comparisons of the numerical solutions from the analytical and the FE models for the local out-of-plane displacement, w for $\tilde{c} = 0.29$ and $\tilde{c} = 2.9$ in the top and the bottom rows, respectively. The left and the right columns correspond to the equilibrium states at $p = 0.99$ and $p = 0.74$, respectively.

$\tilde{c} = 2.9$, at approximately $p = 0.99$ and $p = 0.74$. It is observed in both cases that at $p = 0.99$, *i.e.* close to the secondary bifurcation point, the solutions for $w(z)$ are practically identical from the analytical and the FE models. At $p = 0.74$, shorter wavelengths are observed in the analytical model for both cases of $\tilde{c}$. Figure 5.14 shows the solutions of $w(z)$ for $\tilde{c} \to +\infty$. It is clear that the solutions for $w(z)$ from the two models are almost identical at the equilibrium state that is close to the secondary bifurcation point, where the wavelengths are approximately 166 mm in both models. As the buckling progresses, a reduction in the wavelength is observed in the analytical model whereas the wavelength in the FE model remains at a constant value. Comparing the wavelengths, Λ, at $p = 0.74$ for $\tilde{c} \to +\infty$, the values of the analytical model and the FE model are found to be 129 mm and 166 mm respectively. It is also observed that in the advanced post-buckling cases

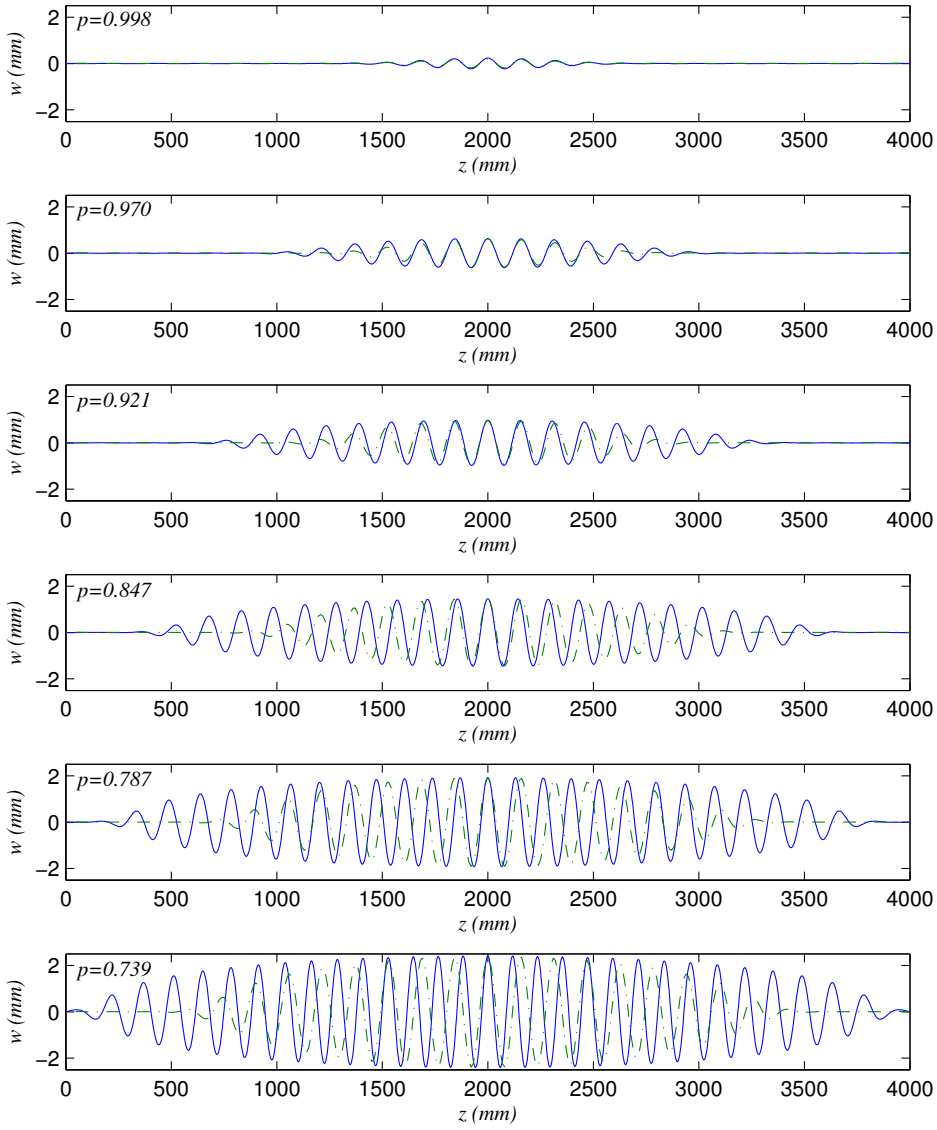

Figure 5.14: Comparisons of the numerical solutions of w for $\tilde{c} \to \infty$ at the same load level as the buckling progresses from the top to the bottom. The analytical model is shown as a solid line, with the ABAQUS model as a dot-dashed line.

the mode shape of w is more modulated in the FE model whereas it is more periodic with a more uniform amplitude for much of the strut length in the analytical model. The difference in the progression of the buckling mode shapes is indicated by the equilibrium path of $w_{\max}/t$ versus q_s as shown in Figure 5.12(c). For the same degree of lateral deflection, the FE model shows a larger maximum but a more modulated local out-of-plane deflection whereas the analytical model shows a smaller maximum but more periodic local out-of-plane deflection with most of the wave amplitudes closer to midspan being more uniform.

Figure 5.15 shows the comparison of a series of 3-dimensional representations of the deflected strut selected from both the analytical model and the FE model. It is observed that for the same degree of global deflection, the FE model always gives a lower bound estimation of the applied load. Similar trends were also observed for sandwich struts with different core bending models, where the analytical model and the numerical model were compared (Wadee *et al.*, 2010). The recent work on cold-formed stainless steel I-section columns (Becque, 2008) also showed a similar comparison between the numerical model and the experiments whereas the current approach correspondingly showed much better comparisons with experiments, as presented in Chapter 3. Furthermore, the changing wavelengths in the local buckling mode pattern was captured experimentally for various structural components such as I-section columns (Becque & Rasmussen, 2009b; Becque & Rasmussen, 2009a) and I-section beams under uniform bending (Wadee & Gardner, 2012). In the author's opinion, the fundamental physics of this system is better captured by the analytical model both qualitatively and quantitatively. It seems clear that for these local–global mode interaction problems that there is an increasing body of experimental evidence showing that the local buckling wavelength changes as the deformation increases, as the system proceeds along the equilibrium paths (Becque & Rasmussen,

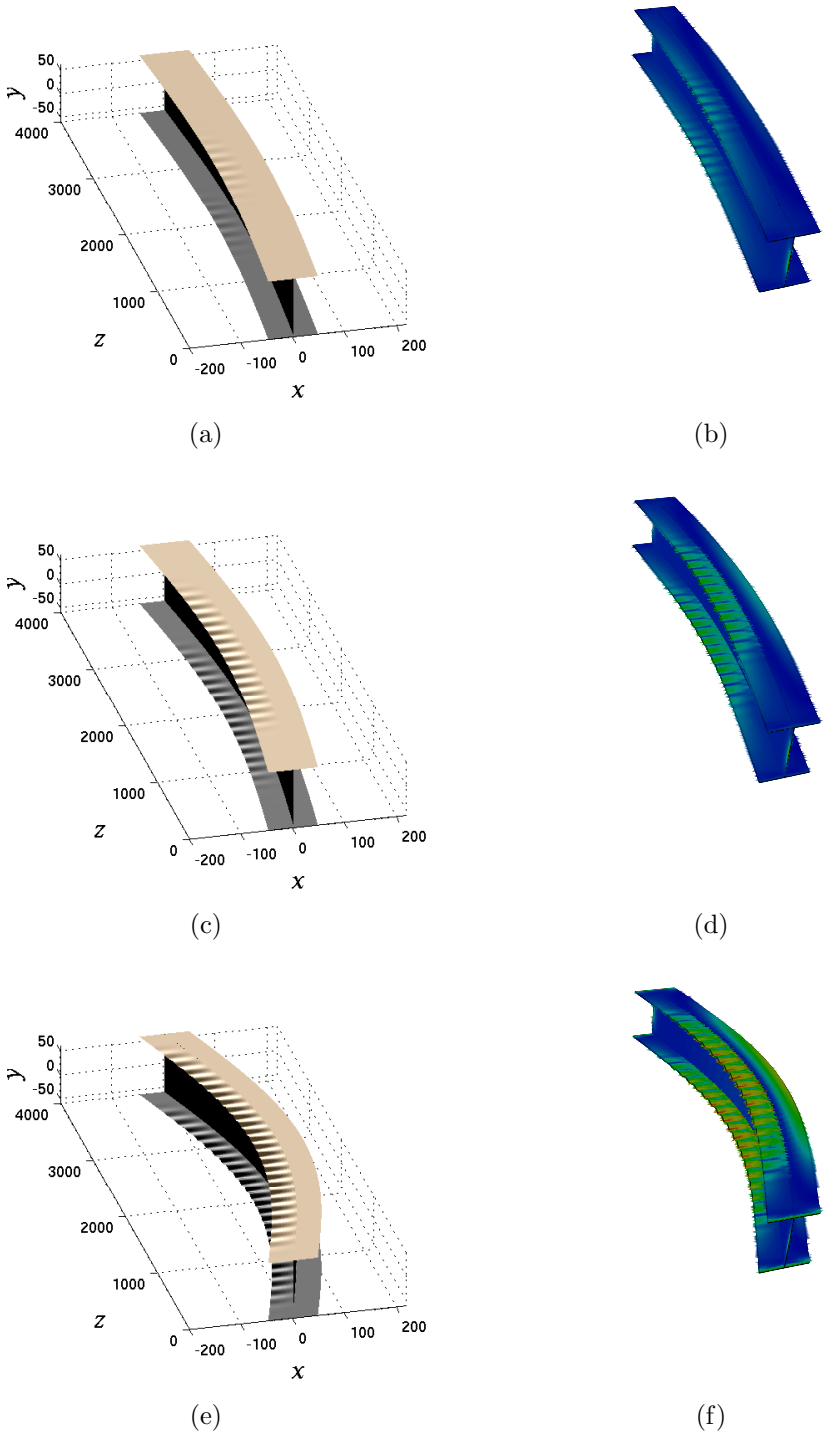

Figure 5.15: Comparisons of the numerical solutions for fully rigid flange–web connection ($\tilde{c} \to \infty$) visualized on 3-dimensional representations of the strut. The results are shown for equilibrium states at $q_s = 0.00585$, 0.00942 and 0.02408 from the top to the bottom row respectively. The left and the right columns are the results from the analytical model and the FE model respectively. All dimensions are in millimetres.

2009b; Becque & Rasmussen, 2009a; Wadee & Gardner, 2012; Wadee & Bai, 2014). There is also evidence that static FE programs find difficulty in modelling the behaviour of such wavelength changes using the standard method of using affine imperfections in both linear eigenmodes (Becque & Rasmussen, 2009b; Wadee & Bai, 2014) and that FE underestimates the post-buckling strength. However, the analytical approach that allows the system to determine its own post-buckling profile after interactive buckling has been triggered seems to be able to track the mechanical response of the physical experiments much better.

5.4.1 Future model enhancements

It seems that the standard method for performing post-buckling analysis using nonlinear FE methods, *i.e.* introducing a small amplitude of an eigenmode, fixes the local buckling wavelength throughout the loading history. This does not seem to match the results from physical experiments (Becque, 2008; Becque & Rasmussen, 2009a; Wadee & Gardner, 2012). A possible way to overcome this problem might be to utilize dynamic (explicit) analysis within ABAQUS, instead of the current Riks analysis, although a more intensive computational effort would be required. Furthermore, the analytical model could be extended to include the possibility of the local buckling in the web in combination with the flanges. With the particular section properties chosen currently, the local critical buckling load for the web is significantly higher than those for the global mode and the flange local mode; the contribution to the strain energies is very small and therefore neglected. However, with increasing local slenderness, the buckling in the web would become more likely and the load-carrying capacity would most likely be reduced.

5.5 Concluding remarks

The nonlinear analytical model for the perfect axially-loaded thin-walled I-section strut with a pinned joint between the section web and flanges has been extended to include a rotational spring between the web and flanges. Numerical examples with varying bending rigidities of the flange–web connection, focusing on the cases where global buckling is critical, are presented. Rapid erosion of the cellular buckling phenomenon is highlighted when the rigidity of the flange–web connection is increased. Finite element models were also developed for validation purposes; the results generally show very good comparisons between the two models particularly for pinpointing the onset of interactive buckling. However, the changing wavelength in the local buckling mode profile is not captured by the finite element model due to the introduced global and local imperfection seeming to fix the local buckling wavelength, which consequently results in the differences in the equilibrium paths as the post-buckling deformation progresses. Nevertheless, since the onset of the interactive buckling has been shown to be captured very well by the analytical model, a parametric study to investigate the practical implications can now be conducted with a degree of confidence.

Chapter 6

Parametric study

The previous chapters introduced variational models for axially compressed thin-walled I-section struts with a varying rigidity of the flange–web connection. The numerical examples, with the chosen section and material properties, focused on the cases where the critical loads for the global and the local buckling modes were sufficiently close where the interaction between the global and the local buckling modes was most likely to take place. The highly unstable post-buckling behaviour was revealed for all cases in the numerical examples, including the cellular and the non-cellular buckling behaviour for the cases where the flange–web connection was assumed to be a pin and fully rigid respectively. However, it was found in the classic work by van der Neut (1969) that the post-buckling behaviour may be approximately neutral, strongly stable or strongly unstable for varying strut length, assuming all other section properties remain constant. In the current chapter, it is therefore expected that with varying cross-section properties, the corresponding variation in global and local slenderness will result in different post-buckling behaviour, which needs to be investigated in detail.

A parametric study, to determine the effect of varying global and local slenderness is conducted with the aid of AUTO currently. The variation in the global and the local slenderness is achieved by varying the strut length and the width of the flange plate respectively. The present work focuses on the cases where the flange–web connection is assumed to be fully pinned or fully rigid, the boundary conditions for which the behaviour of the local buckling of the flange plate is well understood (Bulson, 1970). It is found that when the local critical buckling load is significantly higher than the global critical load, global buckling mode is dominant; conversely when the global critical load is significantly higher than the local critical load, the opposite is true. Under such conditions, there is practically no interaction between the global and the local buckling modes. On the other hand, within the defined interactive region, it is found that the strut exhibits post-buckling equilibrium paths with different characteristics, which are highlighted and discussed in detail. It should be stressed that all the calculations and numerical continuations are performed for elastic systems and that any plasticity effects would change the results. However, for the current case, the effects of plasticity would be negligible, an assertion that is justified later.

6.1 Review of the analytical models

6.1.1 Pinned flange–web connection

The parametric study is first carried out for the perfect system of a strut with a pinned flange–web connection. The coordinate system, section and material properties, global and local displacement functions are fully defined in Chapter 3. The current chapter uses the same definitions and notation. The same sets of governing equilibrium and

integral equations are used in the parametric study, and given by Equations (3.21)–(3.25). Note that the initial out-of-straightness coordinate, q_{s0} can be neglected from the original equations because only the perfect system is being considered. The expression for the global buckling critical load P_o^{C} is given by Equation (3.29). The critical stress for the local buckling σ_l^{C} is evaluated using the well-known plate buckling formula given by Equation (3.30); the local buckling critical load is thus:

$$P_l^{\mathrm{C}} = A\frac{kD\pi^2}{b^2 t}, \tag{6.1}$$

where A is the cross-section area. The coefficient k is approximately 0.426 for a long rectangular plate with three edges pinned and one edge free. It is clear that varying the strut length L only affects the global critical load P_o^{C}, whereas varying the flange width b affects both the global critical load P_o^{C} and the local critical load P_l^{C}. Note that for the section properties satisfying the condition: $P_l^{\mathrm{C}} < P_o^{\mathrm{C}}$, the full set of equilibrium equations are solved, whereas for $P_o^{\mathrm{C}} < P_l^{\mathrm{C}}$, equilibrium equations are solved for w_1 and u_1 only.

6.1.2 Rigid flange–web connection

The analytical model for the perfect system of the strut with a fully rigid flange–web connection was developed in Chapter 5. The current section will use the same definitions and notation for the coordinate system and the section properties. Since the local displacement functions w and u are only introduced in the vulnerable half of the flange, solving for the perfect system where local buckling is critical may be troublesome. Introducing an extra set of displacement functions in the non-vulnerable half of the flange causes computational difficulties for this particular case, where convergence problems often occurred after the second branch switch where global buckling is triggered. A significantly finer discretization and numerous numerical continuation attempts were required to overcome

this problem, which significantly increased the computational time. An alternative approach was used; this involved introducing a local imperfection in the vulnerable half of the flange only, which allows the break in symmetry from the beginning of each numerical continuation. The global mode was then triggered automatically due to the break in symmetry, as shown in Figure 4.3(b). The introduction of the local imperfection follows the same procedure established in Chapter 4. Recall Figure 4.2, the initial out-of-plane deflection, $w_0(x,z)$ has the form:

$$w_0(x,z) = f(x)A_0 \operatorname{sech}\left[\alpha\left(\frac{z}{L}-\frac{1}{2}\right)\right]\cos\left[\beta\pi\left(\frac{z}{L}-\frac{1}{2}\right)\right], \tag{6.2}$$

where $f(x)$ was given by Equation (5.5) and $z \in [0, L]$. Note that the transverse component of the initial out-of-plane deflection, $f(x)$ becomes the function for the rigid flange–web connection. The introduction of the local imperfection provides additional expressions to the local bending, membrane and shear strain energy functions, whereas the global bending energy U_{bo}, strain energy in the rotational spring U_{sp} and the work done $P\mathcal{E}$ remain the same as Equations (3.5), (5.13) and (3.15), respectively. Note also that the expressions for the global lateral deflection W and the rotation of the plane section θ are still given by Equation (3.1). The local displacement functions w and u are defined in Equations (5.4) and (3.3), respectively. The local bending energy U_{bl} accounting for both top and bottom flanges is thus:

$$\begin{aligned} U_{bl} = D\int_0^L \Big[&\{f^2\}_x (\ddot{w}-\ddot{w}_0)^2 + \{f''^2\}_x (w-w_0)^2 \\ &- 2\nu\{ff''\}_x (\ddot{w}w - \ddot{w}_0 w_0) + 2(1-\nu)\{f'^2\}_x (\dot{w}-\dot{w}_0)^2 \Big] \mathrm{d}z, \end{aligned} \tag{6.3}$$

where dots represent derivatives with respect to z as before; the braces with subscript x represent the integral with respect to x evaluated from $-b/2$ to 0. The membrane energy from the direct strain U_d accounting for both top and bottom flanges, including the initial

out-of-plane deflection is thus:

$$U_d = Etb\int_0^L \Bigg\{ \frac{b^2}{12} q_t^2 \frac{\pi^4}{L^2} \sin^2\frac{\pi z}{L} + \frac{1}{6}\dot{u}^2 + \frac{\{f^4\}_x}{4b}\left(\dot{w}^2 - \dot{w}_0^2\right)^2 - \frac{1}{2}\Delta\dot{u} - \frac{\{f^2\}_x}{b}\Delta\left(\dot{w}^2 - \dot{w}_0^2\right) \\ - q_t\frac{b\pi^2}{6L}\sin\frac{\pi z}{L}\left[\dot{u} - \frac{6\{xf^2\}_x}{b^2}\left(\dot{w}^2 - \dot{w}_0^2\right)\right] - \frac{2\{xf^2\}_x}{b^2}\dot{u}\left(\dot{w}^2 - \dot{w}_0^2\right) + \left(1 + \frac{h}{b}\right)\Delta^2 \Bigg\}\mathrm{d}z. \tag{6.4}$$

The membrane energy from the shear strain, U_s accounting for both top and bottom flanges, including the initial out-of-plane deflection is:

$$U_s = Gtb\int_0^L \Bigg\{ \left(q_s - q_t\right)^2 \pi^2 \cos^2\frac{\pi z}{L} + \frac{2}{b^2}\Bigg[u^2 + \frac{b}{2}\{f'^2 f^2\}_x \left(\dot{w}w - \dot{w}_0 w_0\right)^2 \\ - 2\{f'f\}_x u\left(\dot{w}w - \dot{w}_0 w_0\right)\Bigg] - \frac{2}{b}\left(q_s - q_t\right)\pi\cos\frac{\pi z}{L}\Bigg[u - \{f'f\}_x\left(\dot{w}w - \dot{w}_0 w_0\right)\Bigg]\Bigg\}\mathrm{d}z. \tag{6.5}$$

The total potential energy, V is thus:

$$V = U_{bo} + U_{bl} + U_m + U_{sp} - P\mathcal{E}. \tag{6.6}$$

The derivation of the governing equilibrium and integral equations follows the same procedure established in Chapters 3–4. The non-dimensional differential equations for w and u are thus:

$$\begin{aligned} &\ddot{\tilde{w}} - \frac{b^2\phi^2}{2\{f^2\}_x}\left[\nu\left(\{ff''\}_x - \{f'^2\}_x\right) + \{f'^2\}_x\right]\tilde{\ddot{w}} + \frac{b^4\phi^4}{16}\frac{\{f''^2\}_x}{\{f^2\}_x}\tilde{w} \\ &\quad - \frac{\tilde{G}\phi^2\tilde{w}}{16\{f^2\}_x}\Bigg[b^2\{f'^2f^2\}_x\left(\tilde{\ddot{w}}^2 + \tilde{w}\tilde{\ddot{w}}\right) - 2b\{f'f\}_x\tilde{\ddot{u}} + \frac{b\pi^2\{f'f\}_x}{\phi}\left(q_s - q_t\right)\sin\frac{\pi\tilde{z}}{2}\Bigg] \\ &\quad - \frac{\tilde{D}}{8\{f^2\}_x}\Bigg[3\{f^4\}_x\tilde{\ddot{w}}^2\tilde{\ddot{w}} - \frac{4\{xf^2\}_x}{b}\left(\tilde{\ddot{u}}\tilde{\ddot{w}} + \tilde{\ddot{u}}\tilde{\ddot{w}}\right) - 2\{f^2\}_x\tilde{\ddot{w}}\Delta \\ &\quad + \frac{2\pi^2\{xf^2\}_x}{b\phi}q_t\left(\sin\frac{\pi\tilde{z}}{2}\tilde{\ddot{w}} + \frac{\pi}{2}\cos\frac{\pi\tilde{z}}{2}\tilde{\ddot{w}}\right)\Bigg] \\ &\quad = \ddot{\tilde{w}}_0 - \frac{b^2\phi^2}{2\{f^2\}_x}\left[\nu\left(\{ff''\}_x - \{f'^2\}_x\right) + \{f'^2\}_x\right]\tilde{\ddot{w}}_0 + \frac{b^4\phi^4}{16}\frac{\{f''^2\}_x}{\{f^2\}_x}\tilde{w}_0 \\ &\qquad - \frac{\tilde{G}\phi^2 b^2\{f'^2f^2\}_x\tilde{w}}{16\{f^2\}_x}\left(\tilde{\ddot{w}}_0\tilde{w}_0 + \tilde{\ddot{w}}_0{}^2\right) - \frac{\tilde{D}\{f^4\}_x\tilde{\ddot{w}}_0}{8\{f^2\}_x}\left(\tilde{\ddot{w}}\tilde{\dot{w}}_0 + 2\tilde{\dot{w}}\tilde{\ddot{w}}_0\right), \end{aligned} \tag{6.7}$$

$$\begin{aligned} &\tilde{\ddot{u}} - \frac{12\{xf^2\}_x}{b^2}\tilde{\dot{w}}\tilde{\ddot{w}} - q_t\frac{\pi^3}{4\phi}\cos\frac{\pi\tilde{z}}{2} - \frac{3\tilde{G}\phi^2}{\tilde{D}}\Bigg[\tilde{u} - \{f'f\}_x\tilde{w}\tilde{\dot{w}} - \left(q_s - q_t\right)\frac{\pi}{\phi}\cos\frac{\pi\tilde{z}}{2}\Bigg] \\ &\quad = \frac{3\tilde{G}\phi^2}{\tilde{E}}\{f'f\}_x\tilde{w}_0\tilde{\dot{w}}_0 - \frac{12\{xf^2\}_x}{b^2}\tilde{\dot{w}}_0\tilde{\ddot{w}}_0, \end{aligned} \tag{6.8}$$

The non-dimensional integral conditions are:

$$\begin{aligned}
\frac{\partial V}{\partial q_s} &= \pi^2 q_s + \tilde{s}\left(q_s - q_t\right) - \frac{PL^2}{EI_w} q_s - \frac{\tilde{s}\phi}{\pi}\int_0^1 \cos\frac{\pi\tilde{z}}{2}\left[\{f'f\}_x\left(\tilde{w}\tilde{\dot{w}} - \tilde{w}_0\tilde{\dot{w}}_0\right) + \tilde{u}\right]\mathrm{d}\tilde{z} = 0,\\
\frac{\partial V}{\partial q_t} &= \pi^2 q_t - \tilde{t}\left(q_s - q_t\right) + \phi\int_0^1 \left\{\frac{\tilde{t}}{\pi}\cos\frac{\pi\tilde{z}}{2}\left[\{f'f\}_x\left(\tilde{w}\tilde{\dot{w}} - \tilde{w}_0\tilde{\dot{w}}_0\right) + \tilde{u}\right]\right.\\
&\qquad \left. - \sin\frac{\pi\tilde{z}}{2}\left[2\tilde{\dot{u}} - \frac{12\{xf^2\}_x}{b^2}\left(\tilde{\dot{w}}^2 - \tilde{\dot{w}}_0^2\right)\right]\right\}\mathrm{d}\tilde{z} = 0,\\
\frac{\partial V}{\partial \Delta} &= \int_0^1 \left[2\left(1 + \frac{h}{b}\right)\Delta - \frac{1}{2}\tilde{\dot{u}} - \frac{\{f^2\}_x}{b}\left(\tilde{\ddot{w}}^2 - \tilde{\ddot{w}}_0^2\right) - \frac{P}{Etb}\right]\mathrm{d}\tilde{z} = 0.
\end{aligned} \tag{6.9}$$

The boundary conditions for $\tilde{w}$ and $\tilde{u}$ and their derivatives are for pinned end conditions for $\tilde{z} = 0$ and for symmetry at $\tilde{z} = 1$, given by Equation (5.18). The boundary condition from matching the in-plane strain becomes:

$$\frac{1}{3}\tilde{\dot{u}}(0) - \frac{2\{xf^2\}_x}{b^2}\left[\tilde{\dot{w}}^2(0) - \tilde{\dot{w}}_0^2(0)\right] - \frac{1}{2}\Delta + \frac{P}{2Etb} = 0. \tag{6.10}$$

The local critical buckling load is determined using Equation (6.1), where the coefficient k is approximately 1.25 for a rectangular plate with one longitudinal edge fixed and the other being free. For the section properties satisfying the condition: $P_l^{\mathrm{C}} < P_o^{\mathrm{C}}$, the equilibrium equations with local imperfections are solved, whereas for $P_o^{\mathrm{C}} < P_l^{\mathrm{C}}$, equilibrium equations are solved for the perfect system. The amplitude of the initial out-of-plane deflection is kept at a constant value of approximately $0.01t$, where t is the thickness of the flange plate. This value is sufficiently small such that the near perfect system is analysed.

6.2 Solution strategy

6.2.1 Variation in strut length

The investigation begins with varying the global slenderness λ_o, where $\lambda_o = L/r$ with r being the radius of gyration of the cross-section, which is a length scale defined as a

quantity essentially being a ratio of the flexural to the axial stiffness where $r^2 = I/A$. In this case, $I = I_{yy}$, the second moment of area of the cross-section about the weak axis (Trahair *et al.*, 2008). The strut length L is principally changed while all other section properties are kept constant and given in Table 6.1. Theoretical values of the global and

Flange width b	96 mm
Flange thickness t	1.2 mm
Section depth h	120 mm
Section area A	513 mm^2
Young's modulus E	210 kN/mm^2
Poisson's ratio ν	0.3

Table 6.1: Cross-section and material properties. Recall that the thickness of the web $t_w = 2t$.

local critical loads are determined using Equations (3.29) and (6.1) respectively. A critical strut length, denoted as L_c is determined when $P_o^{\mathrm{C}} = P_l^{\mathrm{C}}$. Numerical continuations are first conducted with the strut length L being in the vicinity of L_c. It is obvious that, with such a condition, the secondary instability will be triggered almost simultaneously with the primary instability. Increasing the strut length implies that the global critical load P_o^{C} decreases; global buckling becomes critical and the secondary instability would be triggered at a larger value of q_s. With P_l^{C} being significantly larger than P_o^{C}, it is expected that the flange plates would not buckle until a significant amount of global buckling deflection has developed. In those situations, problems such as plastic deformation may have taken place before any interactive buckling. The current work considers an arbitrary value of $L/500$ as a large global lateral deflection; therefore cases where $q_s > 0.002$ at the secondary bifurcation are considered to be equivalent to no mode interaction. The strut length, where $q_s = 0.002$ at the secondary bifurcation, is determined and denoted as L_o. The interactive region where global buckling is critical is therefore $L_c < L < L_o$, which is illustrated diagrammatically in Figure 6.1(a). The load carrying capacity P_U – determined by the global critical load P_o^{C} for cases where global buckling is critical – and the post-buckling behaviour are studied for the interactive region: $L_c < L < L_o$. Note

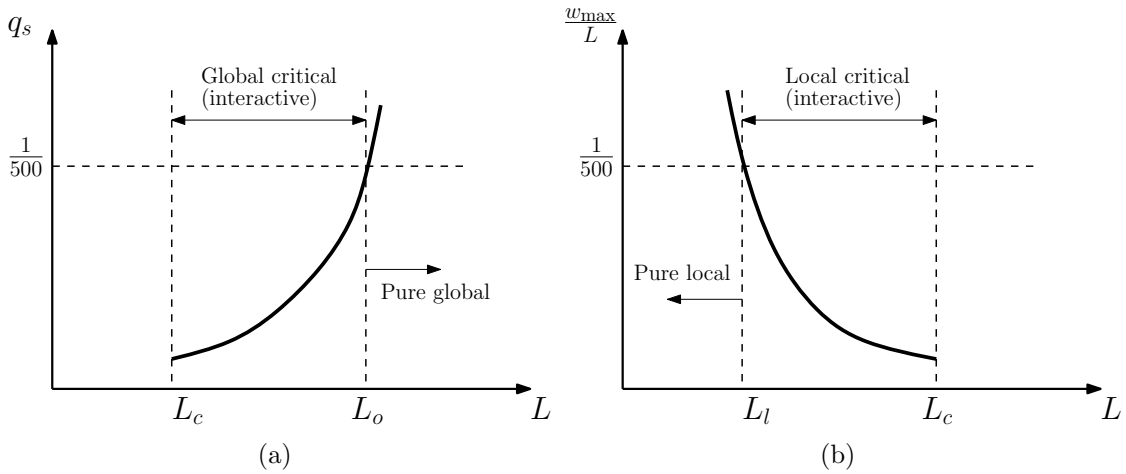

Figure 6.1: Solution strategy for varying the strut length L. The definition $L = L_c$ when $P_l^{\mathrm{C}} = P_o^{\mathrm{C}}$, whereas struts with $L > L_o$ and $L < L_l$ are assumed to exhibit pure global buckling and pure local buckling respectively.

that the value of $L/500$, chosen arbitrarily in the current study, is used as an imperfection for the manufacturing tolerance of cold-formed sections (Saito & Wadee, 2009); adjusting this value changes the range where interactive buckling is most significant. Of course, currently, the aforementioned $L/500$ deflection would be in addition to any imposed initial imperfection.

Conversely, decreasing the strut length implies that the local buckling becomes critical. Since the post-buckling characteristic of the flange plates is stable, the load increases as the local deflection progresses. It has been demonstrated, in the numerical example in Chapter 3, that the system exhibits an unstable interactive post-buckling path after the peak load P_U is reached. A similar hypothesis is used for the maximum local out-of-plane deflection $w_{\max}$ at the peak load, which is illustrated diagrammatically in Figure 6.1(b). Although the limit of $w_{\max}/L$ is set also to $L/500$ currently, this again is chosen arbitrarily. It is considered that the strut with $L < L_l$ exhibits pure local buckling, whereas the interactive region where local buckling is critical lies in the range: $L_l < L < L_c$. The load carrying capacity P_U is determined numerically. The same approach is applied to both

cases where the flange–web connection is pinned and rigid.

6.2.2 Variation in flange width

A similar approach is applied to vary the local slenderness λ_l, where $\lambda_l = b/(2t)$. The flange width b is principally varied; the flange thickness t, the strut length L are kept constant, as given in Table 6.2. For the given strut length, the critical flange width b_c

Strut length L	2150 mm
Flange thickness t	1.2 mm
Section depth h	120 mm
Young's modulus E	210 kN/mm^2
Poisson's ratio ν	0.3

Table 6.2: Geometric and material properties. The flange width b is varied, implying that the section area A and the minor-axis second moment of area I_{yy} are varied accordingly.

is determined when $P_o^{\mathrm{C}} = P_l^{\mathrm{C}}$. Increasing b implies that P_l^{C} would decrease whereas P_o^{C} would increase, due to the increase in the minor-axis second moment of area I_{yy}; the local buckling of the flange plates would therefore be critical. The same hypothesis, as for the cases where the strut length is varied, is applied and shown in Figure 6.2(a). It is considered that the flange with $b > b_l$ exhibits pure local buckling, whereas the interactive region where local buckling is critical is given by $b_c < b < b_l$. Conversely, decreasing b below b_c implies that P_l^{C} would increase whereas P_o^{C} will decrease; global buckling would therefore be critical. Figure 6.2(b) shows the interactive region for b where global buckling is critical. Struts with a flange width smaller than b_o are considered to exhibit a purely global mode with no interactive buckling.

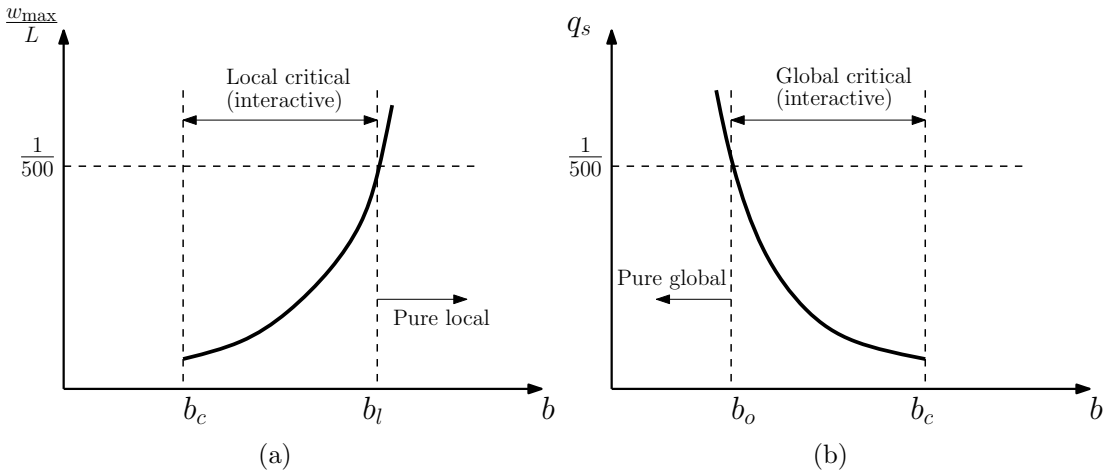

Figure 6.2: Solution strategy for varying the strut length b. The definition $b = b_c$ when $P_l^{\mathrm{C}} = P_o^{\mathrm{C}}$, whereas struts with $b < b_o$ and $b > b_l$ are assumed to exhibit pure global buckling and pure local buckling respectively.

6.2.3 Buckling strength curves

It is well-known that the failure mechanisms are governed by buckling and plasticity, for slender and stocky columns, respectively. First, consider the idealized buckling design curve for perfect columns in terms of the failure stress σ_f versus the global and local slenderness, λ_o and λ_l shown in Figure 6.3(a) and (b), respectively. The value of the

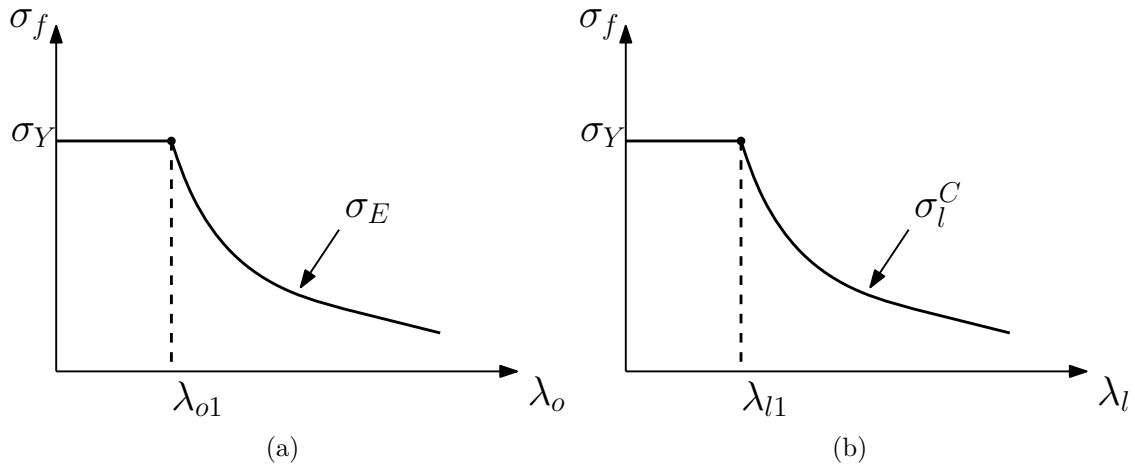

Figure 6.3: The idealized design curve in terms of the failure stress σ_f versus (a) the global slenderness (λ_o) and (b) the local slenderness (λ_l). Parameters λ_{o1} and λ_{l1} are the global and the local slendernesses when $\sigma_Y = \sigma_E$ and $\sigma_Y = \sigma_l^C$, respectively.

yield stress σ_Y varies depending on the grade of the steel, but a high strength steel with $\sigma_Y = 460$ kN/mm is considered in the current study, which is a commonly used value for light-gauge cold worked steel. Recall that $I/A = r^2$ and $L/r = \lambda_o$; the Euler stress can be expressed in terms of λ_o, thus:

$$\sigma_E = \frac{\pi^2 E}{\lambda_o^2}, \tag{6.11}$$

denoting λ_{o1} as the value of λ_o when $\sigma_E = \sigma_Y$, and after a bit of manipulation, the following is obtained:

$$\lambda_{o1} = \pi\sqrt{\frac{E}{\sigma_Y}}. \tag{6.12}$$

A normalized stress $\bar{\sigma}_o$ and a normalized global slenderness $\bar{\lambda}_o$ are defined as σ_f/σ_Y and λ_o/λ_{o1} respectively; a relationship between $\bar{\sigma}_o$ and $\bar{\lambda}_o$ can then be obtained for the elastic global buckling curve, thus:

$$\bar{\sigma}_o = (\bar{\lambda}_o)^{-2}, \tag{6.13}$$

where $\bar{\lambda}_o$ is given by the following expression:

$$\bar{\lambda}_o = \frac{\lambda_o}{\lambda_{o1}} = \frac{L}{r}\left[\frac{1}{\pi}\sqrt{\frac{\sigma_Y}{E}}\right]. \tag{6.14}$$

A normalized local slenderness $\bar{\lambda}_l$ is derived by following a practically identical procedure as for $\bar{\lambda}_o$, by taking the plate buckling stress σ_l^{C} given in Equation (3.30) and finding λ_{l1} for the case where $\sigma_l^{\mathrm{C}} = \sigma_Y$ and so on (Trahair *et al.*, 2008), thus:

$$\bar{\lambda}_l = \frac{b}{2t}\left[\frac{1}{\pi}\sqrt{\frac{\sigma_Y}{E}}\right]\left[\frac{12(1-\nu^2)}{k}\right]^{1/2}, \tag{6.15}$$

and the elastic local buckling curve becomes: $\bar{\sigma}_l = (\bar{\lambda}_l)^{-2}$. The idealized buckling design curves are therefore plotted in terms of the nondimensional stress and slenderness, as sketched in Figure 6.4. It is clear that for $\bar{\lambda}_x > 1$, where $x = \{o, l\}$, columns are slender and elastic buckling dominates; but for $\bar{\lambda}_x < 1$, columns are stocky and plasticity dominates. Moreover, if $\bar{\lambda}_x \gg 1$, the elastic buckling load is approximately the ultimate load and plasticity effects are negligible. In the following section, numerical examples are presented

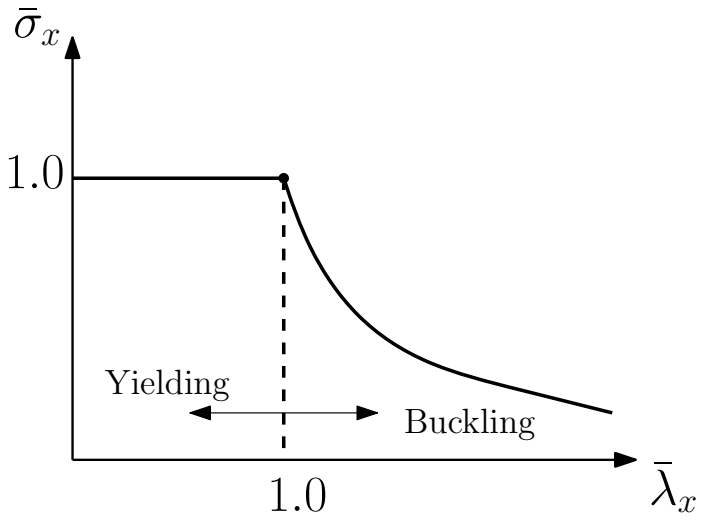

Figure 6.4: The idealized strength curve in terms of the normalized stress at failure $\bar{\sigma}_x$ versus the normalized global and local slendernesses $\bar{\lambda}_x$, where $x = \{o, l\}$.

for an example set of strut lengths and flange widths; the corresponding normalized slendernesses are calculated using Equations (6.14) and (6.15) respectively.

6.3 Numerical results and discussion

6.3.1 Pinned flange–web connection

Numerical continuations are first carried out in AUTO for the strut with a pinned joint between the section web and flanges. The effect of varying the strut length L is first examined. It is observed in Figure 6.5 that for the particular properties given in Table 6.1, struts with lengths between $L_l = 2295$ mm and $L_o = 5842$ mm are most vulnerable to interactive buckling, whereas struts with $L < L_l$ and $L > L_o$ are vulnerable to the pure local buckling and the pure global buckling respectively. The critical strut length L_c when $P_o^{\mathrm{C}} = P_l^{\mathrm{C}}$ is found to be approximately 3740 mm by both the theoretical expressions and the numerical solution. Figure 6.6 shows the load-carrying capacity P_U versus L. It

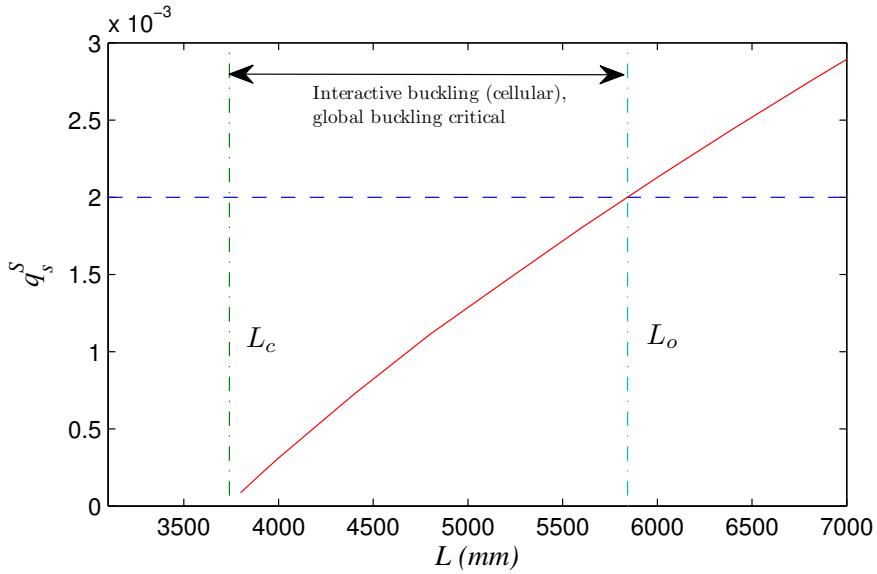

(a)

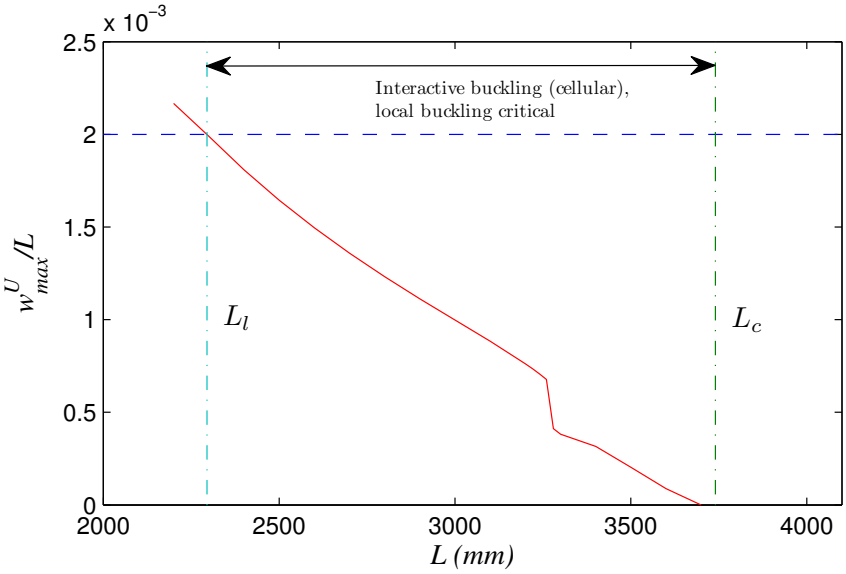

(b)

Figure 6.5: Graphs show (a) the normalized lateral displacement at the secondary bifurcation point q_s^{S} and (b) the normalized maximum local out-of-plane displacement $w^U_{\max}/L$ at the ultimate load P_U, versus the strut length L, for the cases where the global buckling and the local buckling are critical, respectively. The vertical dot-dashed line with label L_c represents the critical strut length where $P_o^{\mathrm{C}} = P_l^{\mathrm{C}}$. The horizontal dashed line represents the amount of displacement, above which interactive buckling is assumed to be insignificant; the interactive region is therefore $L_l < L < L_o$, as shown by the vertical dot-dashed lines.

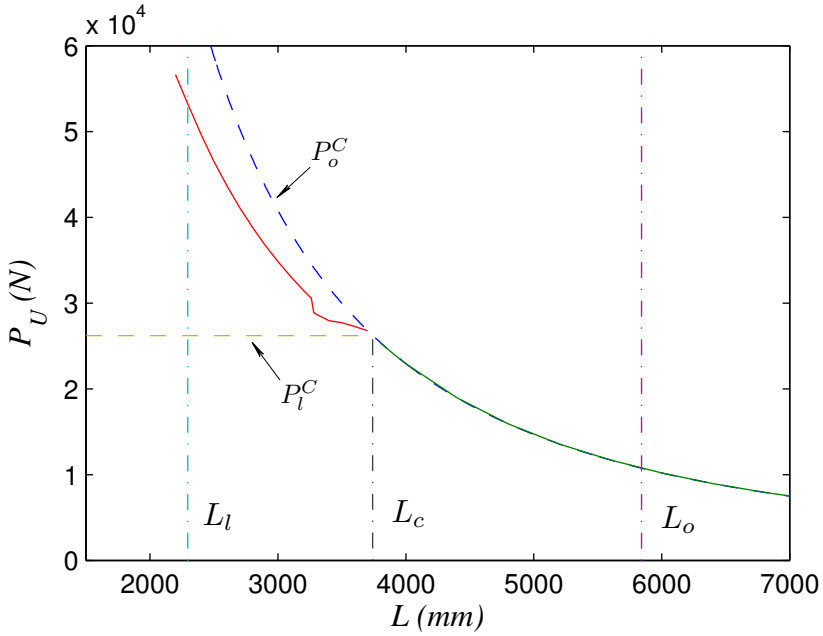

Figure 6.6: The graph shows the ultimate load P_U versus the strut length L. The solid line represents the actual numerical solutions whereas the dashed lines represent the theoretical calculations of the global and local critical loads. Note that the local critical load is independent of the strut length and is therefore represented by the horizontal dashed line. The vertical dot-dashed lines represent lengths L_l, L_c and L_o directly corresponding to Figure 6.5.

is observed that for $L_c < L < L_o$ where global buckling is critical, $P_U = P_o^{\mathrm{C}}$ since the global buckling is only weakly stable, whereas the interactive buckling behaviour, after the secondary instability (for local buckling) is triggered, is highly unstable. For $L_l < L < L_c$ on the other hand, the load-carrying capacity P_U is capable of reaching a higher value than the local critical load P_l^{C}, due to the stable post-buckling behaviour of the flange plates. However, the load is not able to reach the global critical load P_o^{C} due to the mode interaction after the secondary instability (for global buckling) is triggered. Figure 6.6 is transformed, in a similar way as the classic work by van der Neut (1969), into the central graph of Figure 6.7, which shows P_U/P_l^{C} versus $P_o^{\mathrm{C}}/P_l^{\mathrm{C}}$ for varying L. The graphs surrounding the main one show examples of the actual equilibrium paths for different strut lengths corresponding to different parts of the central graph, indicated by the arrows. It is observed that for $L > L_o$, the strut exhibits pure global buckling that is weakly stable after the critical bifurcation point. For $L_c < L < L_o$, the strut exhibits a weakly stable equilibrium path after the critical bifurcation point, followed by an unstable interactive post-buckling path after the secondary bifurcation point. For $L \approx L_c$, the global and the local buckling modes are triggered practically simultaneously; and the strut exhibits an unstable interactive post-buckling path. For $L_l < L < L_c$, the strut exhibits a stable equilibrium path after the critical bifurcation point, followed by an unstable interactive post-buckling path after the secondary bifurcation point. Finally for $L < L_l$, the strut exhibits pure local buckling of the flange plates that is strongly stable. Note that for $L_l < L < L_o$, all equilibrium paths exhibit the sequential snap-backs signifying cellular buckling behaviour.

With the section properties given in Table 6.2 and L being fixed, the numerical continuations are carried out for the varying flange width b. Figures 6.8, 6.9 and 6.10 correspond to Figures 6.5, 6.6 and 6.7, for varying b, respectively. It is observed in Figure 6.8 that

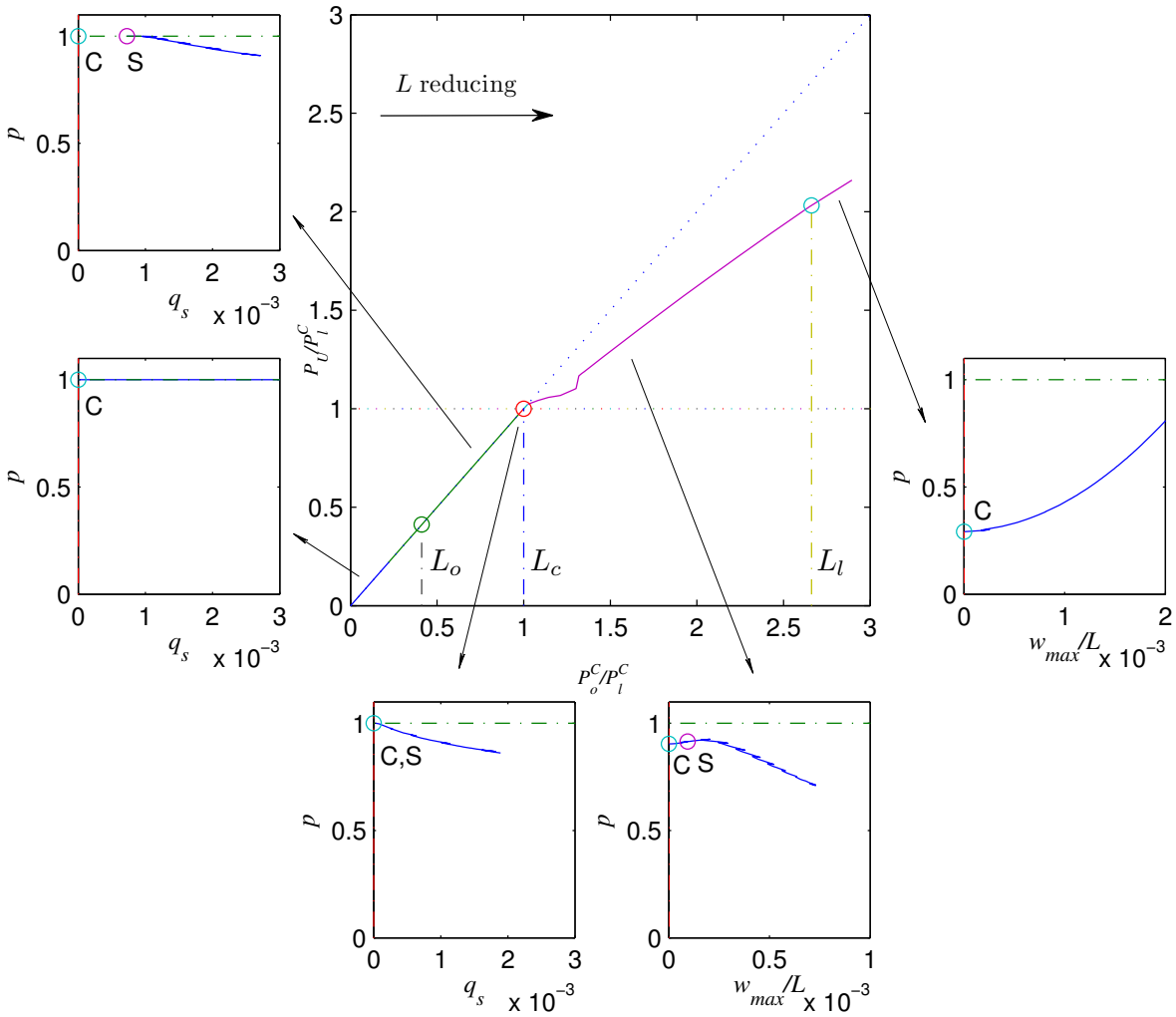

Figure 6.7: The central graph shows the normalized ultimate load P_U/P_l^{C} versus the normalized global critical load $P_o^{\mathrm{C}}/P_l^{\mathrm{C}}$. The solid line represents the actual numerical solutions whereas the dot-dashed lines representing L_l, L_c and L_o correspond directly to Figure 6.6. The surrounding graphs show examples of the equilibrium paths corresponding to the different parts of the central graph, separated by the dot-dashed lines. Labels C and S correspond to the primary and the secondary bifurcation points.

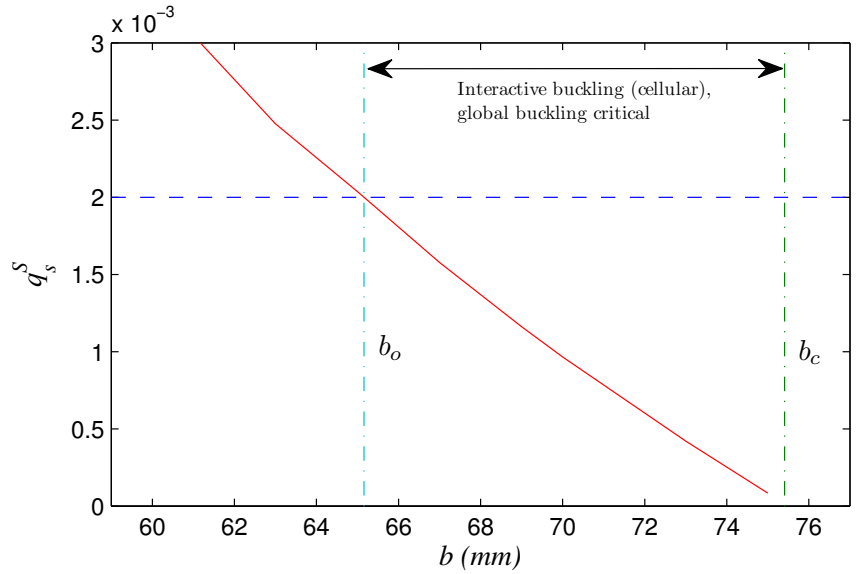

(a)

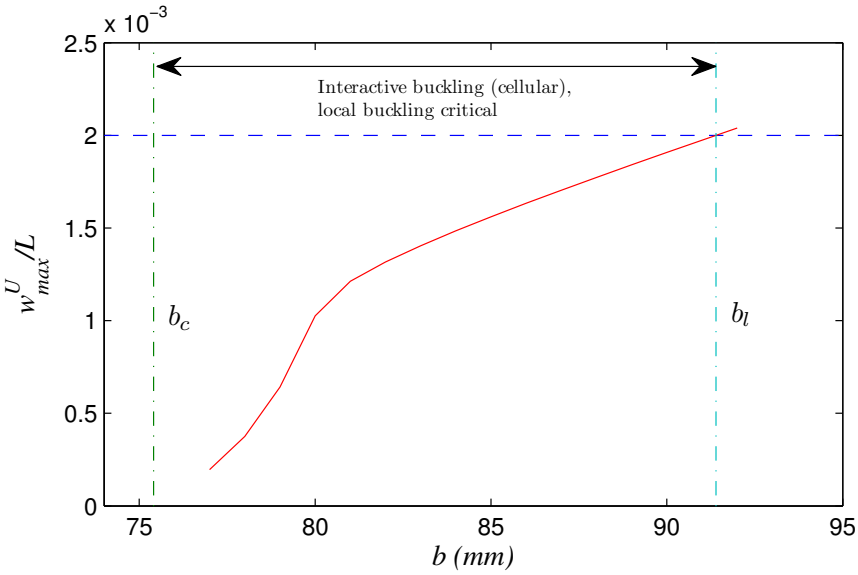

(b)

Figure 6.8: Graphs show (a) the normalized lateral displacement at the secondary bifurcation point q_s^{S} and (b) the normalized maximum local out-of-plane displacement $w_{\max}^U/L$ at the ultimate load P_U, versus the flange width b, for the cases where the global buckling and the local buckling are critical, respectively. The vertical dot-dashed line with label b_c represents the critical flange width when $P_o^{\mathrm{C}} = P_l^{\mathrm{C}}$. The horizontal dashed line represents the amount of displacement, above which interactive buckling is assumed to be insignificant; the interactive region is therefore $b_o < b < b_l$, as shown by the vertical dot-dashed lines.

flanges with widths between $b_o = 65$ mm and $b_l = 91$ mm are most vulnerable to the interactive buckling behaviour, whereas flanges with $b > b_l$ and $b < b_o$ are only vulnerable to pure local buckling and pure global buckling respectively. The critical flange width b_c when $P_o^{\mathrm{C}} = P_l^{\mathrm{C}}$ is found to be approximately 75 mm by both the theoretical expressions and the numerical solution. Figure 6.9 shows the load-carrying capacity P_U versus

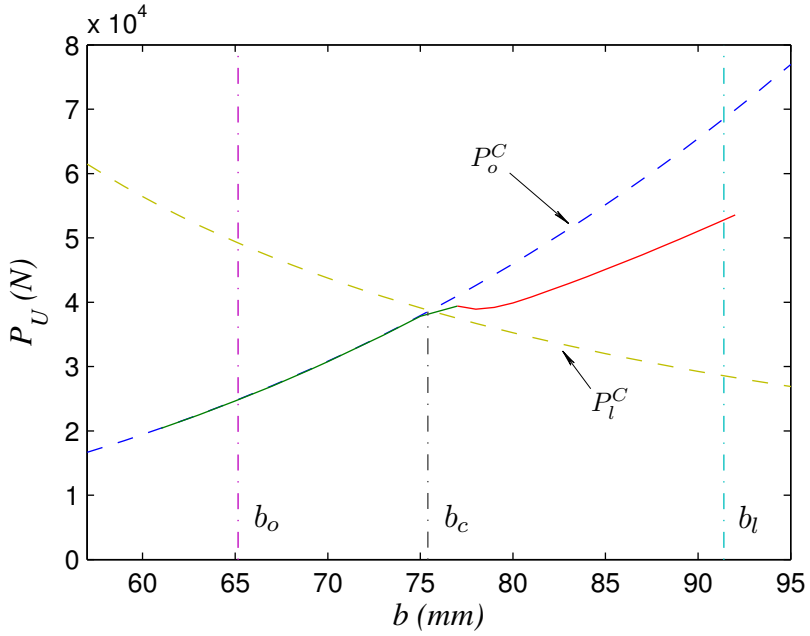

Figure 6.9: The graph shows the ultimate load P_U versus the flange width b. The solid line represents the actual numerical solutions whereas the dashed lines represent the theoretical calculations of the global and local critical loads. Note that increasing b implies that the local critical load decreases whereas the global critical load increases. The vertical dot-dashed lines represent b_l, b_c and b_o directly corresponding to Figure 6.8.

b. It is observed that for $b_o < b < b_c$ where global buckling is critical, $P_U = P_o^{\mathrm{C}}$ since the post-buckling behaviour is only weakly stable, whereas the interactive buckling behaviour, after the secondary instability (for local buckling) is triggered, is highly unstable. For $b_c < b < b_l$, the load-carrying capacity P_U always reaches a value that is higher than the local critical load P_l^{C}, due to the stable post-buckling behaviour of the flange plates, but is not able to reach the global critical load P_o^{C} due to the mode interaction after the secondary instability (for global buckling) is triggered. Figure 6.10 shows a plot of P_U/P_l^{C}

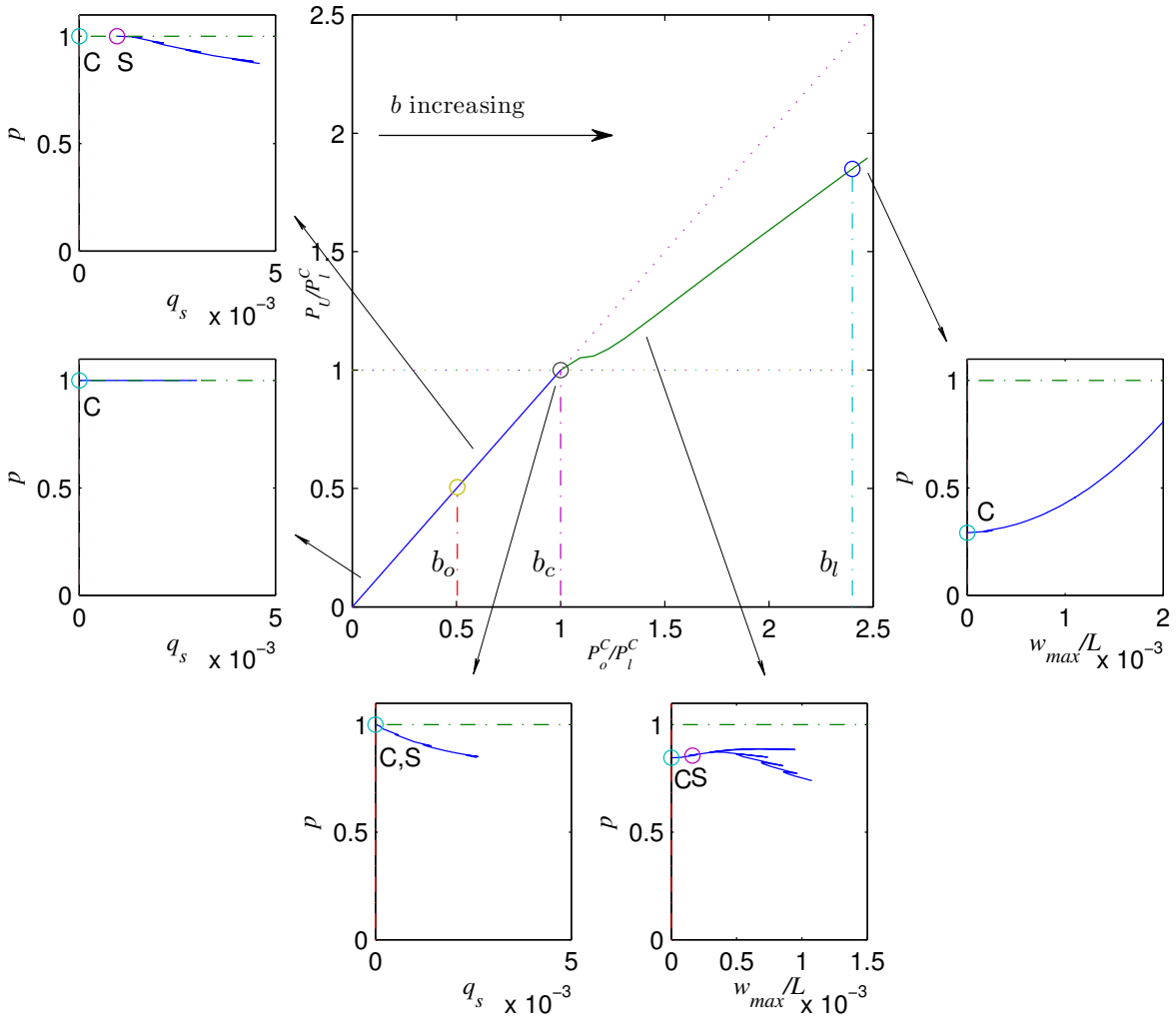

Figure 6.10: The central graph shows the normalized ultimate load P_U/P_l^{C} versus the normalized global critical load $P_o^{\mathrm{C}}/P_l^{\mathrm{C}}$. The solid line represents the actual numerical solutions whereas the dot-dashed lines representing b_l, b_c and b_o correspond directly to Figure 6.9. The surrounding graphs show examples of the equilibrium paths corresponding to the different parts of the central graph, separated by the dot-dashed lines. Labels C and S correspond to the primary and the secondary bifurcation points.

versus $P_o^{\mathrm{C}}/P_l^{\mathrm{C}}$ for varying b and examples of the actual equilibrium paths for different ranges of b are shown. It is observed that for $b < b_o$, the strut exhibits pure global buckling that is weakly stable, after the critical bifurcation point. For $b_o < b < b_c$, the strut exhibits a weakly stable equilibrium path after the critical bifurcation point, followed by an unstable interactive post-buckling path after the secondary bifurcation point. For $b \approx b_c$, the global and the local buckling modes are triggered practically simultaneously and the strut exhibits an unstable interactive post-buckling path. For $b_c < b < b_l$, the strut exhibits a stable equilibrium path after the critical bifurcation point, followed by an unstable interactive post-buckling path after the secondary bifurcation point. Finally for $b > b_l$, the strut exhibits pure local buckling of the flange plates that is strongly stable. It is worth noting again that all equilibrium paths exhibit cellular buckling behaviour within the interactive region.

6.3.2 Fully rigid flange–web connection

In this section, numerical continuations are carried out for the struts with fully rigid joints between the section web and flanges. The strut length L is first varied with the section properties given in Table 6.1. Figures 6.11, 6.12 and 6.13 correspond to Figures 6.5, 6.6 and 6.7, for the fully rigid flange–web connection, respectively. It is observed in Figure 6.11 that struts with lengths between $L_l = 1610$ mm and $L_o = 2680$ mm are most vulnerable to the interactive buckling behaviour, whereas struts with $L < L_l$ and $L > L_o$ are vulnerable to the pure local buckling and the pure global buckling respectively. The critical strut length L_c, when $P_o^{\mathrm{C}} = P_l^{\mathrm{C}}$, is found to be approximately 2185 mm by both the theoretical expressions and the numerical solution. Figure 6.12 shows a very similar trend as in Figure 6.6. However, one distinctive feature is that for 1800 mm $< L <$ 2300 mm, the ultimate load P_U is very close to the local buckling critical load P_l^{C} whereas P_U only starts

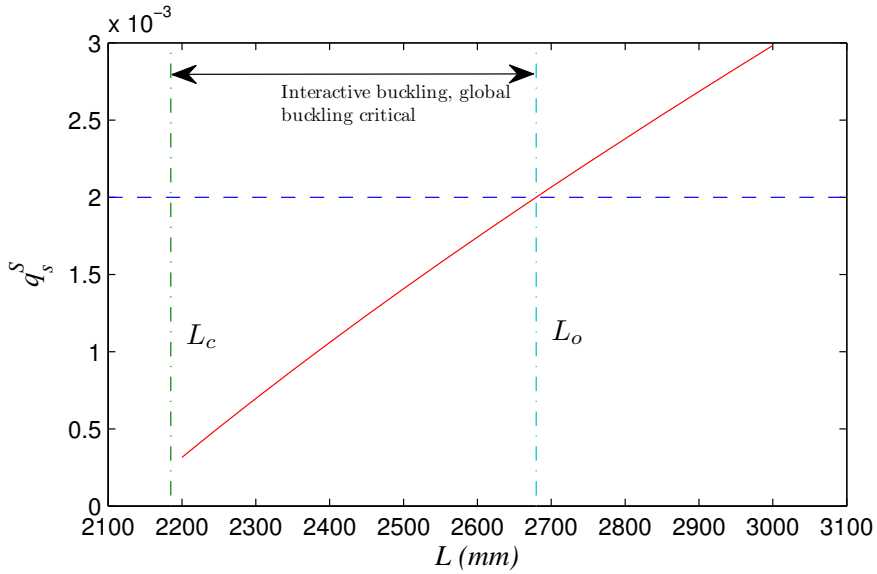

(a)

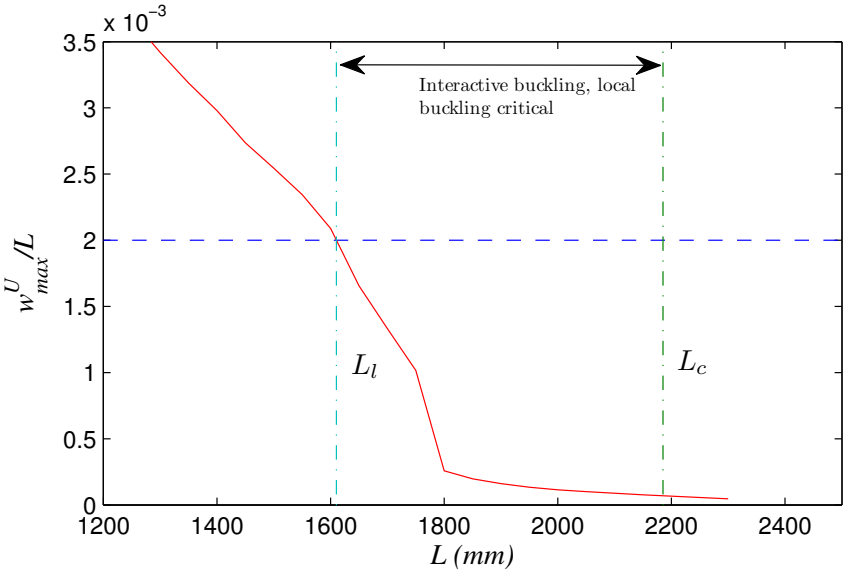

(b)

Figure 6.11: Graphs show (a) the normalized lateral displacement at the secondary bifurcation point q_s^{S} and (b) the normalized maximum local out-of-plane displacement $w^U_{\max}/L$ at the ultimate load P_U, versus the strut length L, for the cases where the global buckling and the local buckling are critical, respectively. The vertical dot-dashed line with label L_c represents the critical strut length where $P_o^{\mathrm{C}} = P_l^{\mathrm{C}}$. The horizontal dashed line represents the amount of displacement, above which the interactive buckling is assumed to be insignificant; the interactive region is therefore $L_l < L < L_o$, as shown by the vertical dot-dashed lines.

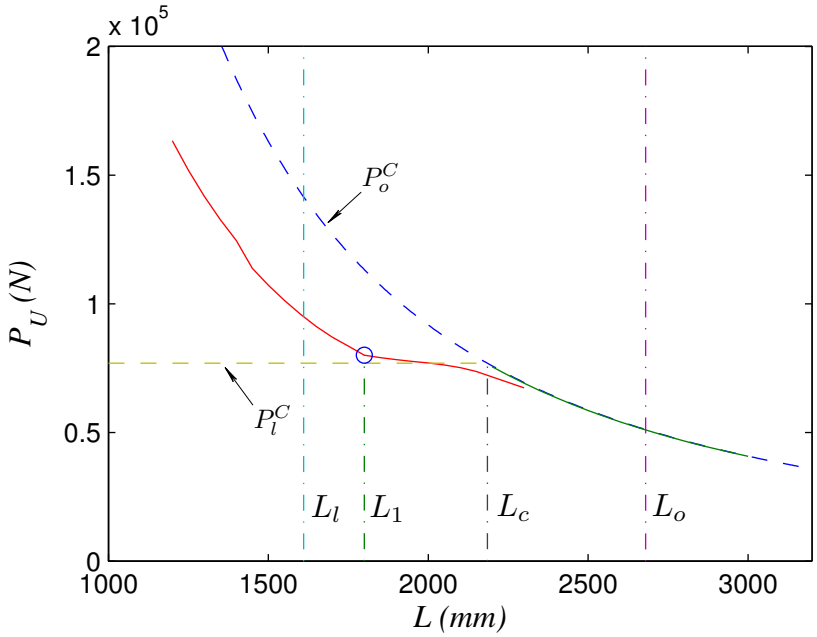

Figure 6.12: The graph shows the ultimate load P_U versus the strut length L. The solid lines represent the actual numerical solutions whereas the dashed lines represent the theoretical calculations of the global and local critical loads. Note that the local critical load is independent of the strut length and therefore represented by the horizontal dashed line. The vertical dot-dashed lines representing L_l, L_c and L_o directly correspond to Figure 6.5. The vertical dot-dashed line L_1 represents the strut length below which P_U begins to deviate from P_l^{C} significantly.

to be significantly higher than P_l^{C} for $L < 1800$ mm. This feature is also indicated by the dramatic change in the slope of the curve in Figure 6.11(b). This is caused by the different post-buckling behaviour after the secondary instability is triggered, which can be observed in Figure 6.13; and such a region is known by van der Neut (1969) as the 'imperfection

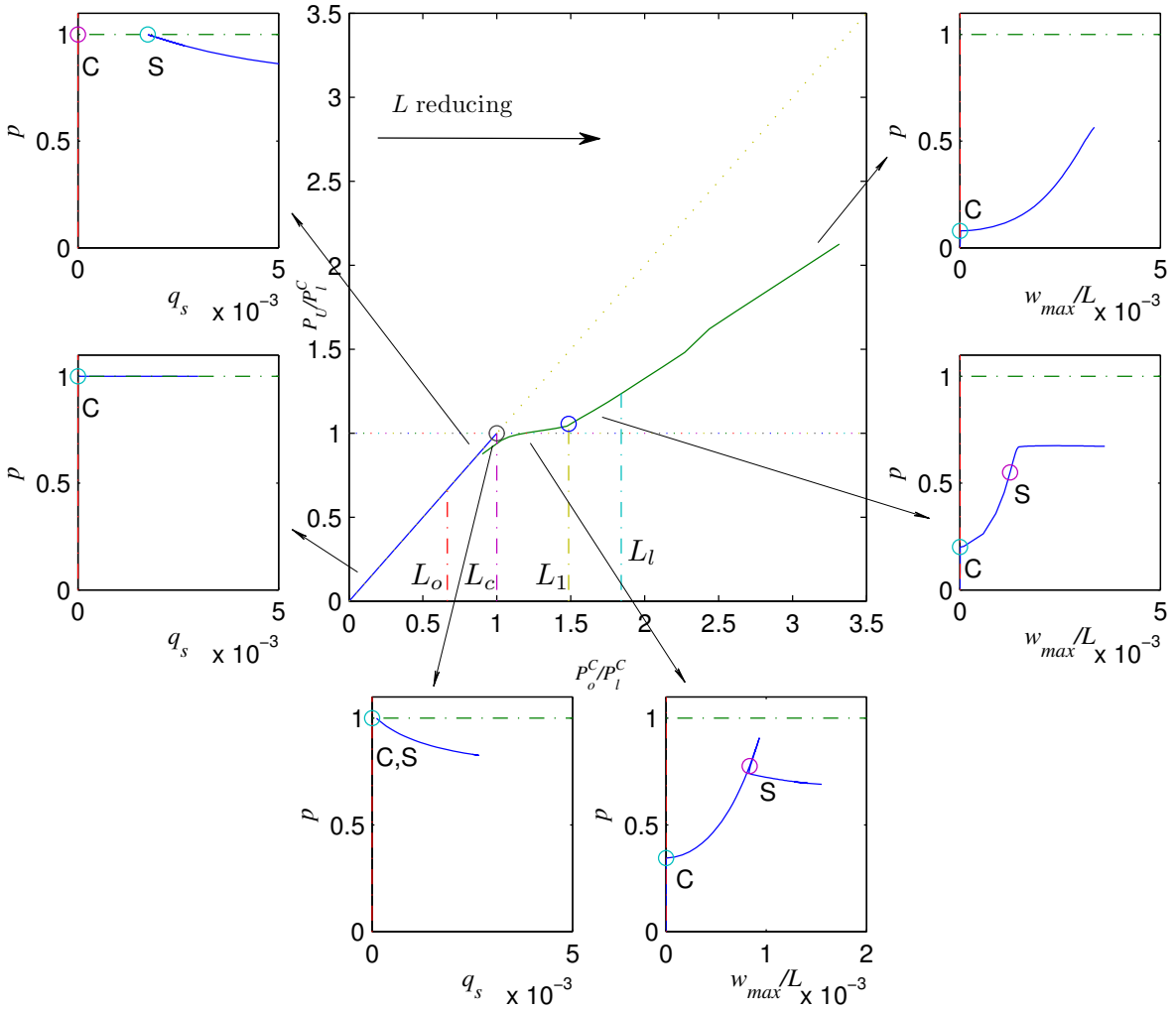

Figure 6.13: The central graph shows the normalized ultimate load P_U/P_l^{C} versus the normalized global critical load $P_o^{\mathrm{C}}/P_l^{\mathrm{C}}$. The solid lines represent the actual numerical solutions whereas the dot-dashed lines representing L_l, L_1, L_c and L_o correspond directly to Figure 6.12. The surrounding graphs show examples of the equilibrium paths corresponding to different parts of the central graph, separated by the dot-dashed lines. Labels C and S correspond to the primary and the secondary bifurcation points.

sensitive' zone. The point where P_U starts to deviate from P_l^{C} is denoted as L_1, as shown

in Figure 6.12. Note that numerical solutions for the cases where local buckling is critical are associated with a small local imperfection whereas the perfect system is analysed for the cases where global buckling is critical. The reduction in P_U caused by the imperfection is approximately 9.8% when $L \approx L_c$. Figure 6.13 shows similar graphs as in Figure 6.7. However, it can be observed in Figure 6.13 that for $L_1 < L < L_c$, the strut exhibits a strongly unstable interactive post-buckling path, whereas for $L_l < L < L_1$, the strut exhibits a weakly unstable (approximately neutral) interactive post-buckling path, after the secondary instability is triggered.

Finally, the flange width b is varied for the strut with the geometric properties in Table 6.2 and length L being fixed, for the fully rigid flange–web connection. It is observed in Figure 6.14 that struts with flange widths between $b_o = 88$ mm and $b_l = 120$ mm are most vulnerable to the interactive buckling behaviour, whereas struts with $b > b_l$ and $b < b_o$ are only vulnerable to pure local buckling and pure global buckling respectively. The critical strut length b_c when $P_o^{\mathrm{C}} = P_l^{\mathrm{C}}$ is found to be approximately 95 mm by both the theoretical expressions and the numerical solution. Figure 6.15 shows a very similar trend as in Figure 6.9. Similar to the case where L is varied, it is observed that for 95 mm $< b <$ 104 mm, the ultimate load P_U follows the local buckling critical load P_l^{C} closely, as shown by the dashed line, whereas P_U only starts to be significantly higher than P_l^{C} for $b >$ 104 mm. Therefore, for the range of flange widths 95 mm $< b <$ 104 mm, increasing the flange width would lead to a reduction in the load-carrying capacity. The point where P_U begins to deviate from P_l^{C} is denoted as b_1. The post-buckling behaviour for the strut with 95 mm $< b <$ 104 mm exhibits a stable, followed by a strongly unstable equilibrium path, whereas for $b >$ 104 mm, the strut exhibits a stable, followed by a weakly unstable equilibrium path, as shown in Figure 6.16.

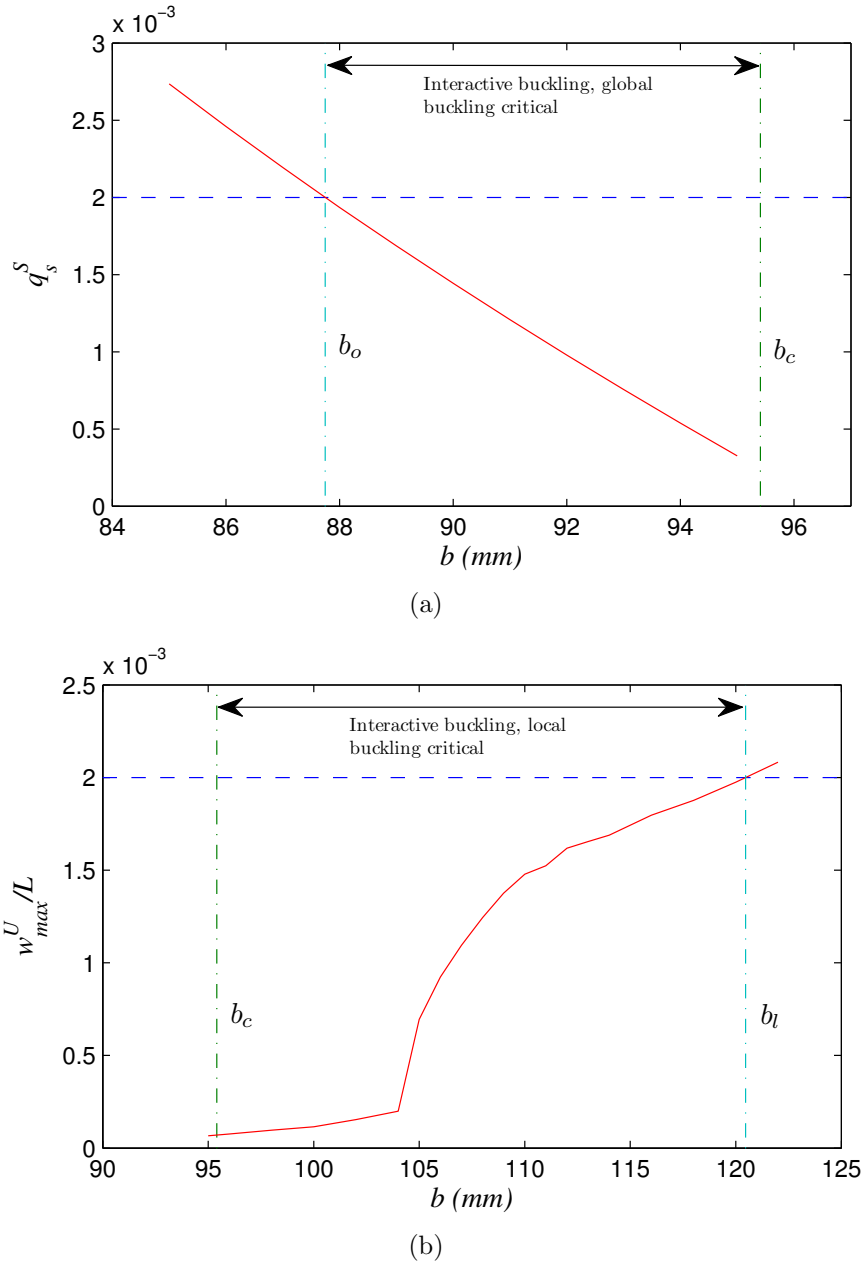

Figure 6.14: Graphs show (a) the normalized lateral displacement at the secondary bifurcation point q_s^{S} and (b) the normalized maximum local out-of-plane displacement $w_{\max}^U/L$ at the ultimate load P_U, versus the flange width b, for the cases where global buckling or local buckling is critical, respectively. The vertical dot-dashed line with label b_c represents the critical flange width where $P_o^{\mathrm{C}} = P_l^{\mathrm{C}}$. The horizontal dashed line represents the amount of displacement, above which interactive buckling is assumed to be insignificant; the interactive region is therefore $b_o < b < b_l$, as shown by the vertical dot-dashed lines.

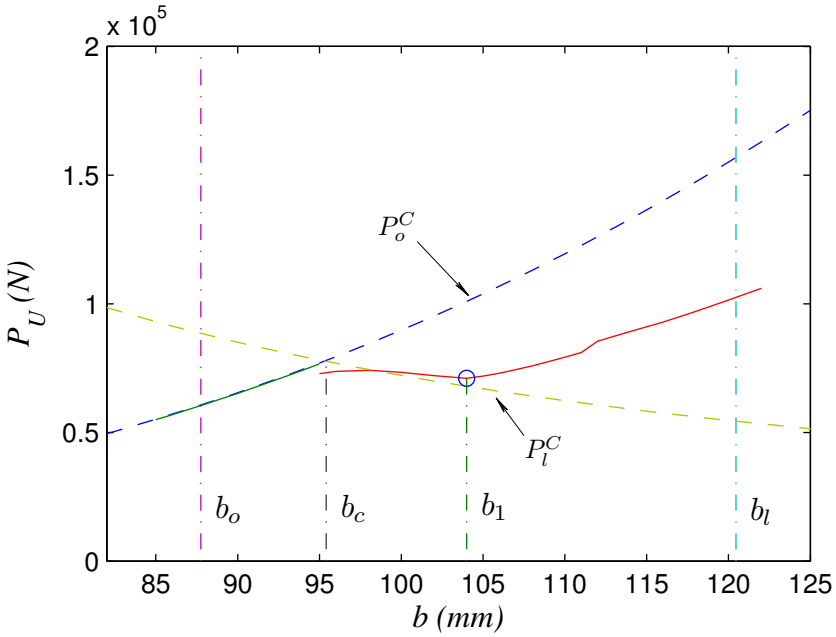

Figure 6.15: The graph shows the ultimate load P_U versus the flange width b. The solid lines represent the actual numerical solutions whereas the dashed lines represent the theoretical calculations of the global and local critical loads. Note that increasing b implies that the local critical load decreases whereas the global critical increases. The vertical dot-dashed lines representing b_l, b_c and b_o directly correspond to Figure 6.14. The vertical dot-dashed line b_1 represents the flange width above which P_U starts to deviate from P_l^{C} significantly.

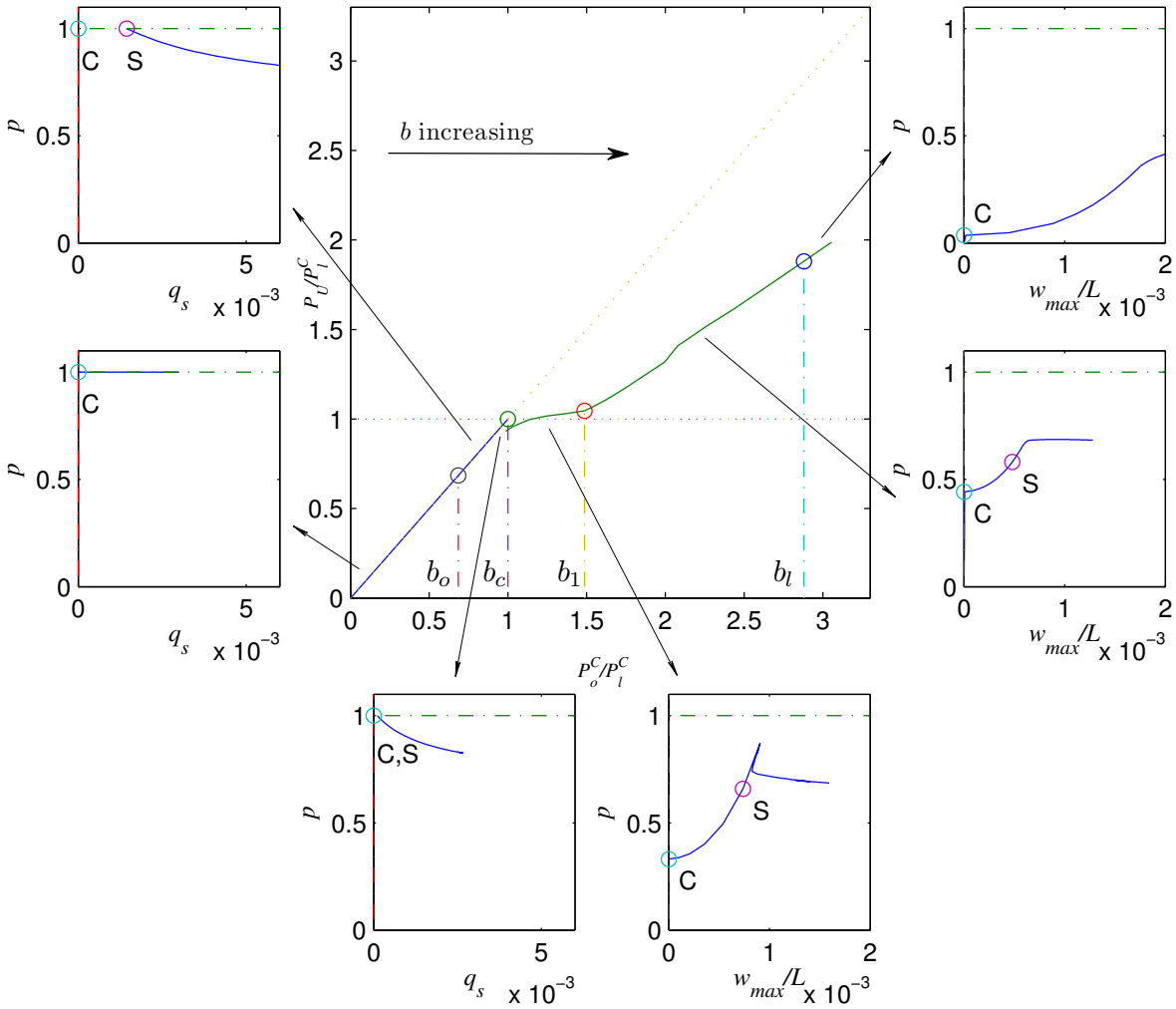

Figure 6.16: The central graph shows the normalized ultimate load P_U/P_l^{C} versus the normalized global critical load $P_o^{\mathrm{C}}/P_l^{\mathrm{C}}$. The solid lines represent the actual numerical solutions whereas the dot-dashed lines representing b_l, b_1 b_c and b_o correspond directly to Figure 6.15. The surrounding graphs show examples of the equilibrium paths corresponding to different parts of the central graph, separated by the dot-dashed lines. Labels C and S correspond to the primary and the secondary bifurcation points.

6.3.3 Interactive buckling zones

Tables 6.3 and 6.4 summarize, for both the pinned and the fully rigid flange–web connection, the region where the interactive buckling is significant and the post-buckling behaviour is highly unstable after the secondary instability is triggered, in terms of the strut length L and the flange width b respectively. It is clear that by increasing the

	$\min(L_l, L_1)$ (mm)	L_c (mm)	L_o (mm)
Pinned	2300	3700	5800
Rigid	1800	2300	2700

Table 6.3: Summary of values for L_l, L_1, L_c and L_o, for struts with the properties given in Table 6.1, for both the pinned and the fully rigid flange–web connection.

	$\min(b_l, b_1)$ (mm)	b_c (mm)	b_o (mm)
Pinned	92	74	65
Rigid	104	95	88

Table 6.4: Summary of values for b_l, b_1, b_c and b_o, for struts with the properties given in Table 6.2, for both the pinned and the fully rigid flange–web connection.

rigidity of the connection between the section web and flanges, the vulnerability to unstable interactive buckling is reduced, in terms of both the strut length L and the flange width b. Tables 6.5 and 6.6 summarize the values of the global and the local normalized slendernesses, $\bar{\lambda}_o$ and $\bar{\lambda}_l$, the values of which are calculated using Equations (6.14) and (6.15), directly corresponding to the values of the strut lengths and the flange widths given in Tables 6.3 and 6.4, respectively. Note that the global and the local normalized slendernesses, for each critical strut length L_c and flange width b_c, are approximately equal, and therefore denoted as a single notation $\bar{\lambda}_c$. Also note that when L is varied, the local normalized slenderness remains unchanged, and therefore $\bar{\lambda}_c = \bar{\lambda}_l$ as seen in Table 6.5. On the other hand, when b is varied, $\bar{\lambda}_c$ differs from both $\bar{\lambda}_l$ and $\bar{\lambda}_o$, as seen in Table 6.6. The values of global and the local normalized slendernesses given in Tables 6.5 and 6.6 are plotted on the idealized strength curves in Figure 6.17. Recall that a

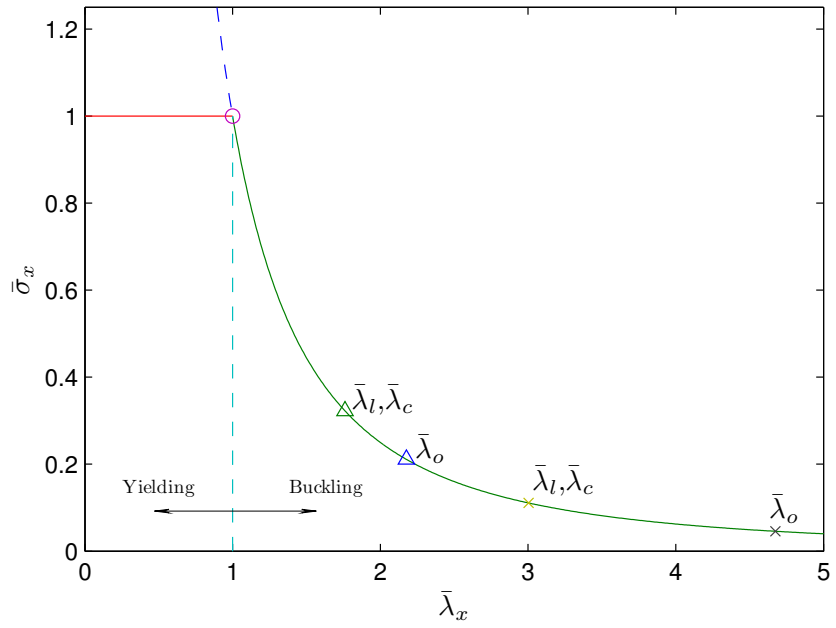

(a)

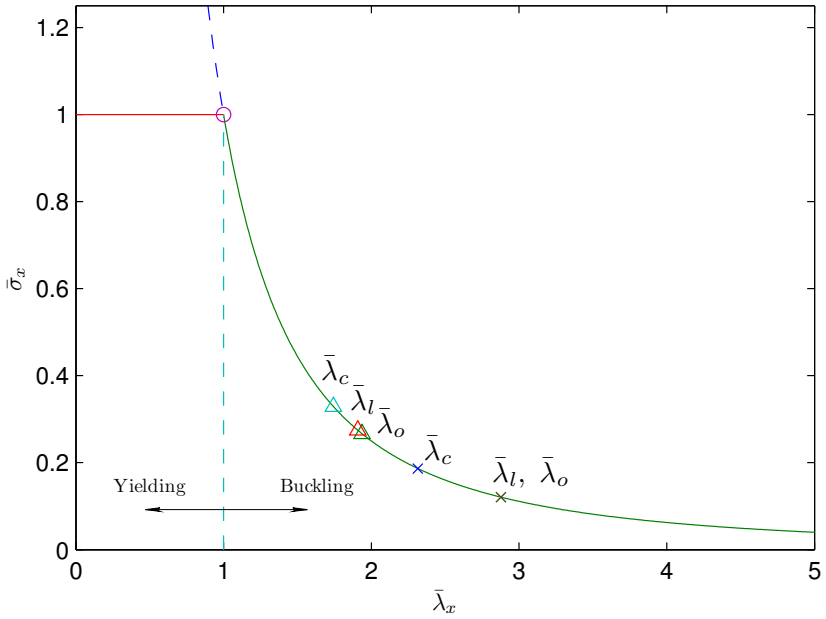

(b)

Figure 6.17: The idealized strength curves with the marks representing the global and the local normalized slendernesses given in Tables 6.5 and 6.6. Triangular marks and crosses represent the cases where the flange–web joint is assumed to be fully rigid and pinned respectively. Note that for the pinned case in (b), the global and the local slendernesses for the given geometry are very close, but not precisely equal.

	$\bar{\lambda}_l$	$\bar{\lambda}_c$	$\bar{\lambda}_o$
Pinned	3.00	3.00	4.68
Rigid	1.76	1.76	2.17

Table 6.5: Summary of values of $\bar{\lambda}_o$, $\bar{\lambda}_c$ and $\bar{\lambda}_l$, directly corresponding to the values of the strut lengths given in Table 6.3.

	$\bar{\lambda}_l$	$\bar{\lambda}_c$	$\bar{\lambda}_o$
Pinned	2.88	2.31	2.88
Rigid	1.91	1.74	1.94

Table 6.6: Summary of values of $\bar{\lambda}_o$, $\bar{\lambda}_c$ and $\bar{\lambda}_l$, directly corresponding to the values of the flange widths given in Table 6.4.

yield stress of 460N/mm^2 is assumed in the current study and that altering this would change the slendernesses. It is observed that for the chosen set of section properties, elastic buckling dominates the failure mechanism in the interactive region for all cases. The struts with fully rigid flange–web joints are less slender than the struts with pinned flange–web joints, and therefore closer to the region where plasticity would begin to alter the behaviour significantly. Nevertheless, for the chosen set of section properties, it is justified that plasticity effects would be negligible. For further studies with a wider range of section properties, the above procedure can be applied to investigate the possibility of any potential plasticity influence, so that a better estimation for the true load-carrying capacity may be obtained.

6.4 Concluding remarks

Parametric studies were conducted for an example set of geometries of a series of thin-walled I-section struts for two limiting cases where the web was assumed to provide a fully pinned or a fully rigid support to the flanges. The model in Chapter 3 is used for the fully pinned case, whereas the model in Chapter 5 is adapted slightly, for computational

reasons, to include a local imperfection, for the fully rigid case. The investigation focuses on changing the global and the local slendernesses by varying the strut length and the flange width respectively. A deflection based criterion was defined such that an interactive buckling dominated region, where the interaction between the weak-axis global (Euler) buckling and the local flange plate buckling, may be determined. For fully pinned flange–web connections, all struts within the interactive region exhibit unstable cellular buckling, including the cases where global buckling or local buckling is critical. For fully rigid flange–web connections, struts for the cases where global buckling is critical, exhibit unstable post-buckling responses without the observation of the cellular behaviour although the post-buckling profiles still exhibit changing wavelengths. However, for the cases where local buckling is critical, it is found that struts may exhibit two distinct post-buckling responses:

- a stable equilibrium path followed by a weakly unstable (approximately neutral) equilibrium path, or,
- a stable equilibrium path followed by a highly unstable equilibrium path.

It is the latter that should be avoided in design because of the high imperfection sensitivity associated with that characteristic response. It is found that by increasing the rigidity of the flange–web connection, the potentially dangerous region, where the highly unstable post-buckling behaviour is caused by the nonlinear mode interaction, becomes more confined.

The current methodology may be applied to determined the dominant interactive region with the section and material properties for a given set of basic geometries so long as the buckling occurs in the elastic range. However, since the normalized slenderness for local

and global buckling properties may be calculated, the analysis can determine whether plasticity effects need to be considered in a more advanced structural analysis.

Chapter 7

General conclusions

7.1 Conclusions

This thesis has presented a series of analytical models with increasing complexity that account for the interactive buckling phenomenon in axially-loaded thin-walled I-section columns with a varying rigidity of the flange–web connection. Using the calculus of variations, the analytical models have been developed based on elasticity theory and total potential energy principles. The models focus on the nonlinear interaction between a weak-axis Euler–type buckling mode and a local buckling mode of the flange plates. The highly unstable post-buckling behaviour has been highlighted; the vulnerability to cellular buckling behaviour has been revealed for columns with weak flange–web connections. Imperfection sensitivity and parametric studies were conducted; highlighting some important behaviour that needs particular attention in the context of structural design.

The investigation began with the focus on a limiting case where the web is assumed to provide a simple support to the flanges. Distinct features were captured by the numerical

examples for the cases where local buckling and global buckling were, in turn, critical. The section geometries were chosen such that the critical loads were sufficiently close so that interactive buckling was most likely to take place. For local buckling being critical, the strut initially followed the trivial fundamental path until the primary bifurcation point was reached; the flange plates then buckled locally and exhibited a stable post-buckling path until the secondary bifurcation point where the global mode was triggered. The local buckling in the less compressed side of the flange was rapidly contaminated by the global mode and the interaction between the local and the global modes resulted in highly unstable post-buckling behaviour. For global buckling being critical, the strut first buckled globally at the primary bifurcation point and followed the weakly stable post-buckling path until the secondary bifurcation point where local buckling of the flange plates was triggered.

Cellular buckling behaviour was revealed for both cases, implying that the struts exhibited a progressive failure which consisted of a sequence of destabilizing and restabilizing paths, known as snap-backs. The local buckling mode profile was initially the solution for a rectangular plate with three edges simply supported and one edge free (Bulson, 1970); each snap-back corresponded to the new formation of a peak or trough in the local buckling mode profile. The wavelength of the local out-of-plane buckling deflection pattern therefore reduced as the deformation progressed. The results compared excellently against recent published experiments and numerical studies (Becque, 2008; Becque & Rasmussen, 2009a; Becque & Rasmussen, 2009b). Most importantly, the experiments clearly showed the changing wavelength of the local buckling mode pattern, although the physical flange–web connection might have a higher rigidity than the simple support, as assumed in the analytical model at that stage. The earlier numerical studies (Becque & Rasmussen, 2009b), however, did not capture such a change in the local buckling wave-

length. Nevertheless, the comparisons were very encouraging and the analytical model was considered to be validated both qualitatively and quantitatively.

The model was then extended to include two types of geometric imperfections: an initial out-of-straightness (global imperfection) and an initial out-of-plane displacement of the flange plates (local imperfection). Imperfection sensitivity studies were carried out for three cases with a global imperfection only, a local imperfection only and both imperfections present. The results revealed the highly imperfection sensitive nature of the struts, with geometries such that the global and local critical loads were in close proximity, for both types of imperfections. Moreover, two forms of the local imperfection, namely a periodic and a modulated imperfection were examined. In order to carry out meaningful comparisons, the initial end shortening $\mathcal{E}_0$ is introduced; it is essentially a measure of the imperfection size that avoids using simply the amplitude. By keeping $\mathcal{E}_0$ constant, it was found that the modulated imperfections always result in a more severe reduction in the load-carrying capacity, although the effect on shorter struts is less severe than that on longer ones. It is also found that the worst case form for larger imperfections (larger $\mathcal{E}_0$) is always associated with a larger number of waves, but a smaller degree of modulation as may have been expected after the perfect case results are considered.

The model was then adapted to investigate the effect of varying rigidity of the flange–web connection, by introducing a rotational spring that restricts the rotation of the supporting edge of the flange about its longitudinal axis. The focus was on the case where global buckling was critical. The results showed a rapid erosion of the cellular behaviour as the stiffness of the rotational spring increases. The local critical buckling mode was associated with a large number of waves for larger rotational stiffnesses; therefore, the snap-backs reduce in number. It was also found that the restabilizing path gets shorter as the ro-

tational stiffness increases. The results were compared against a bespoke finite element model developed in ABAQUS. Shell elements were used and Riks analysis was performed with the introduced imperfection obtained from the linear eigenvalue analysis. The results showed good comparisons between the two models for large rotational stiffnesses, especially for the case where the web was assumed to provide a fixed support to the flanges ($c \to \infty$). However, similar to the numerical studies by Becque (2009b), the FE model does not capture the changing wavelength in the local buckling mode pattern, as the system proceeds along the equilibrium paths, which has been observed in a number of experimental studies (Becque & Rasmussen, 2009a; Wadee & Gardner, 2012). This is perhaps because the introduced local imperfection fixes the local buckling wavelength, which consequently resulted in the slightly larger error in the equilibrium paths. On the other hand, the analytical approach allows the system to find its own post-buckling profile after interactive buckling has been triggered and it seemed to track the physical experiments better than the FE model.

Parametric studies were conducted for two limiting cases where the web was assumed to provide a simple or a fully rigid support to the flanges. The global and local slendernesses were varied by changing the strut length and the flange width respectively. The results were presented in a similar way to the classic curve described by van der Neut (1969), as shown in Figure 2.8. The parametric regions most vulnerable interactive buckling were determined for both limiting cases. Since the global buckling and the local buckling of the flange plates are well understood, the focus was on investigating the post-buckling behaviour for the struts within the interactive region. For the pinned flange–web connection, the interaction between the global and the local mode always resulted in highly unstable cellular buckling behaviour. However, for the fixed flange–web connection, the results revealed a distinctive feature which was a weakly unstable (or approximately neu-

tral) post-buckling response, caused by the global and local mode interaction, for the cases where local buckling was critical. Similar behaviour was captured by van der Neut (1969), as shown in Figure 2.8. The parametric study allowed full investigations on the effect of changing section properties on the buckling and post-buckling behaviour of the thin-walled I-section strut. The analytical model identified the potentially dangerous region where the strut is most vulnerable to the highly unstable interactive and cellular post-buckling behaviour, which have to be treated with great caution in design considerations.

7.2 Future work

Hitherto, the analytical model has been developed to investigate the interaction between the weak-axis Euler buckling and the local buckling of the flange plates. However, in practice, weak-axis bending might be constrained, leading to a higher critical load; the strong-axis buckling may be critical under such conditions. The analytical model can be adapted to consider the interaction between the strong-axis global buckling and the local buckling of the flanges, as shown in Figure 7.1(a) and (b). Note that the local

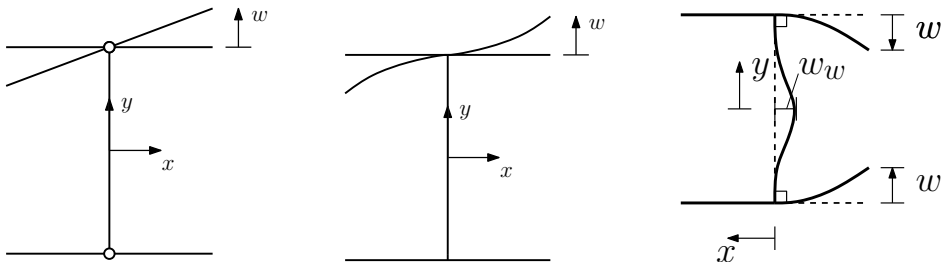

Figure 7.1: (a) and (b) show local buckling mode descriptions for major-axis global buckling for pinned and fully rigid flange–web connections respectively; (c) shows a local buckling mode description for minor-axis global buckling including the local buckling in the web.

buckling in the bottom flange is restricted by the strong-axis bending. Further studies on

the post-buckling load level within the section elements, when the local buckling mode becomes periodic, such that the Maxwell load P^{M} may be investigated, can be conducted by considering the 'body force' as in Hunt and Wadee (1998). Another extension to the current model is to include the effect of the local buckling in the web. Hitherto, the section geometries are chosen such that the critical stress for the local buckling of the web is much higher than that of the flanges. However, with increasing local web slenderness, the effect of web buckling would obviously become more important. This can be achieved by considering the moment continuity at the flange–web joint, hence relating the out-of-plane displacement of web w_w to the out-of-plane displacement of the flange w_f, as shown in Figure 7.1(c). Lipped sections are known to suffer from distortional buckling, with proper modelling of the boundary conditions of the flange plates, the interaction between the global and the distortional buckling mode may also be studied. Furthermore, the interactive buckling behaviour in the plastic range of the material can also be studied. Recall the Shanley model that was discussed in Chapter 2, after the strut has buckled globally, the release of the compressive stress in the convex side of the strut follows a different path in the stress–strain diagram, shown in Figure 2.4. This effect may apply to a piecewise linear or nonlinear stress–strain relationship that can be modelled by extending the current work.

As mentioned before, the current FE model finds difficulty in capturing the wavelength change of the local buckling mode pattern in the post-buckling range. However in a recent study (Brubak & Hellesland, 2011), the snap-back response is captured for a rectangular plate with three edges simply supported and one edge free by both a semi-analytical and an FE model, where the local buckling mode pattern develops from one half-wave to several half-waves in the longitudinal direction. The result encourages future development of the current FE model. Moreover, it has been found in the literature that ABAQUS/Explicit,

which solves equations of motion as opposed to static ones, is potentially capable of tracing sharp snap-backs in the post-buckling response (Degenhardt *et al.*, 2001). Therefore there is potential that future work will focus on treating the problem as a dynamical system within ABAQUS such that snap-backs may be replicated more readily.

Appendix A

Expressions for definite integrals

The full expressions of $\{f^2\}_x$, $\{f''^2\}_x$, $\{ff''^2\}_x$, $\{f'^2\}_x$, $\{f^4\}_x$, $\{xf^2\}_x$, $\{f'^2f^2\}_x$ and $\{f'f\}_x$, defined in Chapter 5 were obtained in MAPLE, thus:

$$\{f^2\}_x = \frac{b}{60\pi^3}\left(6\pi^3 s_2^2 + 15 s_4^2\pi^3 + 10\pi^3 - 15\pi^3 s_2 + 240\pi s_4 - 480\pi s_2 s_4 + 960 s_2 s_4\right), \quad \text{(A.1)}$$

$$\{f''^2\}_x = \frac{1}{4b^3}\left(128 s_2^2 + s_4^2\pi^4 + 64\pi s_2 s_4\right), \quad \text{(A.2)}$$

$$\{ff''^2\}_x = \frac{1}{12\pi b}\left(48\pi s_2 s_4 - 24\pi s_2 - 24\pi s_4 + 16\pi s_2^2 - 3 s_4^2\pi^3 - 192 s_2 s_4\right), \quad \text{(A.3)}$$

$$\{f'^2\}_x = \frac{1}{12\pi b}\left(-96\pi s_2 s_4 + 24\pi + 32\pi s_2^2 - 48\pi s_2 + 48\pi s_4 + 3 s_4^2\pi^3 + 192 s_2 s_4\right), \quad \text{(A.4)}$$

$$\{f^4\}_x = \frac{b}{15120\pi^7}\Big(1512\pi^7 - 5040\pi^7 s_2 + 6480\pi^7 s_2^2 - 3780\pi^7 s_2^3 + 840\pi^7 s_2^4 + 2786918400 s_2^3 s_4 - 69672960 s_2 s_4 \pi^2 + 358400 s_2 s_4^3 \pi^4 - 2903040 s_4 \pi^3 + 45360 s_4^2 \pi^5 + 7560 s_4^2 \pi^7 + 2835 s_4^4 \pi^7 + 362880 s_4 \pi^5 + 94080 s_4^3 \pi^5 + 696729600 \pi s_2^2 s_4 - 1393459200 \pi s_2^3 s_4 - 1451520 s_2 s_4 \pi^5 - 136080 s_2 s_4^2 \pi^5 + 90720 s_2^2 s_4^2 \pi^5 - 544320 s_2^2 s_4^2 \pi^3 + 34836480 s_2 s_4 \pi^3 + 1814400 s_2^2 s_4 \pi^5 - 87091200 s_2^2 s_4 \pi^3 - 725760 s_2^3 s_4 \pi^5 + 58060800 s_2^3 s_4 \pi^3 - 188160 s_2 s_4^3 \pi^5 - 11340 s_2 s_4^2 \pi^7 + 4536 s_2^2 s_4^2 \pi^7 + 544320 s_2 s_4^2 \pi^3\Big), \tag{A.5}$$

$$\{xf^2\}_x = -\frac{b^2}{240\pi^4}\Big(15\pi^4 - 24\pi^4 s_2 + 960\pi^2 s_4 + 11520 s_2 s_4 + 15 s_4^2 \pi^4 - 1440 s_2 s_4 \pi^2 + 10\pi^4 s_2^2 + 60 s_4^2 \pi^2 - 1920 \pi s_4\Big), \tag{A.6}$$

$$\{f'^2 f^2\}_x = \frac{1}{15120\pi^5 b}\Big(17280\pi^5 s_2^4 + 10080\pi^5 - 60480\pi^5 s_2^3 - 45360\pi^5 s_2 + 78624\pi^5 s_2^2 + 278691840 s_2^3 s_4 - 6773760 s_2 s_4 \pi^2 + 116480 s_2 s_4^3 \pi^4 - 241920 s_4 \pi^3 + 37800 s_4^2 \pi^5 + 1260 s_4^2 \pi^7 + 945 s_4^4 \pi^7 + 60480 s_4 \pi^5 + 33600 s_4^3 \pi^5 + 69672960 \pi s_2^2 s_4 - 139345920 \pi s_2^3 s_4 - 241920 s_2 s_4 \pi^5 - 98280 s_2 s_4^2 \pi^5 + 65520 s_2^2 s_4^2 \pi^5 - 151200 s_2^2 s_4^2 \pi^3 + 3386880 s_2 s_4 \pi^3 + 302400 s_2^2 s_4 \pi^5 - 8709120 s_2^2 s_4 \pi^3 - 120960 s_2^3 s_4 \pi^5 + 5806080 s_2^3 s_4 \pi^3 - 67200 s_2 s_4^3 \pi^5 - 1890 s_2 s_4^2 \pi^7 + 756 s_2^2 s_4^2 \pi^7 + 151200 s_2 s_4^2 \pi^3\Big), \tag{A.7}$$

$$\{f' f\}_x = -\frac{1}{2}\left(s_2 - s_4 - 1\right)^2. \tag{A.8}$$

Note that the expressions for s_2 and s_4 can be found in Equation (5.3).

References

Abaqus. 2011. *Version 6.10*. Providence, USA: Dassault Systèmes.

Ádány, S., & Schafer, B. W. 2006. Buckling mode decomposition of single-branched open cross-section members via finite strip method: derivation. *Thin-Walled Struct.*, **44(5)**, 563–584.

Akay, H. U., Johnson, C. P., & Will, K. M. 1977. Lateral and local buckling of beams and frames. *ASCE J. Struct. Eng.*, **103**(ST9), 1821–1832.

Allen, H. G. 1969. *Analysis and design of structural sandwich panels*. Oxford: Pergamon.

Augusti, G. 1964. Stabilitá di strutture elastiche in presenza di grandi spostamenti. *Atti Accad. Sci. fis. mat.*, **4**, No.5.

Basaglia, C., Camotim, D., & Silvestre, N. 2013. Post-buckling analysis of thin-walled steel frames using generalised beam theory (GBT). *Thin-Walled Struct.*, **62**, 229–242.

Becque, J. 2008. *The interaction of local and overall buckling of cold-formed stainless steel columns*. Ph.D. thesis, School of Civil Engineering, University of Sydney, Sydney, Australia.

Becque, J., & Rasmussen, K. J. R. 2009a. Experimental investigation of the interaction of local and overall buckling of stainless steel I-columns. *ASCE J. Struct. Eng.*, **135**(11), 1340–1348.

Becque, J., & Rasmussen, K. J. R. 2009b. Numerical investigation of the interaction of local and overall buckling of stainless steel I-columns. *ASCE J. Struct. Eng.*, **135**(11), 1349–1356.

Brockenbrough, R. L., & Merritt, F. S. 1999. *Structural steel designer's handbook*. 3rd edn. McGraw-Hill Education.

Brubak, L., & Hellesland, J. 2011. Semi-analytical postbuckling analysis of stiffened imperfect plates with a free or stiffened edge. *Comput. Struct.*, **89**, 1574–1585.

Bryan, G. H. 1891. On the stability of plane plate under thrust in its own plane with applications on the buckling of the sides of a ship. *Proc. Lond. Math. Soc.*, **22**, 54.

Budd, C. J., Hunt, G. W., & Kuske, R. 2001. Asymptotics of cellular buckling close to the Maxwell load. *Proc. R. Soc. A*, **457**, 2935–2964.

Budiansky, B. (ed). 1976. *Buckling of structures*. Berlin: Springer. IUTAM symposium.

Bulson, P. S. 1970. *The stability of flat plates*. London, UK: Chatto & Windus.

Burke, J., & Knobloch, E. 2007. Homoclinic snaking: Structure and stability. *Chaos*, **17**(3), 037102.

Chapman, S. J., & Kozyreff, G. 2009. Exponential asymptotics of localised patterns and snaking bifurcation diagrams. *Physica D*, **238**, 319–354.

Cherry, S. 1960. The stability of beams with buckled compression flanges. *The Structural Engineer*, **38**(9), 277–285.

Chilver, A. H. 1967. Coupled modes of elastic buckling. *J. Mech. Phys. Solids*, **15**, 15–28.

Clark, J. W., & Hill, H. N. 1960. Lateral buckling of beams. *ASCE J. Struct. Eng.*, **86**(ST7), 175–196.

Davids, A. J., & Hancock, G. J. 1986. Compression tests of long welded i-section columns. *ASCE J. Struct. Eng.*, **112(10)**, 2281–2297.

de Boor, C., & Swartz, B. 1973. Collocation at gaussian points. *SIAM J. Num. Anal.*, **10**, 582–606.

Degenhardt, R., Klein, H., Kling, A., Temmen, H., & Zimmermann, R. 2001 (October). *Buckling and post-buckling analysis of shells under quasi-static and dynamic loads*. Proceedings: Workshop 'Schwarzer Rumpf' (CFRP for Future Aircraft Structures), Braunschweig.

Den Hartog, J.P. 1961. *Strength of materials*. Dover Publications.

Dinis, P. B., Camotim, D., & Silvestre, N. 2010. On the local and global buckling behaviour of angle, t-section and cruciform thin-walled members. *Thin-Walled Struct.*, **48(10-11)**, 786–797.

Doedel, E. J., & Oldeman, B. E. 2009. AUTO-*07P: Continuation and bifurcation software for ordinary differential equations*. Tech. rept. Department of Computer Science, Concordia University, Montreal, Canada. Available from `http://indy.cs.concordia.ca/auto/`.

Euler, L. 1744. *Methodus inveniendi lineas curvas maximi minimive proprietate gaudentes*. Appendix: De curvis elasticis. Lausanne and Geneva.

Fox, C. 1987. *An introduction to the calculus of variations*. USA: Dover.

Gardner, L., & Nethercot, D. A. 2004a. Experiments on stainless steel hollow sections-part 2: member behaviour of columns and beams. *J. Constr. Steel Res.*, **60(9)**, 1319–1332.

Gardner, L., & Nethercot, D. A. 2004b. Numerical modeling of stainless steel structural components – A consistent approach. *ASCE J. Struct. Eng.*, **130**(10), 1586–1601.

Goltermann, P., & Møllmann, H. 1989. Interactive buckling in thin walled beams—II. applications. *Int. J. Solids Struct.*, **25**(7), 729–749.

Goncalves, R., & Camotim, D. 2004. Gbt local and global analysis of aluminium and stainless steel columns. *Comput. Struct.*, **82**, 1473–1484.

Goncalves, R., & Camotim, D. 2007. Thin-walled member plastic bifurcation analysis using generalized beam theory. *Adv. Eng. Softw.*, **38(8-9)**, 637–646.

Goodier, J. N. 1946. Cylindrical buckling of sandwich plates. *Trans. ASME J. Appl. Mech.*, **13(4)**, A253–A260.

Graves Smith, T. R., & Sridharan, S. 1978. A finite strip method for the post-locally-buckled analysis of plate structures. *Int. J. Mech. Sci.*, **20**, 833–842.

Hancock, G. J. 1978. Local, distortional and lateral buckling of I-beams. *ASCE J. Struct. Eng.*, **104**(11), 1787–1798.

Hancock, G. J. 1981. Interaction buckling in I-section columns. *ASCE J. Struct. Eng.*, **107**(1), 165–179.

Hemp, W. S. 1945. *The theory of flat panels buckled in compression.* Reports and Memoranda, No. 2178. Aeronautical Research Council.

Hunt, G. W., & da Silva, L. S. 1990. Interactive bending behaviour of sandwich beams. *Trans. ASME J. Appl. Mech.*, **57**, 189–196.

Hunt, G. W., & Lucena Neto, E. 1991. Localized buckling in long axially–loaded cylindrical shells. *J. Mech. Phys. Solids*, **39(7)**, 881–894.

Hunt, G. W., & Wadee, M. A. 1998. Localization and mode interaction in sandwich structures. *Proc. R. Soc. A*, **454**(1972), 1197–1216.

Hunt, G. W., Williams, K. A. J., & Cowell, R. G. 1986. Hidden symmetry concepts in the elastic buckling of axially-loaded cylinders. *Int. J. Solids Struct.*, **22(12)**, 1501–1515.

Hunt, G. W., da Silva, L. S., & Manzocchi, G. M. E. 1988. Interactive buckling in sandwich structures. *Proc. R. Soc. A*, **417**, 155–177.

Hunt, G. W., Lord, G. J., & Champneys, A. R. 1999. Homoclinic and heteroclinic orbits underlying the post-buckling of axially-compressed cylindrical shells. *Trans. ASME J. Appl. Mech.*, **170**, 239–251.

Hunt, G. W., Peletier, M. A., Champneys, A. R., Woods, P. D., Wadee, M. A., Budd, C. J., & Lord, G. J. 2000. Cellular buckling in long structures. *Nonlinear Dyn.*, **21**(1), 3–29.

Hunt, G. W., Lord, G. J., & Peletier, M. A. 2003. Cylindrical shell buckling: A characterization of localization and periodicity. *Discrete Contin. Dyn. Syst.-Ser. B*, **3**(4), 505–518.

Hutchinson, J. W., & Koiter, W. T. 1970. Postbuckling theory. *Appl. Mech. Rev.*, **23**, 1353–1366.

Johnson, A., & Winter, G. 1966. Behaviour of stainless steel columns and beams. *ASCE J. Struct. Eng.*, **92(ST5)**, 97–118.

Johnson, C. P., & Will, K. M. 1974. Beam buckling by finite element procedure. *ASCE J. Struct. Eng.*, **100**(ST3), 669–685.

Kawada, T. 2010. *History of the modern suspension bridge: solving the dilemma between economy and stiffness*. American Society of Civil Engineers.

Koiter, W. T. 1943. *The effective width at loads far in excess of the critical load for various boundary conditions*. N.L.L. Report, S287. Amsterdam.

Koiter, W. T. 1945. *On the stability of elastic equilibrium*. Ph.D. thesis, Technische Hogeschool, Delft, The Netherlands.

Koiter, W. T., & Pignataro, M. 1976. *A general theory for the interaction between local and overall buckling of stiffened panels*. Tech. rept. WTHD 83. Delft University of Technology, Delft, The Netherlands.

Lau, S. C. W., & Hancock, G. J. 1986. Buckling of thin flat-walled structures by a spline finite strip method. *ASCE J. Struct. Eng.*, **4**(4), 269–294.

Lau, S. C. W., & Hancock, G. J. 1989. Inelastic buckling analyses of beams, columns and plates using the spline finite strip method. *Thin-Walled. Struct.*, **7**(3-4), 213–238.

Leach, P., & Davies, J. M. 1996. An experimental verification of the generalized beam theory applied to interactive buckling problems. *Thin-Walled Struct.*, **25(1)**, 61–79.

Lord, G. J., Champneys, A. R., & Hunt, G. W. 1997. Computation of localised post-buckling in long axially compressed cylindrical shells. *Proc. R. Soc. A*, **335**, 2137–2150.

Lundquist, E. E., & Stowell, E. Z. 1942a. *Critial compressive stress for outstanding flanges*. Tech. rept. 734. NACA.

Lundquist, E. E., & Stowell, E. Z. 1942b. *Restraint provided a flat rectangular plate by a sturdy stiffener along an edge of the plate*. Tech. rept. 735. NACA.

Meier, M. 2009 (May). *Lüders bands in steel*. Available from http://vimeo.com/4586024.

Menken, C. M., Groot, W. J., & Stallenberg, G. A. J. 1991. Interactive buckling of beams in bending. *Thin-Walled Struct.*, **12**, 415–434.

Menken, C. M., Schreppers, G. M. A., Groot, W. J., & Petterson, R. 1997. Analyzing buckling mode interactions in elastic structures using an asymptotic approach; theory and experiments. *Comput. Struct*, **64**(1-4), 473–480.

Møllmann, H., & Goltermann, P. 1989. Interactive buckling in thin walled beams—I. theory. *Int. J. Solids Struct.*, **25**(7), 715–728.

Monagan, Michael B., Geddes, Keith O., Heal, K. Michael, Labahn, George, Vorkoetter, Stefan M., McCarron, James, & DeMarco, Paul. 2005. *Maple 10 programming guide*. Waterloo ON, Canada: Maplesoft.

Murray, N. W. 1973. Buckling of stiffened panels loaded axially and in bending. *The Structural Engineer*, **51(8)**, 285–301.

Norris, G., & Wagner, M. 2005. *Airbus A380: Superjumbo of the 21st century*. Zenith Press.

Orlebar, C. 2004. *The concorde story*. 6th edn. Osprey.

Plank, R. J., & Wittrick, W. H. 1974. Buckling under combined loading of thin, flat-walled structures by a complex finite strip method. *Int. J. Num. Meth. Eng.*, **8**(2), 323–339.

Powell, G., & Klingner, R. 1970. Elastic lateral buckling of steel beams. *ASCE J. Struct. Eng.*, **96**(ST9), 1419–1432.

Rajasekaran, S., & Murray, D. W. 1973. Coupled local buckling in wide-flange beam-columns. *ASCE J. Struct. Eng.*, **99**(ST6), 1003–1023.

Rasmussen, K. J. R., & Hancock, G. J. 1993. Design of cold-formed stainless steel tubular members. i: columns. *ASCE J. Struct. Eng.*, **119(8)**, 2349–2367.

Reissner, E. 1945. The effect of transverse shear deformation on the bending of elastic plates. *Trans. ASME J. Appl. Mech.*, **12**, A69–A77.

Riks, E. 1972. Application of Newton's method to problem of elastic stability. *Trans. ASME J. Appl. Mech.*, **39**(4), 1060–1065.

Russell, R. D., & Christiansen, J. 1978. Adaptive mesh selection strategies for solving boundary value problems. *SIAM J. Num. Anal.*, **15**, 59–80.

Saint-Venant, M. 1883. Discussion en théorie de l'elasticité des corps solides. *Clebsch*, **704**.

Saito, D., & Wadee, M. A. 2009. Numerical studies of interactive buckling in prestressed steel stayed columns. *Eng. Struct.*, **31(1)**, 1–15.

Schafer, B. W. 2002. Local, distortional, and Euler buckling of thin-walled columns. *ASCE J. Struct. Eng.*, **128**(3), 289–299.

Schafer, B. W. 2011. Cold-formed steel structures around the world – a review of recent advances in applications, analysis and design. *Steel Constr.*, **4(3)**, 1–9.

Schafer, B. W., & Peköz, T. 1999. Laterally braced cold-formed steel flexural members with edge stiffened flanges. *ASCE J. Struct. Eng.*, **125**(2), 118–127.

Schardt, R. 1994. Generalized beam theoryan adequate method for coupled stability problems. *Thin-Walled Struct.*, **19(2-4)**, 161–180.

Sewell, M. J. 1965. The static perturbation technique in buckling problems. *J. Mech. Phys. Solids*, **13**, 247–265.

Sewell, M. J. 1970. On the branching of equilibrium paths. *Proc. R. Soc. A*, **315**, 490–518.

Shanley, F. R. 1947. Inelastic column theory. *J. Aero. Sci.*, **14**(5), 261–276.

Shen, H. S., & Chen, T. Y. 1991. Buckling and postbuckling behaviour of cylindrical shells under combined external pressure and axial compression. *Thin-Walled Struct.*, **12**, 321–334.

Silvestre, N., & Camotim, D. 2003. Non-linear generalized beam theory for cold-formed steel members. *Int. J. Struct. Stab. Dyn.*, **3(4)**, 461–490.

Supple, W. J. 1967. Coupled branching configurations in the elastic buckling of symmetric structural systems. *Int. J. Mech. Sci.*, **9**, 97–112.

Svensson, S. E., & Croll, J. G. A. 1975. Interaction between local and overall buckling. *Int. J. Mech. Sci.*, **17**, 307–321.

Tata Steel. 2011. *Cold formed sections*. Brochure.

Taylor, C., & Dawes, J. H. P. 2010. Snaking and isolas of localised states in bistable discrete lattices. *Phys. Lett. A*, **375**, 14–22.

Thompson, J. M. T., & Hunt, G. W. 1973. *A general theory of elastic stability*. London: Wiley.

Thompson, J. M. T., & Hunt, G. W. 1984. *Elastic instability phenomena*. London: Wiley.

Thompson, J. M. T., & Lewis, G. M. 1972. On the optimum design of thin-walled compression members. *J. Mech. Phys. Solids*, **20**, 101–109.

Thompson, J. M. T., & Supple, W. J. 1973. Erosion of optimum design by compound branching phenomena. *J. Mech. Phys. Solids*, **21**, 135–144.

Timoshenko, S. P. 1910. Einige stabilitätsprobleme der elastizitätsprobleme der elastizitätstheorie. *Zeitschrift fr mathematik und physik*, **337**.

Timoshenko, S. P., & Gere, J. M. 1961. *Theory of elastic stability.* New York, USA: McGraw-Hill.

Timoshenko, S. P., & Woinowsky-Krieger, S. 1959. *Theory of plates and shells.* New York, USA: McGraw-Hill.

Trahair, N. S., Bradford, M. A., Nethercot, D. A., & Gardner, L. 2008. *The behaviour and design of steel structures to EC3.* 4th edn. Taylor & Francis.

Tsai, S. W. (ed). 1979. *Composite materials, testing and design.* New Orleans: American Society for Testing & Materials.

van der Heijden, G. H. M., Champneys, A. R., & Thompson, J. M. T. 2002. Spatially complex localisation in twisted elastic rods constrained to a cylinder. *Int. J. Solids Struct.*, **39**, 1863–1883.

van der Neut, A. 1969. The interaction of local buckling and column failure of thin-walled compression members. *Pages 389–399 of:* Hetényi, M., & Vincenti, W. G. (eds), *Proceedings of the 12th international congress on applied mechanics.* Berlin: Springer.

van der Neut, A. 1973. The sensitivity of thin-walled compression members to column axis imperfection. *Int. J. Solids Struct.*, **9**, 999–1011.

Wadee, M. A. 1998. *Localized buckling in sandwich structures.* Ph.D. thesis, University of Bath, Bath, UK.

Wadee, M. A. 2000. Effects of periodic and localized imperfections on struts on nonlinear foundations and compression sandwich panels. *Int. J. Solids Struct.*, **37**(8), 1191–1209.

Wadee, M. A. 2007. Nonlinear mathematics in structural engineering. *Mathematics Today*, **43**, 104–108.

Wadee, M. A., & Bai, L. 2014. Cellular buckling in I-section struts. *Thin-Walled Struct*, **81**, 89–100.

Wadee, M. A., & Blackmore, A. 2001. Delamination from localized instabilities in compression sandwich panels. *J. Mech. Phys. Solids*, **49(6)**, 1281–1299.

Wadee, M. A., & Edmunds, R. 2005. Kink band propagation in layered structures. *J. Mech. Phys. Solids*, **53**(9), 2017–2035.

Wadee, M. A., & Farsi, M. 2014. Cellular buckling in stiffened plates. *Proc. R. Soc. A.* Submitted.

Wadee, M. A., & Gardner, L. 2012. Cellular buckling from mode interaction in I-beams under uniform bending. *Proc. R. Soc. A*, **468**, 245–268.

Wadee, M. A., & Hunt, G. W. 1998. Interactively induced localized buckling in sandwich structures with core orthotropy. *Trans. ASME J. Appl. Mech.*, **65(2)**, 523–528.

Wadee, M. A., & Yiatros, S. 2011. Discussion: "On interactive buckling in a sandwich structure" by C. D. Coman. *Z. Angew. Math. Phys.*, **62(1)**, 183–188.

Wadee, M. A., Yiatros, S., & Theofanous, M. 2010. Comparative studies of localized buckling in sandwich struts with different core bending models. *Int. J. Non-Linear Mech.*, **45**(2), 111–120.

Wadee, M. K., Hunt, G. W., & Whiting, A. I. M. 1997. Asymptotic and Rayleigh–Ritz routes to localized buckling solutions in an elastic instability problem. *Proc. R. Soc. A*, **453**(1965), 2085–2107.

Wagner, M., & Norris, G. 2009. *Boeing 787 Dreamliner*. MBI Publishing Company.

Wang, S. 1997. A unified timoshenko beam b-spline rayleighritz method for vibration and buckling analysis of thick and thin beams and plates. *Int. J. Num. Meth. Eng.*, **40(3)**, 473–491.

Woods, P. D., & Champneys, A. R. 1999. Heteroclinic tangles and homoclinic snaking in the unfolding of a degenerate reversible hamiltonianhopf bifurcation. *Physica D*, **129**, 147–170.

Yiatros, S., & Wadee, M. A. 2011. Interactive buckling in sandwich beam-columns. *IMA J. Appl. Math.*, **76**, 146–168.